ABSTRACT

CHAMBERS, JAMES JOSEPH. Reactions for Yttrium Silicate High-k Dielectrics. (Under the direction of Dr. Gregory N. Parsons.)

The continued scaling of metal-oxide-semiconductor-field-effect-transistors (MOSFETs) will require replacing the silicon dioxide gate dielectric with an alternate high dielectric constant (high-k) material. We have exploited the high reactivity of yttrium with both silicon and oxygen to form yttrium silicate high-k dielectrics. Yttrium silicate films with composition of $(Y_2O_3)_x \cdot (SiO_2)_{1-x}$ and x = 0.32 to 0.87 are formed by oxidizing yttrium on silicon where yttrium reacts concurrently with silicon and oxygen. The competition between silicon and oxygen for yttrium is studied using X-ray photoelectron spectroscopy (XPS) and medium energy ion scattering (MEIS). The initial yttrium thickness mediates the silicon consumption, and a critical thickness (~40-80 Å) exists below which silicon is consumed to form yttrium silicate and above which Y_2O_3 forms without silicon incorporation. Engineered interfaces modify the silicon consumption, and a nitrided silicon interface results in film with composition close to Y_2O_3. The silicon consumption also depends on the oxidation temperature, and oxidation at higher temperature generally results in greater silicon incorporation with an activation energy of 0.3-0.5 eV. Yttrium silicate films (~40 Å) formed by oxidation of yttrium on silicon have an amorphous microstructure and an equivalent silicon dioxide thickness of ~12 Å with leakage current <1 A/cm^2. Yttrium silicate formation on silicon is also demonstrated using plasma oxidation of yttrium on silicon, reactive sputtering of yttrium and annealing/oxidation of yttrium on thermal SiO_2. The interface reactions described here for yttrium are expected to be active during both physical and chemical vapor deposition of other high-k dielectrics containing Hf, Zr and La.

REACTIONS FOR YTTRIUM SILICATE HIGH-K DIELECTRICS

by

JAMES JOSEPH CHAMBERS

A dissertation submitted to the Graduate Faculty of
North Carolina State University
in partial fulfillment of the
requirements for the Degree of
Doctor of Philosophy

CHEMICAL ENGINEERING

Raleigh

2000

APPROVED BY:

Dr. H. Henry Lamb	Dr. Mehmet C. Ozturk
Dr. Gregory N. Parsons Chair of Advisory Committee	Dr. David F. Ollis Co-chair of Advisory Committee

For Amanda,

who changed my life from the moment we met

JAMES JOSEPH CHAMBERS, son of Donald and Marge Chambers, was born on March 21st, 1969. Jim grew up in Munster, Indiana where he played the role of younger brother to his two older sisters, Dawn and April. His family moved to Parker, Texas just prior to high school. Jim attended school in Plano, Texas and graduated from Plano East Senior High School in 1987. The next stage found Jim at the University of Texas at Austin where he pursued an expansive education. Jim then followed his parents to Albuquerque, New Mexico where he attended the University of New Mexico. A change of venue was again in order, and Jim returned to Texas where he got a dog, Randy, and the dog got him a wife, Amanda. Jim and Amanda were married on March 6, 1993. Jim then took his new bride to luxurious accommodations in Albuquerque, New Mexico to return to school. Jim graduated from the University of New Mexico on May 13th, 1995 with a Bachelor of Science in Chemical Engineering. He then persuaded Amanda to move across the country to Raleigh, North Carolina so he could attend graduate school at the Department of Chemical Engineering at North Carolina State University. Jim performed research under the advisement of Dr. Gregory N. Parson who is probably surprised that Jim stayed for five years. After graduation, Jim and Amanda will finally get back to Dallas, Texas where he will begin his career at Texas Instruments.

ACKNOWLEDGEMENTS

I would like to express my deepest thanks to my parents whose constant support and encouragement was unflappable. I would like to thank my in-laws, Jim and Rebecca Morelock, for supporting Amanda and myself while I dragged their daughter back and forth across the country.

I am grateful to my advisor Dr. Parsons who gave me both the direction and the freedom to thoroughly experience the research process. Dr. Parsons had the wisdom to enable me achieve the most that I could after I came into his office and said that I didn't have enough to do. I just want to let him know that he gave me more than enough to do.

I want to thank Kit Yeung who has been a great technical teacher, a great life teacher and a great friend. I would never have been able to complete my reactor or my car repairs without his help.

I am indebted to my first mentor, Dr. Joseph Cecchi, for spurring my interest in semiconductors and encouraging me to pursue my Ph.D.

I am also grateful to all the members, past and present, of Dr. Parsons' research group including, Dr. Easwar Srinivassan, Dr. Ashfaqul Chowdhury, Dr. Tonya Klein, Dr. Laura Smith, Dr. Bill Epling, Bill Read, Chris Makosiej, Atul Gupta, Kevin Bray, Dong Niu and Jason Kelly. Special recognition is due Ashfaqul, Tonya, Atul and Bill for their helpful discussions and to Laura and Kevin for the AFM images. Special thanks go to Andy Lemmonds, Justin Bennett and Jeff Grimes who made excellent contributions to the reactor construction and research.

I would like to thank my advisory committee, Dr. Lamb, Dr. Ollis and Dr. Ozturk for their excellent mentoring. A special thanks goes to Dr. Kilpatrick and Dr. Misra for joining my mentoring team on short notice.

Thanks to all the guys at the AIF, especially John Phillips, who helped in obtaining the XP spectra.

Thanks to all the cleanroom people, especially Joan, who's all right by me.

Although this volume is dedicated to my wife Amanda, I also understand that this work has been a hardship on her as well and she deserves special recognition for all that she has been through. I am grateful for our life together past, present and future. To my eternal beloved.

J.C.

July 10, 2000

TABLE OF CONTENTS

		PAGE
LIST OF TABLES		x
LIST OF FIGURES		xi
1.	**INTRODUCTION**	1
1.1	HIGH-K DIELECTRICS FOR MOSFET TECHNOLOGY	1
1.2	OBJECTIVE	5
1.3	OVERVIEW OF DISSERTATION	5
1.4	REFERENCES	7
ABSTRACT:	PHYSICAL AND ELECTRICAL PROPERTIES OF YTTRIUM SILICATE THIN FILMS	10
2.	**PHYSICAL AND ELECTRICAL PROPERTIES OF YTTRIUM SILICATE THIN FILMS**	11
2.1	INTRODUCTION	11
2.2	EXPERIMENTAL	13
2.3	RESULTS AND DISCUSSION	14
2.4	CONCLUSIONS	16
2.5	ACKNOWLEDGEMENTS	17
2.6	REFERENCES	18
ABSTRACT:	PHYSICAL AND ELECTRICAL CHARACTERIZATION OF YTTRIUM SILICATE HIGH-K DIELECTRICS	28
3.	**PHYSICAL AND ELECTRICAL CHARACTERIZATION OF YTTRIUM SILICATE HIGH-K DIELECTRICS**	30
3.1	INTRODUCTION	30
3.2	EXPERIMENTAL	34
3.2.1	Sputtering and Surface Pretreatment System	34
3.2.2	Sample Preparation	35
3.2.3	Sputter Conditions	35
3.2.4	Silicidation Conditions	36
3.2.5	Thermal Oxidation Conditions	37
3.2.6	X-ray Photoelectron Spectroscopy	37
3.2.7	Medium Energy Ion Scattering	38
3.2.8	Electrical Measurements	38
3.2.9	Fourier Transform Infrared Spectroscopy	39
3.2.10	Atomic Force Microscopy	39
3.2.11	Transmission Electron Microscopy	39

3.3 RESULTS AND DISCUSSION 40
3.3.1 Analysis of Thick (4500 Å) Y-O-Si Films Formed by Oxidation of Yttrium Silicide 40
3.3.2 Analysis of thin (~40 Å) Y-O-Si Films Formed by Oxidation of Yttrium on Silicon 43
3.3.2.1 Physical characterization 43
3.3.2.2 Electrical characterization 45
3.3.3 Comparison of Thin Films Formed by Oxidation of Yttrium on Silicon with Thin Films Formed by Oxidation of Yttrium Silicide 46
3.3.4 Competition Between Silicide Formation and Oxidation 51
3.3.5 Analysis of Oxidation Kinetics 54
3.4 CONCLUSIONS 56
3.5 ACKNOWLEDGEMENTS 57
3.6 REFERENCES 58

ABSTRACT: YTTRIUM SILICATE FORMATION ON SILICON: EFFECT OF SILICON PRE-OXIDATION AND NITRIDATION ON INTERFACE REACTION KINETICS 95

4. YTTRIUM SILICATE FORMATION ON SILICON: EFFECT OF SILICON PRE-OXIDATION AND NITRIDATION ON INTERFACE REACTION KINETICS 97
4.1 INTRODUCTION 97
4.2 EXPERIMENTAL 98
4.3 RESULTS AND DISCUSSION 98
4.4 CONCLUSIONS 101
4.5 ACKNOWLEDGEMENTS 102
4.6 REFERENCES 103

ABSTRACT: INTERFACE REACTIONS DURING YTTRIUM SILICATE FORMATION ON SILICON 108

5. INTERFACE REACTIONS DURING YTTRIUM SILICATE FORMATION ON SILICON 110
5.1 INTRODUCTION 110
5.2 EXPERIMENTAL 112
5.3 RESULTS AND DISCUSSION 114
5.3.1 Oxidation of Yttrium on Silicon to Form Y-O-Si Films 114
5.3.2 Effect of Silicon Surface Pretreatments on Silicon Incorporation 118
5.3.3 Consumption of SiO_2 by Yttrium 124
5.4 CONCLUSIONS 127
5.5 ACKNOWLEDGEMENTS 128
5.6 REFERENCES 129

ABSTRACT: EFFECT OF OXIDATION TEMPERATURE ON YTTRIUM/SILICON INTERFACE REACTIONS DURING YTTRIUM SILICATE FORMATION ON Si(100) 152

6. EFFECT OF OXIDATION TEMPERATURE ON YTTRIUM/SILICON INTERFACE REACTIONS DURING YTTRIUM SILICATE FORMATION ON Si(100) 154
6.1 INTRODUCTION 154
6.2 EXPERIMENTAL 156
6.3 RESULTS 157
6.4 DISCUSSION 161
6.5 CONCLUSIONS 166
6.6 ACKNOWLEDGEMENTS 167
6.7 REFERENCES 168

ABSTRACT: CHEMICAL BONDING AND STRUCTURAL CHARACTERIZATION OF YTTRIUM SILICATE FILMS FORMED BY REMOTE PLASMA OXIDATION OF YTTRIUM ON SILICON 179

7. CHEMICAL BONDING AND STRUCTURAL CHARACTERIZATION OF YTTRIUM SILICATE FILMS FORMED BY REMOTE PLASMA OXIDATION OF YTTRIUM ON SILICON 181
7.1 INTRODUCTION 181
7.2 EXPERIMENTAL 183
7.3 RESULTS 184
7.4 DISCUSSION 188
7.5 CONCLUSIONS 192
7.6 ACKNOWLEDGEMENTS 192
7.7 REFERENCES 193

ABSTRACT: END-POINT UNIFORMITY SENSING AND ANALYSIS IN SILICON DIOXIDE PLASMA ETCHING USING *IN-SITU* MASS SPECTROMETRY 204

8. END-POINT UNIFORMITY SENSING AND ANALYSIS IN SILICON DIOXIDE PLASMA ETCHING USING *IN-SITU* MASS SPECTROMETRY 206
8.1 INTRODUCTION 206
8.2 EXPERIMENTAL SYSTEM AND PROCEDURE 207
8.2.1 ECR Etching System 207
8.2.2 Mass Spectrometric Process Sensing System 208
8.2.3 Silicon Dioxide Etching Procedure 209

8.3 RESULTS 212
8.3.1 Mass Spectrometric Sensing of Etch Process 212
8.3.2 Mass Spectrometric End-point Uniformity Sensing 212
8.4 UNIFORMITY ANALYSIS AND DISCUSSION 213
8.4.1 Etch End-point Uniformity Sensing 213
8.4.2 Etch End-point Uniformity Model 215
8.5 CONCLUSIONS 220
8.6 ACKNOWLEDGEMENTS 220
8.7 REFERENCES 221

9. SUMMARY 234

9.1 SUMMARY 234
9.1.1 Oxidation of Yttrium Silicide 234
9.1.2 Oxidation of Yttrium on Silicon 234
9.1.3 Yttrium/Silicon Interface Reactions 235
9.1.4 Plasma Oxidation of Yttrium on Silicon 236
9.1.5 End-point Uniformity Sensing 237
9.2 SUGGESTIONS FOR FUTURE WORK 237

APPENDICES 238

A. THERMAL OXIDATION OF SPUTTERED YTTRIUM 239

A.1 TWO-STEP OXIDATION 239
A.2 SPUTTER AUGER ELECTRON SPECTRSCOPY 241
A.3 ADDITIONAL TEM STUDIES 243

B. PLASMA OXIDATION 250

B.1 C-V TESTING OF PLASMA OXIDIZED Y-O-Si FILMS 250
B.2 REMOTE PLASMA OXIDATION OF TANTALUM ON SILICON 251

C. REACTIVE SPUTTERING OF YTTRIUM 253

C.1 ELLIPSOMETRY 253
C.2 FTIR 253
C.3 XPS 254
C.4 ELECTRICAL TESTING 254

LIST OF TABLES

PAGE

3. PHYSICAL AND ELECTRICAL CHARACTERIZATION OF YTTRIUM SILICATE HIGH-K DIELECTRICS

Table 3.1 Free energy of formation per oxygen atom for metal oxides and the expected oxidation products of their metal silicides. 64

8. END-POINT UNIFORMTIY SENSING AND ANALYSIS IN SILICON DIOXIDE PLASMA ETCHING USING *IN SITU* MASS SPECTROMETRY

Table 8.1 Assignments and sources for masses shown in Fig. 8.3. See text for reactions (8.2) to (8.6). 225

LIST OF FIGURES

PAGE

1. **INTRODUCTION**

Figure 1.1 Physical thickness versus EOT for SiO_2, k=15 and k=80. 9

2. **PHYSICAL AND ELECTRICAL PROPERTIES OF YTTRIUM SILICATE THIN FILMS**

Figure 2.1a Schematic depicting crystal structure of $Y_2Si_2O_7$. 19

Figure 2.1b Schematic depicting crystal structure of Y_2SiO_5.................................. 20

Figure 2.2 Y 3d portion of the XPS spectra for Y-O-Si and Y_2O_3. 21

Figure 2.3 Si 2p portion of the XPS spectra for Y-O-Si and SiO_2....................... 22

Figure 2.4 O 1s portion of the XPS spectrum for Y-O-Si, Y_2O_3 and SiO_2. 23

Figure 2.5a Mid-IR region of the FTIR spectrum for Y-O-Si and SiO_2. 24

Figure 2.5b Far-IR region of the FTIR spectrum for Y-O-Si and Y_2O_3. 25

Figure 2.6 AFM image for Y-O-Si with RMS surface roughness of 8.0 nm. 26

Figure 2.7 C-V curve for Y-O-Si with EOT = 5.0 nm. 27

3. **PHYSICAL AND ELECTRICAL CHARACTERIZATION OF YTTRIUM SILICATE HIGH-K DIELECTRICS**

Figure 3.1a Schematic depicting crystal structure of $Y_2Si_2O_7$. 61

Figure 3.1b Schematic depicting crystal structure of Y_2SiO_5.................................. 62

Figure 3.1c Y_2O_3-SiO_2 phase diagram. 63

Figure 3.2 Diagram of system used to sputter yttrium and perform vacuum anneals. 65

Figure 3.3a Y 3d region of the photoelectron spectra of Y-O-Si and Y_2O_3......... 66

Figure 3.3b Si 2p region of the photoelectron spectra of Y-O-Si and SiO_2. 67

Figure 3.3c O 1s region of the photoelectron spectra of Y-O-Si, Y_2O_3 and SiO_2. 68

Figure 3.4 Mid (a) and Far (b) IR regions of the FTIR spectrum for Y-O-Si, Y_2O_3 and SiO_2. 69

Figure 3.5a Survey spectrum for Y-O-Si film formed by oxidation of ~8 Å of yttrium on silicon at 900 °C. 70

Figure 3.5b Y 3d spectrum for Y-O-Si film formed by oxidation of ~8 Å of yttrium on silicon at 900 °C. 71

Figure 3.5c Si 2p spectrum for Y-O-Si film formed by oxidation of ~8 Å of yttrium on silicon at 900 °C. 72

Figure 3.5d O 1s spectrum for Y-O-Si film formed by oxidation of ~8 Å of yttrium on silicon at 900 °C. 73

Figure 3.6 TEM cross-section of a 42 Å Y-O-Si film formed by oxidation of ~8 Å of yttrium on silicon at 900 °C. 74

Figure 3.7 AFM image of an Y-O-Si film formed by oxidation of ~8 Å of yttrium on silicon at 900 °C. 75

Figure 3.8 Typical C-V curves for thin Y-O-Si films formed by oxidation of ~8 Å of yttrium on n- and p-type silicon at 900 °C with Al electrodes. 76

Figure 3.9 C-V curves from 10k-1M Hz for a thin Y-O-Si film formed by oxidation of ~8 Å of yttrium on n-type silicon at 900 °C with Al electrode. 77

Figure 3.10 J-V curves for Y-O-Si films on n- and p-type silicon presented in Fig. 3.8. 78

Figure 3.11a Y 3d spectra for 25 Å yttrium films oxidized at 600 °C and 25 °C. 79

Figure 3.11b Si 2p spectra for 25 Å yttrium films oxidized at 600 °C and 25 °C. 80

Figure 3.11c O 1s (c) spectra for 25 Å yttrium films oxidized at 600 °C and 25 °C. 81

Figure 3.12 Si 2p photoelectron spectra for Y-O-Si films formed by oxidation of yttrium on silicon and yttrium silicide at 900 °C (a) and 600 °C (b). 82

Figure 3.13 Diagram illustrating the processes used to form the films in Fig. 3.11, 3.12 and 3.14. 83

Figure 3.14a Y 3d spectra for films formed by the oxidation at 600 °C of yttrium (30 Å) on silicon and yttrium silicide. 84

Figure 3.14b Si 2p spectra for films formed by the oxidation at 600 °C of yttrium (30 Å) on silicon and yttrium silicide. 85

Figure 3.14c O 1s spectra for films formed by the oxidation at 600 °C of yttrium (30 Å) on silicon and yttrium silicide. 86

Figure 3.15a Y 3d spectra for ~8-240 Å yttrium films on silicon oxidized at 900 °C. Initial yttrium coverage <40 Å results in an Y-O-Si film. 87

Figure 3.15b Si 2p spectra for ~8-240 Å yttrium films on silicon oxidized at 900 °C. 88

Figure 3.15c O 1s spectra for ~8-240 Å yttrium films on silicon oxidized at 900 °C. 89

Figure 3.16 Diagram illustrating the film structure obtained for thin and thick initial yttrium coverage. 90

Figure 3.17 Si-O/Si area ratio for yttrium films on silicon oxidized at 600 ( ) and 900 °C( ) plotted with thickness data from cross-section TEM images for Y-O-Si films oxidized at 900 °C ( ) and from ellipsometry for SiO_2 films grown at 900 °C ( ). 91

Figure 3.18 Cross-sectional TEM image for ~8 Å yttrium film on silicon oxidized for 20 minutes at 900 °C. 92

Figure 3.19 Si 2p region for an ~8 Å yttrium film on silicon oxidized for 20 minutes at 900 °C. 93

Figure 3.20 Y 3d region for ~8 Å yttrium films on silicon oxidized at 900 °C for 6 seconds to 20 minutes. 94

4. YTTRIUM SILICATE FORMATION ON SILICON: EFFECT OF SILICON PRE-OXIDATION AND NITRIDATION ON INTERFACE REACTION KINETICS

Figure 4.1 Y 3d photoelectron spectra for films formed on a) silicon, b) silicon oxide, c) nitrided oxide and d) nitrided silicon.................... 104

Figure 4.2 O 1s photoelectron spectra for films formed on a) silicon, b) silicon oxide, c) nitrided oxide and d) nitrided silicon.................... 105

Figure 4.3 Si 2p photoelectron spectra for films formed on a) silicon, b) silicon oxide, c) nitrided oxide and d) nitrided silicon.................... 106

Figure 4.4 MEIS energy spectra for films formed on a) silicon and d) nitrided silicon.. 107

5. INTERFACE REACTIONS DURING YTTRIUM SILICATE FORMATION ON SILICON

Figure 5.1a Y 3d region of the XP spectrum for a Y-O-Si film formed by oxidation of an ~8 Å yttrium film on silicon at 900 °C for 15 seconds.. 131

Figure 5.1b Si 2p region of the XP spectrum for a Y-O-Si film formed by oxidation of an ~8 Å yttrium film on silicon at 900 °C for 15 seconds. 132

Figure 5.1c O 1s region of the XP spectrum for a Y-O-Si film formed by oxidation of an ~8 Å yttrium film on silicon at 900 °C for 15 seconds. 133

Figure 5.2 MEIS spectrum for a Y-O-Si film formed by oxidation of an ~8 Å yttrium film on silicon at 900 °C for 15 seconds. 134

Figure 5.3a Angle resolved XPS of the Y 3d region for a Y-O-Si film formed by oxidation of a ~25 Å yttrium film on silicon at 900 °C for 2 minutes.. 135

Figure 5.3b Angle resolved XPS of the Si 2p region for a Y-O-Si film formed by oxidation of a ~25 Å yttrium film on silicon at 900 °C for 2 minutes.. 136

Figure 5.3c Angle resolved XPS of the O 1s region for a Y-O-Si film formed by oxidation of a ~25 Å yttrium film on silicon at 900 °C for 2 minutes.. 137

Figure 5.4	Cross-sectional TEM image of a Y-O-Si film formed by oxidation of an ~8 Å yttrium film on silicon at 900 °C for 15 seconds.	138
Figure 5.5	Typical 1 MHz C-V curve for an Al/Y-O-Si/n-type capacitor.	139
Figure 5.6	Si 2p (a) and N 1s (b) spectra for the silicon surface pretreatments used in this study: (1) clean silicon, (2) plasma oxidized silicon, (3) plasma nitrided-oxidized silicon, and, (4) plasma nitrided silicon.	140
Figure 5.7a	Y 3d regions of the XP spectra for the Y-O-Si films formed on: (1) clean silicon, (2) plasma oxidized silicon, (3) plasma nitrided-oxidized silicon, and, (4) plasma nitrided silicon.	141
Figure 5.7b	Si 2p region of the XP spectra for the Y-O-Si films formed on: (1) clean silicon, (2) plasma oxidized silicon, (3) plasma nitrided-oxidized silicon, and, (4) plasma nitrided silicon.	142
Figure 5.7c	O 1s region of the XP spectra for the Y-O-Si films formed on: (1) clean silicon, (2) plasma oxidized silicon, (3) plasma nitrided-oxidized silicon, and, (4) plasma nitrided silicon.	143
Figure 5.8	MEIS spectra for the Y-O-Si films formed on: (1) clean silicon, (2) plasma oxidized silicon, (3) plasma nitrided-oxidized silicon, and, (4) plasma nitrided silicon.	144
Figure 5.9	Calculated MEIS depth profiles for the Y-O-Si films formed on (1) clean silicon and (4) nitrided silicon.	145
Figure 5.10a	Y 3d spectra for a 40 Å reference SiO_2 and ~25 Å yttrium films on 40 Å SiO_2 oxidized at 600 and 900 °C for 2 minutes.	146
Figure 5.10b	Si 2p spectra for a 40 Å reference SiO_2 and ~25 Å yttrium films on 40 Å SiO_2 oxidized at 600 and 900 °C for 2 minutes.	147
Figure 5.10c	O 1s spectra for a 40 Å reference SiO_2 and ~25 Å yttrium films on 40 Å SiO_2 oxidized at 600 and 900 °C for 2 minutes.	148
Figure 5.11a	Y 3d spectra for a 40 Å reference SiO_2 and a ~25 Å yttrium film on 40 Å SiO_2 annealed in vacuum at 600 °C for 2 minutes.	149
Figure 5.11b	Si 2p spectra for a 40 Å reference SiO_2 and a ~25 Å yttrium film on 40 Å SiO_2 annealed in vacuum at 600 °C for 2 minutes.	150

Figure 5.11c O 1s (c) spectra for a 40 Å SiO_2 and a ~25 Å yttrium film on 40 Å SiO_2 annealed in vacuum at 600 °C for 2 minutes. 151

6. EFFECT OF OXIDATION TEMPERATURE ON YTTRIUM/SILICON INTERFACE REACTIONS DURING YTTRIUM SILICATE FORMATION ON Si(100)

Figure 6.1a Y 3d region of the photoelectron spectra for oxidation at 25 to 900 °C of 25 Å yttrium films on silicon. 170

Figure 6.1b Si 2p region of the photoelectron spectra for oxidation at 25 to 900 °C of 25 Å yttrium films on silicon. 171

Figure 6.1c O 1s region of the photoelectron spectra for oxidation at 25 to 900 °C of 25 Å yttrium films on silicon. 172

Figure 6.2 Y 3d angle resolved XPS spectra for take-off angles from 20° to 90° for 25 Å yttrium films on silicon oxidized at 600 and 900 °C. 173

Figure 6.3 Si 2p angle resolved XPS spectra for take-off angles from 20° to 90° for 25 Å yttrium films on silicon oxidized at 600 and 900 °C. 174

Figure 6.4 O 1s angle resolved XPS spectra for take-off angles from 20° to 90° for 25 Å yttrium films on silicon oxidized at 600 and 900 °C. 175

Figure 6.5 MEIS proton energy spectra for 25 Å yttrium films on silicon oxidized at 600 and 900 °C. 176

Figure 6.6 Compilation of the results presented in Figs. 1 and 5. The Y $3d_{5/2}$ ( ) and Si 2p ( ) binding energies, Si-O/Y area ratio ( ), Si/Y ratio ( ) and thickness (♦) are plotted versus the oxidation temperature. 177

Figure 6.7 Arrhenius plot of the Si-O/Si area ratio ( ) and MEIS silicon fraction times thickness ( ) versus inverse temperature for oxidation from 500 to 900 °C. 178

7. CHEMICAL BONDING AND STRUCTURAL CHARACTERIZATION OF YTTRIUM SILICATE FILMS FORMED BY REMOTE PLASMA OXIATION OF YTTRIUM ON SILICON

Figure 7.1a Y 3d region of the photoelectron spectra for (1) 30 Å yttrium on silicon remote N_2O plasma oxidized for 60 minutes at 100 °C, (2) 30 Å yttrium on silicon remote N_2O plasma oxidized for 60 minutes at 300 °C, and, (3) 30 Å yttrium on silicon remote N_2O plasma oxidized for 60 minutes at 100 °C followed by post-oxidation anneal for 4 hours at 900 °C in 1 atm. N_2. 194

Figure 7.1b Si 2p region of the photoelectron spectra for (1) 30 Å yttrium on silicon remote N_2O plasma oxidized for 60 minutes at 100 °C, (2) 30 Å yttrium on silicon remote N_2O plasma oxidized for 60 minutes at 300 °C, and, (3) 30 Å yttrium on silicon remote N_2O plasma oxidized for 60 minutes at 100 °C followed by post-oxidation anneal for 4 hours at 900 °C in 1 atm. N_2. 195

Figure 7.1c O 1s region of the photoelectron spectra for (1) 30 Å yttrium on silicon remote N_2O plasma oxidized for 60 minutes at 100 °C, (2) 30 Å yttrium on silicon remote N_2O plasma oxidized for 60 minutes at 300 °C, and, (3) 30 Å yttrium on silicon remote N_2O plasma oxidized for 60 minutes at 100 °C followed by post-oxidation anneal for 4 hours at 900 °C in 1 atm. N_2. 196

Figure 7.2.1 Cross-sectional TEM image of a 30 Å yttrium film on silicon remote N_2O plasma oxidized for 60 minutes at 100 °C. 197

Figure 7.2.3 Cross-sectional TEM image of a 30 Å yttrium film on silicon remote N_2O plasma oxidized for 60 minutes at 100 °C followed by a post-oxidation anneal for 4 hours at 900 °C in N_2. 197

Figure 7.3.1 RHEED image of a 30 Å yttrium film on silicon remote N_2O plasma oxidized for 60 minutes at 100 °C. 198

Figure 7.3.2 RHEED image of a 30 Å yttrium film on silicon remote N_2O plasma oxidized for 60 minutes at 300 °C. 198

Figure 7.3.3 RHEED image of a 30 Å yttrium film on silicon remote N_2O plasma oxidized for 60 minutes at 100 °C followed by a post-oxidation anneal for 4 hours at 900 °C in N_2. 199

Figure 7.4 AFM images for (1) 30 Å yttrium on silicon remote N_2O plasma oxidized for 60 minutes at 100 °C (RMS = 8.9 Å), (2) 30 Å yttrium on silicon remote N_2O plasma oxidized for 60 minutes at 300 °C (RMS = 1.4 Å), and, (3) 30 Å yttrium on silicon remote N_2O plasma oxidized for 60 minutes at 100 °C followed by post-oxidation anneal for 4 hours at 900 °C in 1 atm. N_2 (RMS = 1.7 Å)........ 200

Figure 7.5 AFM images for 30 Å yttrium on silicon remote N_2O plasma oxidized for zero (a), 5 (b), 10 (c) and 20 minutes (d) at 100 °C........ 201

Figure 7.6 Results of AFM RMS roughness measurements for 30 Å yttrium on silicon remote N_2O plasma oxidation for zero, 5, 10, 20 and 60 minutes at 100 °C ( ), remote N_2O plasma oxidized for 60 minutes at 300 °C ( ) and film post-oxidation annealed for 4 hours at 900 °C in 1 atm. N_2 ( )....... 202

Figure 7.7 Results of J-V testing of a 30 Å yttrium on silicon remote N_2O plasma oxidation for 60 minutes at 300 °C. 203

8. END-POINT UNIFORMTIY SENSING AND ANALYSIS IN SILICON DIOXIDE PLASMA ETCHING USING *IN SITU* MASS SPECTROMETRY

Figure 8.1 Electron cyclotron resonance plasma reactor used for silicon dioxide etching........ 223

Figure 8.2 Schematic of the two stage differentially pump mass spectrometer system utilized in these investigations. 224

Figure 8.3 Real-time intensity signals for the masses monitored in these investigations........ 226

Figure 8.4 Real-time CO^+ intensity for wafer uniformly (97.7%) covered by 1000 Å oxide (solid line), 67% thickness uniformity (50% 1000 Å SiO_2 coverage) wafer (dashed line) and 60% thickness uniformity (75% 1000 Å SiO_2 coverage) wafer (dotted line). 227

Figure 8.5 Real-time CO^+ intensity for uniformity series performed on uniform oxide films........ 228

Figure 8.6 Real-time CO^+ intensity for uniformity series performed on uniform oxide films........ 229

Figure 8.7 Averaged slope of real-time CO^+ intensity for 94.7%, 92.1% and 86.2% uniformity versus time. 230

Figure 8.8 Uniformity versus the inverse of the initial slope [s/a.u./10^{10}] for the uniform and non-uniform films (solid points) and first derivative [s-cm^3/moles/2.6 X 10^{12}] of the model (solid line). 231

Figure 8.9 First derivative versus time of COF_2 concentration from material balance model. The first derivative at the end-point beginning ($t=z_o/a$) is correlated with the uniformity in Fig. 8.8. 232

Figure 8.10 Average slope of real-time CO^+ intensity for the 94.7% uniformity case. 233

APPENDIX A TWO-STEP OXIDATION

Figure A.1 C-V curves for one- (a) and two-step (b) oxidation processes. 240

Figure A.2 AES surface spectrum (a) and AES depth profile (b) for ~8 Å yttrium film on silicon oxidized for 15 seconds in 1 atm. air. 242

Figure A.3.1 TEM images for 6 second (a) and 15 second (b) oxidation. 244

Figure A.3.2 TEM image for 60 second (c) oxidation. 245

Figure A.4.1 TEM images for 1 second (a) and 15 second (b) oxidation. 246

Figure A.4.2 TEM images for 1 minute (c) and 2 minute (d) oxidation. 247

Figure A.4.3 TEM image for 20 minute (e) oxidation. 248

Figure A.5 TEM images for 15 second oxidation taken at different transmission thickness. 249

APPENDIX B PLASMA OXIDATION

Figure B.1 C-V of Y-O-Si film formed by remote N_2O plasma oxidation. 250

Figure B.2 Ta 4f, Si 2p and O 1s regions of the XP spectrum for Ta films on silicon remote plasma oxidized at 100 °C. 252

APPENDIX C REACTIVE SPUTTERING OF YTTRIUM

Figure C.1 Thickness (a) and refractive index (600 nm) (b) from ellipsometry for reactively sputtered Y-O-Si films. 256

Figure C.2 FTIR spectra for reactively sputtered Y-O-Si films. The films were deposited with a Ar:N_2O ratio of 1:2 at a substrate temperature of 25 °C.. 257

Figure C.3 Y 3d, Si 2p and O 1s regions of the XP spectra for Y-O-Si films deposited by reactive sputtering. 258

Figure C.4 C-V characteristic of Y-O-Si film deposited by reactive sputtering... 259

CHAPTER 1

INTRODUCTION

1.1 HIGH-K DIELECTRICS FOR MOSFET TECHNOLOGY

Silicon dioxide has been the gate dielectric of choice since 1960 when it was first proposed that thermally grown SiO_2 should be used as the gate insulator in metal-oxide-semiconductor-field-effect-transistors (MOSFETs).[1] Research, development and production over the past four decades have shown SiO_2 to exhibit superior low-defect interfacial properties and to provide excellent passivation of the silicon surface from contamination. The properties of silicon dioxide have been characterized as well as any other dielectric, and SiO_2 is entrenched as one of the most basic components in silicon technology. Progress in silicon integrated circuit technology has been dominated by the reduction in gate length to increase device performance and integration. To keep pace with drive current demands, the silicon dioxide gate dielectric thickness must also scale in accordance with the gate length. In the past, scaling the gate dielectric thickness has simply been handled by a recipe change where either the oxidation time or temperature was decreased to net a thinner dielectric. However, scaling the dielectric thickness has resulted in device degradation in recent years.

As a result of device scaling, boron penetration from the polysilicon gate electrode through the silicon dioxide gate dielectric into the channel region has become a major concern. Boron depletion causes both an increase in the equivalent oxide thickness (EOT) and threshold voltage shifting. However, incorporating nitrogen into the silicon dioxide gate dielectric has been demonstrated to reduce boron penetration, reduce electrically active traps and defects at the SiO_2/Si interface and improve device reliability.[2,3] Many techniques have

been explored to achieve the desired nitrogen profiles in the thin silicon dioxide, including furnace annealing, rapid thermal annealing and remote plasma nitridation.[3-5] Even though nitridation has played an important role in device scaling, it is only a near term solution, since the gate dielectric thickness rapidly approaches the quantum tunneling regime where the exponential increase in current with decreasing thickness is one of the more fundamental limits to device scaling.

Since the silicon dioxide thickness is rapidly approaches the quantum tunneling regime, the latest addition to the "show stopper" list is the proposed physical limit of 20-15 Å for the silicon dioxide gate dielectric.[6] The physical limit is derived from analysis of the quantum mechanical tunneling of electrons, which for a change of dielectric thickness of ~35 to ~15 Å increases ~13 orders of magnitude from 10^{-12} A/cm^2 to 10 A/cm^2.[6] This drastic increase in leakage current raises severe reliability and power consumption concerns for device operation in this regime, which has prompted interest in the development of alternative high dielectric constant (high-k) materials.

The integration of high-k dielectrics into current MOSFET technology can potentially enable continued device scaling. Since capacitance scales as the dielectric constant over the dielectric thickness, a high-k dielectric should provide sufficient physical thickness to block electron tunneling, while maintaining the specific desired capacitance. When designing a new device technology, this specific capacitance is usually described in terms of an equivalent oxide thickness (EOT). Figure 1.1 illustrates the potential roadblock associated with scaling the silicon dioxide thickness and the potential advantages high-k dielectrics can provide. Figure 1.1 plots the physical thickness versus the device generation and EOT for SiO_2 (k = 3.9) and high-k dielectrics with k = 15 and k = 80. The EOT values for each device generation are derived from the International Technology Roadmap for

Semiconductors (ITRS).[7] For each high-k dielectric, three curves are presented where the high-k is assumed to be on an interfacial SiO_2 layer of zero, 7 and 15 Å, where the physical thickness is calculated using a simple capacitors in series model. The proposed tunneling limit for SiO_2 is illustrated in Fig. 1.1 as the dashed line at a physical thickness of 15 Å. It is clear from Fig. 1.1 that SiO_2 will cross the tunneling limit somewhere around the 100-50 nm device nodes. Therefore, a high-k dielectric will be necessary to achieve the device performance required of a 50 nm device. A high-k material with a dielectric constant of 15 without an interfacial SiO_2 layer will enable EOT = 10 Å while remaining above the tunneling limit. A high-k with a dielectric constant of 80 can afford up to 7 Å of interfacial SiO_2 and still achieve EOT = 10 Å while remaining above the proposed tunneling limit. With these considerations in mind, recent interest in high dielectric constant (high-k) materials currently focuses on the eventual replacement of silicon dioxide.

To replace silicon dioxide as the gate insulator in MOSFET technology, high-k dielectrics must exhibit properties similar to the SiO_2/Si system. Any high-k dielectric must provide low levels of interface defects with interface trap density (D_{it}) ~10^{10} $cm^{-2} \cdot eV^{-1}$ and fixed charges (Q_f) $<5 \times 10^{10}$ cm^{-2}. High breakdown fields in excess of 10 MeV/cm are also necessary. The increased physical thickness of a high-k dielectric should limit tunneling current to <1 A/cm^2, but the tunneling current is also exponentially dependent on the barrier height. Therefore, a high-k dielectric should possess a suitably large bandgap and barrier height. However, the bandgap is inversely proportional to the dielectric constant for many high-k dielectrics, consequently the bandgap decreases as the dielectric constant increases.[8] The danger exists that the leakage reduction achieved by an increase in the dielectric constant (physical thickness) will be lost due to a decrease in the barrier height. Even though the barrier height may not be directly proportional to the bandgap, a large

bandgap should increase the chance of obtaining a suitably large barrier height. The physical properties of any potential high-k dielectric are also crucial, and a covalent amorphous microstructure is advantageous, since grain boundaries may provide high conductivity pathways. The stability between the high-k dielectric and silicon is of paramount importance. Instability of the high-k/Si or polysilicon/high-k interface resulting in excess formation of SiO_2 can reduce the effective dielectric constant of the stack and negate the benefits of the high-k, as illustrated in Fig. 1.1. Integration of a high-k dielectric into the current process flow requires the high-k to remain stable during the particularly strenuous dopant “drive-in” anneal (~1000 °C, ~30s). As of today, no one material has been identified that meets all these requirements.

The most common materials proposed to replace silicon dioxide are the metal oxides, including Ta_2O_5, TiO_2, HfO_2, ZrO_2, Y_2O_3, and Al_2O_3, and the metal silicates, including Hf, Zr and Y silicates.[9-15] The major drawbacks associated with the metal oxides are: 1) instability on silicon, namely for Ta_2O_5 and TiO_2, resulting in low-k interface layers,[12] 2) pure metal oxides tend to crystallize at relatively low temperatures (~200 °C),[16] and, 3) pure metal oxides tend to conduct oxygen, and the oxygen diffusion can lead to oxidation of the silicon substrate, as well as, oxygen vacancies that act as traps.[17] Silicate films may alleviate some of these problems by combining the high-k advantages of the pure metal oxide with the electrical advantages of SiO_2. MOS capacitors using Hf, Zr or Y silicates as the dielectric have been demonstrated with k~12.[9,15] Furthermore, amorphous microstructure has been demonstrated for Hf and Zr silicates after annealing at 1050 °C (~20s) and for Y silicate after oxidation at 700 °C (1 hr).[9,15]

1.2 OBJECTIVE

Developing an alternate high-k material to replace silicon dioxide as the gate dielectric in MOSFET technology is an arduous undertaking, and the ITRS has set an aggressive timetable for implementation for these materials. Taking into consideration the present knowledge and future needs of high-k dielectrics we have outlined certain goals for this work. The first is to evaluate and develop processes to form yttrium silicate films on silicon. Specifically, we will appraise oxidation of yttrium on silicon, both thermal and plasma, and reactive sputtering of yttrium as methods toward yttrium silicate formation. Next, we must determine of the physical properties of yttrium silicate films on silicon, including their microstructure and local bonding configurations. Another goal is to demonstrate yttrium silicate films with EOT $\cong$ 10 Å and leakage current <1 A/cm^2. And finally, we will show the effect of metal-silicon bonds on silicon consumption and interface formation.

1.3 OVERVIEW OF DISSERTATION

This dissertation focuses on the development of yttrium silicate as a high-k replacement for silicon dioxide in MOSFET technology, the physical and electrical properties of yttrium silicate and the role of metal-silicon bonds on silicon incorporation and interface formation. The main approach we use to form yttrium silicate thin films is the thermal oxidation of yttrium metal on silicon. The yttrium silicate forms through a competition for yttrium through reactions with silicon and oxygen. This competition can be mediated by the thickness of the initial yttrium film, the oxidation temperature and through the implementation of engineered interfaces.

In CHAPTER TWO, we demonstrate the formation of yttrium silicate by the thermal oxidation of yttrium silicide, compare the physical properties of yttrium silicate to

SiO_2 and Y_2O_3, evaluate the surface morphology of yttrium silicate and characterize yttrium silicate MOS capacitors.

In CHAPTER THREE, we discuss the physical and electrical properties of yttrium silicate thin films, compare the film formation by oxidation of yttrium on silicon and by oxidation of yttrium silicide, describe the competition between silicide formation and oxidation, and finally, analyze the oxidation kinetics of yttrium films on silicon.

In CHAPTER FOUR, we demonstrate the ability to control silicon consumption through the use of engineered interfaces.

In CHAPTER FIVE, we further analyze the effect of oxidized silicon and nitrided silicon interface layers on the consumption of silicon during the oxidation of yttrium and we demonstrate the interface reaction between yttrium and SiO_2 to form yttrium silicate.

In CHAPTER SIX, we describe the effect of oxidation temperature on silicon consumption and analyze the energetics of silicon incorporation.

In CHAPTER SEVEN, we present the chemical bonding and structural characterization of yttrium silicate thin films formed by the remote N_2O plasma oxidation of yttrium on silicon.

In CHAPTER EIGHT, we present a study on the use of mass spectrometry to sense silicon dioxide etch end point uniformity and propose a model to explain the observed mass spectrometry signal.

In CHAPTER NINE, we summarize the major results of this work.

An APPENDICES section includes additional information not found in the body of the text.

1.4 REFERENCES

1 M. M. Atalla, U.S. Patent 3,206,670 (1960).

2 H. Hwang, W. Ting, D.-L. Kwong, and J. Lee, IEEE Electron Device Lett. **12** (1991).

3 Y. Wu, H. Niimi, H. Yang, G. Lucovsky, and R. B. Flair, J. Vac. Sci. Tecnol. B **17,** 1813 (1999).

4 H. Hwang, W. Ting, B. Maiti, D.-L. Kwong, and J. Lee, Appl. Phys. Lett. **57,** 1010 (1990).

5 D. Bouvet, P. A. Clivaz, M. Dutoit, C. Coluzza, J. Almeida, G. Margaritondo, and F. Pio, J. Appl. Phys. **79,** 7114 (1996).

6 D. A. Buchanan, IBM J. Res. Dev. **43,** 245 (1999).

7 S. I. Association, *The International Technology Roadmap for Semiconductors, 1997 edition* (Austin, TX, 1997).

8 S. A. Campbell, D. C. Gilmer, X. Wang, M. T. Hsieh, H. S. Kim, W. L. Gladfelter, and J. H. Yan, IEEE Trans. Electron Devices **44,** 104 (1997).

9 M. Gurvitch, L. Manchanda, and J. M. Gibson, Appl. Phys. Lett. **51,** 919-921 (1987).

10 B. He, T. Ma, S. A. Campbell, and W. L. Gladfelter, Tech. Dig. Int. Electron Devices Meet.**,** 1038 (1998).

11 L. Manchanda, W. H. Lee, J. E. Bower, F. H. Baumann, W. L. Brown, C. J. Case, R. C. Keller, Y. O. Kim, E. J. Laskowski, M. D. Morris, R. L. Opila, P. J. Silverman, T. W. Sorsch, and G. R. Weber, Tech. Dig. Int. Electron Devices Meet.**,** 605 (1998).

12 K.-A. Son, A. Y. Mao, B. Y. Kim, F. Liu, E. D. Pylant, D. A. Hess, J. M. White, D. L. Kwong, D. A. Roberts, and R. N. Vrtis, J. Vac. Sci. Technol. A **16,** 1670 (1998).

13 M. Balog, M. Schieber, S. Patai, and M. Michman, J. Cryst. Growth **17,** 298 (1972).

14 M. Copel, M. Gribelyuk, and E. Gusev, Appl. Phys. Lett. **76,** 436 (2000).

15 G. D. Wilk, R. M. Wallace, and J. M. Anthony, J. Appl. Phys. **87,** 484 (2000).

16 S. A. Campbell, H.-S. Kim, D. C. Gilmer, B. He, T. Ma, and W. L. Gladfelter., IBM J. Res. Dev. **43,** 383 (1999).

17 A. Kumar, D. Rajdev, and D. L. Douglas, J. Am. Chem. Soc. **55,** 439 (1972).

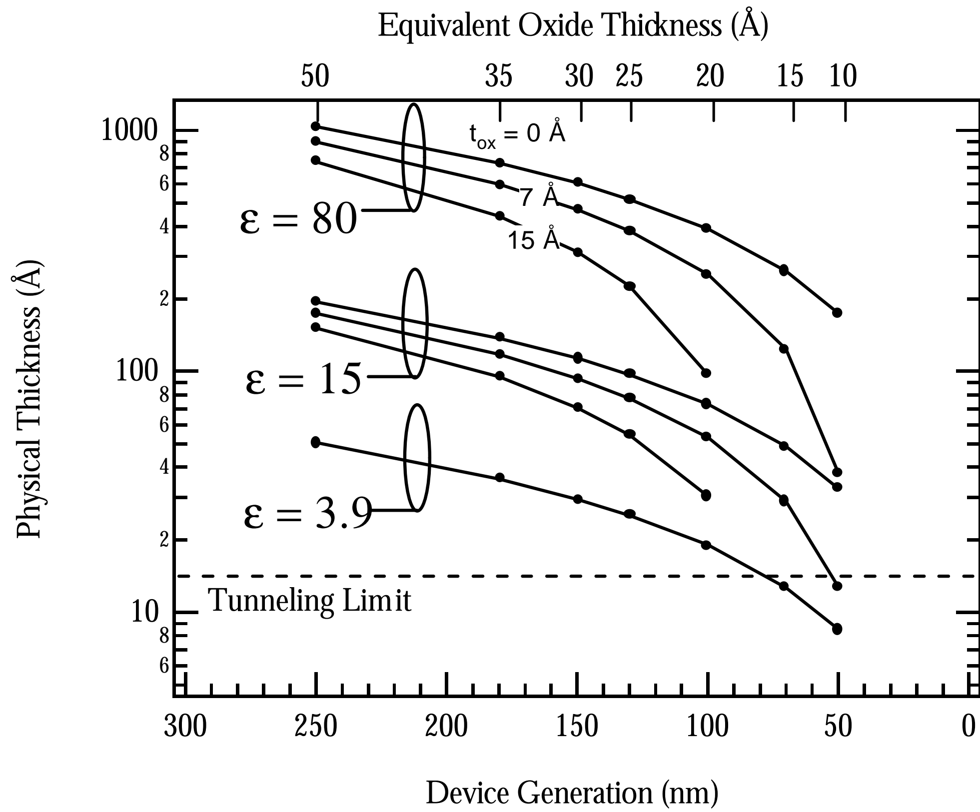

Figure 1.1 Physical thickness versus EOT for SiO_2, k=15 and k=80. A device generation of 50 nm can be achieved with k = 15 with no interfacial oxide.

Chapter 2 is a reprint of a manuscript that will appear in Materials Research Society Symposia Proceedings Vol. 611

PHYSICAL AND ELECTRICAL PROPERTIES OF YTTRIUM SILICATE THIN FILMS

J. J. Chambers and G. N. Parsons

ABSTRACT

This article reports on the physical and electrical properties of yttrium silicate, which is a possible high k replacement for the SiO_2 gate dielectric in CMOS devices. The yttrium silicate $(Y_2O_3)_x\cdot(SiO_2)_y$ films are formed by sputtering yttrium onto clean silicon, annealing in vacuum to form yttrium silicide and oxidizing in N_2O to form the silicate. Shifts in the Y 3d, Si 2p and O 1s photoelectron spectra with respect to Y_2O_3 and SiO_2 indicate that the films are fully oxidized yttrium silicate. FTIR results that reveal a Si-O stretching mode at 950 cm^{-1} and Y-O stretching modes in the far-IR are consistent with XPS. XPS and FTIR results are in accordance with the donation of electron density from the yttrium to the Si-O bond in the silicate. AFM reveals the yttrium silicate films a RMS roughness of 8.0 nm. The yttrium silicate films contain a fixed charge density of ~$9x10^{10}$ cm^{-2} negative charges as calculated from measured C-V curves. The properties of ultra-thin yttrium silicate films with an equivalent silicon dioxide thickness (electrical) of ~1.0 nm will be discussed elsewhere.

CHAPTER 2

PHYSICAL AND ELECTRICAL PROPERTIES OF YTTRIUM SILICATE THIN FILMS

2.1 INTRODUCTION

The continuous scaling of complementary-metal-oxide-semiconductor (CMOS) devices towards smaller dimensions will require replacing the gate SiO_2 with an alternate high dielectric constant (high-k) material. Metal silicates are appealing materials, since they are expected to posses a greater dielectric constant than SiO_2 and remain amorphous during annealing. Yttrium silicate possesses desirable thermodynamic, dielectric and structural properties that make it attractive as a high-k candidate. The Y-O bond is quite strong, since the free energy of formation[1] (at 25 °C, per oxygen atom) is -2.40×10^{-22} kcal compared to -1.70×10^{-22} kcal for SiO_2, which implies an yttrium silicate should be stable on silicon. Capacitance measurements[2] on MOS capacitors with an $Al/Y_{2.45}Si_{0.55}O_5/Si$ structure yielded a dielectric constant for the silicate layer of ~12, which should be suitably large to obtain EOT < 1.0 nm with low tunneling. Figure 2.1a depicts the mineral keiviite ($Y_2Si_2O_7$), which consists of a $Si_2O_7^{6-}$ structural unit with yttrium connecting the two corner sharing SiO_4 tetrahedra.[3] Figure 2.1b shows the yttrium orthosilicate (Y_2SiO_5) structure where four of the oxygen atoms are bound in a silicon tetrahedron with each corner joining two yttrium octahedron and the fifth oxygen atoms, which are not involved with the silicon tetrahedron, are shared between four yttrium octahedron in a rod-like chain.[4] $Y_2O_3 \cdot 2SiO_2$ and $Y_2O_3 \cdot SiO_2$ exhibit low lattice mismatch with silicon, since the lattice constants $a(Y_2Si_2O_7) = 0.554$ nm

and $a(Y_2SiO_5)$ = 1.041 nm are closely match with a (Si) = 0.543 and a(Si)·2 = 1.086 nm, respectively. Also, yttrium silicate films exhibit low oxygen permeability and should provide excellent passivation.[5] These advantageous properties make yttrium silicate an suitable materials choice for CMOS technology.

We form yttrium silicate films on silicon by oxidation of yttrium silicide, where the silicide films are formed by vacuum annealing of yttrium films on cleaned silicon. A similar approach has been utilized elsewhere to investigate the oxidation properties of silicides, where hafnium silicide is oxidized to from hafnium silicate.[6] One problem with the oxidation of silicides is that oxidation does not always result in silicate formation, but results in a SiO_2 film on silicide, as in the case of nickel silicide and cobalt silicide.[7] It has been postulated that oxidation of a metal silicide will result in silicate formation if the metal-oxygen bond posses a more negative free energy of formation than the silicon-oxygen bond.[8] Since the Y-O bond is stronger than the Si-O bond, we expect oxidation of yttrium silicide to result in silicate formation.

This article reports on the physical and electrical properties of yttrium silicate (Y-O-Si) as compared to the properties of SiO_2 and Y_2O_3. X-ray photoelectron spectroscopy (XPS) is used to compare the oxidation state of yttrium, silicon and oxygen in Y-O-Si, SiO_2 and Y_2O_3. Fourier transform infrared spectroscopy (FTIR) is used to identify the Si-O and Y-O vibrational modes in Y-O-Si, SiO_2 and Y_2O_3. Y-O-Si film topology is investigated using scanning electron microscopy (SEM). The electrical quality of Y-O-Si is tested using capacitance versus voltage (C-V) measurements.

2.2 EXPERIMENTAL

Substrates were p-type Si(100) with resistivity 0.1-0.3 Ω cm. Samples were prepared by dipping for 5 minutes in JTB 100 (a tetramethylammonium hydroxide based alkaline solution with a carboxylate buffer), rinsing in deionized water, etching in buffered hydrogen fluoride for 30 seconds with no final rinse and loading immediately into vacuum.

Y-O-Si films were formed by sputtering yttrium onto cleaned silicon, vacuum annealing and oxidizing in N_2O. The exact composition of the films reported here is unknown and we will denote our films as Y-O-Si or simply as yttrium silicate. Sputtering was performed at 25 °C in 4.3 mTorr Ar, a radio frequency (rf) power of 420 W at 13.56 MHz and an yttrium target dc bias of –1000 V in a system with an ultimate vacuum of $5x10^{-8}$ Torr. The yttrium films on silicon were annealed *in situ* in vacuum (< $1x10^{-6}$ Torr) at 600 °C to form yttrium silicide. The yttrium silicide was thermally oxidized *ex-situ* in a standard tube furnace in 1 atm N_2O at 900 °C. SiO_2 films were thermally grown (~100 nm) by wet oxidation. Y_2O_3 films were formed by sputtering yttrium onto ~50 nm SiO_2 and oxidizing in N_2O for 20 minutes.

Y-O-Si films for XPS, FTIR and SEM analysis were formed by sputtering 240 nm of yttrium onto cleaned silicon, annealing in vacuum for 30 minutes and oxidizing in N_2O for 20 minutes. XPS was performed *ex situ* using a Riber LAS3000 utilizing a single-pass, field retarded cylindrical mirror analyzer and non-monochromatic Mg Kα ($h\nu$ = 1253.6 eV). Spectra were collected using 0.1 eV step sizes and a resolution of ~1.0 eV. The binding energies of the core levels were corrected by setting the adventitious carbon 1s peak at 285 eV. FTIR spectra were collected using a Nicolet Magna 750 configured for both mid- and far-IR data acquisition. FTIR spectra were collected in the absorbance mode and

normalized to the silicon substrate. The thin SiO_2 buffer that the Y_2O_3 films were formed on was substracted from the Y_2O_3 FTIR spectra. High resitivity (15 Ω-cm) silicon wafers were used for FTIR analysis to minimize free carrier absorption in the substrate. These substrates were single side polished and "orange peel" roughened on the backside to reduce background interference fringes.

Y-O-Si films for electrical testing were formed by sputtering 2.5 nm of yttrium onto cleaned silicon, annealing in vacuum for 5 minutes and oxidizing at 900 °C in N_2O for 15 seconds. Front-side electrical contact (no back-side metal employed) was made to the Y-O-Si films using a Four Dimensions CV map 92-A mercury probe. Capacitance measurements were taken at 1 MHz using a HP 4284a LCR meter.

2.3 RESULTS AND DISCUSSION

Chemical bonding in Y-O-Si, SiO_2 and Y_2O_3 was investigated using XPS. Figure 2.2 presents the Y 3d photoelectron spectra for Y-O-Si and Y_2O_3. The Y 3d peak is a doublet resulting from the Y $3d_{3/2}$ and the Y $3d_{5/2}$ (the more intense component where peak position is referenced) components of the spin-orbit splitting. The Y 3d peak for Y_2O_3 is measured at 156.8 eV binding energy (BE) and reported in the literature[9] at 156.8 eV. The Y 3d peak for yttrium silicate is measured at 157.6 eV.

The Y 3d spectra for Y-O-Si and Y_2O_3 in Fig. 2.2 indicate that the yttrium in both films is fully oxidized, since a metallic Y 3d peak at 156.0 eV is not observed.[10] There is no evidence for Y-Si bonds (155.8 eV) in the yttrium silicate Y 3d spectrum. Since yttrium and silicon are only bonded to oxygen in the yttrium silicate crystal structures exhibited in Figs. 2.1a and 2.1b, the absence of Y-Si bonding in Y-O-Si films is expected. The Y 3d peak for Y-O-Si is shifted to higher BE than the Y 3d peak for Y_2O_3. This is likely due to increased donation of electron density to the Si-O bond in the silicate compared to the electron

density donation from yttrium to oxygen in Y_2O_3, consistent with the relative electronegativities of yttrium, silicon and oxygen (1.2, 1.8, 3.5 on the Pauling scale).

Figure 2.3 shows the Si 2p portion of the XPS signal for Y-O-Si and SiO_2. The Si 2p photoelectron peak position for SiO_2 is measured and reported in the literature[10] at 103.3 eV. The Si 2p photoelectron peak position for Y-O-Si is measured at 101.0 eV. The yttrium silicate Si 2p peak is shifted to lower BE than that for SiO_2, indicating the silicon in yttrium silicate is in a lower oxidation state than the silicon in SiO_2. This is consistent with yttrium donating electron density to the Si-O bond. The observation that the Y 3d and Si 2p peak positions for the Y-O-Si are different than either Y 3d in Y_2O_3 or Si 2p in SiO_2 indicates the presence of a uniform material with the absence of phase separated Y_2O_3 or SiO_2.

Figure 2.4 presents the O 1s spectra for Y-O-Si, Y_2O_3 and SiO_2. The peak positions for the Y-O-Si, Y_2O_3 and SiO_2 are 530.5, 529.25 and 533.0 eV, respectively. The shoulder observed on the Y_2O_3 spectrum at 531.5 eV is assigned to O-H bonding in the film likely acquired during post-deposition exposure to ambient water.[9] The O 1s peak for Y-O-Si is measured to fall between Y_2O_3 and SiO_2, as expected considering the electronegativity differences between yttrium and silicon. Again, the absence of an O 1s peak for SiO_2 or Y_2O_3 in the Y-O-Si spectrum indicates the absence of any phase segregation in the silicate.

Analysis of the bonding environments in Y-O-Si, SiO_2 and Y_2O_3 were investigated using FTIR. Figure 2.5a presents the mid-IR region of the FTIR spectrum for Y-O-Si and Y_2O_3. The SiO_2 FTIR spectrum presented in Fig. 2.5a exhibits three characteristic vibrational modes of SiO_2. The peaks located at 1077, 810 and 400 cm^{-1} are the Si-O-Si asymmetric stretching, bending and rocking modes, respectively. These peaks are typical for a stoichiometric and relaxed amorphous SiO_2 network. The dominant peak in the Y-O-Si FTIR spectrum in Fig. 2.5a is at 950 cm^{-1}. Although the peak at 950 cm^{-1} in the Y-O-Si

FTIR spectrum is broader and shifted to lower frequency, it is similar in shape to the asymmetric stretch measured at 1077 cm^{-1} and is assigned to Si-O stretching in the Y-O-Si. The frequency shift and broadening of the Si-O stretch in the yttrium silicate is consistent with a weakening of the Si-O bond resulting from the combined effects of transfer of electron density from the yttrium to the Si-O bond and a wider distribution of Si-O bond angles available in the silicate. Figure 2.5b presents the far-IR region of the FTIR spectrum for Y-O-Si and Y_2O_3. The Y_2O_3 spectrum in Fig. 2.5b exhibits vibrational modes at 374, 335 and 303 cm^{-1} characteristic of Y-O stretching in Y_2O_3.[11] The Y-O-Si spectrum in Fig. 2.5b displays two broad peaks assigned to Y-O stretching in the silicate.

Figure 2.6 presents an AFM image of a Y-O-Si film with a root mean square surface roughness of 8.0 nm. It has been reported that vacuum annealing of yttrium films on silicon forms an epitaxial silicide with grain sizes on the order of 70 nm.[12] The roughness inherent in the yttrium silicide is consistent with the observed roughness in the Y-O-Si film.

Capacitance-voltage testing of Y-O-Si films was performed to ascertain their electrical quality and the results are depicted in Fig. 2.7. The equivalent oxide thickness (EOT) for this film was calculated to be ~5.0 nm. The ideal flat band voltage (V_{fb}) for a mercury-oxide-semiconductor ($N_a = 1x10^{17}$ cm^{-3}) is -0.55 V. V_{fb} for the C-V curve displayed in Fig. 2.7 is calculated at –0.51 V, which corresponds to a fixed charge density of ~$9x10^{10}$ cm^{-2} and suggests the presence of negative fixed charges in the silicate.

2.4 CONCLUSIONS

We have shown the physical and electrical properties of Y-O-Si films formed on silicon by oxidation of yttrium silicide. The shift of the Y 3d photoelectron peak to higher BE compared Y_2O_3, the shift of the Si 2p peak to lower BE compared to SiO_2 and the intermediate location of the O 1s peak compared to Y_2O_3 and SiO_2 indicate the presence of

Y-O-Si bonding structure. There is no evidence in the XPS spectra for the presence of SiO_2, Y_2O_3 or yttrium silicide. XPS spectra are consistent with FTIR spectra where a Si-O stretching peak is measured at 950 cm^{-1} and Y-O stretching peaks are measured in the far-IR, which are also consistent with the formation of Y-O-Si. These results are consistent with the donation of electron density from yttrium to the Si-O bond in the silicate. C-V measurements reveal that the Y-O-Si films are of low defect density. Based on these results, we have investigated ultra-thin (EOT = ~1.0 nm) Y-O-Si films and will report the results elsewhere.

2.5 ACKNOWLEDGEMENTS

We acknowledge funding from the SRC/SEMATECH Center for Front End Processes at North Carolina State University. We would like to thank Bruce Rayner and Dr. Gerald Lucovsky for their assistance in obtaining the far-IR spectra.

2.6 REFERENCES

1. I. Barin, *Thermochemical Data of Pure Substances* (VCH Verlagsgesellschaft, Weinheim, Germany, 1989).
2. M. Gurvitch, L. Manchanda, and J. M. Gibson, Appl. Phys. Lett. **51,** 919-921 (1987).
3. N. G. Batalieva and Y. A. Pyatenko, Zhurnal Strukturnoi Khimii **8,** 548-549 (1967).
4. B. A. Maksimov, V. V. Ilyukhin, Y. A. Kharitonov, and N. V. Belov, Kristallografiya **15,** 926-933 (1970).
5. J. D. Webster, M. E. Westwood, F. H. Hayes, R. J. Day, R. Taylor, A. Duran, M. Aparicio, K. Rebstock, and W. D. Vogel, J. European Ceram. Soc. **18,** 2345-2350 (1998).
6. S. P. Murarka and C. C. Chang, Appl. Phys. Lett. **37,** 639-641 (1980).
7. F. M. Dheurle, Thin Solid Films **105,** 285-292 (1983).
8. S. P. Murarka, J. Vac. Sci. Technol. **17,** 775 (1980).
9. O. G. Alekseev, N. V. Krivosheev, M. Y. Khodos, V. R. Galakhov, V. V. Shumilov, V. M. Cherkashenko, E. Z. Kurmaev, and V. A. Gubanov, Inorg. Mater. **22,** 1748-1751 (1986).
10. J. F. Moulder, W. F. Stickle, P. E. Sobol, and K. D. Bomben, *Handbook of X-ray Photoelectron Spectroscopy* (Perkin-Elmer Corporation, Eden Prairie, MN, 1992).
11. Y. Nigara, M. Ishigame, and T. Sakurai, J. Phys. Soc. Japan **30,** 453 (1971).
12. Y. K. Lee, N. Fujimura, and T. Ito, J. Alloys Compound. **193,** 289-291 (1993).

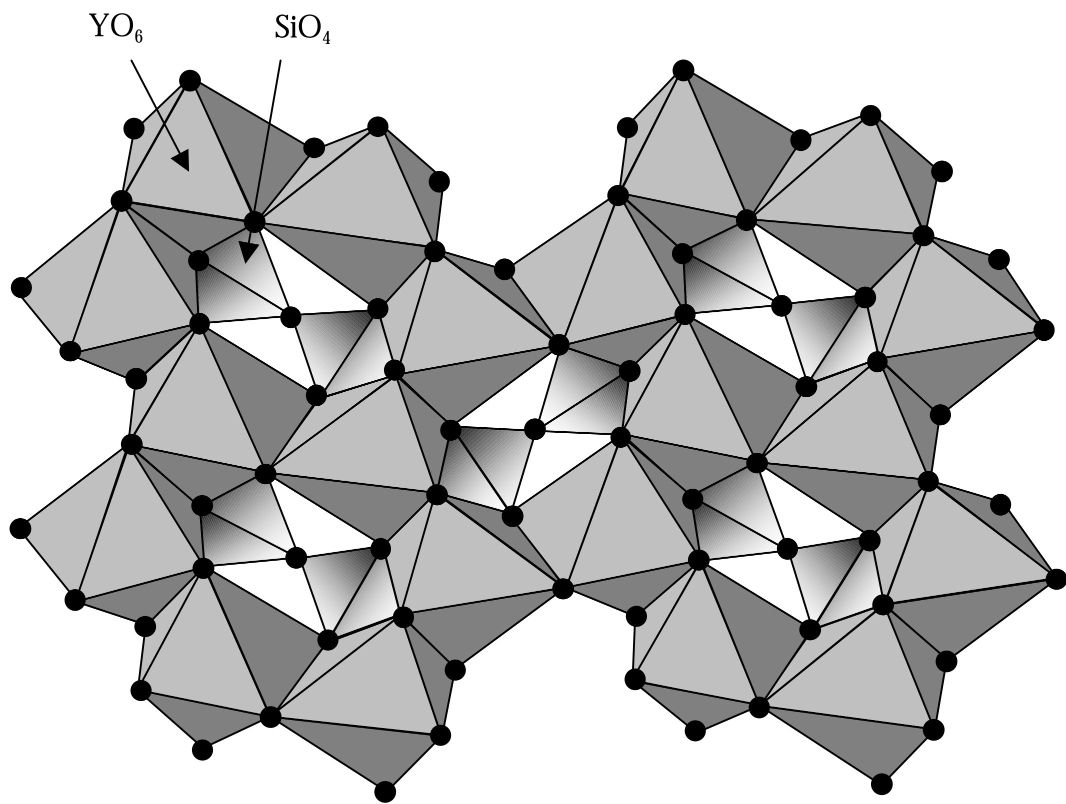

Figure 2.1a Schematic depicting crystal structure of $Y_2Si_2O_7$.

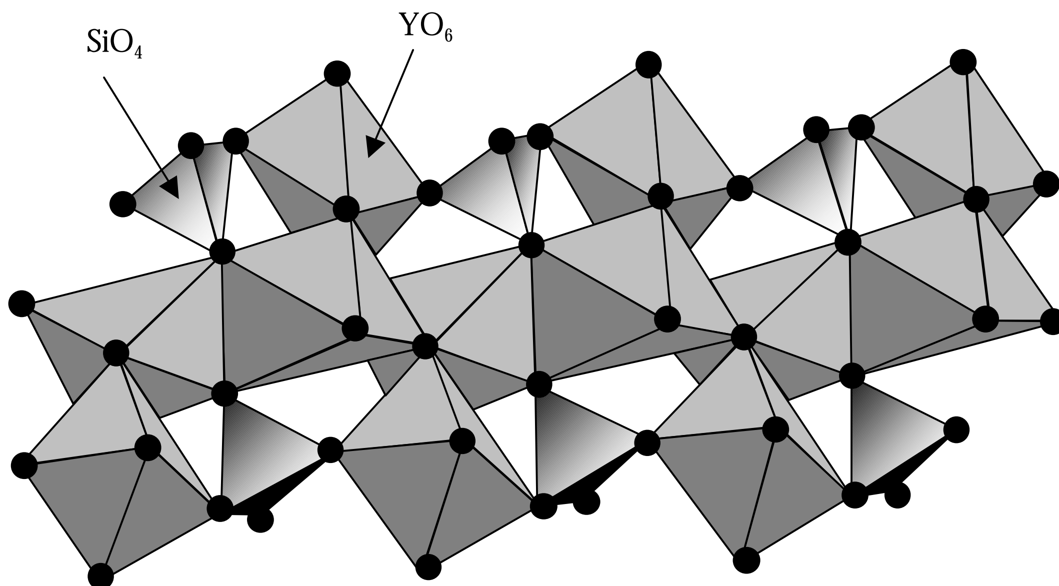

Figure 2.1b Schematic depicting crystal structure of Y_2SiO_5.

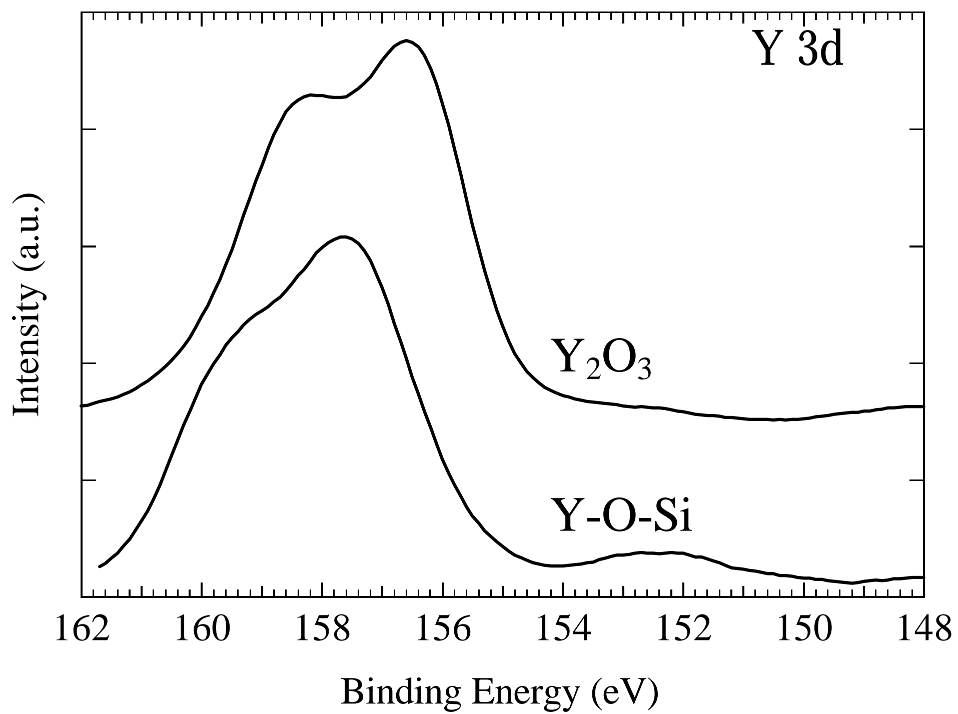

Figure 2.2 Y 3d portion of the XPS spectra for Y-O-Si and Y_2O_3.

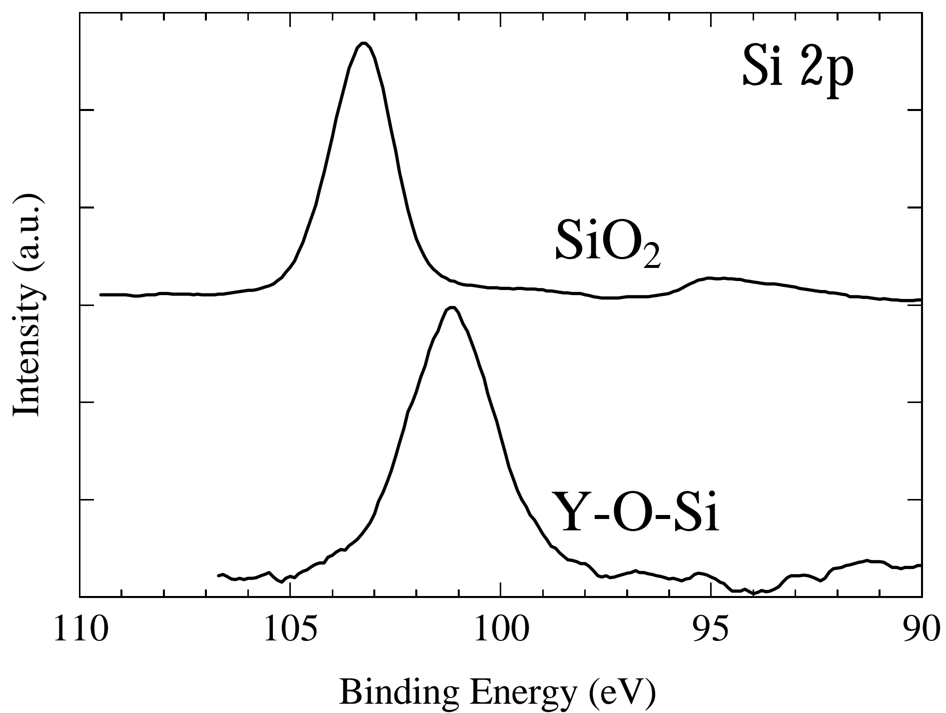

Figure 2.3 Si 2p portion of the XPS spectra for Y-O-Si and SiO_2.

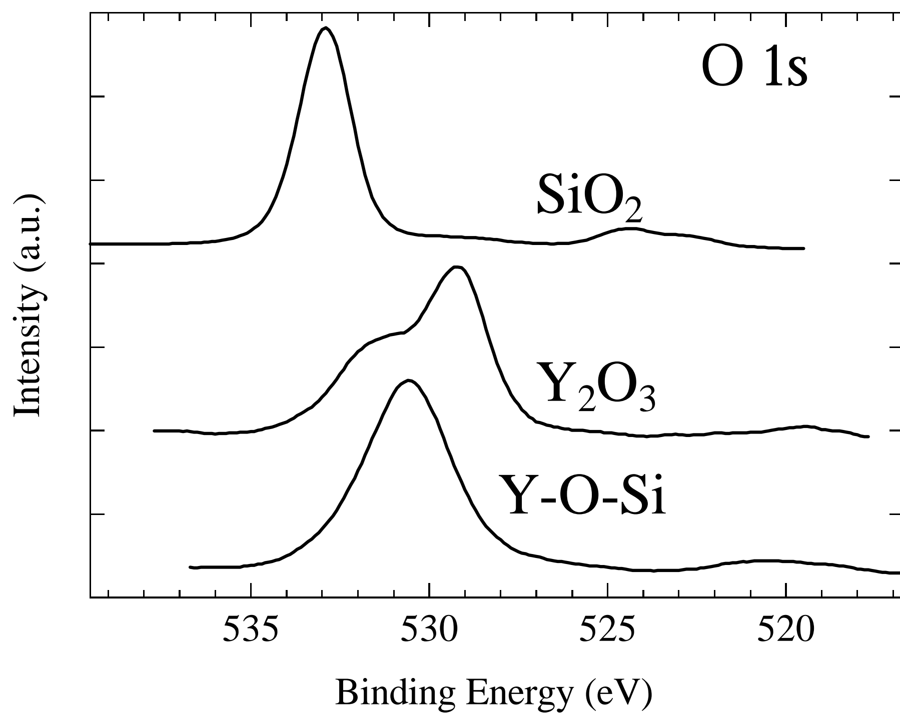

Figure 2.4 O 1s portion of the XPS spectrum for Y-O-Si, Y_2O_3 and SiO_2.

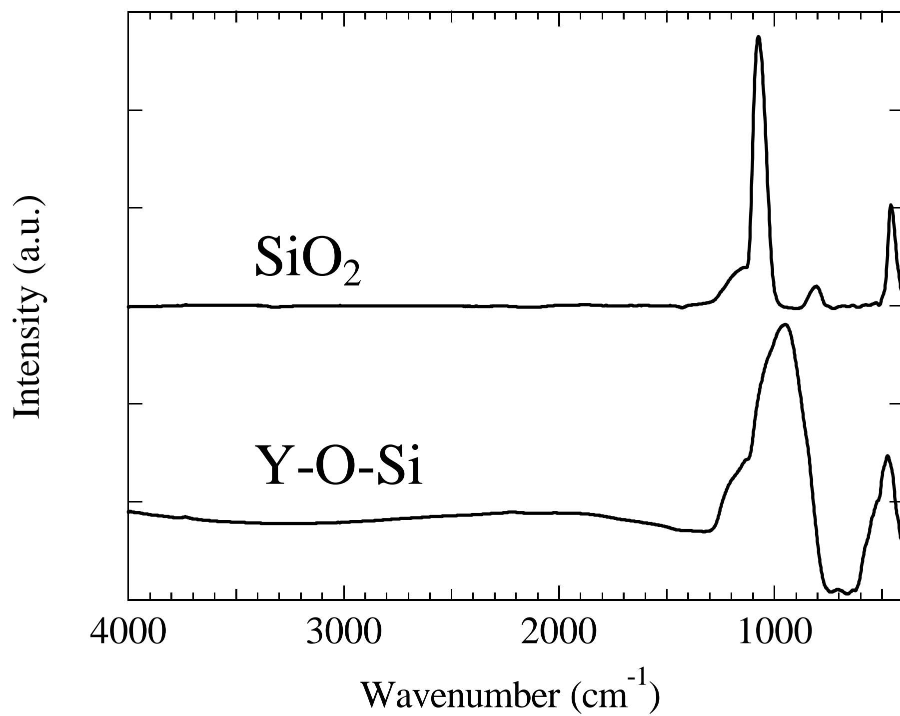

Figure 2.5a Mid-IR region of the FTIR spectrum for Y-O-Si and SiO_2.

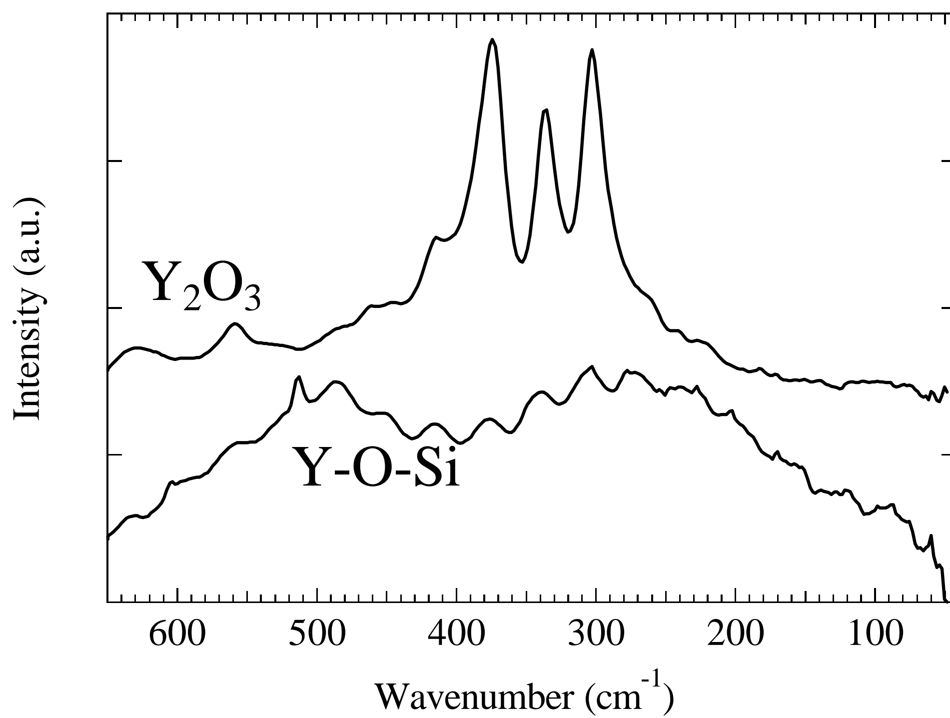

Figure 2.5b Far-IR region of the FTIR spectrum for Y-O-Si and Y_2O_3.

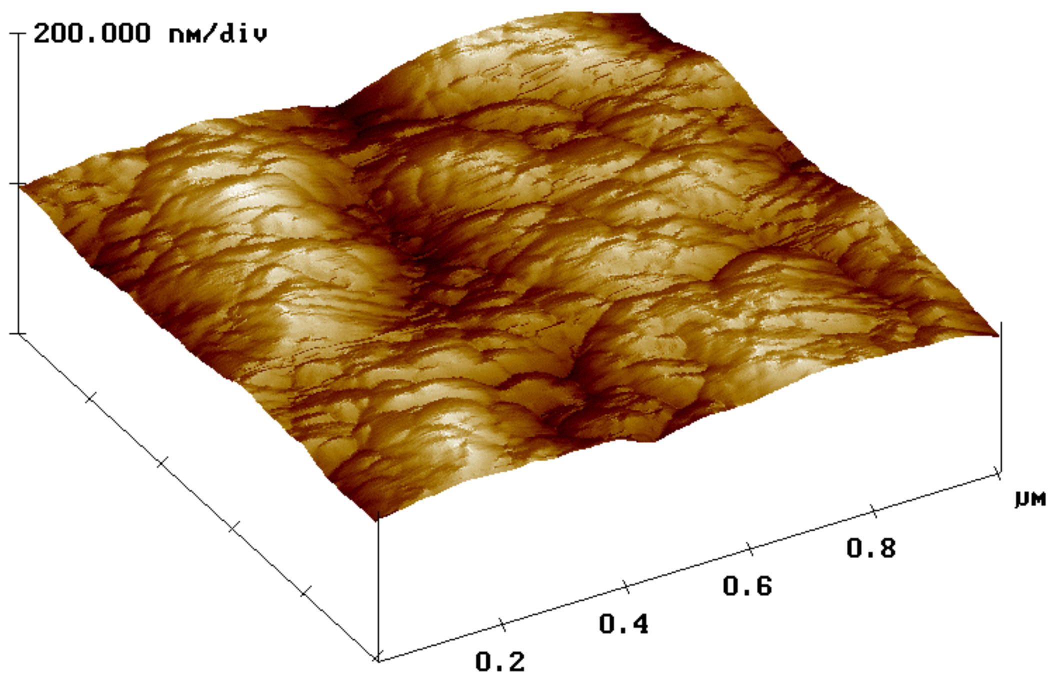

Figure 2.6 AFM image for Y-O-Si with RMS surface roughness of 8.0 nm.

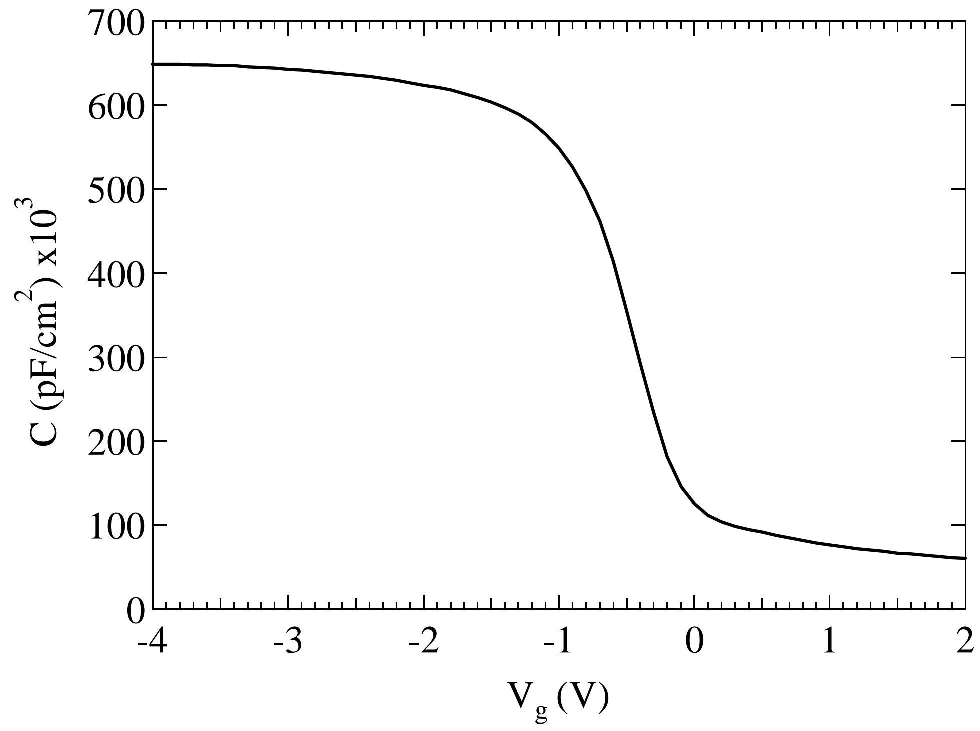

Figure 2.7 C-V curve for Y-O-Si with EOT = 5.0 nm.

Chapter 3 is a reprint of a manuscript to be submitted to the Journal of Applied Physics

PHYSICAL AND ELECTRICAL CHARACTERIZATION OF YTTRIUM SILICATE HIGH-K DIELECTRICS

J. J. Chambers and G. N. Parsons

ABSTRACT

The physical and electrical properties of yttrium silicate thin films are described. The reactivity of yttrium metal with silicon and oxygen is exploited to form interface layer free yttrium silicate thin films. X-ray photoelectron spectroscopy (XPS) and Fourier transform infrared spectroscopy (FTIR) are used to determine chemical bonding and composition of yttrium silicate films. Capacitance-voltage testing is used to determine the quality of the dielectric and the electrical thickness. The oxidation of yttrium on silicon to form amorphous yttrium silicate films (~40 Å) with EOT ≅ 1.0 nm has been demonstrated. We establish that the oxidation of yttrium silicide also results in an yttrium silicate film. The oxidation of yttrium on silicon results in a films nearly identical, although with a lower silicon fraction, to films formed by the oxidation of yttrium silicide. These results suggest that the yttrium silicate forms through a competition between yttrium-silicon reaction and oxidation. This competition results in an yttrium silicate film for thin (<40 Å) initial yttrium coverage and in an Y_2O_3/Y-O-Si bi-layer at thick (>80 Å) initial yttrium coverage. Analysis of the oxidation kinetics reveals fast oxidation during yttrium silicate film formation and

slow oxidation during consumption of the silicon substrate. It is the high reactivity of yttrium that enables complete oxidation of the yttrium silicate while avoiding excessive oxidation of the silicon substrate. In principle, the oxidation of other metals on silicon of the metal oxides of interest as high-k dielectrics (such as, ZrO_2, HfO_2 and La_2O_3) is expected to result in a metal silicate film.

CHAPTER 3

PHYSICAL AND ELECTRICAL CHARACTERIZATION OF YTTRIUM SILICATE HIGH-K DIELECTRICS

3.1 INTRODUCTION

The semiconductor industry improves performance by decreasing the gate length with each successive complementary metal oxide semiconductor (CMOS) device generation. With each generation, the silicon dioxide gate dielectric thickness scales with gate length to promote high channel transconductance. The *International Technology Roadmap for Semiconductors* predicts that a 50 nm device generation will require the equivalent of a sub-1.0 nm silicon dioxide.[1] Reducing the silicon dioxide thickness to the sub-1.0 nm regime may not be feasible because significant leakage and reliability issues become major concerns below ~2.0-1.5 nm[2] due to direct tunneling, which is exponentially dependent on the dielectric thickness. Maintaining low tunneling current requires an increase in the gate dielectric thickness and an accompanying increase in the dielectric constant (k), since capacitance scales as k/thickness, to obtain the desired equivalent silicon dioxide thickness (EOT).

A variety of metal oxides, including Y_2O_3, Ta_2O_5, TiO_2, HfO_2, ZrO_2 and Al_2O_3, have been suggested as high-k ($k > k_{SiO_2} = 3.9$) replacements for silicon dioxide.[3-8] A Ta_2O_5 ($k \cong 25$) gate dielectric can be made approximately 6 times thicker than the equivalent silicon dioxide gate, assuming the silicon/high-k interface does not contain any SiO_2, which would decrease the capacitance of the gate stack and counteract the advantage of the high-k

material. Thermodynamic calculations have been used to evaluate the stability, with respect to no silicide or SiO_2 formation, of binary metal oxides in contact with silicon. Y_2O_3, ZrO_2, HfO_2 and the rare earth oxides are the most promising binary metal oxides from using this thermodynamic analysis.[9] However, pure metal oxides tend to crystallize at relatively low temperatures[10] resulting in possible high conductivity pathways along grain boundaries counteracting the benefits of the high-k dielectric. Therefore, scaling the gate insulator into the sub-1.0 nm regime requires a material with suitably high-k that remains stable and amorphous during typical annealing cycles.

Recently, zirconium silicate and hafnium silicate have been demonstrated as potential high-k gate dielectrics with k ~ 11 and an amorphous microstructure after annealing at 1050 °C for 20 seconds.[11] Yttrium silicate also possesses desirable thermodynamic, dielectric and structural properties that make it attractive as a high-k candidate. The Y-O bond is quite strong, since the free energy of formation per oxygen atom ($-\Delta G_f$) (at 25 °C) is 2.40×10^{-22} kcal for Y_2O_3 compared to 1.70×10^{-22} kcal for SiO_2.[12] The mineral keiviite ($Y_2Si_2O_7$) (Fig. 3.1a) consists of a $Si_2O_7^{6-}$ structural unit with yttrium connecting the two corner sharing SiO_4 tetrahedra.[13] In the yttrium orthosilicate (Y_2SiO_5) structure (Fig. 3.1b), four of the oxygen atoms are bound in a silicon tetrahedron where each corner joins two yttrium octahedron, and the fifth oxygen atoms, which are not involved with the silicon tetrahedron, are shared between four yttrium octahedron arranged in a chain.[14] $Y_2Si_2O_7$ and Y_2SiO_5 exhibit low lattice mismatch with silicon, since the lattice constants $a(Y_2Si_2O_7) = 0.554$ nm and $a(Y_2SiO_5) = 1.041$ nm are closely match with $a(Si) = 0.543$ and $a(Si) \cdot 2 = 1.086$ nm, respectively.[13,14] The yttrium silicate phase diagram (Fig. 3.1c) indicates a two-phase region between 50% and 67% mole fraction SiO_2 where Y_2SiO_5 and $Y_2Si_2O_7$ form a stable mixture. This contrasts the

phase diagrams of the group IV silicates (i.e. zircon and hafnon)[15] where the two-phase regions are silicate with metal oxide or SiO_2. Yttrium silicate films exhibit low oxygen permeability and should provide excellent passivation.[16]

Previous studies have demonstrated the formation of yttrium silicate by the oxidation of yttrium on silicon in dry air at 500-700 °C.[3] Yttrium silicate films with the composition $Y_{2.45}Si_{0.55}O_5$ approximately 26.0 nm thick were created using this process. Capacitance measurements on MOS capacitors with an Al/$Y_{2.45}Si_{0.55}O_5$/Si structure yielded k~12 for the silicate layer, which should be suitably large to obtain EOT < 1.0 nm with low tunneling. These films also exhibited acceptable current-voltage and breakdown characteristics.

Formation of YSi_{2-x} by vacuum annealing of yttrium films on silicon is a well-characterized process where the silicide is formed by the fast diffusion of silicon into the metal film.[17,18] Hexagonal YSi_{2-x} films have been epitaxially grown on Si(100) by annealing yttrium films on silicon above 550 °C in vacuum.[19] Yttrium silicide formation occurs at relatively low temperatures (120 to 140 °C) and at a very rapid rate (estimated as 40 to 50 Å/s at 350 °C).[20] Furthermore, films created in this manner have been found to oxidize up to ~15 times faster than crystalline silicon.[21] This creates a situation where thin yttrium silicate films can be formed on silicon with minimal or no oxidation of the underlying silicon substrate.

The possibility of forming silicate materials on silicon by oxidizing the metal silicide is intriguing. The oxidation of silicides has been addressed in terms of the free energy of formation per oxygen atom ($-\Delta G_f$) for metal oxides compared with that of SiO_2.[22] If the $-\Delta G_f$ of a metal oxide is less than that of SiO_2, the metal oxide can be reduced by silicon.

Conversely, if the $-\Delta G_f$ of a metal oxide is greater than that of SiO_2, the metal oxide can reduce SiO_2. It has been proposed that oxidizing a metal silicide where the metal oxide has a $-\Delta G_f$ greater than that of SiO_2 will result in a mixed metal oxide/SiO_2 film and oxidizing a metal silicide where the metal oxide has a $-\Delta G_f$ less than that of SiO_2 will result in preferential oxidation of silicon.[22] Table 3.1 presents $-\Delta G_f$ for a variety of metal oxides and the expected oxidation product of the metal silicide on silicon. For example, the oxidation of $MoSi_2$, WSi_2 and $TaSi_2$ (see Table 3.1) on silicon has been reported to result in the formation of a metal-free SiO_2 film on a silicide layer over silicon.[23-25] The SiO_2 forms through the oxidation of silicon that has diffused through the silicide, which remains stable. The silicides were found to oxidize only when the silicides were on SiO_2 or polycrystalline Si on SiO_2, where there is a limited supply of silicon. However, the oxidation of hafnium silicide has been demonstrated to result in an Hf-O-Si layer.[26] Y_2O_3 has a greater $-\Delta G_f$ than SiO_2. Therefore, yttrium silicide is expected to oxidize to form a Y-O-Si film. It is worth noting that, for other metal oxides of interest as high-k dielectrics, oxidation of their respective metal silicide is expected to result in a metal-O-Si film.

This article investigates the formation of Y-O-Si films by oxidation of yttrium on silicon and by oxidation of yttrium silicide. This article is divided into an experimental section, followed by a results and discussion section and, finally, the results are summarized in the conclusion section. X-ray photoelectron and Fourier transform infrared spectroscopies are used to identify the chemical structure of the Y-O-Si films. Current- and capacitance-voltage testing is used to determine the electrical quality of the dielectrics. Transmission electron and atomic force microscopies are used to identify film morphology. In the results and discussion section, it is demonstrated that exposure of yttrium silicide to

an oxidizing ambient results in oxidation of the silicide, and the oxidation of yttrium on silicon results in the mixing of yttrium and silicon. The extreme reactivity of yttrium with silicon and oxygen enables the formation of interface-free Y-O-Si thin (~40 Å) films using the methods described in this article. Y-O-Si films with EOT ≅ 1.0 nm are demonstrated, which encourages further study of films formed by oxidation of yttrium on silicon and oxidation of yttrium silicide.

3.2 EXPERIMENTAL

3.2.1 SPUTTERING AND SURFACE PRETREATMENT SYSTEM

Yttrium films were sputtered in the two-chamber vacuum system shown in Fig. 3.2. The system is equipped with a load-lock and a plasma processing chamber. A base pressure of 1×10^{-7} Torr is attained in the load-lock using a hybrid-turbo and dry diaphragm pumping system. Silicon samples are transferred from the load-lock to a manipulator with full X, Y, Z and θ motion in the processing chamber. A base pressure of 5×10^{-8} Torr in the processing chamber is achieved with a hybrid-turbo and dry scroll pump combination, which doubles as the process gas pumping system. The process pressure can be controlled from 1.0-100 mTorr via a closed loop system containing a motorized 20 cm butterfly valve located directly above the hybrid-turbo and a capacitance monometer located near the sample in the processing chamber. The processing chamber is outfitted with a cylindrical plasma source that can be configured to run in a remote plasma mode to perform *in situ* silicon surface preparations and in a direct plasma mode to sputter yttrium thin films. The cylindrical plasma source consists of a 500 W, 13.56 MHz radio frequency (rf) power supply and auto-tuned matching network, a quartz plasma tube 5 X 15.25 cm (diameter X length) and an air-cooled excitation coil (grounded at one end) of 0.95 cm nominal diameter copper tubing with 2 turns of 12.7 cm diameter spanning 5 cm enclosed in a stainless steel electrostatic

shield. The Ar, N_2 and N_2O process gas flows are supplied to the chamber through the front of the plasma tube and regulated from 1-100 sccm (N_2) with mass flow controllers. The processing chamber is equipped with a retractable yttrium (99.1%, Ta as the major impurity) sputter target that can be isolated from the system by a gate valve. A 200 W DC power supply provides up to -1000 V of bias to the sputter target and is run in a constant voltage mode. A 600 W radiant heater enables substrate temperatures up to 650 °C. All post-deposition vacuum anneals were performed *in situ*. The plasma processing chamber is also compatible with *in situ* plasma oxidation, which will be presented in a separate publication. For the results in this article, oxidation is performed *ex situ* from the processing chamber in a standard 10 cm diameter tube furnace at temperatures from 500-900 °C in 1 atm N_2O or air.

3.2.2 SAMPLE PREPARATION

Substrates were n- (1.0-2.0 Ω-cm) or p-type (0.1-0.3 Ω-cm) Si(100) cut from commercial wafers into 2.5 X 2.5 cm samples. Samples were prepared by dipping for 5 minutes in JTB 100 (a tetramethylammonium hydroxide based alkaline solution with a carboxylate buffer), rinsing in deionized water (DI), etching in buffered hydrogen fluoride (HF) for 30 seconds with no final rinse and loading immediately into vacuum.

3.2.3 SPUTTER CONDITIONS

Sputtering was performed at room temperature in 4.3 mTorr Ar and an rf power of 420 W. During sputtering, the yttrium target was fully extended into the plasma and biased at –1000 VDC. Yttrium metal is reactive, and residual oxygen or water in the system will affect the target surface and sputter rate. To control this problem, the target was conditioned before loading samples and performing runs by sputtering for 30-60 minutes at the standard conditions. The target current typically was observed to decrease from ~10 to

~5 mA during this time, and the target was considered clean when the target current stabilized at ~5 mA. When performing runs, the samples were rotated into the line-of-sight of the target at a distance of ~1.25 cm from the target. To calibrate the yttrium sputter rate, a series yttrium films with thickness of 200-1000 Å were blanket deposited onto 1000 Å of wet oxidized SiO_2. After deposition, one-half of each sample was masked with photoresist and soft baked for 2 minutes at 70 °C. The masked samples were then etched in Al etch (phosphoric/nitric/acetic acid mixture), rinsed in DI and dried with N_2. After etching, the photoresist was stripped in acetone. The samples were then rinsed in DI and dried with N_2. Film thickness was determined by taking five step height measurements across the sample with an Alpha-Step 500 and taking the average value. Uniformity across the sample was ~85 %. The average thickness was plotted versus sputter time, and the sputter rate was taken as the slope of a least squares fit. The fits with the y-intercept set at zero were excellent ($R^2 \cong 0.998$), and the sputter deposition rate was typically 40 Å/minute. Yttrium film thickness for each run was determined by monitoring the sputter time while maintaining a constant sputter rate. The conditions for plasma ignition and stabilization were achieved using an auto-tuned matching network. Typical thin metal (~8 Å) required a sputter time of 15 seconds. Plasma initiation was rapid (< 1s) and, therefore, not expected to affect the initial sputter rate.

3.2.4 SILICIDATION CONDITIONS

Silicide films were prepared by sputtering yttrium onto cleaned silicon at room temperature and *in situ* annealing in vacuum (maximum pressure was ~5×10^{-6} Torr). The temperature ramp for the annealing step was performed at ~0.5 °C/s up to a temperature of 600 °C where the sample was held for 20 minutes. During the annealing step, the yttrium

sputter target was isolated from the system. After annealing, the silicide films were allowed to cool in vacuum for 5 minutes and in 1 atm N_2 for an additional 5 minutes.

3.2.5 THERMAL OXIDATION CONDITIONS

Oxidation was performed *ex situ* in the furnace described in Section 3.2.1 at temperatures between 500 and 900 °C for times from 6 seconds to 20 minutes. Samples were placed onto a quartz boat and quickly (~1 s) pushed by hand to the center of the furnace, and the oxidation time was the time the sample spent at the center of the furnace. N_2O and air were used as oxidizers. When N_2O was used as the oxidizer, the flow rate was 5 slpm (N_2).

3.2.6 X-RAY PHOTOELECTRON SPECTROSCOPY

X-ray photoelectron spectroscopy (XPS) was performed *ex situ* using a Riber LAS3000 equipped with a MAC2 analyzer (single-pass cylindrical mirror analyzer with an input lens). The photoelectrons were excited using non-monochromatic Mg Kα ($h\nu$ = 1253.6 eV) or Al Kα ($h\nu$ = 1486.6 eV) radiation. The base pressure of the surface analysis chamber was 2×10^{-10} Torr. Survey and detailed spectra were collected at a take-off angle of 90° using 1 eV and 0.1 eV step sizes, respectively. No overlap of any Auger peaks with the primary Y 3d, Si 2p, O 1s and C 1s photoelectron peaks was observed when using either Mg Kα or Al Kα radiation. When the films were thin enough to detect the silicon substrate peak, the binding energies of the core levels were corrected by setting the silicon substrate 2p photoelectron peak to 99.3 eV, which set the adventitious carbon 1s peak near 285 eV. When the overlayer was thick enough to shield the silicon substrate photoelectrons, the binding energy was corrected by setting the adventitious carbon peak at 285 eV. The raw spectra were smoothed using an eleven point Savitsky-Golay algorithm. When peak fitting

was necessary to locate peak position or integrate area, Gaussian functions were generated by minimizing the misfit error.

3.2.7 MEDIUM ENERGY ION SCATTERING

Medium-energy ion scattering (MEIS)[27], a low-energy (50-300 kEV) high resolution (~5 Å) version of Rutherford backscattering spectroscopy, is used to obtain proton energy spectra. Energy spectra of the scattered protons (~100 keV) are collected using a double-aligned geometry. The compositions determined by MEIS of the films reported here are average values throughout each film and generally correspond to $(Y_2O_3)_x{\cdot}(SiO_2)_{1-x}$ where x ranges from 0.3 to 0.6. The known yttrium silicates correspond to x=0.5 (yttrium orthosilicate) and x=0.33 (keiviite).[15] In this article, we generally refer to all the films as yttrium silicate or simply as Y-O-Si.

3.2.8 ELECTRICAL MEASUREMENTS

Metal-insulator-semiconductor capacitors were formed by evaporating 2000 Å of Al onto blanket Y-O-Si films through a contact mask with holes ranging from 50-500 μm in diameter. Active area was determined using scanning electron microscopy. Contact was made to the backside of each sample with 2000 Å of evaporated Al. Samples typically underwent a post-metallization anneal in 90% N_2 and 10% H_2 at 400 °C for 30 minutes. Capacitance-voltage (C-V) measurements were taken at 1 MHz using a HP 4284a LCR meter. Electrical thickness is described as an equivalent SiO_2 thickness (EOT) determined from a fit of the C-V curve that includes the quantum mechanical effect. Samples were swept from inversion to accumulation with no initial light source. Current-voltage (J-V) measurements were taken using a Kiethly 236 source measure unit and scanned at least 2 V past flat band to ensure carrier generation would not limit the current.

3.2.9 FOURIER TRANSFORM INFRARED SPECTROSCOPY

Fourier transform infrared spectroscopy (FTIR) was performed using a Nicolet Magna 750 configured for both mid- and far-IR data acquisition. The spectrometer is purged with dry air to avoid absorption from ambient H_2O and CO_2. High resistivity (15 Ω-cm) silicon wafers were used for FTIR analysis to minimize free carrier absorption in the substrate. The substrates were single side polished and "orange peel" roughened on the backside to reduce background interference fringes. For each spectrum, 256 scans were taken at a resolution of 4.0 cm^{-1}. FTIR spectra were collected in the transmittance mode, converted to the absorbance mode after acquisition and normalized to the appropriate substrate (i.e. silicon or SiO_2/Si). The normalized spectra were smoothed and base line corrected using the OMNIC software available from Nicolet.

3.2.10 ATOMIC FORCE MICROSCOPY

Surface morphology was imaged using a Digital Instruments Dimension 3000 in an intermittent-contact mode. The atomic force microscopy (AFM) was performed in a vibration-shielded hood to improve image quality. The cantilever probes were c-Si with nominal tip radius of 5-10 nm.

3.2.11 TRANSMISSION ELECTRON MICROSCOPY

Microstructure and film thickness was investigated using cross-sectional transmission electron microscopy (TEM). The cross-sectional TEM samples were prepared using a conventional "sandwich" technique. Two pieces of the sample were glued face-to-face using epoxy, mechanically thinned to ~50 um using abrasive paper, dimpled to ~5 um and milled to perforation by a 5 KeV Ar ion-beam. The images were obtained using a Topcon 002B High Resolution TEM with point-to-point resolution of 0.18 nm.

3.3 RESULTS AND DISCUSSION

3.3.1 ANALYSIS OF THICK (4500 Å) Y-O-Si FILMS FORMED BY OXIDATION OF YTTRIUM SILICIDE

Thick Y-O-Si films (4500 Å, determined from cross-sectional SEM) were formed by sputtering 2500 Å of yttrium onto clean Si, annealing in vacuum for 20 minutes to form yttrium silicide, then oxidizing by annealing in air for 20 minutes at 900 °C. Y_2O_3 films were prepared by sputtering 2500 Å of yttrium onto 500 Å of SiO_2 and annealing in air for 20 minutes at 900°C. SiO_2 films (1000 Å) were formed by wet oxidation.

XPS results comparing chemical bonding in Y-O-Si to Y_2O_3 and SiO_2 are presented in Fig. 3.3. Figure 3.3a presents the Y 3d photoelectron spectra for Y-O-Si and Y_2O_3. Consistent with literature values for Y_2O_3,[28] the Y $3d_{3/2}$ and Y $3d_{5/2}$ components of the spin-orbit splitting are measured at 158.8 and 156.8 eV, respectively. The Y $3d_{5/2}$ peak for Y-O-Si at 158.2 eV is at higher binding energy than the 156.8 eV measured for Y_2O_3, indicating the Y-O-Si has bonding significantly different from Y_2O_3. The splitting between the Y $3d_{3/2}$ and Y $3d_{5/2}$ components of the Y-O-Si is almost obscured indicating the presence of yttrium in multiple oxidation states. The Y 3d spectra for Y-O-Si and Y_2O_3 in Fig. 3.3a indicate that the yttrium in both films is fully oxidized, since a metallic Y 3d peak at 156.0 eV is not observed. The binding energy for Y 3d and Si 2p in yttrium silicide are expected to be ~0.2 and ~0.6 eV, respectively, lower than the metallic peak positions.[29] There is no evidence for Y-Si bonds in the Y-O-Si Y 3d spectrum. The feature at ~153.0 eV results from a combination of the Si-O Si 2s and Y 3d satellite peaks. Figure 3.3b shows the Si 2p portion of the XPS signal for Y-O-Si and SiO_2. Consistent with reference spectra for SiO_2,[28] the Si 2p photoelectron peak position is measured at 103.3 eV. The Si 2p peak for Y-O-Si (101.6

eV) is measured at lower binding energy than for SiO_2. The full-width-half-maximum (FWHM) of the Si-O Si 2p peak for SiO_2 and Y-O-Si are measured at 1.8 and 2.4 eV, respectively, indicating a wider range of silicon bonding environments available in the Y-O-Si. Figure 3.3c presents the O 1s spectra for Y-O-Si, Y_2O_3 and SiO_2. The O 1s peak at 531.8 eV is intermediate between O 1s for SiO_2 (533.0 eV) and Y_2O_3 (529.5 eV). The shoulder observed on the Y_2O_3 spectrum at 531.8 eV is assigned to O-H bonding in the film likely acquired during post-deposition exposure to ambient water.[30] The measured FWHM of O 1s in Y-O-Si is 3.1 eV, which is greater than expected for an elemental oxide (i.e. measured FWHM of SiO_2 is 1.8 eV) indicating the presence of multiple oxygen bonding configurations in the Y-O-Si.

Exposing an yttrium silicide film to an oxidizing ambient results in oxidation of the silicide to form a film with a significant fraction of Y-O-Si bonds. The photoelectron spectra of Figs. 3.3a and 3.3b do not indicate the presence of Y-Si bonds (within detectable limits). Since yttrium and silicon are only bound to oxygen in the yttrium silicate crystal structures exhibited in Figs. 3.1a and 3.1b, the absence of Y-Si bonding in Y-O-Si films is expected. The chemical shifts of the Y 3d, Si 2p and O 1s (Figs. 3.3a, 3.3b and 3.3c, respectively) peaks for Y-O-Si compared to Y_2O_3 and SiO_2 are consistent with donation of electron density from yttrium to the Si-O bond in the Y-O-Si in accordance with the relative electronegativities of yttrium, silicon and oxygen (1.2, 1.8, 3.5 on the Pauling scale). The observation that the Y 3d and Si 2p peak positions for the Y-O-Si are different than either Y 3d in Y_2O_3 or Si 2p in SiO_2 indicates the presence of a uniform material with the absence of phase separated Y_2O_3 (at 156.8 eV) or SiO_2 (at 103.3 eV) (within detectable limits) after annealing in an oxidizing ambient at 900 °C.

Analysis of the bonding environments in Y-O-Si, SiO_2 and Y_2O_3 were investigated using FTIR. Figure 3.4a presents the mid-IR (1600-400 cm^{-1}) region of the FTIR spectrum for Y-O-Si and SiO_2. The mid-IR spectrum of SiO_2 exhibits three characteristic vibrational modes of SiO_2. The peaks located at 1077, 810 and 400 cm^{-1} are the Si-O-Si asymmetric stretching, bending and rocking modes, respectively. These peaks are typical for a stoichiometric and relaxed amorphous SiO_2 network. The mid-IR spectrum of Y-O-Si exhibits several broad bands in the Si-O stretching region above 800 cm^{-1}. The broad peak in the range of 500 to 400 cm^{-1} may correspond to the superposition of rocking Si-O vibrations and Y-O bond vibrations. Figure 3.4b presents the far-IR region (650-45 cm^{-1}) of the FTIR spectrum for Y-O-Si and Y_2O_3. The far-IR spectrum of Y_2O_3 exhibits vibrational modes at 374, 335 and 303 cm^{-1} characteristic of Y-O-Y stretching in Y_2O_3.[31] The Y-O-Si far-IR displays two broad peaks assigned to Y-O stretching in the Y-O-Si film.

The infrared spectroscopy results of Figs. 3.4a and 3.4b are consistent with a dominant Y-O-Si bond structure after oxidation of yttrium silicide. In the mid-IR (Fig. 3.4a), the broad bands above 800 cm^{-1} in the Y-O-Si are assigned to Si-O vibrations, consistent with a weakened Si-O bond resulting from electron density transfer from yttrium to the Si-O bond and a wide distribution of Si-O bond angles in the Y-O-Si. In the far-IR (Fig. 3.4b), the broadening of the Y-O stretching is consistent with a wider distribution of bond angles in the Y-O-Si compared to Y_2O_3. The small oscillations in the Y-O-Si spectrum are due to interference. The observation that the FTIR spectra peak positions for the Y-O-Si are different than either Y_2O_3 or SiO_2 indicates the presence of a uniform material with the absence of phase separated Y_2O_3 or SiO_2 (within detectable limits) after annealing in an oxidizing ambient at 900 °C.

The oxidation of yttrium silicide is different than the oxidation characteristics of many silicides. As described in Section 3.1, oxidation of a metal silicide where the metal oxide has a $-\Delta G_f$ per oxygen atom greater than that of SiO_2 will result in a mixed metal oxide/SiO_2 film. Since Y_2O_3 has a greater $-\Delta G_f$ per oxygen atom than SiO_2, oxidation of yttrium silicide is expected to form a Y-O-Si film. This is demonstrated in Figs. 3.3 and 3.4, where XPS and FTIR results show that oxidation of yttrium silicide produces a film with spectroscopic properties different than either Y_2O_3 or SiO_2. The formation of a Y-O-Si film accounts for these spectroscopic differences.

3.3.2 ANALYSIS OF THIN (~40 Å) Y-O-Si FILMS FORMED BY OXIDATION OF YTTRIUM ON SILICON

3.3.2.1 Physical characterization

XPS results for a thin Y-O-Si film (~40 Å) formed by oxidizing ~8 Å of yttrium on silicon for 15 seconds at 900 °C are presented in the survey, Y 3d, Si 2p and O1s spectra of Figs. 3.5a-d, respectively. The photoelectron peaks for yttrium, oxygen, silicon and adventitious carbon are clearly evident in the survey spectra (Fig. 3.5a). The Y $3d_{3/2}$ and Y $3d_{5/2}$ peaks in Fig. 3.5b are measured at 160.8 and 159.0 eV, respectively. The Y 3d peak positions are consistent with Y-O bonding, but at higher binding energy than Y_2O_3 reference spectra (156.8 eV)[28], and the spin-orbit splitting is 1.8 eV, which is less than Y_2O_3 reference spectra (2.0 eV)[28]. In the Si 2p spectrum (Fig. 3.5c), the peak at 99.3 eV is assigned to silicon in the substrate, and the peak at 102.9 eV is assigned to Si-O bonding in the Y-O-Si, which is lower than the expected binding energy for SiO_2 (103.3 eV), but within the expected range for silicates (102-103 eV).[28] The O 1s peak (Fig 3.5d) is a broad peak (FWHM = 3.0 eV) at 532.8 eV and is intermediate between O 1s for SiO_2 (533.0 eV) and Y_2O_3 (529.5 eV). The

composition calculated from the MEIS spectrum (not shown) of a film formed by oxidation at 900 °C of a ~8 Å yttrium film on silicon is $(Y_2O_3)_{0.32}\cdot(SiO_2)_{0.68}$, which is within the experimental error (x ± 0.04) of keiviite ($Y_2Si_2O_7$).

Similar to the oxidation of yttrium silicide, oxidation of a thin yttrium film on silicon results in the formation of a film with a significant fraction of Y-O-Si bonds. In Figs. 3.5b and 3.5c, there is no evidence for Y-Si bonds either as a low energy (<99.3 eV) feature on the silicon substrate peak or as a peak at 155.6 eV in the Y 3d spectrum. Again, yttrium and silicon are only bound to oxygen in the yttrium silicate crystal structures exhibited in Figs. 3.1a and 3.1b, and no Y-Si bonding is expected. The chemical shifts of the yttrium, silicon and oxygen indicate that the dominant bonding structure in the film is not Y_2O_3 or SiO_2, rather the material is uniform and consists of a large fraction of Y-O-Si bonds. The Y 3d and Si 2p (Figs 3.5b and 3.5c, respectively) peak positions for the film formed by oxidation of thin yttrium on silicon are both shifted to higher binding energy compared to the thick film formed by oxidation of yttrium silicide (Figs. 3.3a and 3.3b). This is due to differences in composition and will be discussed in a separate publication, where the dependence of the Y 3d and Si 2p peak positions on film composition will be presented in detail.[32]

The morphology of films formed by oxidizing ~8 Å of yttrium on silicon for 15 seconds at 900 °C was investigated using TEM and AFM. Figure 3.6 contains a high resolution TEM image of a 42 Å Y-O-Si film with an Al capping layer. The Al was evaporated after Y-O-Si formation and the stack did not undergo a post-metallization anneal. The Y-O-Si/Si interface is sharp and does not exhibit any indication of oxidation of the silicon substrate to form SiO_2. Lattice fringes are observed in the c-Si and Al, however, lattice fringes are not observed in the Y-O-Si layer indicating an amorphous film. Surface morphology was investigated using AFM, and the results are presented as the three

dimensional image in Fig. 3.7. The root mean square (RMS) roughness of this film is 1.0 Å, which is near the RMS roughness of 0.5-0.9 Å measured for c-Si.

3.3.2.2 Electrical characterization

Y-O-Si (~40 Å) films were formed by oxidizing ~8 Å of yttrium on silicon for 15 seconds in N_2O at 900 °C. The C-V characteristics of films formed on p- and n-type Si are presented in Fig. 3.8. Analysis of the C-V traces for Al/Y-O-Si/Si capacitors yields EOT of 12 and 11 Å for n- and p-type silicon, respectively. The physical thickness of these films obtained from TEM (see above in Section *3.3.2.1*) is ~42 Å, which corresponds to k ≅ 14. The expected ideal flat band voltages (V_{fb}) for aluminum gate MOS capacitors with $5x10^{15}$ cm^{-3} n-type and $1x10^{17}$ cm^{-3} p-type are –0.057 and –0.79 V, respectively. The measured V_{fb} are -0.74 and –1.63 V for capacitors on n- and p-type silicon, respectively, indicating positive fixed charges in the film on both n- and p-type substrates. There is a slight frequency dependence of the capacitance between 10 kHz and 1 MHz, as observed in Fig. 3.9, possibly indicating the presence of slow traps. Hysteresis was ~1 and ~10 mV on n- and p-type, respectively. The J-V characteristics for these films formed on n- and p-type silicon are presented in Fig. 3.10. The current densities in accumulation are J_g(1.0 V) = 0.5 A/cm^2 and J_g(-2.5 V) = 5.0 A/cm^2 for capacitors on n- and p-type, respectively.

The C-V curves presented in Figs. 3.8 and 3.9 demonstrate the scalability of an yttrium silicate dielectric. The V_{fb} shifts of -0.68 and -0.84 V for n- and p-type, respectively, suggest the presence of positive fixed charge in the dielectric of sufficient density to be problematic. Dangling bonds resulting from yttrium's preference to be six-fold coordinated and silicon's preference to be four-fold coordinated may contribute to the large charge densities, although the bonding configurations seen in Figs. 3.1a and 3.1b would satisfy all bonds. Initial results suggest the large charge density may result from competition between

yttrium/silicon reaction and oxidation leaving unsatisfied bonds, but this finding requires further investigation. The leakage current for the n-type capacitor is less than for a silicon dioxide of equivalent capacitance (J_g ~ 100-1000 A/cm^2)[2], but the leakage is greater than that expected for a SiO_2 of similar physical thickness (~1x10^{-9} A/cm^2)[33]. The large fixed charge density in the film possibly contributes to a trap state conduction mechanism, which accounts for the discrepancy in leakage current.

3.3.3 COMPARISON OF THIN FILMS FORMED BY OXIDATION OF YTTRIUM ON SILICON WITH THIN FILMS FORMED BY OXIDATION OF YTTRIUM SILICIDE

Figure 3.11 presents the Y3d, Si 2p and O 1s photoelectron spectra for two samples, both with 25 Å of yttrium on silicon, one with oxidation for 20 minutes at 600 °C and the other exposed to ambient conditions (1 atm air, 25 °C) for ~1 day (i.e. no thermal treatment). The Y 3d peak for the film exposed in ambient is measured at higher binding energy (158.2 eV) than expected for yttrium metal (156.0 eV)[28]. The film oxidized at 600 °C is shifted an additional 0.3 eV to 158.5 eV. The Y 3d spectrum for the film exposed in ambient exhibits a clear shoulder at 156.0 eV consistent with yttrium metal or possibly Y_2O_3 (156.8 eV). The Si 2p spectra for both films display a silicon substrate peak at 99.3 eV and a feature at higher binding energy assigned to Si-O bonding, although the area of the feature for the film exposed in ambient is 60% smaller than the feature for the film oxidized at 600 °C. The Si-O features are measured at 102.0 and 102.5 eV for the films exposed in ambient and oxidized at 600 °C, respectively. The O 1s peaks for the films exposed in ambient and oxidized at 600 °C are measured near 532.0 eV, however the O 1s peak for the film exposed

in ambient is measured at slightly higher binding energy and displays a slight shoulder at 530.5 eV.

The spectra in Fig. 3.11 for yttrium films on silicon exposed in ambient and oxidized at 600 °C are surprisingly similar. The XPS results for the 25 Å yttrium film on silicon oxidized at 600 °C are consistent with a Y-O-Si film, and, even without a thermal treatment, the spectra in Fig. 3.11 for 25 Å of yttrium on silicon exposed in ambient are also consistent with a Y-O-Si film. The chemical shift of the Y 3d peak for the film exposed in ambient is consistent with Y-O bonding, and more specifically, Y-O-Si bonding, since the peak is shifted to higher binding energy than Y_2O_3. There is either a small fraction of yttrium metal or Y_2O_3 present in the film exposed in ambient, as evident by the shoulder near 156.0 eV on the Y 3d spectrum. The presence of Y_2O_3 is more likely, since the shoulder at 530.5 eV on the O 1s spectrum for the film exposed in ambient is consistent with Y-O-Y bonding. The film exposed in ambient also contains Si-O bonding, as evident by the feature at 102.0 eV in the Si 2p spectrum of Fig. 3.11. The presence of oxidized yttrium and silicon is interesting, since the film did not undergo exposure to an oxidizing atmosphere at elevated temperature. The amount of Si-O bonding in the film is significantly greater than for a clean silicon sample exposed to ambient for ~1 day. It is clear from the XPS results of Fig. 3.11 that yttrium metal can react with both oxygen and silicon at room temperature. This reaction is not complete, since the Y 3d peak for the un-oxidized film is shifted 0.3 eV from the Y 3d peak of the film oxidized at 600 °C and the Si-O feature for the un-oxidized film is only ~40 % as large and is shifted to 0.5 eV lower binding energy than the Si-O feature of the film oxidized at 600 °C. The presence of oxidized silicon in the film exposed to ambient indicates that Y-O-Si film formation may occur through mixing of yttrium and silicon to

form silicide-like bonds concurrent with oxidation to form a Y-O-Si film. This hypothesis is tested by comparing the oxidation of yttrium on silicon to the oxidation of yttrium silicide.

Figure 3.12 displays the Si 2p photoelectron spectra for three films: (i) yttrium silicide formed by vacuum annealing a 550 Å yttrium film on silicon at 600 °C, (ii) an Y-O-Si film formed by oxidation of yttrium silicide, and, (iii) an Y-O-Si film formed by oxidation of yttrium on silicon. Figure 3.13 illustrates the processes employed to form the three films. The pathway along arrow (i) describes the process used to form yttrium silicide films, where yttrium films on silicon are annealed in vacuum. The pathway along arrow (ii) describes the process for films formed by oxidation of yttrium silicide, where the silicide is formed by the vacuum annealing step along arrow (ii) and then exposed at elevated temperature to an oxidizing ambient along arrow (ii). The pathway along arrow (iii) describes the process for films formed by the oxidation of yttrium on silicon, where the yttrium film is exposed to an oxidizing ambient at elevated temperature. In Fig. 3.12a, the two Y-O-Si films started with the same yttrium thickness (~8 Å) and were oxidized for the same time and temperature (15 seconds at 900 °C) with the only difference being silicide formation at 600 °C in vacuum before oxidation for one of the samples. In Fig. 3.12b, the two Y-O-Si films started with the same yttrium thickness (25 Å) and were oxidized for the same time and temperature (20 minutes at 600 °C) with the only difference being silicide formation at 600 °C in vacuum before oxidation for one of the samples. The photoelectron spectrum for yttrium silicide is presented for reference in Figs. 3.12a and 3.12b. The photoelectron spectrum for yttrium silicide shows a peak at 98.5 eV assigned to yttrium silicide and a peak at 102.0 eV assigned to Si-O bonding in the yttrium silicide. The Si-O peak results from oxidation of the yttrium silicide during *ex situ* transfer to the analysis chamber. In both Figs. 3.12a and 3.12b, the silicide peak at 98.5 eV is not evident in the spectra for either films oxidized at 600 or 900

°C. For oxidation at 600 or 900 °C, the Si-O peak positions for the film formed by oxidation of yttrium on silicon and for the film formed by oxidation of yttrium silicide are nearly identical. However, the area of the Si-O feature for the film formed by oxidation of yttrium on silicon at 900 °C (Fig. 3.12a) is ~40% smaller than the Si-O feature for the film formed by oxidation of yttrium silicide at 900 °C, and the area of the Si-O feature for the film formed by oxidation of yttrium on silicon at 600 °C (Fig. 3.12a) is ~20% smaller than the Si-O feature for the film formed by oxidation of yttrium silicide at 600 °C. For both oxidation at 600 and 900 °C, the Y 3d and O1s spectra (not shown) are similar.

The similarity between the Si 2p peak (Figs. 3.12a and 3.12b) positions for oxidation of yttrium on silicon and oxidation of yttrium silicide at 600 or 900 °C indicates that the Y-O-Si films created by either method are nearly identical. This concept is illustrated using the cartoon presented in Fig. 3.13. Whether, the oxidation of yttrium silicide (arrow ii) or the oxidation of yttrium on silicon (arrow iii) is chosen, the end result is essentially the same Y-O-Si film, with the possible exception of greater silicon incorporation into the Y-O-Si films formed by oxidation of yttrium silicide. The possible pathways for the incorporation of silicon into the Y-O-Si film during the oxidation of yttrium on silicon are: (1) no reaction of yttrium metal with silicon, oxidation of yttrium to Y_2O_3 and decomposition of Y_2O_3 during reaction with silicon; or (2) complete reaction between yttrium and silicon to form yttrium silicide and oxidation of all Y-Si bonds; or (3) a combination of (1) and (2). The formation of yttrium silicide has been shown to occur at relatively low temperatures (can be spontaneous for ultra-thin films at room temperature)[34] at a fast rate (~50 Å/s)[20]. The XPS results of Fig. 3.11 also demonstrate that this reaction can occur at room temperature. The similarity between the film formed by oxidation of yttrium on silicon and the film formed by

oxidation of yttrium silicide indicates that silicide formation is a possible intermediate step during the oxidation of yttrium on silicon, as illustrated by the dashed arrow in Fig. 3.13, where along the arrow (iii) there is also an intermediate pathway for silicide formation. However, it is likely that, since the yttrium films on silicon are annealed in an oxidizing ambient, competition between yttrium reaction with silicon and yttrium oxidation silicide causes a reduced silicon fraction in the film compared to a Y-O-Si film formed by oxidation of yttrium silicide. An *in vaccuo* XPS study would confirm the presence of Y-Si bonds during oxidation of yttrium on silicon.

The competition between yttrium reaction with silicon and yttrium oxidation is expected to depend on the deposited metal thickness. As the initial metal film thickness increases, it will be less likely that all the metal will react with silicon before the metal can oxidize directly. To demonstrate this, Y-O-Si films were formed by oxidation of metal and oxidation of silicide starting with 30 Å of yttrium. Figure 3.14 presents Y 3d, Si 2p and O 1s spectra (a, b, and, c, respectively) for 30 Å of yttrium deposited onto silicon and oxidized for 20 minutes at 600 °C and 30 Å of yttrium deposited onto silicon, annealed in vacuum at 600 °C to form yttrium silicide and oxidized for 20 minutes at 600 °C. The Y 3d, Si 2p and O 1s peak positions for the Y-O-Si film formed by oxidation of yttrium silicide are at 158.5, 102.0 and 531.9 eV, respectively, consistent with a Y-O-Si film. The Y 3d, Si 2p and O 1s peak positions for the film formed by oxidation of 30 Å of yttrium on silicon are at 158.0, 102.3 and 532.8 eV. The Si 2p spectra in Fig. 3.14b both display an attenuated silicon substrate peak at 99.3 eV and a Si-O feature at ~102 eV. However, the Si-O feature for the film formed by oxidation of yttrium silicide is clearly larger than the Si-O feature for the film formed by oxidation of 30 Å of yttrium on silicon. The O 1s spectrum (Fig. 3.14c) for the

film formed by oxidation of 30 Å of yttrium on silicon exhibits a strong shoulder on the lower binding energy side (530.5 eV) of the main peak.

The XPS results of Fig. 3.14 indicate that oxidizing a 30 Å yttrium film on silicon is close to the transition between the competition for yttrium reacting with silicon and yttrium oxidation. For the film formed by oxidation of 30 Å of yttrium on silicon, the Y 3d peak position (158.0 eV) is shifted towards the expected peak position for Y_2O_3 (156.8 eV), the Si-O feature (~102 eV) in the Si 2p spectrum (Fig 3.14b) is ~60% smaller than the Si-O feature for the film formed by oxidation of yttrium silicide and the shoulder at 530.5 eV on the O 1s spectrum (Fig. 3.14c) for the film formed by oxidation of 30 Å of yttrium on silicon is near the expected peak position for oxygen in Y_2O_3 (529.5 eV). Compared to the film formed by oxidation of yttrium silicide, these results are indicative of a film with a decreased silicon fraction, which results from a competition between silicide formation and oxidation.

3.3.4 COMPETITION BETWEEN SILICIDE FORMATION AND OXIDATION

When a reactive metal is deposited onto Si and exposed to an oxidizing ambient at elevated temperature, the metal can react with Si and oxidize. If the metal layer is sufficiently thick relative to the reaction rates, these two processes can be spatially separated. (i.e. M-Si reaction at the M/Si interface and metal oxidation reaction at the ambient/metal interface). The effect of metal overlayer thickness on oxidation/reaction products is shown in Figs. 3.15a-c, which presents photoelectron spectra for initial yttrium thickness of ~8 to 240 Å (10 minute oxidation at 900 °C). For an initial yttrium coverage of ~8 to 40 Å, the photoelectron spectra are consistent with a Y-O-Si film: a) the Y 3d peak (Fig. 3.15a) is measured at the expected Y-O-Si peak position of 159.0 eV; b) in Fig. 3.15b, the Si-O peak is measured at 102.9 eV and the silicon substrate peak at 99.3 eV becomes increasingly

attenuated; and, c) slight shifting is observed in the O 1s spectra (Fig. 3.15c), but the peaks are near the expected O 1s position for Y-O-Si (~532 eV). When the initial yttrium coverage is 40 Å, the spin-orbit splitting of the Y 3d spectrum (Fig. 3.15a) exhibits blurring of the splitting between the Y $3d_{3/2}$ and Y $3d_{5/2}$ components indicating the presence of multiple yttrium oxidation states. When the initial yttrium coverage is 80 to 240 Å, the photoelectron spectra are consistent with an Y_2O_3 film: a) the Y 3d (Fig. 3.15a) peak position is measured near the expected Y_2O_3 peak position of 156.8 eV; b) silicon (Fig. 3.15b) is not evident (up to the escape depth of Si 2p photoelectrons, $3\lambda \cong 75$ Å) in the film; and, c) the O 1s spectra (Fig. 3.15c) exhibit a main peak at 529.5 eV with a strong shoulder at 531.8 eV, which is assigned to O-H bonding in the film likely acquired during post-deposition exposure to ambient water.

The photoelectron spectra for the yttrium thickness series (Figs. 3.15a-c) illustrate the film formation mechanism that results from a competition between silicide formation at the yttrium/silicon interface and oxidation at the atmosphere/yttrium interface. The XPS results (Figs. 3.15a-c) clearly indicate that oxidation of a thin (<40 Å) yttrium film on silicon produces a Y-O-Si film. Oxidation of a thick (80 Å) yttrium film on silicon results in a top layer comprised of Y_2O_3 (at least up to the escape depth of the Si 2p photoelectrons, $3\lambda \cong 75$ Å). For an initial yttrium thickness of 40 Å, a thin Y_2O_3 or silicon-poor layer is beginning to form on the Y-O-Si film, since the blurring of the spin-orbit splitting in the Y 3d spectrum (Fig. 3.15a) indicates the presence of yttrium in multiple oxidation states. For thin (< 40 Å) yttrium coverage, the reaction at the yttrium/silicon interface to form yttrium silicide is fast enough to consume most, if not all, of the yttrium film before the oxidation reaction can form a significant amount of Y_2O_3, as illustrated by the process labeled "Thin Initial Yttrium" in Fig. 3.16. The process labeled "Thin Initial Yttrium" starts with a thin

yttrium film (<40 Å), which is then to an oxidizing ambient at elevated temperature resulting in a thin Y-O-Si film on silicon. For thicker initial yttrium layers, exposure to an elevated temperature oxidizing ambient results in Y_2O_3, and the top layer does not contain any silicon (up to the detection limit). When the initial yttrium is thicker than some critical thickness (somewhere around 40-80 Å), the silicide reaction is not fast enough to completely consume the yttrium film and Y_2O_3 is formed at the top interface while silicide is formed at the bottom interface. When the oxidation front meets the silicide front, a Y-O-Si film is produced. This mechanism produces an Y_2O_3/Y-O-Si bi-layer at thick yttrium coverage, as illustrated by the process labeled "Thick Initial Yttrium" in Fig. 3.16. The process labeled "Thick Initial Yttrium" starts with a thick yttrium film (>80 Å) and exposes it to an oxidizing ambient at elevated temperature. The competition for yttrium between silicide formation and oxidation results in the Y_2O_3/Y-O-Si bi-layer structure seen in Fig. 3.16. The following reactions can be written for this materials system:

$$Y_{(s)} + O_{2\,(g)} \rightarrow Y_2O_{3\,(s)} \tag{3.1}$$

$$Y_{(s)} + Si_{(s)} \rightarrow YSi_{(s)} \tag{3.2}$$

$$YSi_{(s)} + O_{2\,(g)} \rightarrow \text{Y-O-Si}_{(s)} \tag{3.3}$$

In the thin (<40 Å) initial yttrium regime, reaction (3.2) seems to dominate, since no Y_2O_3 is observed in the XPS spectra. In the thick (>80 Å) initial yttrium regime, reaction (3.1) seems to dominate, since no silicon is observed in the XPS spectra. It would be convenient to assume yttrium oxidation or yttrium silicide oxidation (reaction "3.1" or "3.3") is the rate-limiting step in the thin initial yttrium regime. However, the concentration of silicon incorporated during oxidation of yttrium depends on the oxidation temperature, and 900 °C oxidation compared to 600 °C oxidation generally results in increased silicon incorporation into the Y-O-Si film.[32] Therefore, the rates seem to be comparable, and the

detailed analysis required to deconvolute reactions (3.1)-(3.3) is beyond the scope of this article.

3.3.5 ANALYSIS OF OXIDATION KINETICS

Oxidation of yttrium (25 Å) on silicon was studied at 600 °C for times from 30 seconds to 20 minutes using XPS, and oxidation of yttrium (~8 Å) on silicon was studied at 900 °C for times from 6 seconds to 20 minutes using TEM and XPS. For comparison, the oxidation of Si(100) was studied at 900 °C for times from 15 seconds to 20 minutes. The Si-O/Si area ratio and the total physical thickness versus oxidation time are presented in Fig. 3.17. The Si-O/Si area ratios of Y-O-Si films formed at 600 and 900 °C are calculated by resolving the silicon-oxygen and silicon substrate peaks in the Si 2p spectrum, integrating both peaks and taking the area ratio. The total physical thickness of Y-O-Si and SiO_2 films formed at 900 °C is measured using cross-sectional TEM images and ellipsometry ($\lambda = 632.8$ nm), respectively. The physical thickness and Si-O/Si area ratio of Y-O-Si films are observed to rapidly increase for oxidation time <1 minute and to slowly increase for oxidation time >2 minutes. For times <1 minute, the Si-O/Si area ratio of Y-O-Si films increases at the same rate for oxidation at 600 and 900 °C. For times >1-2 minutes, the Si-O/Si area ratio is observed to increase more rapidly for films oxidized at 900 °C than for films oxidized at 600 °C. The thickness of Y-O-Si films is observed to increase more rapidly than the thickness of SiO_2 films for times <2 minutes, but oxidation of both films approaches the same rate for times >2 minutes. Figure 3.18 presents a high-resolution TEM image of an 8 Å yttrium film oxidized for 20 minutes at 900 °C, where the total thickness is 75 Å. The lattice fringes in the c-Si and the amorphous nature of the epoxy capping-layer are clearly visible. Only slight contrast exists between the bottom of the Y-O-Si layer and

the SiO_2 layer. After oxidizing an 8 Å yttrium film for 20 minutes, the Si-O peak in Fig. 3.19 is observed at 103.3 eV compared to 102.9 eV for the 15 second oxidized film in Fig. 3.5c. This shift to higher binding energy for the 20 minute oxidized film is consistent with the oxidation of the silicon substrate to form a buried SiO_2 layer. Also, the spectrum in Fig 3.19 shows that the silicon substrate peak at 99.3 eV has been attenuated, indicating an increase in thickness. The Y 3d spectra for 8 Å yttrium films oxidized for 6 seconds to 20 minutes at 900 °C is presented in Fig. 3.20. The Y 3d spectrum (Fig. 3.20) shifts from 158.4 to 159.1 eV as the oxidation time increases from 6 seconds to 2 minutes. After 2 minutes of oxidation, the Y 3d peak stays fixed at 159.1 eV upon oxidation up to 20 minutes. The absence of phase separated Y_2O_3 in the Y 3d spectrum indicate the stability of Y-O-Si after annealing in an oxidizing ambient for 20 minutes. During 6 seconds to 20 minutes of oxidation, the Y 3d peak position is consistent with Y-O bonding, and the spectra provide no evidence for any Y_2O_3 or yttrium silicide bonding indicating the stability of the films.

Two regions of oxidation kinetics in Y-O-Si films are observed in the XPS and TEM results of Fig. 3.17. At short times, fast oxidation results in a rapid increase in film thickness. At longer times, slow oxidation results in a gradual increase in total thickness. During the fast oxidation (oxidation time <2 minutes), the shifting to higher binding energy of the Y 3d peak position observed in Fig. 3.20 indicates chemical changes occurring in the Y-O-Si film. The fast oxidation is attributed to the oxidation of yttrium-silicon bonds, which oxidize rapidly. The oxidation rate at 900 °C for times <2 minutes of the yttrium films on silicon is estimated from the TEM data of Fig. 3.17 as 45 Å/minute, which is ~6 times faster than the oxidation rate of ~8 Å/minute at 900 °C for c-Si(100) estimated from the same time scale in the ellipsometry data. During the slow oxidation (oxidation time from 2-20 minutes), the Y 3d peak position does not change, which indicates that the oxidation at long times observed

in Fig. 3.17 does not occur within the Y-O-Si film, but results from oxidation of the silicon substrate. The oxidation of the silicon substrate is illustrated in Fig. 3.19, where the shift of the Si-O peak (103.3 eV) and the attenuation of the silicon substrate peak are consistent with a buried SiO_2 layer, as pictured in the TEM image of Fig. 3.18. The slow oxidation at long oxidation time is consistent with oxidation of the silicon substrate. As expected, the oxidation rate of the silicon substrate at 900 °C is faster than the oxidation rate of the silicon substrate at 600 °C, as evident in the slope of the Si-O/Si versus oxidation time data for times >1-2 minutes. The oxidation rate between 2-20 minutes at 900 °C of the substrate is estimated from the TEM and ellipsometry data of Fig. 3.17 as ~2 Å/minute.

3.4 CONCLUSIONS

High-k dielectrics often contain metals that have a high affinity for oxygen and form stable silicides. When a metal, such as yttrium, that has a high affinity for oxygen and forms stable silicides is deposited on silicon and oxidized, the above results indicate that a competition between metal-silicon reaction and metal oxidation develops. When the thickness of the metal is less than some critical thickness (~40-80 Å), the metal-silicon reaction consumes the metal layer before significant metal oxidation can occur resulting in a metal-O-Si film. When the metal is thicker than some critical thickness, the above results indicate that significant metal oxidation can occur before the metal-silicon reaction can consumes the entire metal film resulting in a metal oxide/silicate bi-layer. In the process described here where a thin metal is deposited onto silicon then oxidized, the high reactivity of yttrium with silicon and oxygen is an advantage that enables the formation of a Y-O-Si interface free of SiO_2. However, when the desired product is a metal oxide, the high reactivity of the metal can be a disadvantage that leads to the formation of a silicate interface layer. The formation of thin Y-O-Si films is thought to result from concurrent yttrium-

silicon reaction and oxidation to form Y-O-Si bonding units. XPS and FTIR demonstrate the formation of yttrium silicate when thick yttrium silicide films are oxidized, and similar XPS results are observed for the oxidation of thin yttrium films on silicon and the oxidation of thin yttrium silicides. Amorphous yttrium silicate films (~40 Å) with EOT = 11 Å have been formed by the oxidation of thin yttrium films on silicon. These results demonstrate that an yttrium-based silicate can be scaled down to the EOT ~ 10 Å regime. In principle, oxidation of other metals, such as Hf, Zr and La, on silicon is expected to result in a metal silicate film.

3.5 ACKNOWLEDGEMENTS

The authors acknowledge E. Garfunkel and B. W. Busch at Rutgers University for the MEIS results. The authors thank B. Rayner and G. Lucovsky at NCSU for their assistance in obtaining the far-IR spectra. Support is from the SRC/SEMATECH Center for Front End Processes and NSF CTS – 0072784.

3.6 REFERENCES

1. S. I. Association, *The International Technology Roadmap for Semiconductors, 1999 edition* (Austin, TX, 1999).
2. D. A. Buchanan and S.-H. Lo, Micro. Engineer. **36,** 13 (1997).
3. M. Gurvitch, L. Manchanda, and J. M. Gibson, Appl. Phys. Lett. **51,** 919-921 (1987).
4. K.-A. Son, A. Y. Mao, B. Y. Kim, F. Liu, E. D. Pylant, D. A. Hess, J. M. White, D. L. Kwong, D. A. Roberts, and R. N. Vrtis, J. Vac. Sci. Technol. A **16,** 1670 (1998).
5. B. He, T. Ma, S. A. Campbell, and W. L. Gladfelter, Tech. Dig. Int. Electron Devices Meet.**,** 1038 (1998).
6. M. Balog, M. Schieber, S. Patai, and M. Michman, J. Cryst. Growth **17,** 298 (1972).
7. J. Shappir, A. Anis, and I. Pinsky, IEEE Trans. Electron Devices **ED-33,** 442 (1986).
8. L. Manchanda, W. H. Lee, J. E. Bower, F. H. Baumann, W. L. Brown, C. J. Case, R. C. Keller, Y. O. Kim, E. J. Laskowski, M. D. Morris, R. L. Opila, P. J. Silverman, T. W. Sorsch, and G. R. Weber, Tech. Dig. Int. Electron Devices Meet.**,** 605 (1998).
9. K. J. Hubbard and D. G. Schlom, J. Mater. Res. **11,** 2757-2776 (1996).
10. S. A. Campbell, H.-S. Kim, D. C. Gilmer, B. He, T. Ma, and W. L. Gladfelter, IBM J. Res. Dev. **4,** 383 (1999).
11. G. D. Wilk, R. M. Wallace, and J. M. Anthony, J. Appl. Phys. **87,** 484 (2000).
12. I. Barin, *Thermochemical Data of Pure Substances* (VCH Verlagsgesellschaft, Weinheim, Germany, 1989).
13. N. G. Batalieva and Y. A. Pyatenko, Zhurnal Strukturnoi Khimii **8,** 548 (1967).

14 B. A. Maksimov, V. V. Ilyukhin, Y. A. Kharitonov, and N. V. Belov, Kristallografiya **15,** 926 (1970).

15 E. M. Levin, C. R. Robbins, and H. F. McMurdie, *Phase Diagrams for Ceramists: 1969 Supplement*, Vol. Figure 2388 (The American Ceramic Society, Columbus, Ohio, 1969).

16 J. D. Webster, M. E. Westwood, F. H. Hayes, R. J. Day, R. Taylor, A. Duran, M. Aparicio, K. Rebstock, and W. D. Vogel, J. Euro. Ceram. Soc. **18,** 2345-2350 (1998).

17 J. E. E. Baglin, F. M. Dheurle, and C. S. Petersson, J. Appl. Phys. **52,** 2841-2846 (1981).

18 A. Pellissier, R. Baptist, and G. Chauvet, Surf. Sci. **210,** 99-113 (1989).

19 Y. K. Lee, N. Fujimura, and T. Ito, J. Alloys Compounds **193,** 289-291 (1993).

20 P. Mazurek, Z. Mitura, K. Paprocki, M. Subotowicz, and P. Mikolajczak, Vacuum **46,** 531-535 (1995).

21 A. Mesarwi and A. Ignatiev, Surf. Sci. **244,** 15-21 (1991).

22 S. P. Murarka, J. Vac. Sci. Technol. **17,** 775 (1980).

23 T. Mochizuki and M. Kashiwagi, J. Electrochem. Soc. **127,** 1128-1135 (1980).

24 S. Zirinsky, W. Hammer, F. Dheurle, and J. Baglin, Appl. Phys. Lett. **33,** 76-78 (1978).

25 S. P. Murarka, D. B. Fraser, W. S. Lindenberger, and A. K. Sinha, J. Appl. Phys. **51,** 3241-3245 (1980).

26 S. P. Murarka and C. C. Chang, Appl. Phys. Lett. **37,** 639 (1980).

27 E. P. Gusev, H. C. Lu, T. Gustafsson, and E. Garfunkel, Phys. Rev. B **52,** 1759-1775 (1995).

28 J. F. Moulder, W. F. Stickle, P. E. Sobol, and K. D. Bomben, *Handbook of X-ray Photoelectron Spectroscopy* (Perkin-Elmer Corporation, Eden Prairie, MN, 1992).

29 R. Baptist, A. Pellissier, and G. Chauvet, Sol. State Commun. **68**, 555 (1988).

30 O. G. Alekseev, N. V. Krivosheev, M. Y. Khodos, V. R. Galakhov, V. V. Shumilov, V. M. Cherkashenko, E. Z. Kurmaev, and V. A. Gubanov, Inorg. Mater. **22,** 1748-1751 (1986).

31 Y. Nigara, M. Ishigame, and T. Sakurai, J. Phys. Soc. Japan **30,** 453 (1971).

32 J. J. Chambers and G. N. Parsons, to be submitted.

33 K. H. Lee and S. A. Campbell, J. Appl. Phys. **73,** 4434 (1993).

34 T. L. Lee and L. J. Chen, J. Appl. Phys. **73,** 8258-8266 (1993).

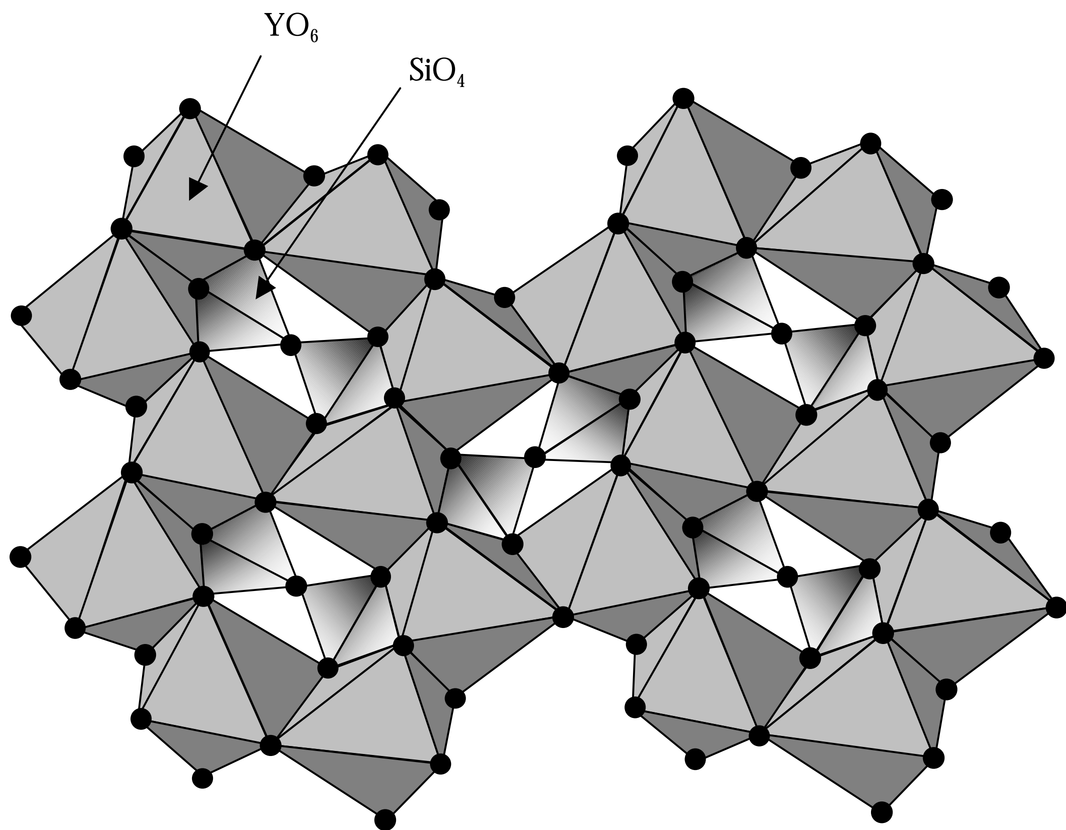

Figure 3.1a Schematic depicting crystal structure of $Y_2Si_2O_7$. Note that $Y_2Si_2O_7$ contains an oxygen atom that is only bound to silicon atoms.

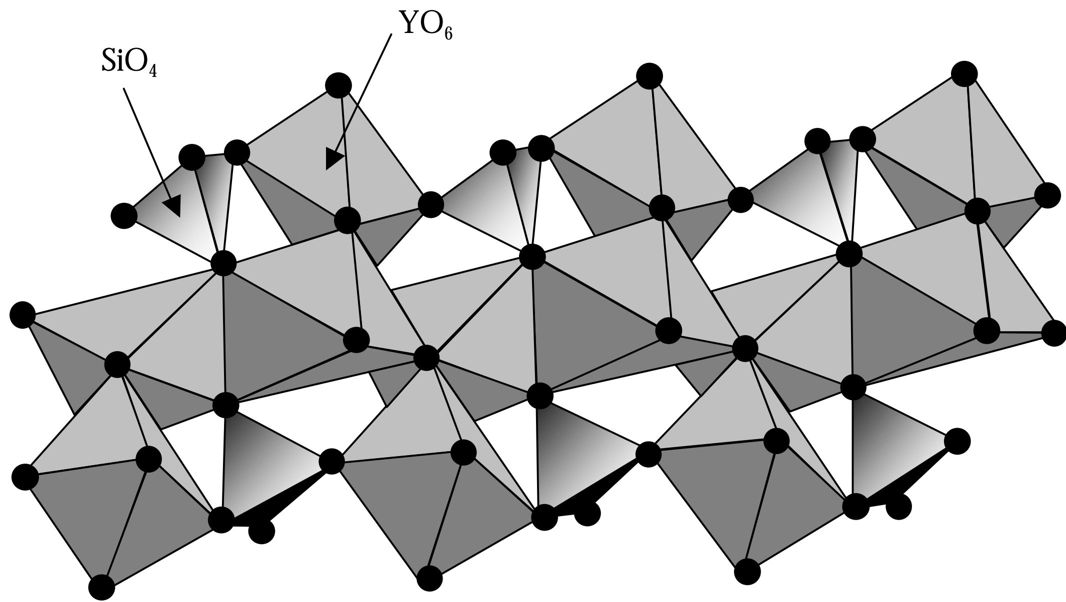

Figure 3.1b Schematic depicting crystal structure of Y_2SiO_5. Note that Y_2SiO_5 contains an oxygen atom that is only bound to yttrium atoms.

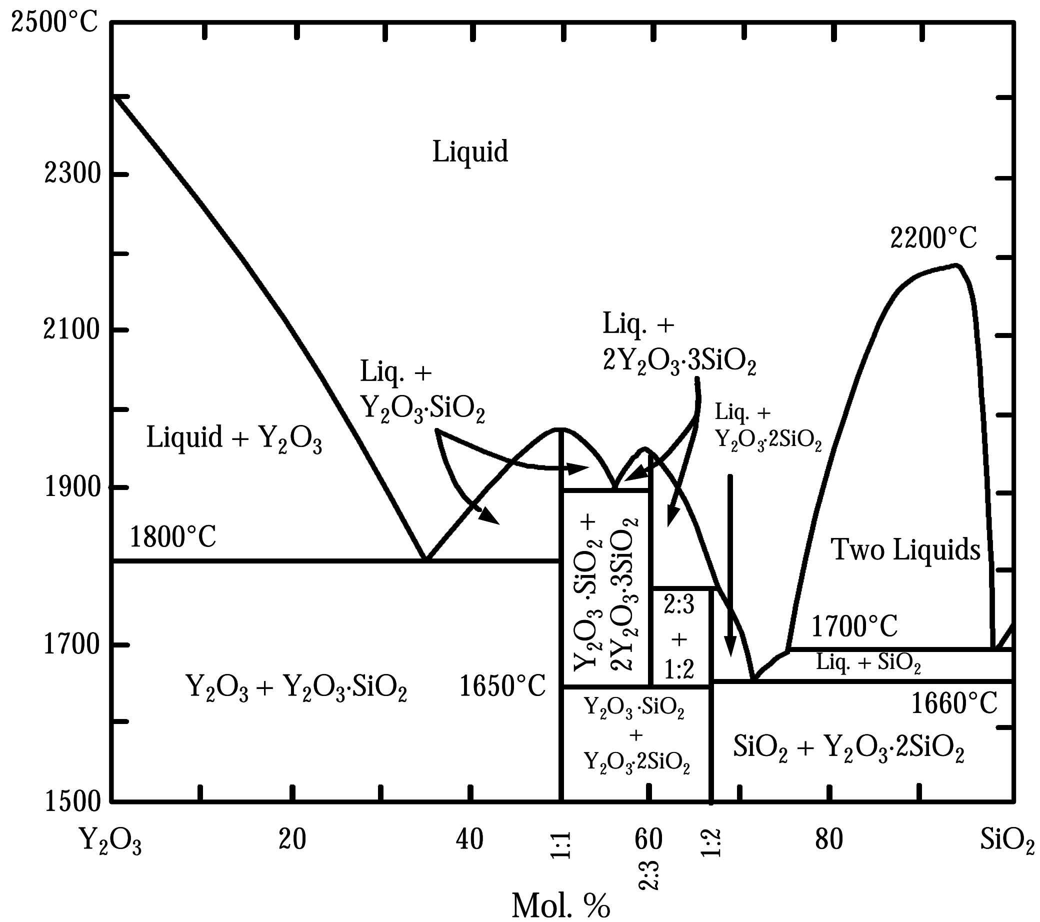

Figure 3.1c Y_2O_3-SiO_2 phase diagram. A region exists where the 1:1 and 1:2 compositions coexist.

Table 3.1 Free energy of formation per oxygen atom for metal oxides[12] and the expected oxidation products of their metal silicides.

Metal	$-\Delta G_f$ (10^{-22} kcal/O atom) of Metal Oxide	Expected Oxidation Product of Metal Silicide on Silicon
Si	1.70	-
Ta	1.52	$SiO_2/TaSi_2/Si$
Mo	0.88	$SiO_2/MoSi_2/Si$
W	1.01	$SiO_2/WSi_2/Si$
Y	2.40	$Y_2O_3 \cdot SiO_2/Si$
La	2.26	$La_2O_3 \cdot SiO_2/Si$
Zr	2.06	$ZrO_2 \cdot SiO_2/Si$
Hf	2.16	$HfO_2 \cdot SiO_2/Si$

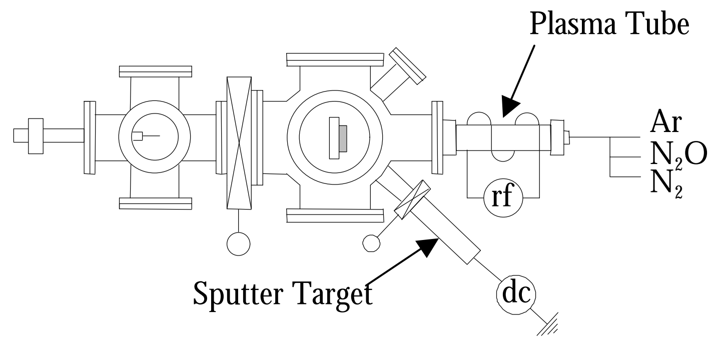

Figure 3.2 Diagram of system used to sputter yttrium and perform vacuum anneals. The plasma processing chamber employs a retractable sputter target that can be isolated from the processing chamber.

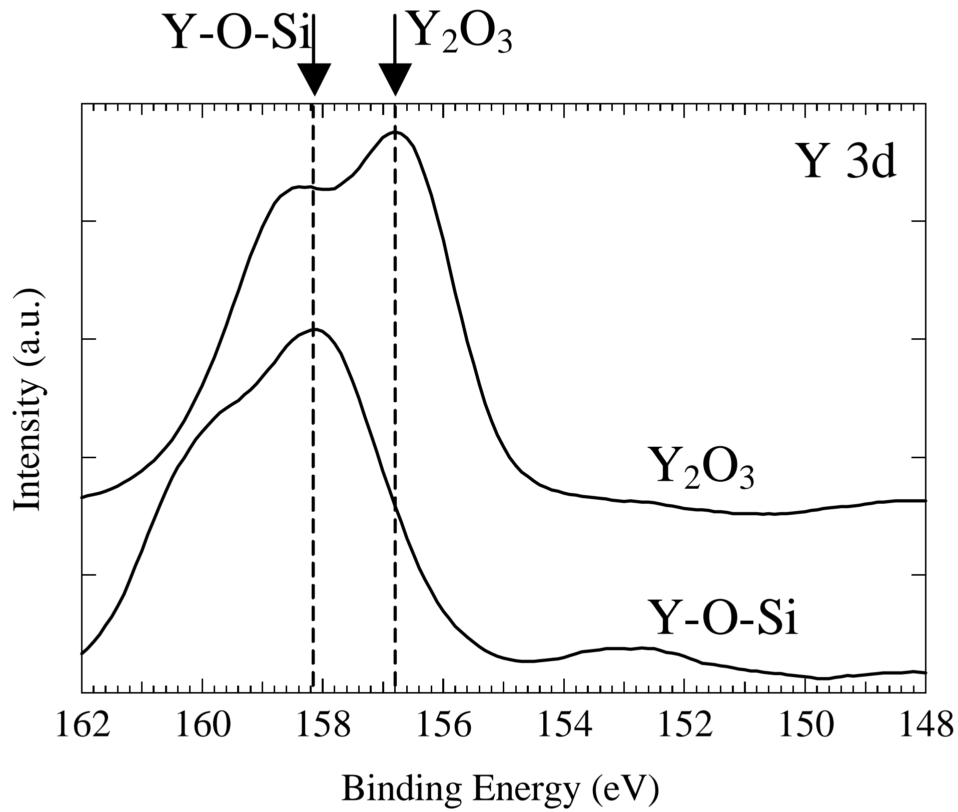

Figure 3.3a Y 3d region of the photoelectron spectra of Y-O-Si and Y_2O_3. The Y-O-Si spectra indicate the presence of Y-O-Si bonds with no evidence for phase separated Y_2O_3 or SiO_2.

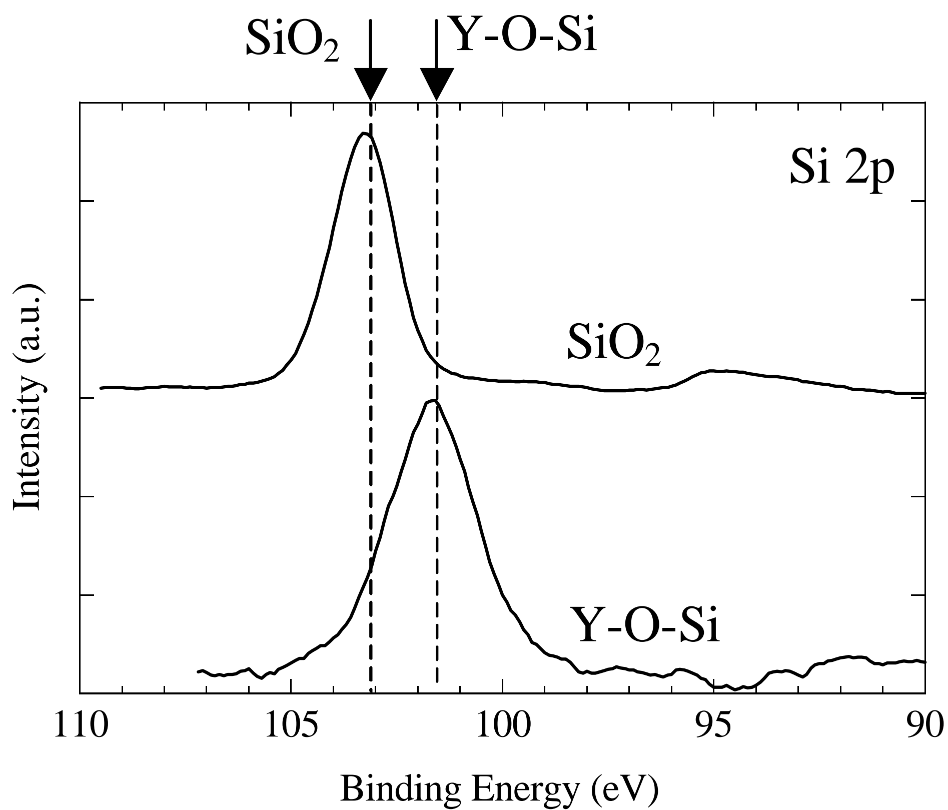

Figure 3.3b Si 2p region of the photoelectron spectra of Y-O-Si and SiO_2. The Si-O feature for Y-O-Si is measured at lower binding energy than Si-O in SiO_2.

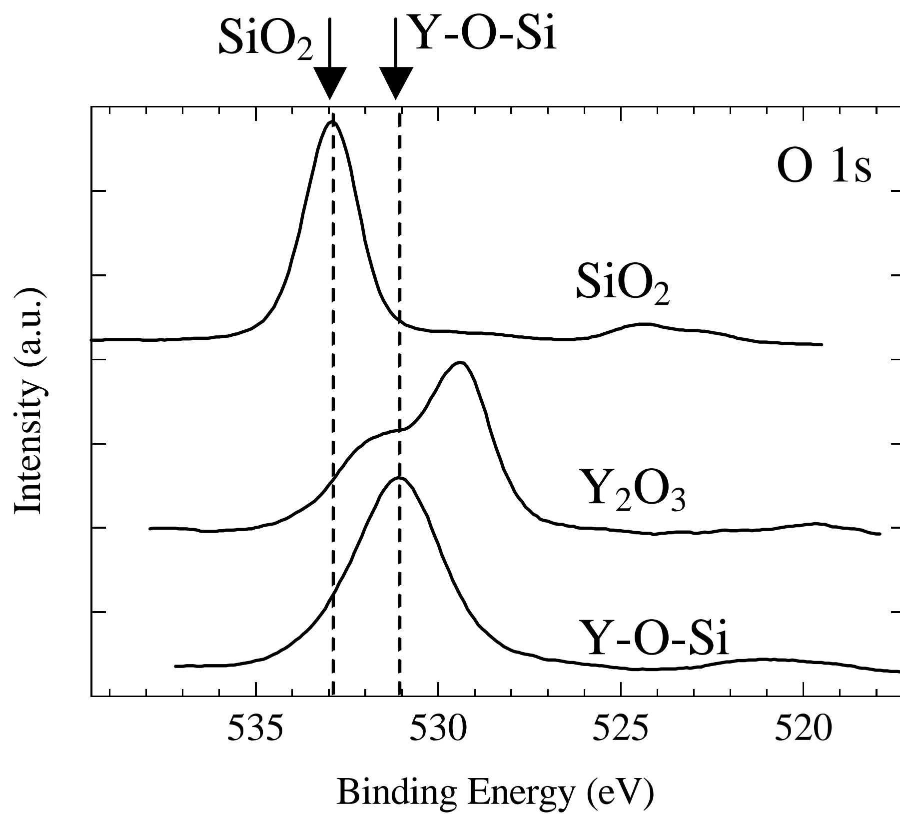

Figure 3.3c O 1s region of the photoelectron spectra of Y-O-Si, Y_2O_3 and SiO_2. O 1s in Y-O-Si is measured at an intermediate binding energy between SiO_2 and Y_2O_3.

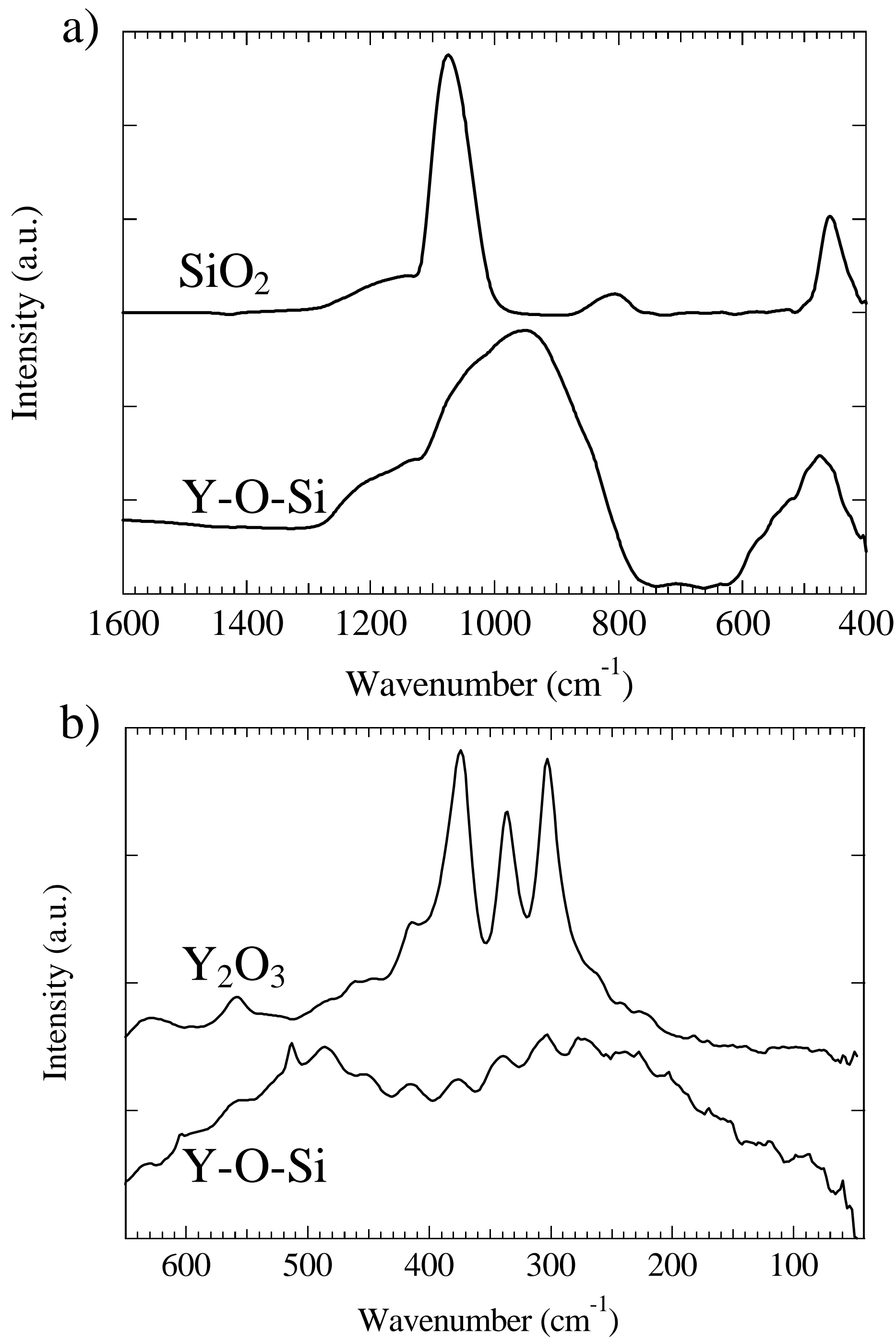

Figure 3.4 Mid (a) and Far (b) IR regions of the FTIR spectrum for Y-O-Si, Y_2O_3 and SiO_2. The Si-O feature (800-1200 cm^{-1}) for the Y-O-Si film is shifted to lower wavenumber and broadened compared to the spectra for SiO_2. The Y-O feature (600-100 cm^{-1}) for the Y-O-Si film is broader than observed for Y_2O_3.

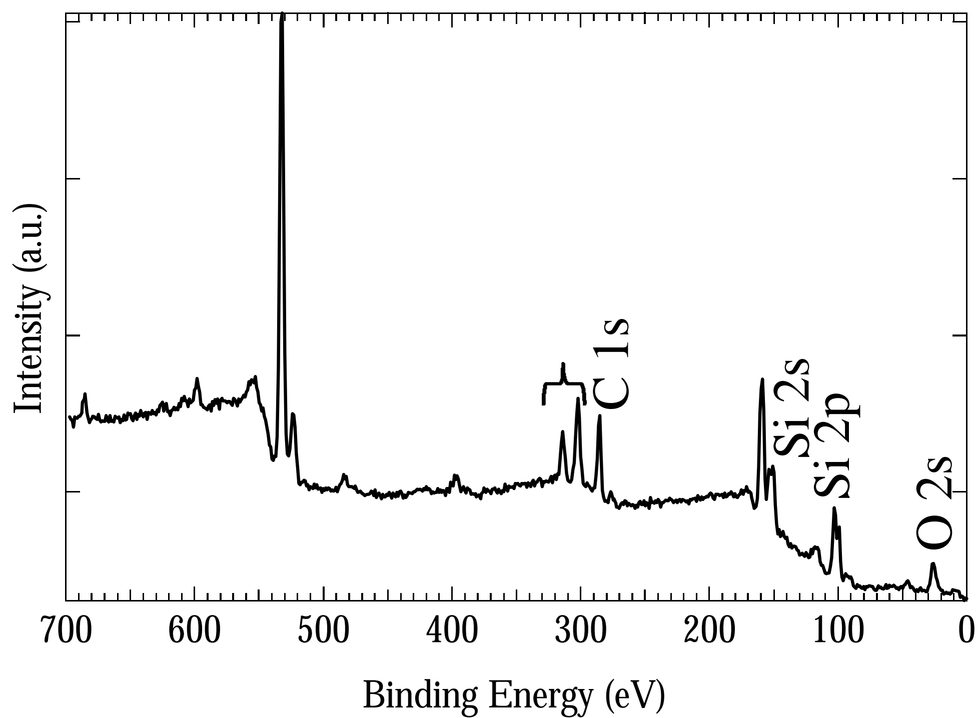

Figure 3.5a Survey spectrum for Y-O-Si film formed by oxidation of ~8 Å of yttrium on silicon at 900 °C.

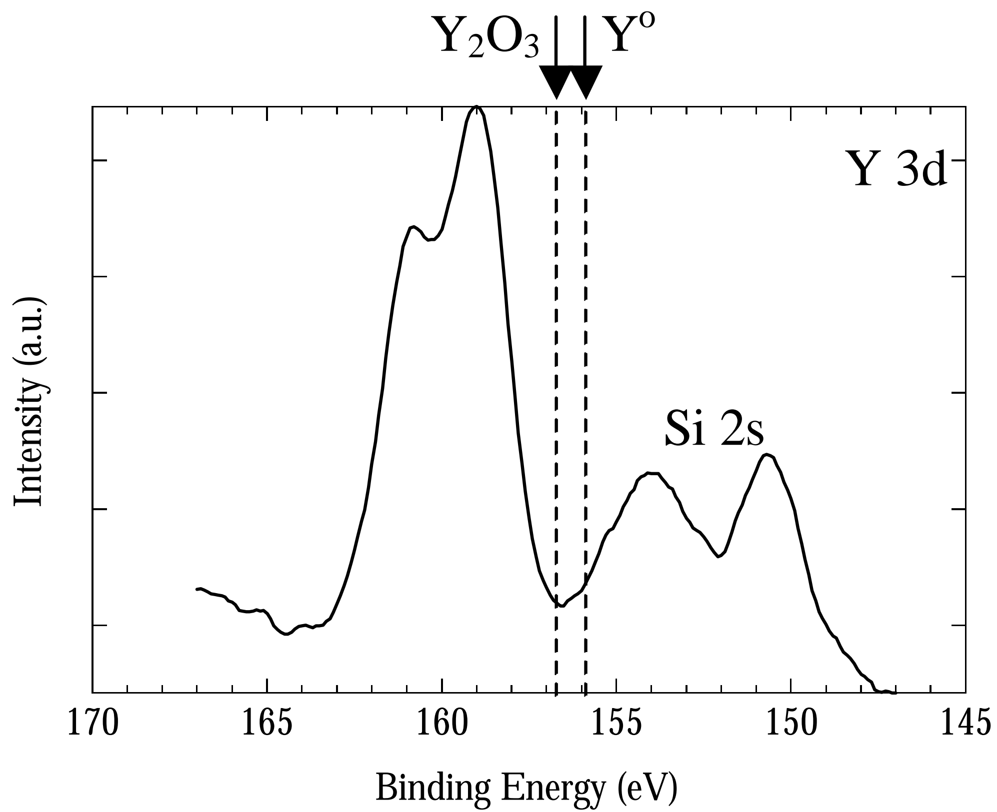

Figure 3.5b Y 3d spectrum for Y-O-Si film formed by oxidation of ~8 Å of yttrium on silicon at 900 °C.

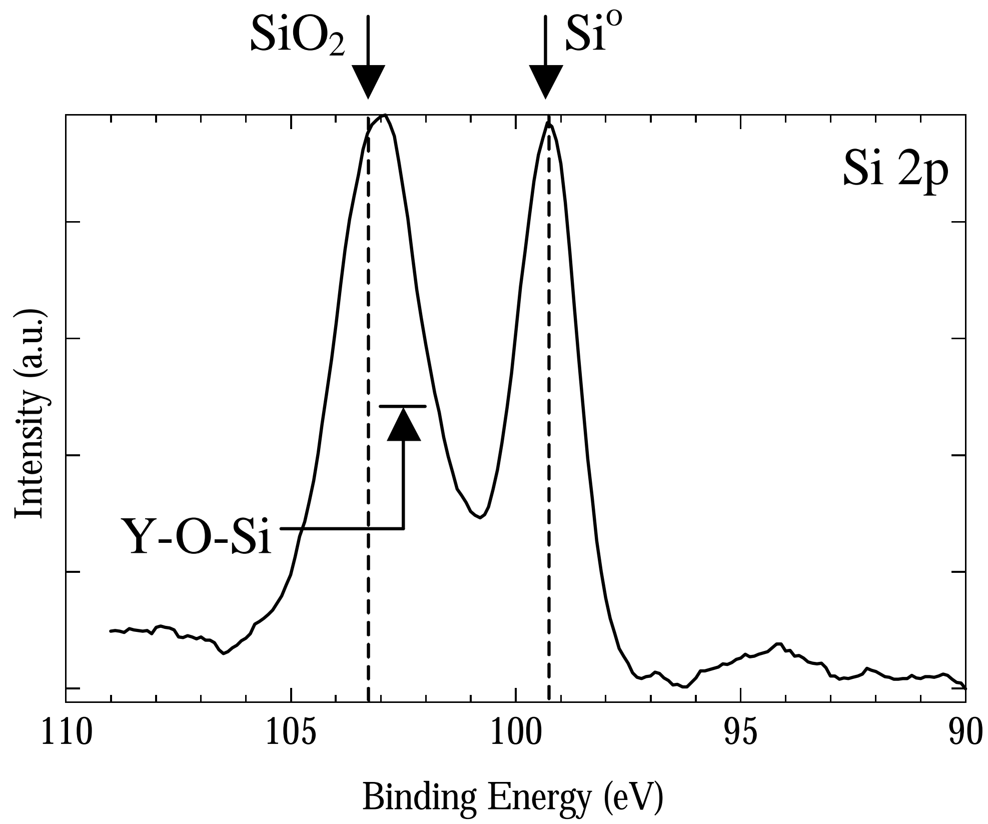

Figure 3.5c Si 2p spectrum for Y-O-Si film formed by oxidation of ~8 Å of yttrium on silicon at 900 °C.

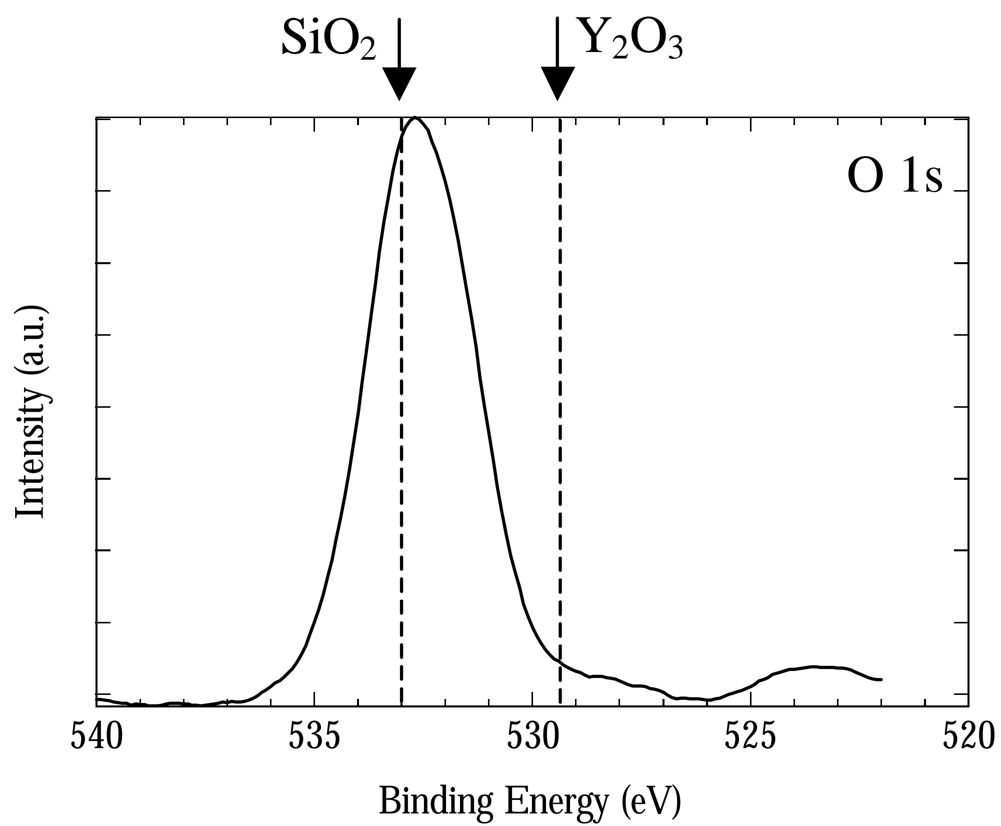

Figure 3.5d O 1s spectrum for Y-O-Si film formed by oxidation of ~8 Å of yttrium on silicon at 900 °C.

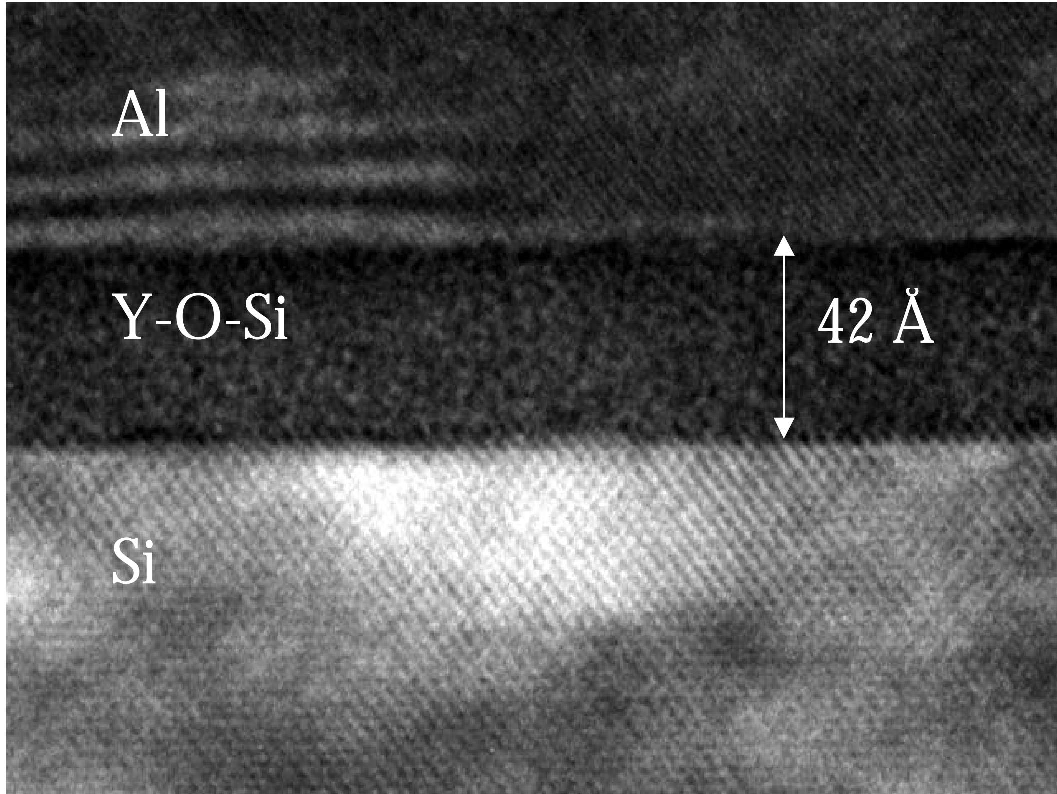

Figure 3.6 TEM cross-section of a 42 Å Y-O-Si film formed by oxidation of ~8 Å of yttrium on silicon at 900 °C. The amorphous nature of the Y-O-Si film and interfacial layer free interface with silicon are observed.

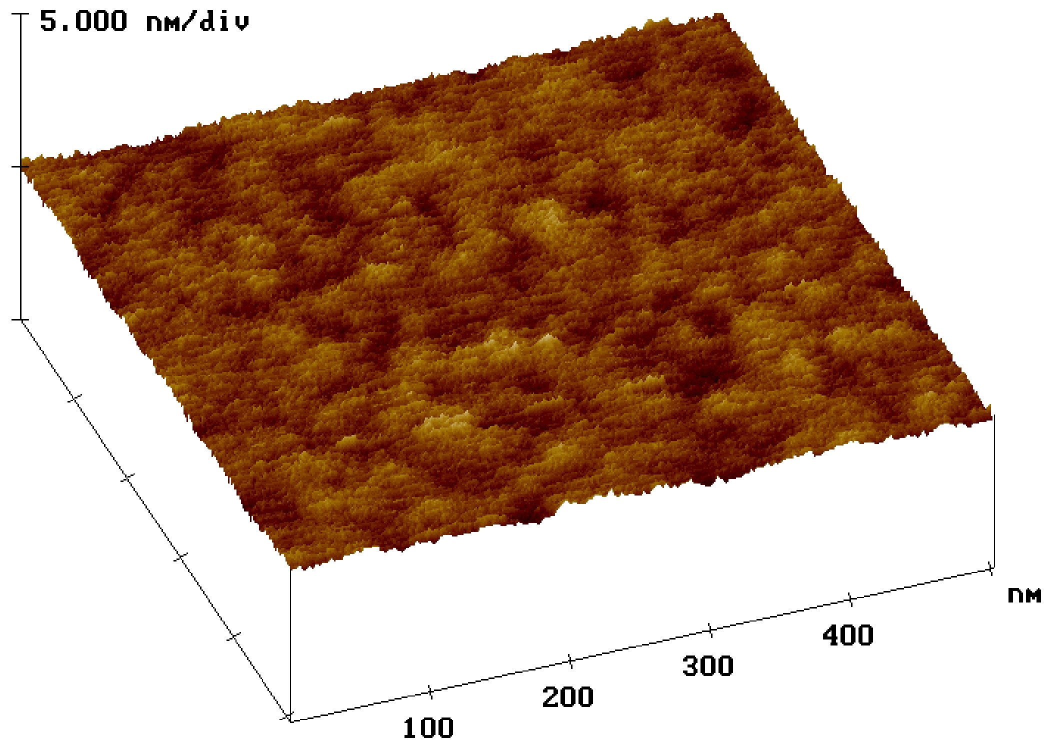

Figure 3.7 AFM image of an Y-O-Si film formed by oxidation of ~8 Å of yttrium on silicon at 900 °C. The RMS roughness is 1.0 Å.

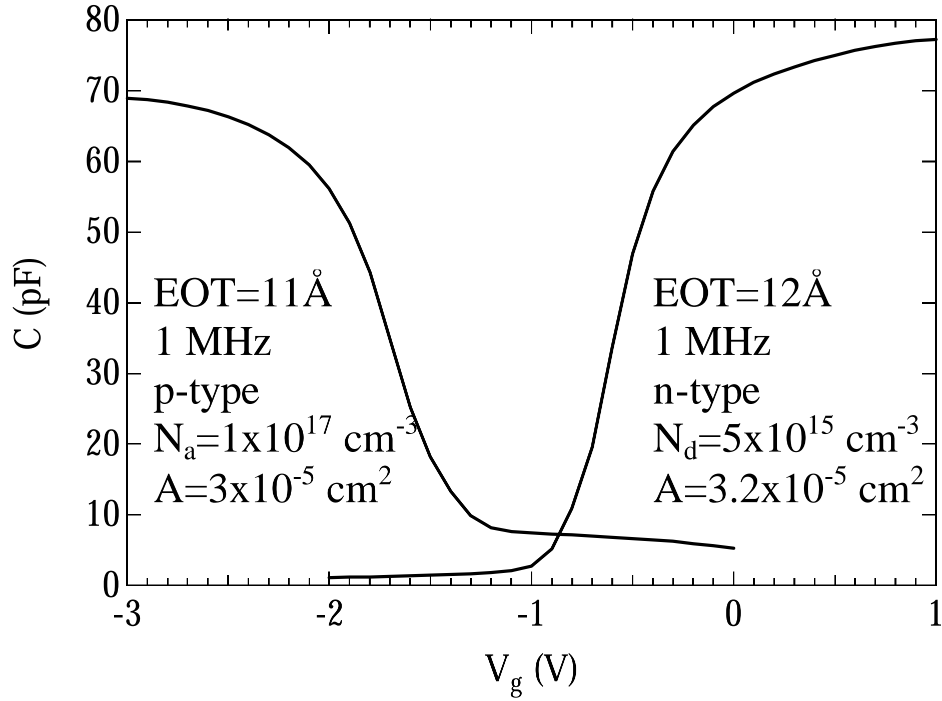

Figure 3.8 Typical C-V curves for thin Y-O-Si films formed by oxidation of ~8 Å of yttrium on n- and p-type silicon at 900 °C with Al electrodes. Analysis of the C-V curves that includes the quantum correction yields EOT ~ 10 Å.

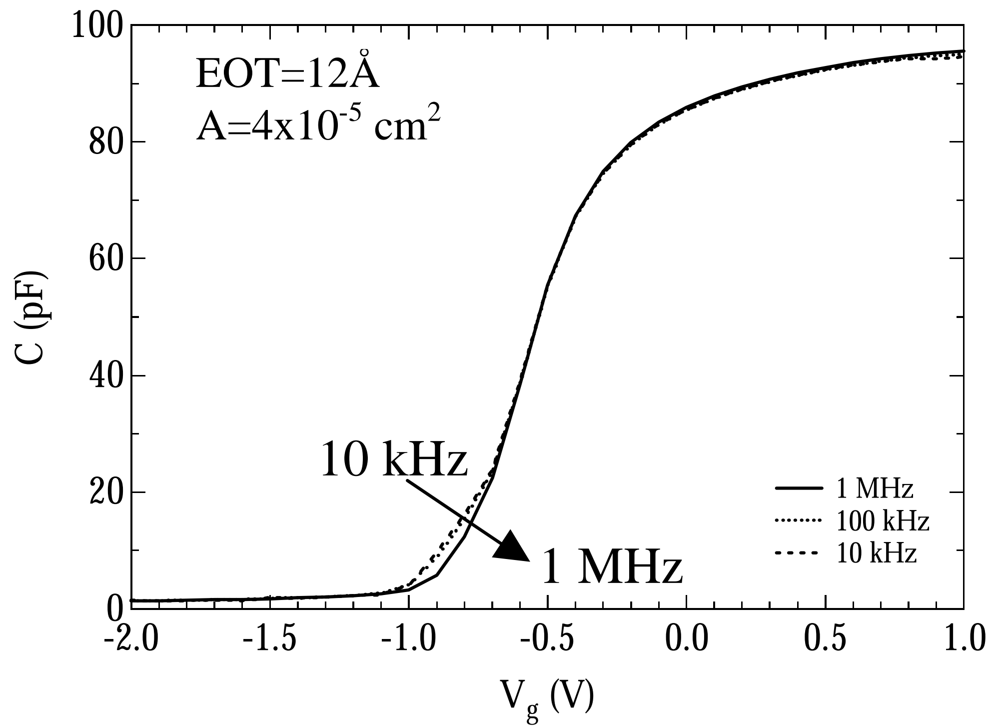

Figure 3.9 C-V curves from 10k-1M Hz for a thin Y-O-Si film formed by oxidation of ~8 Å of yttrium on n-type silicon at 900 °C with Al electrode. Slight frequency dispersion indicates the presence of slow traps.

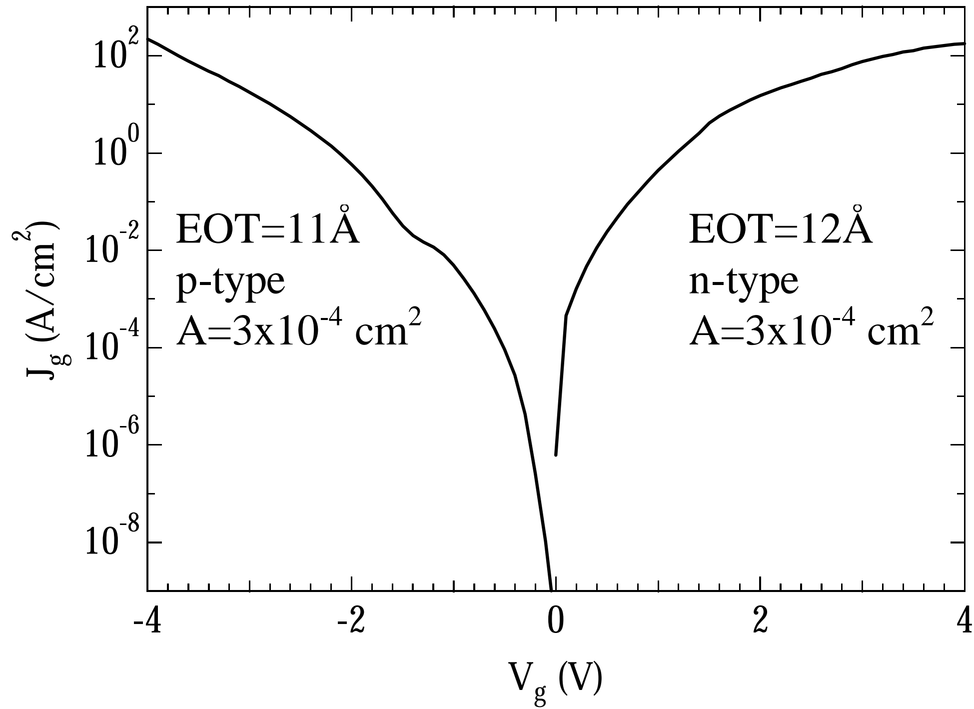

Figure 3.10 J-V curves for Y-O-Si films on n- and p-type silicon presented in Fig. 3.8. The leakage currents are higher than expected for a ~40 Å physically thick film.

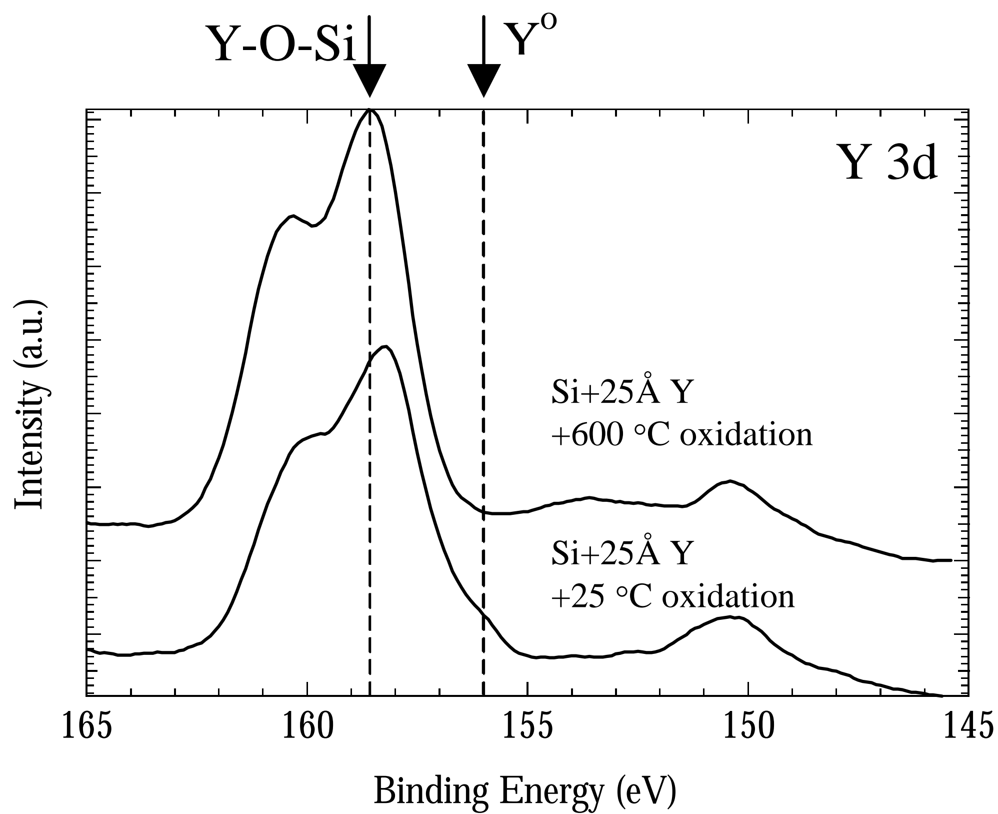

Figure 3.11a Y 3d spectra for 25 Å yttrium films oxidized at 600 °C and 25 °C. The yttrium film on silicon mixes with silicon and oxidizes when exposed to ambient conditions.

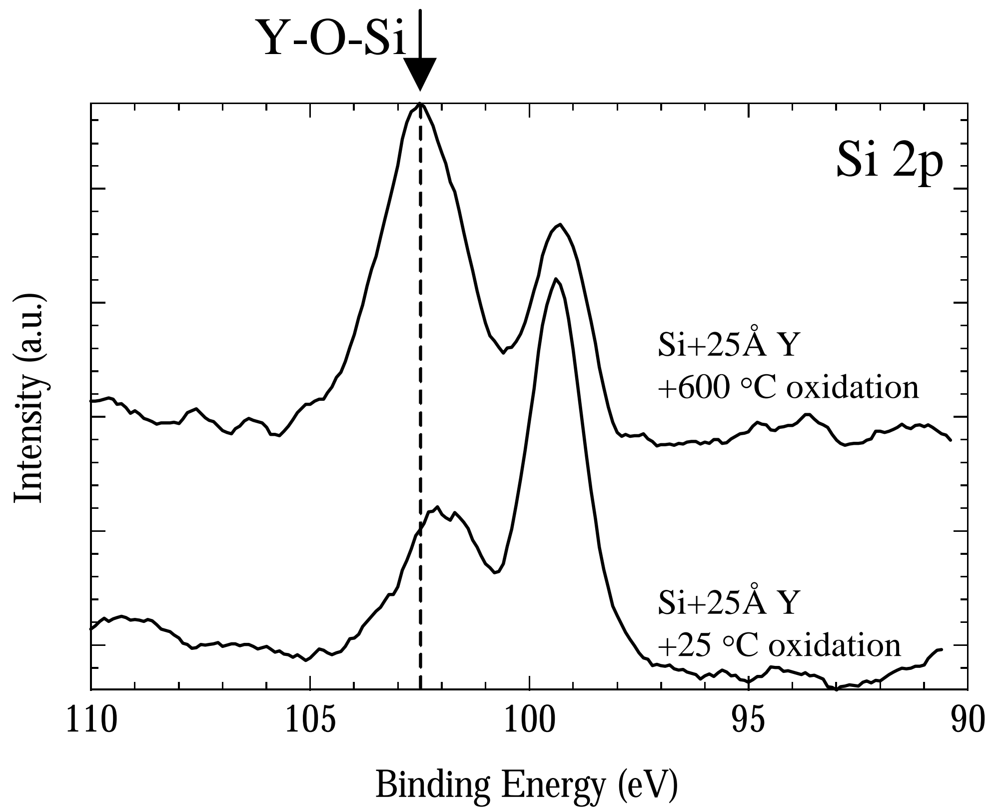

Figure 3.11b Si 2p spectra for 25 Å yttrium films oxidized at 600 °C and 25 °C.

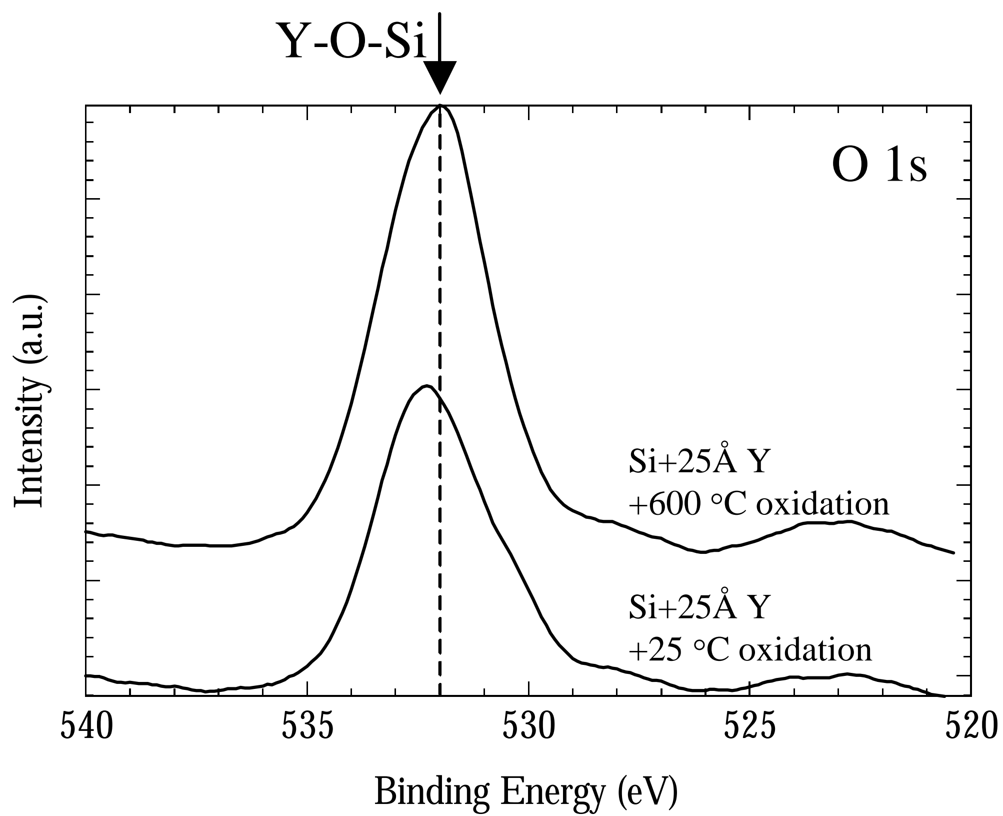

Figure 3.11c O 1s (c) spectra for 25 Å yttrium films oxidized at 600 °C and 25 °C.

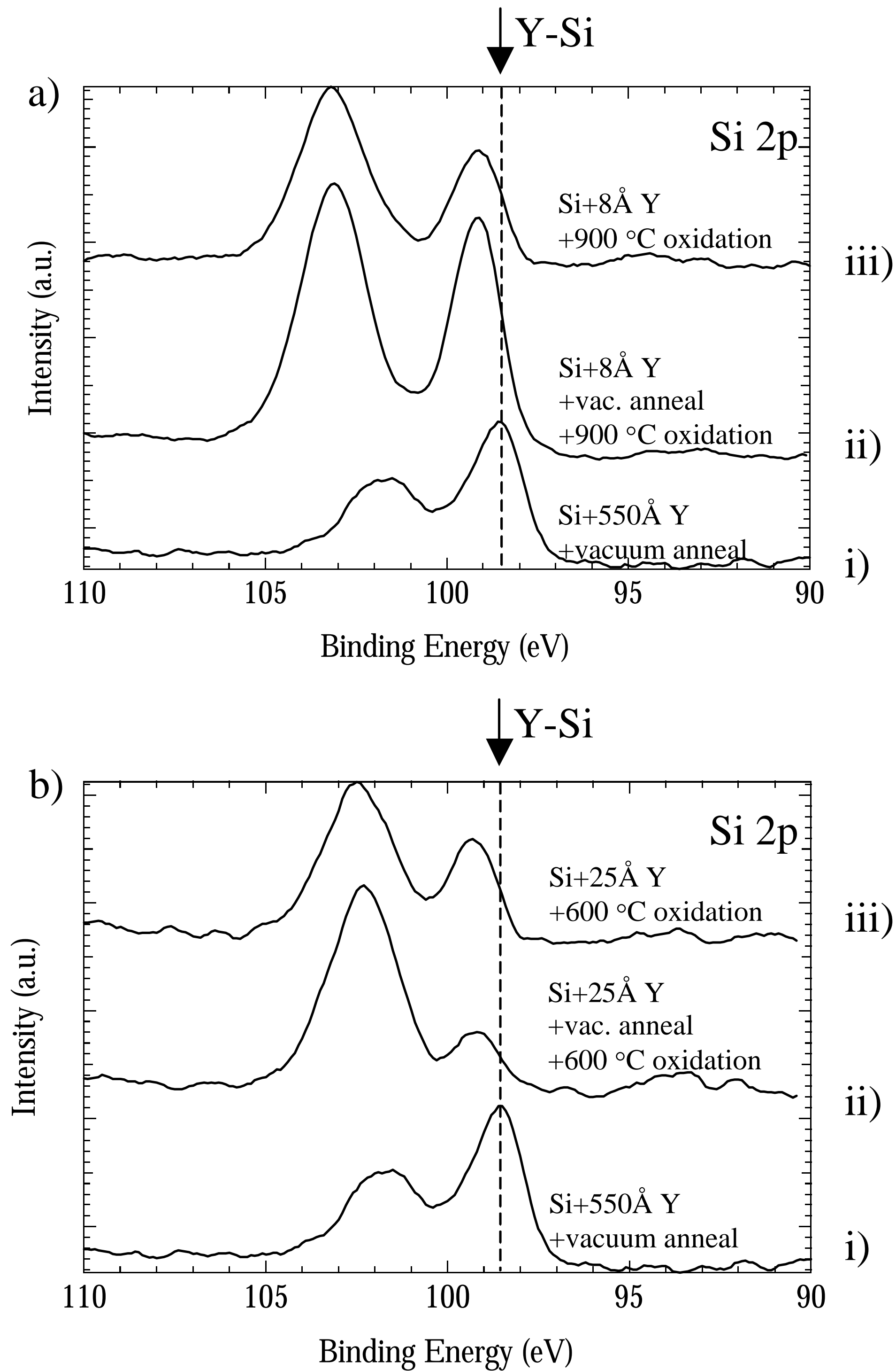

Figure 3.12 Si 2p photoelectron spectra for Y-O-Si films formed by oxidation of yttrium on silicon and yttrium silicide at 900 °C (a) and 600 °C (b). The spectrum for yttrium silicide is presented as a reference in (a) and (b).

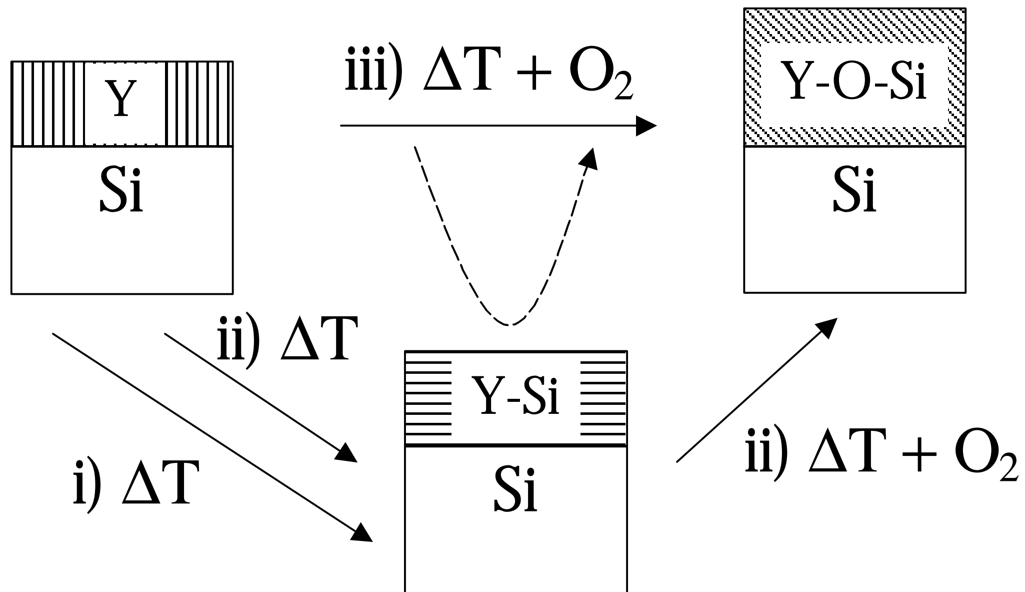

Figure 3.13 Diagram illustrating the processes used to form the films in Fig. 3.11, 3.12 and 3.14. Y-Si films are formed by annealing yttrium films on silicon in vacuum (i). Y-O-Si films formed by the oxidation of yttrium silicide follow the pathway (ii). Y-O-Si films formed by oxidation of yttrium on silicon follow the pathway denoted by the arrow (iii). The oxidation of yttrium films on silicon to form Y-O-Si is believed to occur through a concurrent silicide step denoted by the dashed arrow.

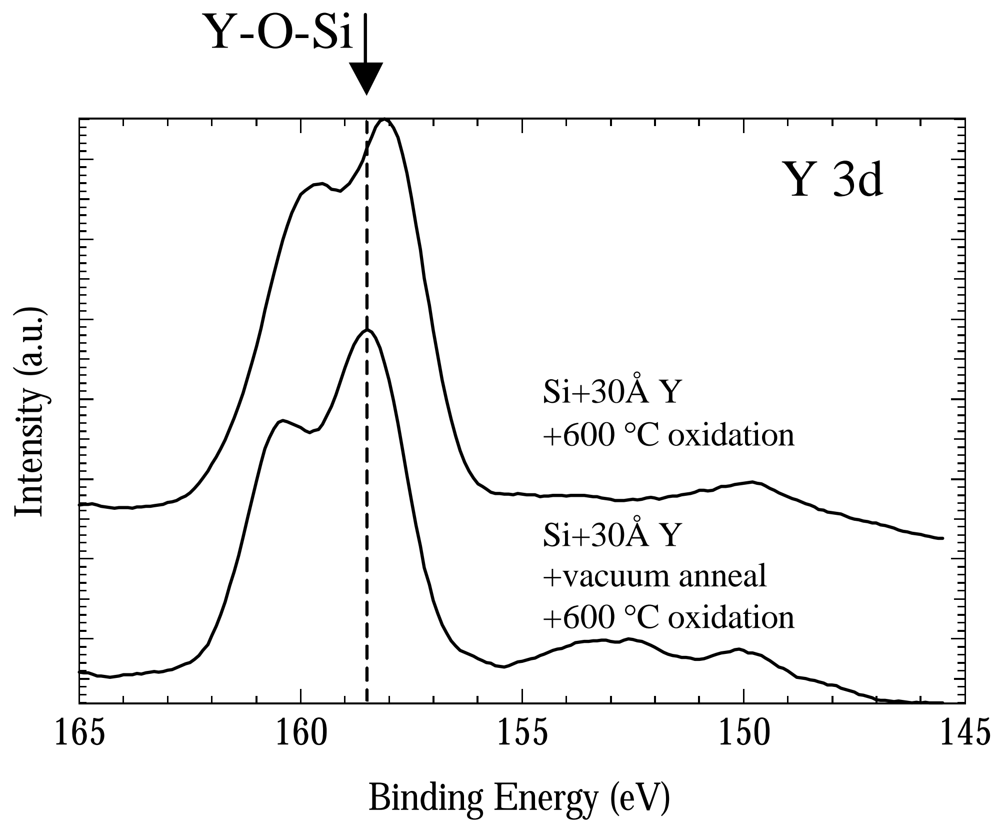

Figure 3.14a Y 3d spectra for films formed by the oxidation at 600 °C of yttrium (30 Å) on silicon and yttrium silicide.

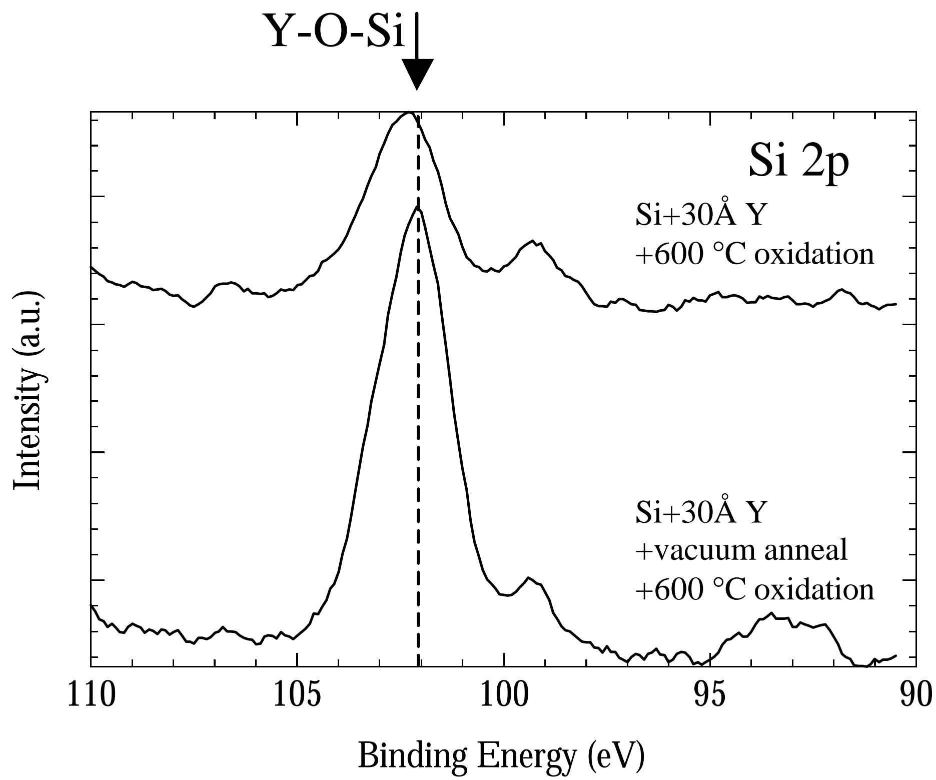

Figure 3.14b Si 2p spectra for films formed by the oxidation at 600 °C of yttrium (30 Å) on silicon and yttrium silicide.

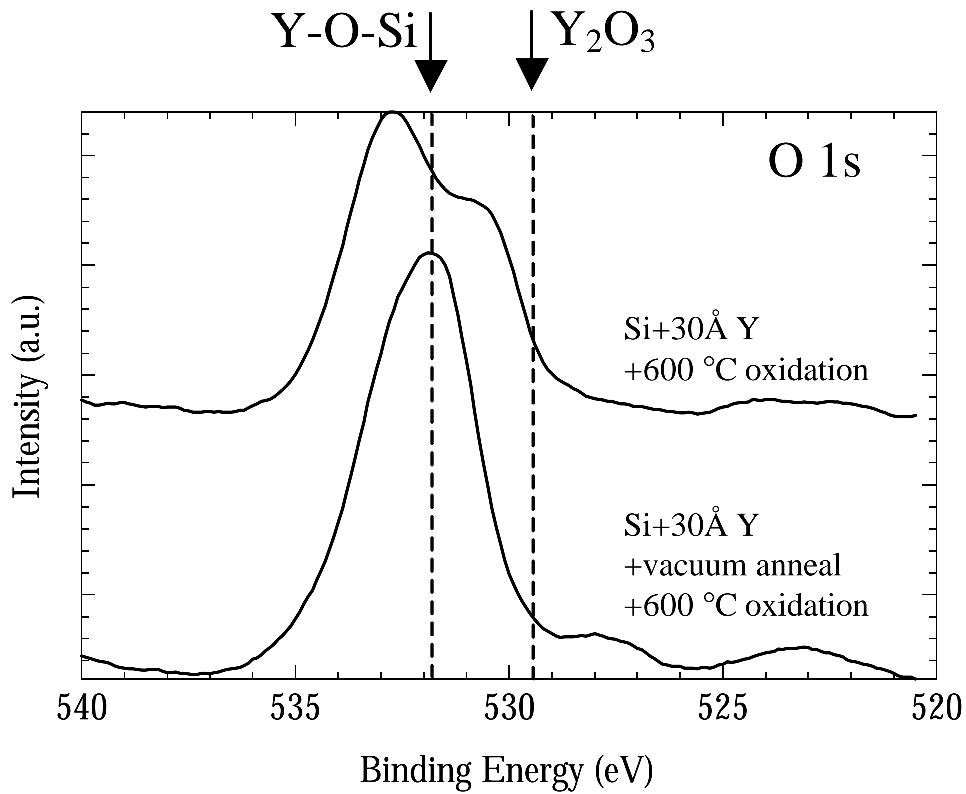

Figure 3.14c O 1s spectra for films formed by the oxidation at 600 °C of yttrium (30 Å) on silicon and yttrium silicide.

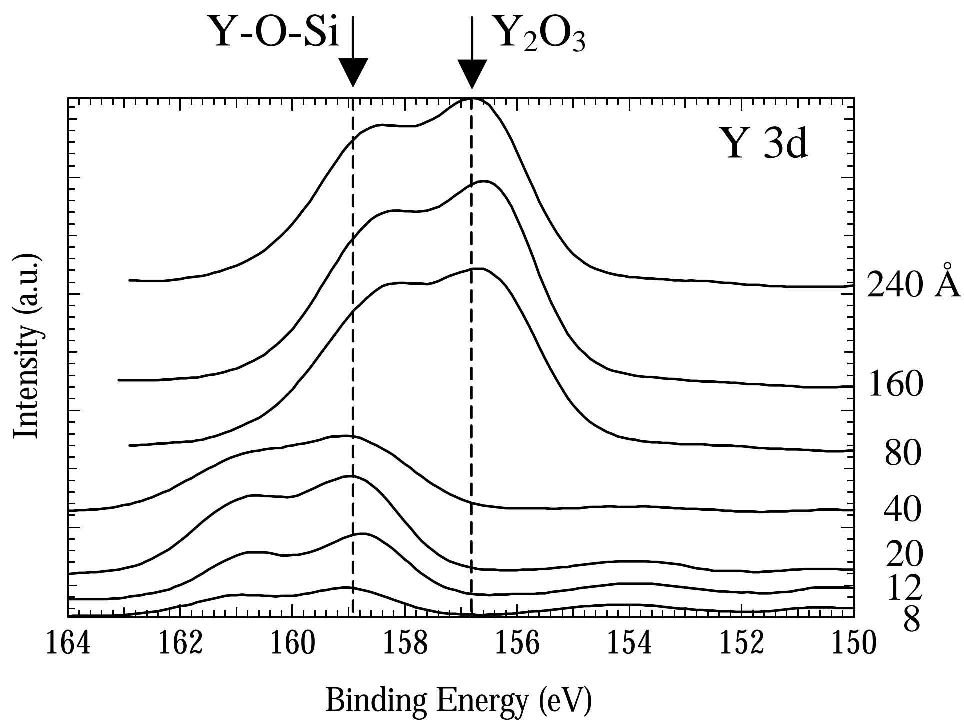

Figure 3.15a Y 3d spectra for ~8-240 Å yttrium films on silicon oxidized at 900 °C. Initial yttrium coverage <40 Å results in an Y-O-Si film. Initial yttrium coverage >80 Å results in an Y_2O_3/Y-O-Si/Si stack layer. This structure results from a competition for yttrium between oxygen and silicon.

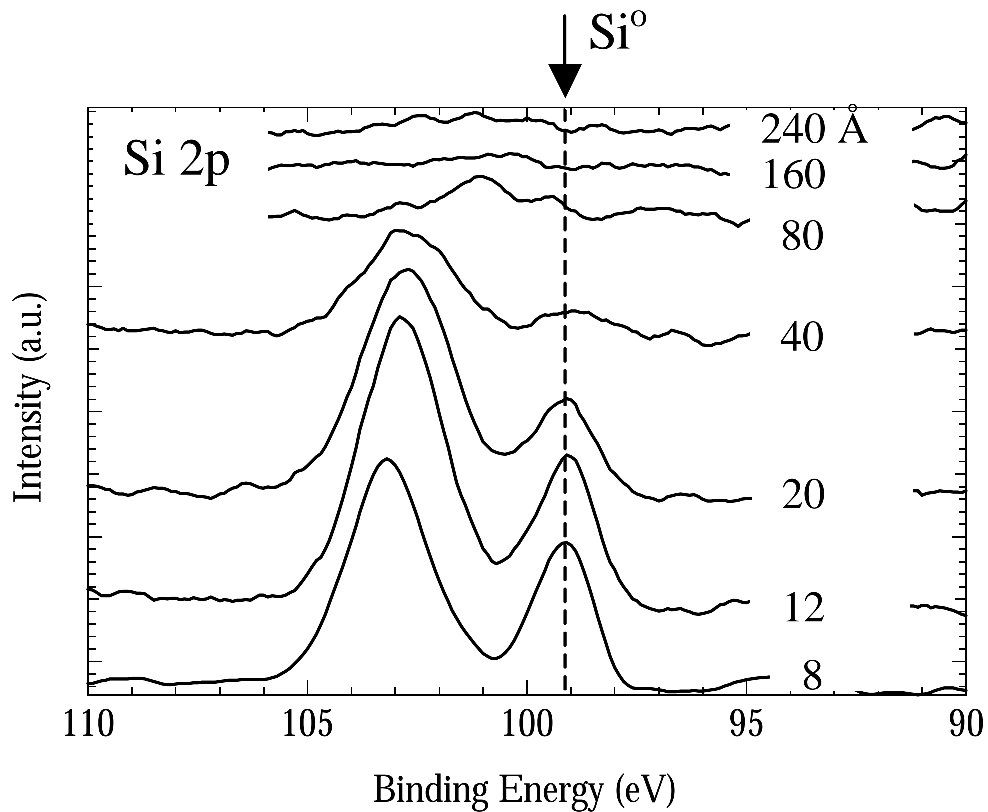

Figure 3.15b Si 2p spectra for ~8-240 Å yttrium films on silicon oxidized at 900 °C.

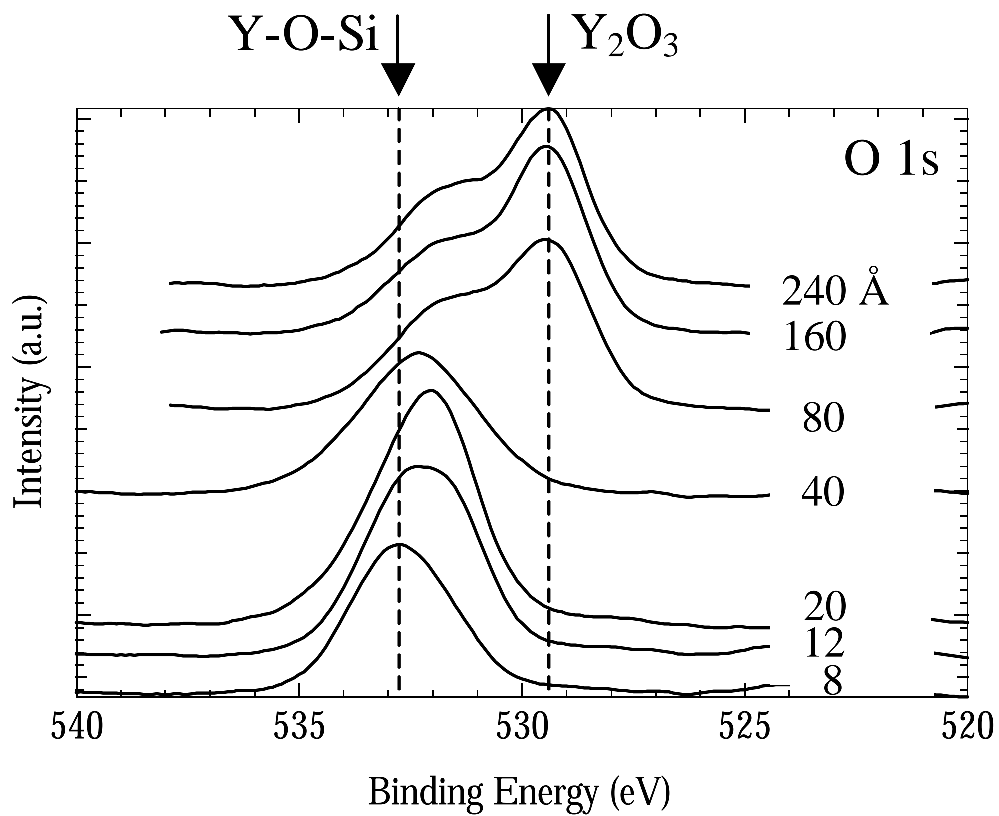

Figure 3.15c O 1s spectra for ~8-240 Å yttrium films on silicon oxidized at 900 °C.

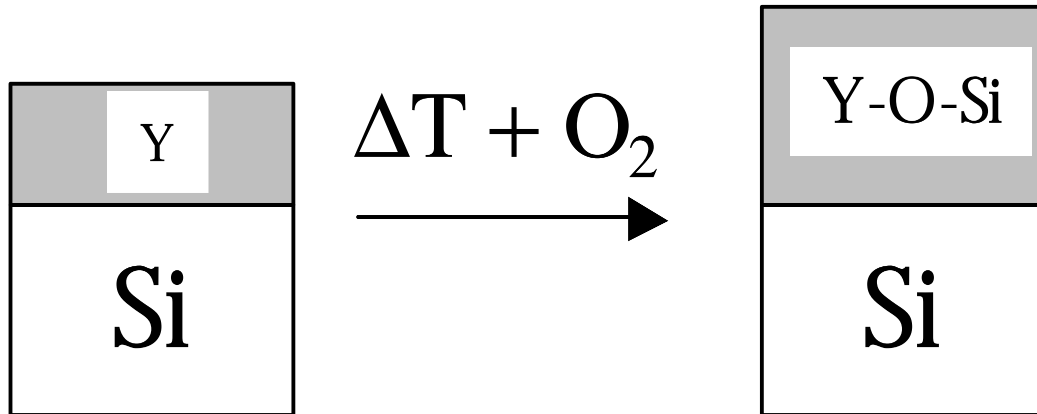

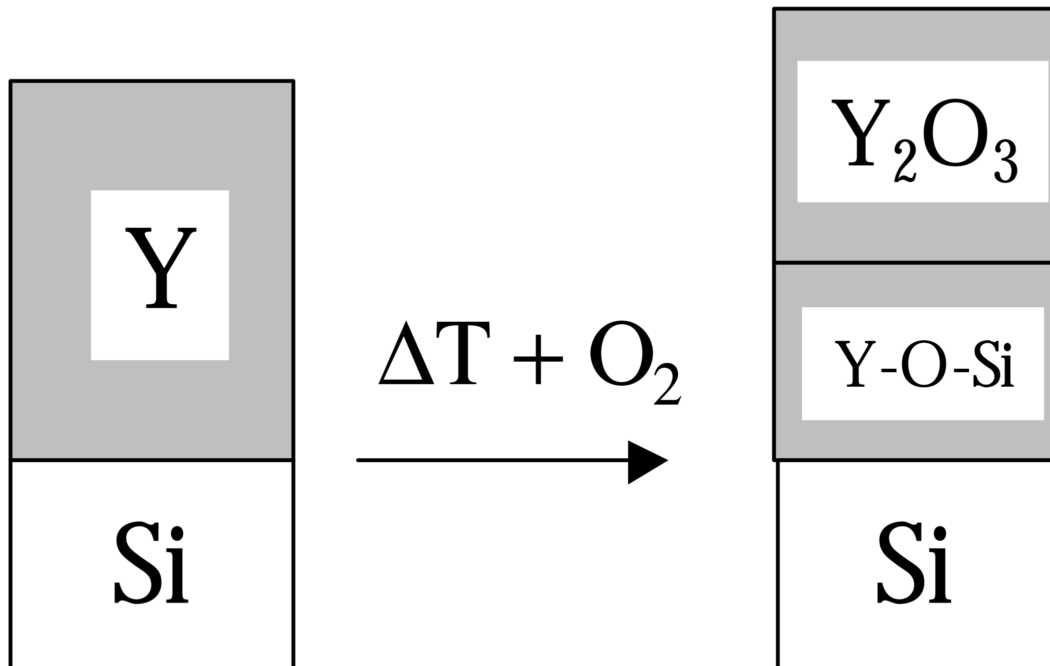

Figure 3.16 Diagram illustrating the film structure obtained for thin and thick initial yttrium coverage. For thin initial yttrium coverage, mixing of the yttrium and silicon results in a Y-O-Si film. For thick initial yttrium coverage, the reaction between yttrium and silicon is not fast enough to consume the entire yttrium film and Y_2O_3 is formed at the top interface.

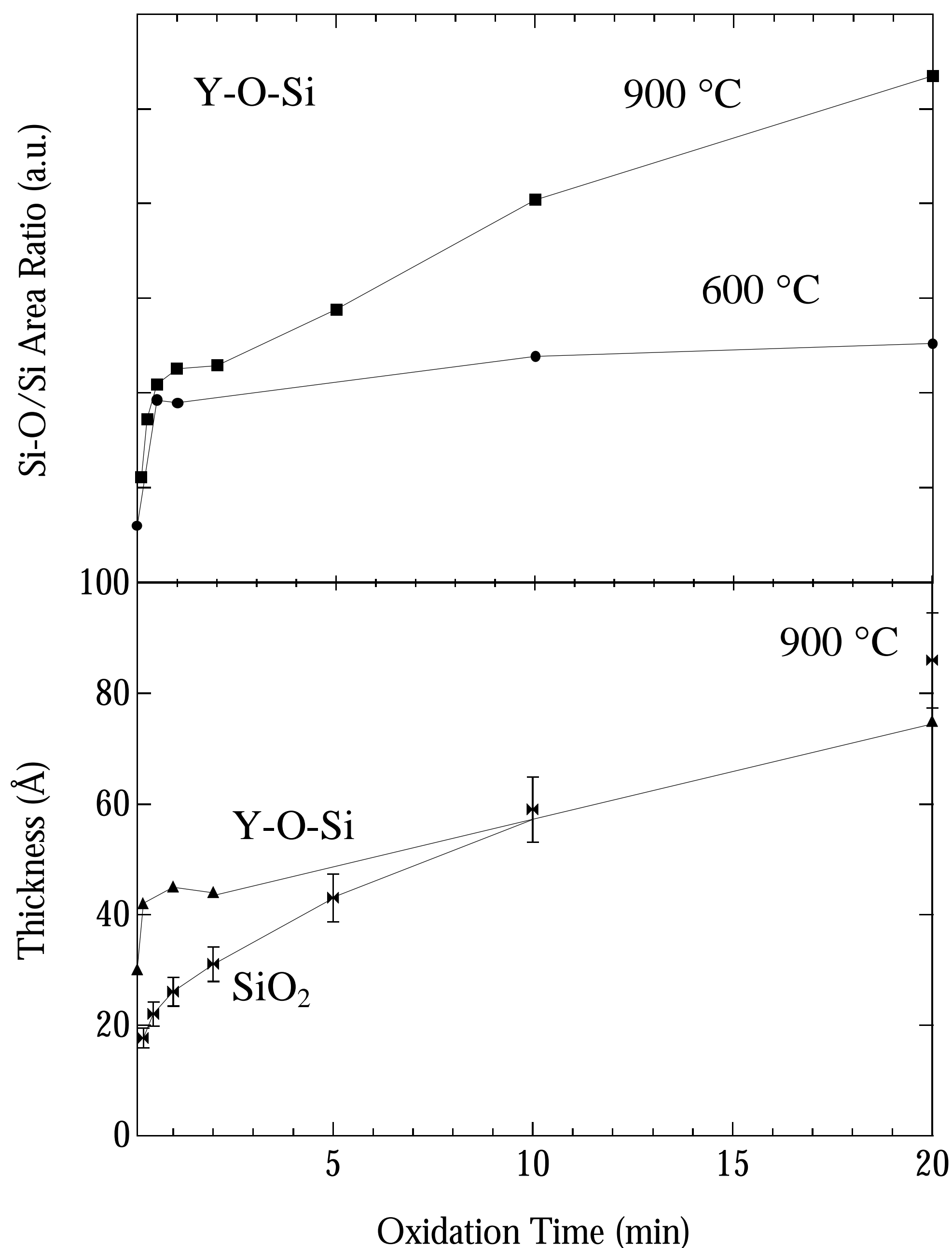

Figure 3.17 Si-O/Si area ratio for yttrium films on silicon oxidized at 600 ( )and 900 °C( ) plotted with thickness data from cross-section TEM images for Y-O-Si films oxidized at 900 °C ( ) and from ellipsometry for SiO_2 films grown at 900 °C ( ). The two regions of oxidation kinetics observed for the oxidation of yttrium on silicon represent Y-O-Si film formation (times <2 minutes) and silicon substrate oxidation (times >2 minutes).

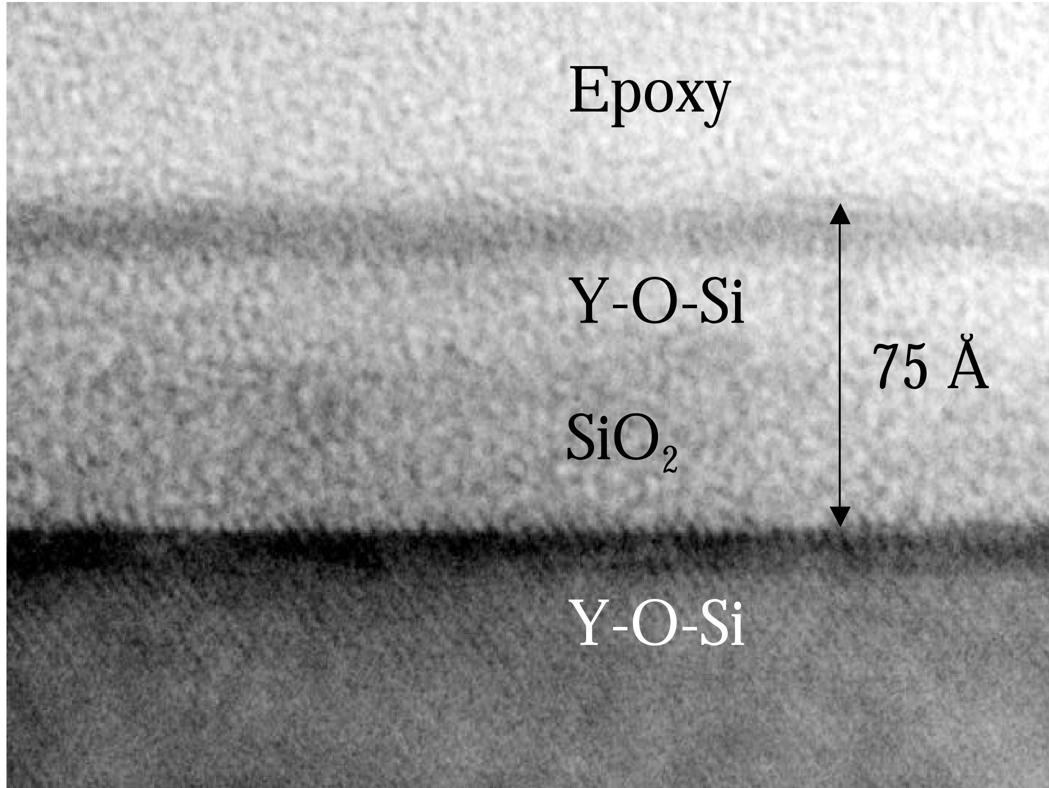

Figure 3.18 Cross-sectional TEM image for ~8 Å yttrium film on silicon oxidized for 20 minutes at 900 °C. The total thickness is 75 Å, which includes a buried SiO_2 layer formed by oxidation of the silicon substrate.

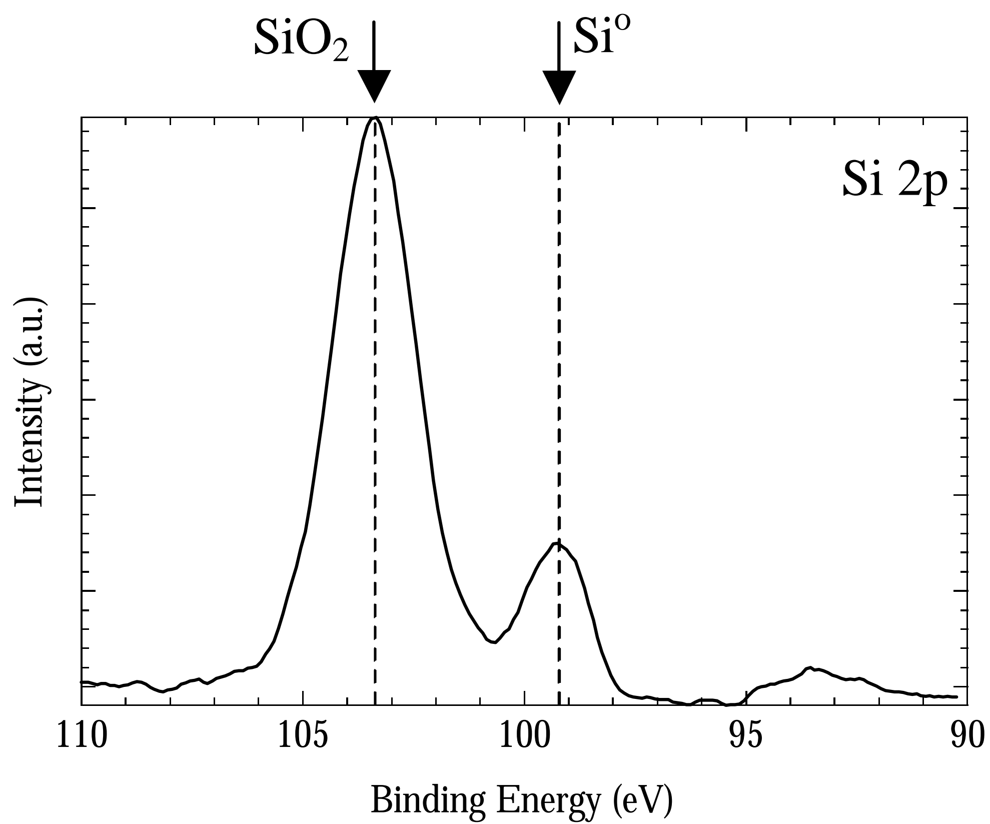

Figure 3.19 Si 2p region for an ~8 Å yttrium film on silicon oxidized for 20 minutes at 900 °C. The Si-O peak is consistent with SiO_2 and the attenuation of the silicon substrate peak is consistent with a thick overlayer.

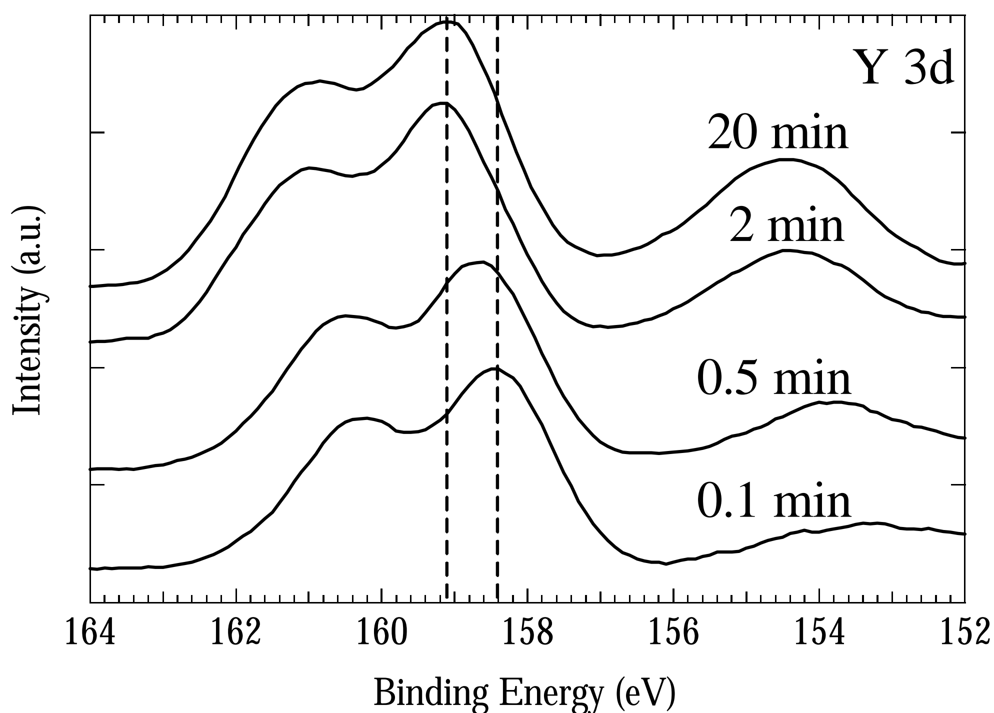

Figure 3.20 Y 3d region for ~8 Å yttrium films on silicon oxidized at 900 °C for 6 seconds to 20 minutes. The Y 3d peak is observed to shift to higher binding energy for times up to 2 minutes where it remains fixed at 159.1 eV for times up to 20 minutes. The shifting of the Y 3d peak indicates chemical changes occurring in the Y-O-Si film.

Chapter 4 is a reprint of a manuscript accepted for publication in Applied Physics Letters

YTTRIUM SILICATE FORMATION ON SILICON: EFFECT OF SILICON PRE-OXIDATION AND NITRIDATION ON INTERFACE REACTION KINETICS

J. J. Chambers and G. N. Parsons

ABSTRACT

The effects of oxygen and nitrogen pretreatments on interface reaction kinetics during yttrium silicate formation on silicon are described. X-ray photoelectron spectroscopy (XPS) and medium energy ion scattering (MEIS) are used to determine chemical bonding and composition of films formed by oxidation of yttrium deposited on silicon. Capacitance-voltage testing is used to determine the quality of the dielectric and the electrical thickness. The effect of ultra-thin silicon oxide, nitrided oxide and nitrided silicon interfaces on metal oxidation kinetics is also described. When yttrium is deposited on clean silicon and oxidized, XPS and MEIS indicate significant mixing of the metal and the silicon, resulting in a film with Y-O-Si bonding and composition close to yttrium orthosilicate ($Y_2O_3{\cdot}SiO_2$). A thin (~10 Å) *in situ* pre-oxidation step is not sufficient to impede the metal/silicon reaction, whereas a nitrided silicon interface significantly reduces the silicon consumption rate, and the resulting film is close to Y_2O_3. The mechanisms described for yttrium are expected to occur in a variety of oxide and silicate deposition processes of interest for high-k dielectrics.

Therefore, in addition to thermodynamic stability, understanding the relative rates of elementary reaction steps in film formation is critical to control composition and structure at the dielectric/Si interface.

CHAPTER 4

YTTRIUM SILICATE FORMATION ON SILICON: EFFECT OF SILICON PRE-OXIDATION AND NITRIDATION ON INTERFACE REACTION KINETICS

4.1 INTRODUCTION

Advanced complementary-metal-oxide-semiconductor (CMOS) devices will require high dielectric constant (high-k) gate insulators to maintain sufficient capacitance and minimize tunneling. Physical vapor deposition (PVD) and chemical vapor deposition (CVD) of high-k materials (including Ta_2O_5, HfO_2, ZrO_2, Al_2O_3, Y_2O_3, and metal silicates) often results in lower-k interface layers[1-4] that result from unwanted reactions with the silicon substrate.[5] These reactions are generally not predicted from equilibrium thermodynamics of the Si and bulk metal oxide,[6] but result from the non-equilibrium nature of the deposition, where the relative rates and energetics of the individual elementary reaction steps, as well as thermodynamics, determine interface composition and structure. High-k CVD from metal-organic sources on clean Si involves breaking of a metal-ligand bond, chemisorption of the metal complex (likely forming metal-silicon bonds) and subsequent oxidation. Understanding the role of metal-silicon bonds and engineered interfaces on silicon consumption reaction kinetics is a critical issue for integration of high-k dielectrics with silicon.

4.2 EXPERIMENTAL

In this work, dielectric films were formed by sputtering thin (25 Å) yttrium films onto clean and *in situ* modified silicon, then oxidizing in N_2O at 600-900 °C. The effects of interface oxidation and nitridation on silicon consumption during thermal oxidation of deposited yttrium are reported. Yttrium has a strong affinity for oxygen, and Y_2O_3 is expected to be stable on silicon at high temperature.[6] Materials were analyzed *ex situ* using X-ray photoelectron spectroscopy (XPS, referenced to Si 2p at 99.3eV) and medium-energy ion scattering (MEIS)[7].

4.3 RESULTS AND DISCUSSION

In the first experiment, 25 Å of yttrium is sputtered onto clean Si(100) and annealed at 600°C in N_2O at 1 atm. XPS analysis of the resulting film (sample a) is shown in Figures 4.1a, 4.2a, and 4.3a for the Y 3d, O 1s, and Si 2p regions, respectively. The Y 3d spectrum (Fig. 4.1a) shows a doublet due to spin-orbit splitting into the Y $3d_{3/2}$ and Y $3d_{5/2}$ components at 160.3 and 158.3 eV, respectively. The peak at 158.3 eV is higher than the 156.8 eV reported for Y $3d_{5/2}$ in Y_2O_3[8], indicating that the oxidized layer has bonding structure substantially different from Y_2O_3. The O 1s peak at 532.0 eV is intermediate between O 1s for SiO_2 (533.0 eV) and Y_2O_3 (529.5 eV) and is broader than expected for either elemental oxide. The two peaks in the Si 2p spectrum (Fig. 4.3a) are assigned to silicon in the substrate (99.3 eV)[8] and silicon bound to oxygen in the film (102.2 eV), but the peak at ~102 eV lies between the silicon substrate peak and the expected peak position for SiO_2 (103.3 eV)[8]. The chemical shifts in Figs. 4.1a, 4.2a and 4.3a are consistent with a thin film containing a significant fraction of silicate (Y-O-Si) bonding units[8] where electron density is donated from yttrium to neighboring Si-O bonds, in agreement with the electronegativities of Y, Si and O (1.2, 1.8, 3.5 on the Pauling scale). MEIS results for

sample (a) (Fig 4.4a), show a high-energy (87.0 keV) shoulder on the silicon substrate peak, indicating Si in the film. The composition of this film calculated from the MEIS spectrum is $(Y_2O_3)_{0.6}\cdot(SiO_2)_{0.4}$. The XPS and MEIS data are consistent with the film being an yttrium orthosilicate ($Y_2O_3\cdot SiO_2$) mixed with some additional Y_2O_3. Other stable yttrium silicates are also known,[9] with (Y_2O_3):(SiO_2) ratio <1. The absence of phase separated Y_2O_3 in the Y 3d XPS spectrum may be due to instrument sensitivity, or due to bond strain in the clustered Y_2O_3 network. Capacitance voltage analysis of similarly prepared films indicates that good quality dielectric layers with equivalent oxide thickness of ~12 Å and dielectric constant in the range of 12-15 can be formed using this procedure.[10] As discussed below, the silicate structure likely results from relatively fast silicon diffusion into the metal leading to a metal silicide layer that is subsequently oxidized to form Y-O-Si bonds. No evidence for yttrium silicide bonds is observed in any of the oxidized films discussed here.

Various Si surface pretreatments were explored to modify and control the silicon/metal interaction and oxidation behavior. Pretreatments included plasma oxidation of silicon, plasma oxidation followed by nitridation, and plasma nitridation of silicon. Each of these steps were performed *in situ* using a remote N_2O or N_2 plasma source (N_2O^* or N_2^*, respectively).[10] Oxidation and nitridation conditions were controlled to attain ultra-thin (~10 Å) pretreatment layers, as determined by XPS.[10] Each pretreatment was followed by *in situ* yttrium deposition (25 Å) and *ex situ* annealing at 600 °C in N_2O at 1 atm.

The oxidation pretreatment results in a ~10 Å SiO_2 layer with a well-defined Si-O feature at 103.3 eV, as shown in Fig. 4.3(b´). When yttrium is deposited on this surface and oxidized, the XPS spectra of the resulting film (spectra 'b' in Figs. 4.1, 4.2, and 4.3), are indistinguishable from the film formed directly on silicon without the oxide pretreatment

(sample a) with possibly a slight shift (~0.1 eV) to lower binding energy (BE). No evidence for the SiO_2 feature at 103.3 eV is observed in Fig. 4.3b, indicating conversion of SiO_2 to silicate during oxidation. MEIS analysis (not shown) provides a composition of $(Y_2O_3)_{0.63}\cdot(SiO_2)_{0.37}$ indistinguishable, within experimental error (~0.04), from the clean Si case.

In the next experiment, a clean Si sample was oxidized as above, then exposed to a remote N_2 plasma under conditions that resulted in 1 monolayer of nitrogen at the SiO_2/Si interface. When yttrium is deposited on this nitrided oxide surface and oxidized as above, the Y 3d peak (Fig. 4.1c) is shifted to lower BE, and the O 1s peak (Fig. 4.2c) is shifted slightly to higher BE compared to the film formed directly on silicon. A slight shoulder at 530.0 eV (near the expected O 1s position for Y_2O_3) is observed in the O 1s spectrum of Fig. 4.2c. No evidence for the SiO_2 feature at 103.3 eV is observed in Si 2p spectrum (Fig. 4.3c), again indicating conversion of SiO_2 to silicate during oxidation. MEIS yields a composition of $(Y_2O_3)_{0.73}\cdot(SiO_2)_{0.27}$, indicating that the silicon fraction is reduced compared to the film formed on clean silicon. This is consistent with the nitrogen slowing the interaction between the silicon substrate and the deposited metal, with the SiO_2 layer still available for reaction with the metal.

The fourth sample consists of the clean Si being exposed only to the N_2^* pretreatment prior to yttrium deposition and oxidation. The resulting oxidized yttrium film is significantly different than when the starting surface is clean or oxidized silicon. For the oxidized yttrium film on N_2^*-treated silicon, the Y 3d peak (Fig. 4.1d) is shifted 0.8 eV to lower binding energy compared to films formed on clean or oxidized Si (Figs. 4.1a and 4.1b, respectively), and the O 1s spectrum (Fig. 4.2d) exhibits a strong shoulder at 530.0 eV. For Y_2O_3, Y $3d_{5/2}$ is at 156.8 eV and O 1s is at 529.5 eV compared to 158.2 and 532 eV,

respectively, for the silicate formed on clean Si. The chemical shifts for the film formed on nitrided silicon are consistent with the dielectric layer having composition close to Y_2O_3. Figure 4.4 shows MEIS results for dielectric films formed on N_2* treated surfaces (spectrum d), compared to those formed on clean silicon (spectrum a). For spectrum (d), a signal due to interface N is observed at ~76 keV, consistent with ~1 monolayer of nitrogen localized at the silicon/dielectric interface after yttrium deposition and oxidation. In spectrum (a), a signal at 87.0 keV is clearly seen due to Si in the film indicating significant mixing of metal and silicon before or during the oxidation process. Samples with oxidation and oxidation/nitridation pretreatments show MEIS spectra qualitatively similar to spectrum (a), indicating Si mixing with the metal. However, in spectrum (d), corresponding to the N_2*-treated silicon, the silicon signal at 87.0 keV is nearly indiscernible and the composition is Y_2O_3 with ~15% yttrium silicate consistent with the XPS results.

4.4 CONCLUSIONS

It is well known that at relatively low temperature, silicon will readily inter-diffuse with some metals, including Hf, Zr, La, and Y[11,12], to form silicides. The above results indicate that when yttrium (which forms a silicide and a stable oxide) is deposited onto silicon and oxidized, the silicon diffuses to form a silicide[11,12], and subsequent oxidation results in a layer with significant silicate composition (sample "a" in Figs. 4.1-4). This intermixing also occurs when the surface is oxidized before metal deposition. Because yttrium has a very high affinity for oxygen, annealing results in reduction of the available silicon oxide, leading to a silicate layer (i.e. samples b and c in Figs. 4.1-3). When ~1 monolayer of nitrogen is present at the interface, the silicon diffusion from the substrate is impeded. Any silicon oxide on top of the N layer will still react with the metal to form a silicate (spectra c in Figs. 4.1-3). However, when only nitrided silicon is present (spectra d in

Figs. 4.1-4), oxidation of deposited metal results in a structure closer to pure metal oxide, consistent with impeded silicon diffusion through the nitrided layer. These reactions are demonstrated here for the case of yttrium, but similar results are expected for other metals that form silicides and stable oxides on silicon including Hf, Zr, La, etc. Elementary reaction steps in metal oxide CVD will also include metal-silicon bond formation and oxidation, so similar mechanistic processes described here for PVD films are expected in CVD processes, and these mechanisms are likely responsible for interface layers commonly observed in these systems. This demonstrates that, in addition to thermodynamic stability of the metal oxide, the relative energetics and rates of the elementary reaction steps in film formation is critical for controlling composition and structure at the dielectric/Si interface.

4.5 ACKNOWLEDGEMENTS

The authors acknowledge E. Garfunkel and B. W. Busch at Rutgers University for the MEIS results. Support is from the SRC/SEMATECH Center for Front End Processes and NSF CTS.

4.6 REFERENCES

1. K. A. Son, A. Y. Mao, B. Y. Kim, F. Liu, E. D. Pylant, D. A. Hess, J. M. White, D. L. Kwong, D. A. Roberts, and R. N. Vrtis, J. Vac. Sci. Technol. A **16,** 1670-1675 (1998).
2. B. H. Lee, L. Kang, R. Nieh, W. J. Qi, and J. C. Lee, Appl. Phys. Lett. **76,** 1926 (2000).
3. G. B. Alers, D. J. Werder, Y. Chabal, H. C. Lu, E. P. Gusev, E. Garfunkel, T. Gustafsson, and R. S. Urdahl, Appl. Phys. Lett. **73,** 1517-1519 (1998).
4. S. K. Kang, D. H. Ko, E. H. Kim, M. H. Cho, and C. N. Whang, Thin Sol. Films **353,** 8-11 (1999).
5. T. M. Klein, D. Niu, W. S. Epling, W. Li, D. M. Maher, C. C. Hobbs, R. I. Hegde, I. J. R. Baumvol, and G. N. Parsons, Appl. Phys. Lett. **75,** 4001-4003 (1999).
6. K. J. Hubbard and D. G. Schlom, J. of Mater. Res. **11,** 2757-2776 (1996).
7. E. P. Gusev, H. C. Lu, T. Gustafsson, and E. Garfunkel, Phys. Rev. B **52,** 1759-1775 (1995).
8. J. F. Moulder, W. F. Stickle, P. E. Sobol, and K. D. Bomben, *Handbook of X-ray Photoelectron Spectroscopy* (Perkin-Elmer Corporation, Eden Prairie, MN, 1992).
9. E. M. Levin, C. R. Robbins, and H. F. McMurdie, *Phase Diagrams for Ceramists: 1969 Supplement*, Vol. Figure 2388 (The American Ceramic Society, Columbus, Ohio, 1969).
10. J. J. Chambers and G. N. Parsons, to be submitted.
11. J. E. E. Baglin, F. M. Dheurle, and C. S. Petersson, J. Appl. Phys. **52,** 2841-2846 (1981).
12. A. Pellissier, R. Baptist, and G. Chauvet, Surf. Sci. **210,** 99-113 (1989).

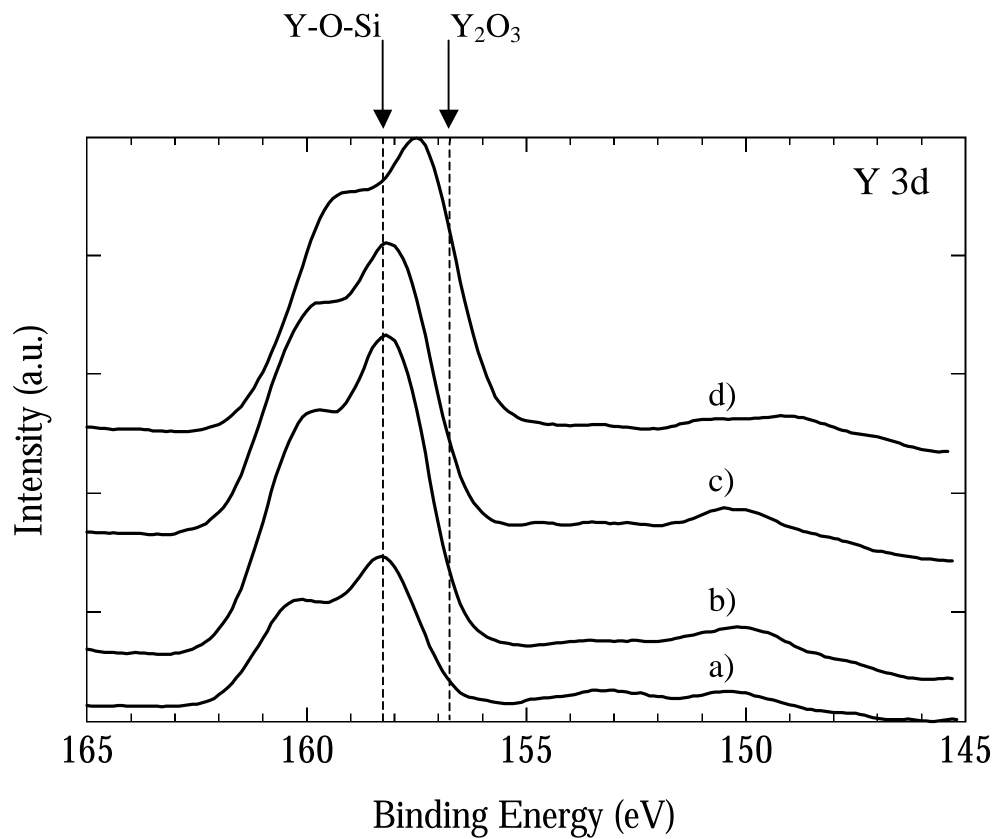

Figure 4.1 Y 3d photoelectron spectra for films formed on a) silicon, b) silicon oxide, c) nitrided oxide and d) nitrided silicon. Nitrided silicon impedes silicon incorporation in the film causing the Y 3d peak to shift to lower binding energy.

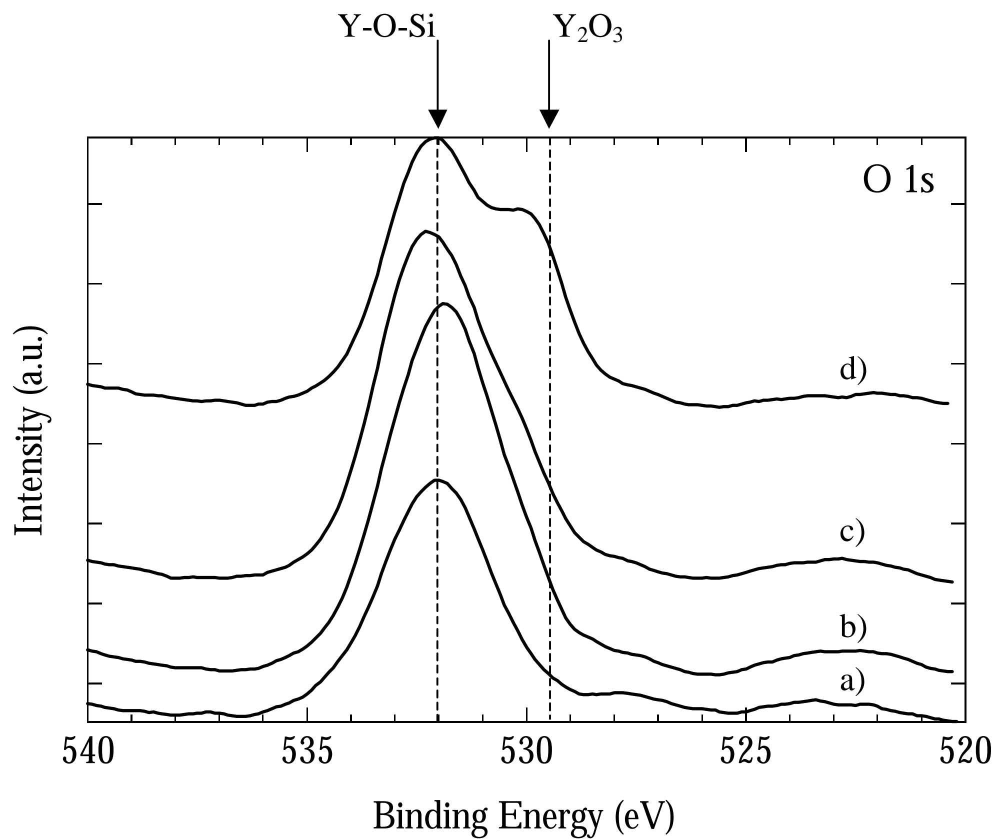

Figure 4.2 O 1s photoelectron spectra for films formed on a) silicon, b) silicon oxide, c) nitrided oxide and d) nitrided silicon. The shoulder at 530.0 eV indicates an increase in O-Y-O bonding.

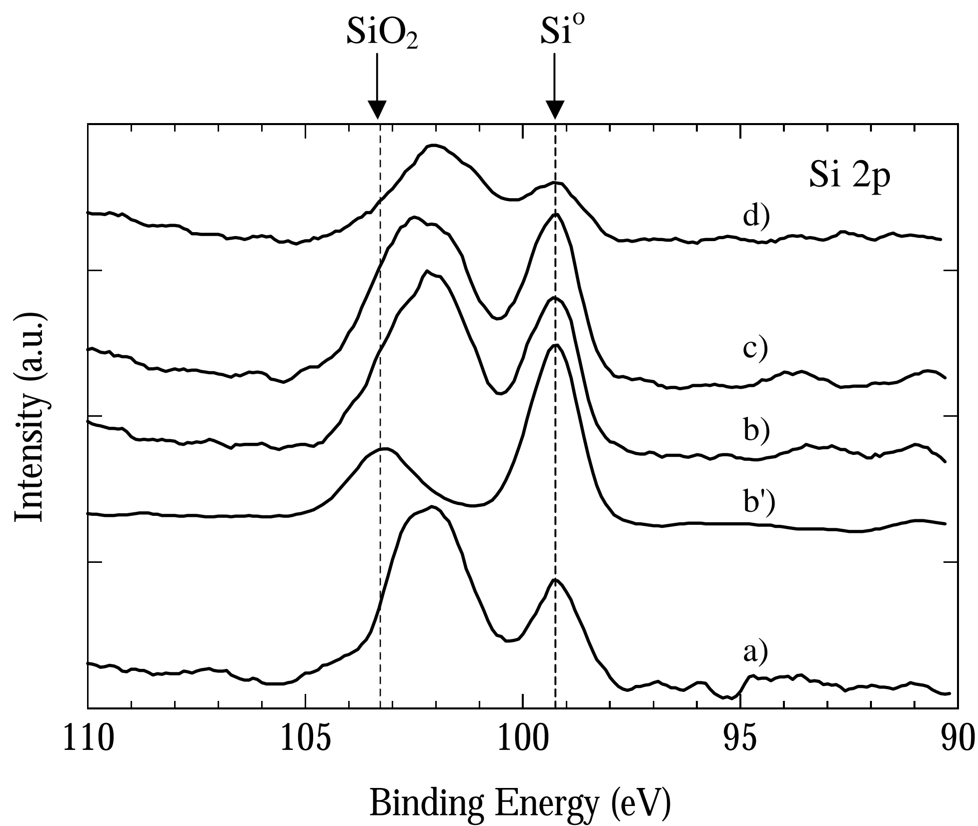

Figure 4.3 Si 2p photoelectron spectra for films formed on a) silicon, b) silicon oxide, c) nitrided oxide and d) nitrided silicon. The spectrum for plasma oxidized silicon is presented as b´). For a), b) and c), the peak at 102.2 eV is consistent with a Y-O-Si.

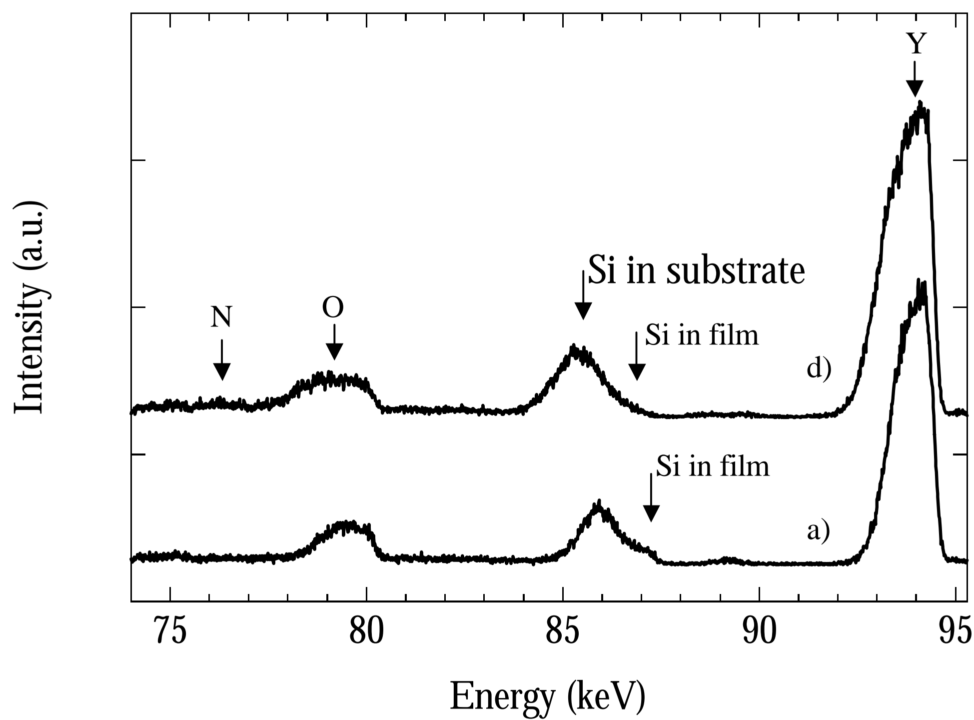

Figure 4.4 MEIS energy spectra for films formed on a) silicon and d) nitrided silicon. The shoulder at 87.0 keV representing silicon in the film is clearly larger for the film formed on a) silicon than d) nitrided silicon.

Chapter 5 is a reprint of a manuscript to be submitted to the Journal of Applied Physics

INTERFACE REACTIONS DURING YTTRIUM SILICATE FORMATION ON SILICON

J. J. Chambers, B. W. Busch, E. Garfunkel, S. Wang, D. M. Maher,

T. M. Klein and G. N. Parsons

ABSTRACT

X-ray photoelectron spectroscopy (XPS) and medium energy ion scattering (MEIS) are used to determine chemical bonding and composition of yttrium, silicon, oxygen alloys. Alloyed films were formed by oxidation of yttrium deposited on silicon and pretreated silicon. XPS and MEIS analyses indicate that oxidation of yttrium on clean silicon results in a significant fraction of Y-O-Si bonding. TEM indicates that the Y-O-Si films are amorphous, and TEM and XPS analysis indicate the Y-O-Si films form a silicon interface free of SiO_2. Capacitance-voltage testing demonstrates that an equivalent oxide thickness of ~10 Å can be achieved. The effect of ultra-thin silicon oxide, nitrided-oxide and nitrided silicon interfaces on silicon consumption during oxidation of yttrium is investigated. Oxidation of yttrium on a thin (~10 Å) oxidized silicon surface pretreatment results in Y-O-Si films with similar bonding and composition as Y-O-Si films formed on clean silicon. However, a nitrided silicon interface (~10 Å) significantly reduces the silicon consumption rate, and the resulting film is close to Y_2O_3. The conversion of SiO_2 to silicate is demonstrated for both the

oxidation and vacuum annealing of yttrium on SiO_2. These results indicate that metal-silicon bonds play an important role in the film formation described here and are expected to be involved in interface formation during chemical vapor deposition of other high-k dielectrics of interest. Integration of high-k dielectrics with existing silicon technology will require an understanding of interface layer formation mechanisms including the effects of metal-silicon bonds and engineered interfaces on silicon consumption.

CHAPTER 5

INTERFACE REACTIONS DURING YTTRIUM SILICATE FORMATION ON SILICON

5.1 INTRODUCTION

The current scaling rate of metal-oxide-semiconductor-field-effect-transistors (MOSFETs) has stimulated interest in alternative high dielectric constant (high-k) gate materials. Traditionally, the semiconductor industry reduces the thickness of the silicon dioxide gate dielectric to increase channel capacitance and keep pace with transistor drive current requirements. However, the industry rapidly approaches proposed physical limits for the thin silicon dioxide.[1] The limits placed on silicon dioxide depend on the allowable leakage current due to quantum mechanical tunneling, which increases exponentially with inverse thickness, and the oxide reliability.[2] The exact limit will vary with the device application (i.e. low-power or high-performance), but current estimates for a lower limit of a 10-20 Å silicon dioxide place the insertion point for high-k dielectrics somewhere around the 100-65 nm nodes.[1] Since the capacitance scales as the dielectric constant over thickness, high-k materials should allow a thicker dielectric (compared to silicon dioxide) to combat tunneling, while maintaining sufficient capacitance to enable high channel transconductance.

High-k materials, including Y_2O_3,[3] Ta_2O_5,[4] TiO_2,[5] HfO_2,[6] ZrO_2[7] and Al_2O_3,[8] are currently being investigated as replacements for silicon dioxide. However, chemical vapor deposition (CVD) and physical vapor deposition (PVD) of these high-k dielectrics often results in lower-k interface layers[4,9,10] that form due to unwanted silicon substrate consumption.[11] Thermodynamic stability between the bulk metal oxide and silicon, such as

Al_2O_3/Si,[12] does not alone preclude interface reactions from occurring, but interface layer formation also depends on the individual reaction steps during the deposition process.[11] For example, metal-organic CVD of a high-k dielectric on silicon proceeds by breaking a metal-ligand bond, chemisorption of the metal complex (possibly involving a metal-silicon bond) and subsequent oxidation of the metal complex. It is reasonable to assume that metal-silicon bonds formed during deposition can affect the formation of interface layers. In an attempt to control or eliminate unwanted interface layer formation, silicon nitride and silicon oxy-nitride engineered interfaces have been used to inhibit reaction with the substrate during high-k deposition. Integration of high-k dielectrics with existing silicon technology will require an understanding of interface layer formation including the effects of metal-silicon bonds and engineered interfaces on silicon consumption.

In this work, we have used X-ray photoelectron spectroscopy and medium energy ion scattering to investigate silicon consumption during oxidation of yttrium on clean and *in situ* modified silicon. We report that oxidation of yttrium on clean silicon results in mixing of yttrium and silicon to form a Y-O-Si film. Similar results are also obtained when the surface is oxidized silicon. However, when the silicon surface is nitrided prior to yttrium deposition, oxidation creates a structure closer to pure metal oxide consistent with the nitrided silicon impeding reaction with the substrate. These results indicate that metal-silicon bonds may play an important role in interface formation during deposition of high-k dielectrics.

5.2 EXPERIMENTAL

Samples were Si(100) p-type with resistivity 0.1-0.3 Ω-cm cut from commercial wafers into 2.5 X 2.5 cm substrates. The samples were prepared by dipping for 5 minutes in JTB 100 (a tetramethylammonium hydroxide based alkaline solution with a carboxylate buffer), rinsing in deionized water (DI), etching in buffered hydrogen fluoride (HF) for 30 seconds with no final rinse and immediately loading into vacuum. Thermal (40 Å) SiO_2 substrates were cleaned by by dipping for 5 minutes in JTB 100, rinsing in DI and immediately loading into vacuum.

Yttrium sputtering and vacuum annealing were performed in the system described in detail elsewhere.[13] A cylindrical plasma source on the processing chamber can be configured to run in a remote plasma mode to perform *in situ* silicon surface pretreatments and in a direct plasma mode to sputter yttrium thin films. Plasma oxidation and nitridation were used to form silicon surface pretreatments at 300 °C, 50 mTorr, a radio frequency (rf) power of 400 W in 100 sccm (N_2) N_2O and N_2, respectively. The processing chamber is equipped with a retractable yttrium (99.1%, Ta is the major impurity) sputter target that can be isolated from the system by a gate valve. The sputter target was isolated from the processing chamber during the silicon surface pretreatment. Sputtering was performed at room temperature in 4.3 mTorr Ar, an rf power of 420 W and a yttrium target dc bias of –1000 V. The sputter rate was 25 Å/minute and was monitored using the target current (3.4 mA). Annealing was performed in vacuum better than $5x10^{-6}$ Torr at 600 °C for 2 minutes in the same chamber as the yttrium deposition. A standard 10 cm diameter tube furnace was used for *ex situ* oxidation at temperatures from 600-900 °C in 1 atm. N_2O or air.

The following experiments were designed to investigate how silicon surface pretreatments affect silicon consumption. Yttrium (25 Å) was sputtered onto:

(1) clean (HF last) silicon

(2) 20 minute plasma oxidized silicon

(3) 20 minute plasma oxidized silicon followed by 10 minute plasma nitridation

(4) 20 minute plasma nitrided silicon, and,

then oxidized in 1 atm. N_2O at 600 °C for 2 minutes. The plasma silicon surface pretreatments were grown in the same vacuum chamber as the yttrium deposition.

X-ray photoelectron spectroscopy (XPS) was performed *ex situ* using a Riber LAS3000 equipped with a MAC2 analyzer (single-pass cylindrical mirror analyzer with an input lens) and an Mg Kα ($h\nu$ = 1253.6 eV) non-monochromatic X-ray source. Detailed spectra were collected at a take-off angle of 90° and a 0.1 eV step size. The raw spectra were smoothed using an eleven point Savitsky-Golay algorithm. When peak fitting was necessary to locate peak position or integrate area, Gaussian functions were generated by minimizing the misfit error.

Angle resolved XPS was performed *ex situ* using a Kratos Axis 165 and Al Kα ($h\nu$ = 1486.6 eV). The resolution was ~ 0.8 eV, and the spot size was 120 μm. The step size was 0.1 eV and the take-off angle was varied from 20° to 90° at 10° increments. The angle resolved XPS data were not smoothed.

Medium-energy ion scattering (MEIS),[14] a low-energy (50-300 kEV) high resolution (~5 Å) version of Rutherford backscattering spectroscopy, was performed *ex situ* to obtain proton energy spectra. Energy spectra of the scattered protons (~100 keV) are collected

using a double-aligned geometry. The energy spectra are converted to a density versus depth scale using a kinematic factor calculated within a binary collision model. The compositions determined by MEIS of the films reported here are average values throughout each film and generally correspond to $(Y_2O_3)_x{\cdot}(SiO_2)_{1-x}$ where x ranged from 0.32 to 0.87. The known yttrium silicates correspond to x = 0.33 (keiviite) and x = 0.5 (yttrium orthosilicate).[15] In this article, we generally refer to all the films as yttrium silicate or simply as Y-O-Si.

Metal-insulator-semiconductor capacitors were formed by evaporating 2000 Å of Al onto blanket Y-O-Si films through a contact mask with holes ranging from 50-500 μm in diameter. Active area was determined using scanning electron microscopy. Samples underwent a post-metallization anneal in 90% N_2 and 10% H_2 at 400 °C for 30 minute. Capacitance-voltage (C-V) measurements were taken at 1 MHz using a HP 4284a LCR meter. Electrical thickness is described as an equivalent SiO_2 thickness (EOT) determined from a fit of the C-V curve that includes the quantum mechanical effect. Samples were swept from inversion to accumulation with no initial light source.

5.3 RESULTS AND DISCUSSION

5.3.1 OXIDATION OF YTTRIUM ON SILICON TO FORM Y-O-SI FILMS

Thin dielectric films were formed by oxidizing ~8 Å yttrium films on silicon at 900 °C for 15 seconds. The XPS analysis of these films is presented in the Y 3d, Si 2p and O 1s spectra of Fig. 5.1. The Y 3d spectrum of Fig. 5.1a exhibits a doublet resulting from the spin-orbit splitting of the Y $3d_{3/2}$ and Y $3d_{5/2}$ peaks at 160.8 and 159.0 eV, respectively, whereas the reference peak positions for Y $3d_{3/2}$ and Y $3d_{5/2}$ for Y_2O_3 are 158.8 and 156.8 eV,[16] respectively. The two peaks at 154 and 151 eV in the Y 3d spectrum result from a combination of the Y 3d satellite, Si-O Si 2s and substrate Si 2s peaks. Peaks assigned to the

silicon substrate (99.3 eV) and Si-O bonding (102.9 eV) are observed in the Si 2p spectrum of Fig. 5.1b. The measured Si-O peak is at lower binding energy than expected for SiO_2 (103.3 eV), but within the expected range (102-103 eV)[16] for Si-O bonding in metal silicates. The Si-O peak is a broad peak (full-width-half-maximum (FWHM) = 2.4 eV, compared to a measured Si-O peak FWHM = 1.8 eV for SiO_2) consistent with a wide range of bonding environments available to silicon. No peaks for Y-Si at ~0.2 and ~0.6 eV lower than the metallic yttrium and silicon peaks, respectively, are observed in the Y 3d or Si 2p spectra. The O 1s peak (Fig. 5.1c) (broad peak with FWHM = 3.0 eV compared to a measured O 1s FWHM = 1.8 eV for SiO_2) is measured at 532.8 eV and is intermediate between O 1s for SiO_2 (533.0 eV) and Y_2O_3 (529.5 eV).

Figure 5.2 presents the MEIS proton energy spectrum for a Y-O-Si film form by oxidizing an ~8 Å yttrium film on silicon for 15 seconds at 900 °C. In agreement with the XPS spectra of Fig. 5.1, peaks for yttrium (~96 keV), silicon (~86.5 keV) and oxygen (~80.5 keV) are observed in the MEIS spectrum of Fig. 5.2. The silicon peak at ~86 keV exhibits a shoulder at ~87 keV, which is assigned to silicon in the Y-O-Si film.

The bonding in Y-O-Si films was investigated as a function of depth using angle resolved XPS. Figure 5.3 presents the angle resolved XPS spectrum for a film formed by oxidizing a ~25 Å yttrium film on silicon at 900 °C for 2 minutes. In Fig. 5.3, the take-off angle is changed from 20° to 90° from grazing to normal incidence in order to probe the near surface and far surface, respectively. The Y $3d_{5/2}$ peak in Fig. 5.3a remains fixed at 159.6 eV for take-off angles from 20° to 90°. The silicon substrate peak (99.3 eV) in Fig. 5.3b is observed to increase in magnitude as the take-off angle is varied from 20° to 90° consistent with the increased depth probed at normal incidence. The Si-O feature (103.4

eV) in Fig. 5.3b remains fixed at 103.4 eV for take-off angles from 20° to 90°. The O 1s peak shifts from 532.9 eV at 20° to 532.5 eV at 40° where it remains fixed up to 90°. The slight shift of the O 1s peak at the near surface is attributed to either adsorbed water or adventitious carbon on the surface.

The morphology of a Y-O-Si film formed by oxidizing ~8 Å of yttrium on silicon at 900 °C for 15 seconds was studied using cross-sectional TEM (Fig. 5.4). Lattice fringes are detected in the aluminum capping layer and the silicon substrate, but the Y-O-Si layer is free of lattice fringes indicating the amorphous nature of the film. The Y-O-Si film is 42 Å thick. The interface between the Y-O-Si and the silicon substrate is sharp with no indication for an interface layer between the two materials.

The C-V curve for a Y-O-Si capacitor on n-type Si(100) with an Al electrode is presented in Fig. 5.5. The Y-O-Si film was formed by oxidizing an ~8 Å yttrium film on silicon at 900 °C for 15 seconds in 1 atm. N_2O. Analysis of the C-V curve that includes the correction for the quantum confinement of electrons in the semiconductor yields EOT = 12 Å. Similar films exhibit leakage current of 0.5 A/cm^2. Since a thickness of 42 Å is measured for films undergoing the same processing, a k ~ 14 is estimated for the Y-O-Si film. The flatband voltage (V_{fb}) is measured at V_{fb} = -0.74 V, which is shifted –0.68 V from the expected V_{fb} for an ideal capacitor.

When a reactive metal is deposited onto silicon and oxidized at elevated temperature, the metal can react with silicon and oxidize. Consistent with the XPS and MEIS spectra of Figs. 5.1, 5.2 and 5.3, the oxidation of a thin yttrium layer on silicon results in a film with a significant fraction of Y-O-Si bonds. The Y 3d, Si 2p and O 1s (Fig. 5.1) peak positions for a film formed by oxidizing a thin yttrium layer on silicon are different than for either Y_2O_3

or SiO_2 indicating the presence of Y-O-Si bonding structure. The chemical shifts of the Y 3d, Si 2p and O 1s peaks are due to charge transfer from yttrium to neighboring Si-O bonds consistent with the relative electronegativity of yttrium, silicon and oxygen (1.2, 1.8, 3.5 on the Pauling scale). The Y 3d, Si 2p and O 1s spectra do not indicate the presence (within detectable limits) of phase separated Y_2O_3, SiO_2 or Y-Si. The broadness (FWHM = 3.0 eV) of the O 1s peak is consistent with a combination of oxygen bound to yttrium and oxygen bound to silicon. Analysis of the MEIS spectrum in Fig. 5.2 yields a composition of $(Y_2O_3)_{0.32}{\cdot}(SiO_2)_{0.68}$, which is within the experimental error ($x \pm 0.04$) of the known silicate $Y_2Si_2O_7$ ($x = 0.33$). The angle resolved XPS spectra (Fig. 5.3) indicate that the oxidation of a thin yttrium layer on silicon results in a Y-O-Si film with homogeneous chemical bonding and an interface with silicon free of SiO_2. The constancy as a function of take-off angle of the Y 3d, Si 2p and O 1s peak positions in the angle resolved spectra signifies the consistency of the chemical states within the Y-O-Si film. As discussed in detail elsewhere,[17] the Y 3d and Si 2p peaks in a Y-O-Si film shift considerably (up to >1.0 eV) when the composition of the Y-O-Si film changes. Since angle resolved XPS does not detect any shifting in the Y 3d and Si 2p peaks positions, the Y-O-Si films are of constant composition throughout the depth of the film. The Si-O features in the Si 2p spectra of Fig. 5.3 do not exhibit any asymmetry resulting from the presence of a buried SiO_2 layer. The O 1s spectra of Fig. 5.3 are also symmetrical denoting that the ratio of oxygen bound to silicon and oxygen bound to yttrium does not vary with depth into the film. The C-V curve of Fig. 5.5 illustrates the scalability of a Y-O-Si dielectric down to the 10 Å EOT regime. However, the sizeable flatband shift suggests the presence of positive fixed charge in a sufficient density to be a concern. The leakage current of 0.5 A/cm^2 is less than for a silicon dioxide of

equivalent capacitance (J_g ~ 100-1000 A/cm^2),[2] but the leakage is greater than that expected for a SiO_2 of similar physical thickness (~1x10^{-9} A/cm^2)[18].

As discussed in detail elsewhere,[13] the chemical bonding structure of Y-O-Si films formed using the method described here likely results from a competition between yttrium-silicon reaction to form a silicide-like material and oxidation of the yttrium and silicon to form Y-O-Si. The following reactions are all possible in this materials system:

$$Y_{(s)} + O_{2\,(g)} \rightarrow Y_2O_{3\,(s)} \tag{5.1}$$

$$Y_{(s)} + Si_{(s)} \rightarrow YSi_{(s)} \tag{5.2}$$

$$YSi_{(s)} + O_{2\,(g)} \rightarrow \text{Y-O-Si}_{(s)} \tag{5.3}$$

$$Si_{(s)} + O_{2\,(g)} \rightarrow SiO_{2\,(s)} \tag{5.4}$$

$$Y_{(s)} + SiO_{2\,(s)} \rightarrow \text{Y-O-Si}_{(s)} \tag{5.5}$$

None of the results support defining any one of these reactions as the rate-limiting step. However, the degree of silicon consumption depends on the oxidation temperature[17] and the initial thickness of the yttrium film[13], therefore, reactions (5.1) and (5.2) occur at comparable rates. Engineered interfaces can also be implemented to control silicon consumption during oxidation of thin yttrium films.[19]

5.3.2 EFFECT OF SILICON SURFACE PRETREATMENTS ON SILICON INCORPORATION

The consumption of silicon during oxidation of yttrium films was studied using the following pretreatments: (1) clean silicon, (2) oxidized silicon, (3) nitrided-oxidized silicon, and (4) nitrided silicon. Figure 5.6 presents the Si 2p and N 1s spectra of the silicon surface pretreatments before yttrium deposition and oxidation. The silicon substrate peak (99.3 eV) in the Si 2p spectra (Fig. 5.6a) is clearly visible for each pretreatment. A high binding energy

(102-103 eV) feature is observed in the Si 2p spectra for each of the plasma treated surfaces (Fig. 5.6a.2-4), but not for the clean silicon surface (Fig. 5.6a.1). The feature at 103.3 eV for the plasma oxidized silicon (Fig. 5.6a.2) and plasma oxidized silicon followed by nitridation (Fig. 5.6a.3) is assigned to SiO_2. The feature at 102.4 eV on the plasma nitrided silicon (Fig. 5.6a.4) surface is assigned to silicon bound to nitrogen. The thickness of the oxidized silicon and nitrided silicon layers was estimated from the attenuation of the Si^o feature to be ~5-10 Å. No detectable nitrogen is observed on the surface of the cleaned silicon (Fig. 5.6b.1). The N 1s spectra for the plasma oxidized silicon (Fig. 5.6b.2), plasma oxidized silicon followed by nitridation (Fig. 5.6b.3) and the plasma nitrided silicon (Fig. 5.6b.4) all display a nitrogen feature near 398 eV. The plasma nitrided silicon clearly contains the most nitrogen, but the N 1s feature of the plasma nitrided-oxidized silicon pretreatment is larger (~70%) in area than the N 1s of the plasma oxidized silicon.

Figure 5.7 presents the Y 3d (Fig. 5.7a), Si 2p (Fig. 5.7b) and the O 1s (Fig. 5.7c) spectra after yttrium deposition and oxidation for experiments (1)-(4). For oxidation of yttrium deposited onto clean silicon (Fig. 5.7a.1), the Y $3d_{5/2}$ peak is measured at 158.3 eV consistent with a Y-O-Si film. The Y $3d_{5/2}$ peak positions for the films formed on oxidized silicon (Fig. 5.7a.2) and oxidized silicon with nitridation (Fig. 5.7a.3) are measured near 158.3 eV, with perhaps slight shifting to lower binding energy for the film formed on the nitrided-oxide. However, when yttrium is deposited on nitrided silicon and oxidized (Fig. 5.7a.4), the Y $3d_{5/2}$ peak shifts 0.8 eV to lower binding energy compared to the Y 3d position of the Y-O-Si film formed on clean silicon. As the Y 3d peak shifts to lower binding energy, it moves toward the expected peak position for Y_2O_3 (156.8 eV) and indicates an increase Y-O-Y bonding. A silicon substrate feature at 99.3 eV and a feature at ~102 eV are observed in the Si 2p spectra (Fig. 5.7b.1-4) for the films formed on each silicon surface pretreatment. The

Si 2p spectrum for the film formed on clean silicon (Fig. 5.7b.1) exhibits a peak at 102.2 eV consistent with a Y-O-Si film. The Si 2p spectra for the films formed on oxidized silicon (Fig. 5.7b.2) and nitrided-oxidized silicon (Fig. 5.7b.3) exhibits similar features at ~102 eV. The spectrum for the plasma oxidized silicon from Fig. 5.6a.2 is reproduced in Fig. 5.7b.2´ for reference. The feature at 102.0 eV for the film formed on nitrided silicon (Fig. 5.7b.4) is shifted 0.2 eV toward lower binding energy and is ~50% of the area of the film formed on clean silicon. The O 1s peak at 532.0 eV measured for the Y-O-Si film formed on clean silicon (Fig. 5.7c.1) is a broad peak resulting from the combined effects of oxygen bound to yttrium and oxygen bound to silicon. Slight shifting of the O 1s peak maximum is observed when comparing the spectra for the films formed on oxidized silicon (Fig. 5.7c.2), nitrided-oxidized silicon (Fig. 5.7c.3) and nitrided silicon (Fig. 5.7c.4) to the spectrum for the film formed on clean silicon (Fig. 5.7c.1). However, the most pronounced difference between these spectra are the shoulders at ~530.0 eV observed in the O 1s spectrum of the films formed on nitrided-oxidized silicon and nitrided silicon. The shoulders at ~530.0 eV are near the expected binding energy for O 1s in Y_2O_3 (529.5 eV) and indicate an increase in the O-Y-O bonding in the films.

The results of the MEIS analysis of the films formed on pretreated silicon are presented in Fig. 5.8. The proton energy spectra for the films formed on clean silicon (Fig. 5.8.1), oxidized silicon (Fig. 5.8.2), nitrided-oxidized silicon (Fig. 5.8.3) and nitrided silicon (Fig. 5.8.4) all exhibit peaks for yttrium (~96 keV), silicon (~86 keV) and oxygen (~80.5 keV). The shoulder (~87 keV) on the silicon substrate peak is clearly evident in the spectrum of the Y-O-Si film formed on clean silicon. However, this shoulder is barely evident in the spectrum of the film formed on nitrided silicon indicating less silicon content relative to the

Y-O-Si film formed on clean silicon. The difference between the silicon content of the Y-O-Si film formed on clean silicon and the film formed on nitrided silicon is clearly indicated in the calculated MEIS depth profiles for these films. As presented in Fig. 5.9, the silicon distribution is constant at $0.4x10^{22}$ atoms/cm^3 for the Y-O-Si formed on clean silicon (Fig. 5.9.1), whereas the silicon distribution increases from approximately zero to $0.1x10^{22}$ atoms/cm^3 for the film formed on nitrided silicon (Fig. 5.9.4). The silicon profile can only be calculated to a depth of 1.0 nm due to complications arising from the overlap of the silicon substrate peak. The film formed on nitrided silicon displays a feature for nitrogen in the proton energy spectrum at ~76.5 keV, which is detected but not visually apparent in the raw spectra of the films formed on the oxidized silicon and nitrided-oxidized silicon and below the detection limit (<0.3 monolayer) for the film formed on clean silicon. The depth profile for the film formed on nitrided silicon (Fig. 5.9.4) indicates that $2x10^{22}$ atoms/cm^3 of nitrogen remains localized at the interface after yttrium deposition and oxidation.

The XPS and MEIS results (Figs. 5.7-9) demonstrate the effects that oxygen and nitrogen silicon surface pretreatments have on silicon consumption during oxidation of deposited yttrium. When yttrium is deposited onto silicon and oxidized (experiment "1" in Figs. 5.7-9), the yttrium and silicon react and oxidize to form a film with a significant fraction of Y-O-Si bonds. The chemical shifts of the Y 3d, Si 2p and O 1s peaks (Fig. 5.7.1) are consistent with yttrium donating electron density to neighboring Si-O bonds in agreement with the relative electronegativity of yttrium, silicon and oxygen (1.2, 1.8, 3.5 on the Pauling scale). This bonding structure likely results from the high reactivity of the yttrium metal contributing to concurrent silicide and oxidation reactions. The peak (~87 keV) for silicon in the film is clearly largest for the Y-O-Si films formed on clean silicon. The composition of this film is $(Y_2O_3)_{0.60}\cdot(SiO_2)_{0.40}$ consistent with yttrium orthosilicate

(Y_2SiO_5) containing ~33% Y_2O_3. Phase separated Y_2O_3 is not detected at 156.8 eV in the XPS spectra, perhaps due to dispersal of Y_2O_3 groups within the silicate bulk or bond strain in Y_2O_3 clusters.

Similar results are observed in the XPS and MEIS (Figs. 5.7.2-3 and 5.8.2-3) results for experiments (2) and (3) where yttrium is deposited on oxidized silicon and nitrided-oxidized silicon, respectively, and the stacks are then oxidized. Films formed by the oxidation of yttrium on an oxidized silicon pretreatment contain considerable amounts of Y-O-Si bonding, although the film formed on nitrided-oxidized silicon contains slightly less silicon than the films formed on clean and oxidized silicon. The Y 3d, Si 2p and O 1s results for both cases are similar to the Y-O-Si film formed on clean silicon. However, more O-Y-O bonding is observed in the O 1s spectra for the film formed on nitrided-oxidized silicon. The composition of the film formed on oxidized silicon is $(Y_2O_3)_{0.63}\cdot(SiO_2)_{0.37}$, which is indistinguishable from the Y-O-Si formed on clean silicon (experimental error x ± 0.04), and the composition of the film formed on nitrided-oxidized silicon is $(Y_2O_3)_{0.73}\cdot(SiO_2)_{0.27}$, which does not represent a significant departure from the Y-O-Si formed on clean silicon. The spectrum for the oxidized silicon pretreatment is presented as a reference in Fig. 5.7.b.2´. The Si 2p spectra for the films formed on oxidized silicon and nitrided-oxidized silicon do not provide any indication (shoulder or additional peak at 103.3 eV) that the interfacial SiO_2 layer has remained after yttrium deposition and oxidation. When subjected to an oxidizing ambient at elevated temperature, yttrium deposited on a SiO_2 layer will covert the oxide to a silicate, as discussed in detail in Section 5.3.3. When the yttrium is deposited on oxidized silicon (experiment "2"), the yttrium consumes the oxide layer and continues to consume silicon from the substrate until the silicon fraction is the same as the Y-O-Si film formed on clean silicon. However, when yttrium is deposited on a nitrided-oxidized silicon (experiment

“3”), the yttrium consumes the SiO_2 up to the interfacial nitrogen where consumption of silicon is impeded resulting in a slightly reduced silicon fraction.

When the silicon surface is nitrided prior to yttrium deposition and oxidation (experiment “4”), the XPS and MEIS results indicate a reduced silicon content compared to the Y-O-Si film formed on clean silicon. As a result of the decreased silicon fraction in the film, the Y 3d peak for the film formed on nitrided silicon is shifted toward more Y_2O_3-like bonding, the O 1s peak exhibits a definite shoulder near the expected O 1s position for Y_2O_3 and the MEIS peak for silicon in the film is diminished. The composition determined from MEIS is $(Y_2O_3)_{0.87}\cdot(SiO_2)_{0.13}$, which corresponds to a Y_2O_3 film with ~15% yttrium silicate. The MEIS depth profile for the film formed on nitrided silicon demonstrates that the nitrided interface has remained intact after yttrium deposition and oxidation. The interfacial nitrogen is responsible for reducing the consumption of silicon by providing a silicon diffusion barrier that impedes the reaction between yttrium and silicon and allows formation of Y_2O_3.

The inter-diffusion of silicon and some metals, including Y, Hf, Zr and La, to form silicides at relatively low temperatures is a well-known phenomenon.[20,21] When yttrium (which forms a silicide and stable oxide) on silicon is oxidized (experiment “1”), the above results indicate that yttrium and silicon react and oxidize to form a Y-O-Si film. Similar films are observed when the silicon surface is pre-oxidized before yttrium deposition and oxidation (experiments “2” and “3”). When the silicon surface is pretreated with a nitrided-oxide (experiment “3”), the yttrium consumes the SiO_2 layer up to the interfacial nitrogen, and further reaction with the silicon substrate is inhibited. However, when the silicon surface is nitrided prior to yttrium deposition and oxidation (experiment “4”), the reaction between yttrium and silicon is greatly impeded resulting in an Y_2O_3 film with a small fraction

(~15%) of silicate bonding. Recently, nitrided oxide and silicon nitride films have been used as diffusion barriers to reduce boron penetration into the gate oxide.[22,23] It is reasonable to assume that the silicon nitride pretreatment described in this work provides a sufficient silicon diffusion barrier to suppress the reaction between the yttrium and silicon.

5.3.3 CONSUMPTION OF SiO_2 BY YTTRIUM

Reaction between yttrium and SiO_2 to form Y-O-Si was postulated to explain the consumption of silicon by yttrium in experiments (2) and (3) in Section 5.3.2. Yttrium films (25 Å) on thermal SiO_2 (40 Å) were subjected to oxidizing or vacuum annealing conditions and probed using XPS to confirm the conversion of SiO_2 to Y-O-Si. Figure 5.10 presents XPS results for the oxidation of yttrium films on SiO_2 at 600 and 900 °C in 1 atm. N_2O for 2 minutes. The spectra of the 40 Å SiO_2 film prior to yttrium deposition and oxidation is presented in Fig. 5.10 as a reference. The Y $3d_{5/2}$ peaks (Fig. 5.10a) for the films after oxidation at 600 and 900 °C are measured at 158.8 and 159.2 eV, respectively, consistent with Y-O-Si bonding. The spectrum for oxidation at 600 °C exhibits blurring of the spin-orbit splitting indicating the presence of multiple yttrium oxidation states. The Si 2s peaks for SiO_2 are visible in the Y 3d window at 154.9 and 150.6 eV for the Si-O and substrate peaks, respectively. The silicon substrate peak (99.3 eV) is observed in the Si 2p spectra (Fig. 5.10b) for SiO_2 and for the films after oxidation of yttrium on SiO_2. The Si-O peak is measured at 103.6 eV for SiO_2 and at 102.9 eV for the films after oxidation of yttrium on SiO_2. The Si-O feature for the films after oxidation of yttrium on silicon are consistent with yttrium silicate and do not exhibit evidence for SiO_2 (within detectable limits). Consistent with an increase in overlayer thickness, the silicon substrate and Si-O peaks for the films after yttrium deposition and oxidation are attenuated relative to the original SiO_2 layer. The Si-O peaks for the films after yttrium deposition and oxidation are broader (FWHM = 2.2

eV) compared to the Si-O peak for SiO_2 (FWHM = 1.8 eV) consistent with a wider range of bonding configurations for silicon in the films after yttrium deposition and oxidation. The Si-O feature for the film oxidized at 600 °C is 50% smaller in area than the Si-O feature of the film oxidized at 900 °C. The O 1s peaks (Fig. 5.10c) for yttrium/SiO_2 oxidized at 600 °C, yttrium/SiO_2 oxidized at 900 °C and SiO_2 are measured at 532.7, 532.4 and 533.5 eV, respectively. The FWHM for yttrium/SiO_2 oxidized at 600 °C, yttrium/SiO_2 oxidized at 900 °C and SiO_2 are 3.4, 2.4 and 1.8 eV, respectively. The O 1s peaks for the films after yttrium deposition and oxidation are broad peaks consistent with the combination of oxygen bound to yttrium and silicon. The O 1s peak for yttrium on SiO_2 oxidized at 600 °C displays asymmetry on the low binding energy side of the peak consistent with O-Y-O bonding. Figure 5.11 presents the XPS results for yttrium on SiO_2 annealed at 600 °C in vacuum for 2 minutes. Again, the spectrum for the 40 Å SiO_2 is presented as a reference. The Y $3d_{5/2}$ (Fig. 5.11a), Si-O Si 2p (Fig. 5.11b) and O 1s (Fig. 5.11c) peaks for yttrium on SiO_2 annealed in vacuum are measured at 158.2, 102.0 and 531.7 eV similar to the peaks for the yttrium film on SiO_2 oxidized at 600 and 900 °C. The Si-O feature (FWHM = 2.3 eV) for the yttrium on silicon annealed in vacuum does not exhibit any evidence for SiO_2. The O 1s peak is a broad peak (FWHM = 3.1 eV) resulting from oxygen bound to yttrium and silicon.

The spectra of Figs. 5.10 and 5.11 confirms the conversion of SiO_2 to Y-O-Si when yttrium on silicon is exposed to oxidizing or vacuum annealing conditions. When yttrium on SiO_2 is oxidized or vacuum annealed, the Y 3d, Si 2p and O1s peak positions are consistent with Y-O-Si bonding, with only subtle differences between films formed by oxidizing yttrium on SiO_2 and by oxidizing yttrium on silicon. The yttrium film on SiO_2 oxidized at 900 °C (Fig. 5.10) is similar to the Y-O-Si film formed by oxidation of yttrium on silicon at

900 °C (Fig. 5.1), since the spectra for both films are similar in shape and position. The yttrium film on SiO_2 annealed in vacuum at 600 °C (Fig. 5.11) has structure similar to the Y-O-Si film formed by oxidation of yttrium on silicon at 600 °C (Fig. 5.7.1), since the spectra for both films are similar in shape and position. Although the spectra of the film formed by oxidizing yttrium on SiO_2 at 600 °C (Fig. 5.10) indicate a significant fraction of Y-O-Si bonding, the blurring of the Y 3d spin-orbit spitting, the reduced Si-O feature size and the broadness of the O 1s feature suggest the presence of Y_2O_3-like bonding. When yttrium on SiO_2 is exposed to an oxidizing ambient, there exists a competition between oxidation of the yttrium (reaction "5.1") and consumption of the SiO_2 (reaction "5.5"). Perhaps, the reaction between yttrium and SiO_2 during oxidation at 600 °C does not completely consume the yttrium leaving metal available for oxidation to Y_2O_3. In any case, there is enough evidence in Fig. 5.10 for Y-O-Si bonding (i.e. binding energy of Y $3d_{5/2}$, Si-O Si 2p and O 1s) to conclude that the yttrium has converted most of the SiO_2. These results contrast a previous study where zirconium thin films on SiO_2 were annealed in vacuum and a $ZrO_2/Zr_5Si_4/SiO_2$ multi-layered structure formed, however, the oxygen content of the mixed zirconium and silicon layer could not be determined due to overlap of the oxygen signal from the SiO_2 substrate.[24] The results presented here are in agreement with the ionized cluster beam growth of Y_2O_3 where a thin layer of yttrium is deposited on a SiO_2 substrate at 500 °C before being exposed to oxygen, which results in an amorphous SiO_x layer that can be attributed to a Y-O-Si film.[3] Since the free energy of formation ($-\Delta G_f$) for Y_2O_3 ($-\Delta G_f$ = 434.0 kcal/mol at 25 °C) is greater than for SiO_2 ($-\Delta G_f$ = 204.6 kcal/mol at 25 °C), yttrium can reduce silicon with Y_2O_3 and Si being the expected products.[12] However, the XPS results of Figs. 5.10 and 5.11 indicate the conversion of SiO_2 to Y-O-Si. The lack of

thermodynamic data for $Y_2Si_2O_7$ and Y_2SiO_5 prevents complete evaluation of the unbalanced reaction $Y + SiO_2 + O_2 \rightarrow (Y_2Si_2O_7 \text{ or } Y_2SiO_5)$ to determine if the silicates are energetically favorable products. However, previous researchers have measured the enthalpy of formation ($-\Delta H_f$) for Y_2SiO_5 as $-\Delta H_f$ (25 °C) = 685.3 kcal/mol.[25] The experiments described here are performed at relatively moderate temperatures (600-900 °C) with no phase changes. Under these conditions, the entropy change can be considered negligible, and ΔG_f can be approximated as $\Delta G_f \cong \Delta H_f$, since $\Delta G = \Delta H - T\Delta S$, where T is the temperature and ΔS is the entropy change. For the reaction $2Y + SiO_2 + 3/2\ O_2 \rightarrow Y_2SiO_5$, $\Delta G_f \cong \Delta H_f = -480.7$ kcal/mol, which implies that the formation of Y-O-Si is thermodynamically favorable. This processes provides an interesting method to convert the existing SiO_2 gate dielectric to a high-k dielectric in a straightforward manner using thermal oxidation of silicon followed by metal deposition, annealing and re-oxidation.

5.4 CONCLUSIONS

The above results indicate that deposition of yttrium onto a clean silicon surface followed by oxidation results in a film with a substantial Y-O-Si component. Silicon from the substrate is consumed and incorporated into the Y-O-Si film. Oxidation of the silicon surface prior to yttrium deposition and oxidation results in a Y-O-Si film similar to the films formed on clean silicon. A nitrided interface can impede silicon incorporation from the substrate. However, any silicon oxide on top of the nitrided interface can react with the metal. Oxidation of yttrium deposited on a surface with only nitrided silicon results in a structure closer to pure metal oxide, consistent with impeded silicon diffusion through the nitrided layer. Conversion of SiO_2 to Y-O-Si is demonstrated for both oxidation and vacuum annealing of yttrium on silicon dioxide, and may be a route for conversion of SiO_2

to a high-k dielectric. The silicon consumption reactions reported here for the case of yttrium are expected for other metals that form silicides and stable oxides on silicon including Hf, Zr, La, etc. CVD of metal oxides may also include formation of metal-silicon bonds, so similar reactions reported here for PVD films are expected to be active during CVD, and these reactions probably play an important role in interface layer formation.

5.5 ACKNOWLEDGMENTS

The authors gratefully acknowledge support from the SRC/SEMATECH Center for Front End Processes and NSF CTS – 0072784.

5.6 REFERENCES

1. S. I. Association, *The International Technology Roadmap for Semiconductors, 1999 edition* (Austin, TX, 1999).
2. D. A. Buchanan and S.-H. Lo, Microelectronic Engineering **36,** 13 (1997).
3. D.-H. Lee, T.-Y. Seong, M.-H. Cho, and C.-N. Whang, J. Electrochem. Soc. **146,** 3028 (1999).
4. K.-A. Son, A. Y. Mao, B. Y. Kim, F. Liu, E. D. Pylant, D. A. Hess, J. M. White, D. L. Kwong, D. A. Roberts, and R. N. Vrtis, J. Vac. Sci. Technol. A **16,** 1670 (1998).
5. B. He, T. Ma, S. A. Campbell, and W. L. Gladfelter, Tech. Dig. Int. Electron Devices Meet.**,** 1038 (1998).
6. M. Balog, M. Schieber, S. Patai, and M. Michman, J. Cryst. Growth **17,** 298 (1972).
7. J. Shappir, A. Anis, and I. Pinsky, IEEE Trans. Electron Devices **ED-33,** 442 (1986).
8. L. Manchanda, W. H. Lee, J. E. Bower, F. H. Baumann, W. L. Brown, C. J. Case, R. C. Keller, Y. O. Kim, E. J. Laskowski, M. D. Morris, R. L. Opila, P. J. Silverman, T. W. Sorsch, and G. R. Weber, Tech. Dig. Int. Electron Devices Meet.**,** 605 (1998).
9. G. B. Alers, D. J. Werder, Y. Chabal, H. C. Lu, E. P. Gusev, E. Garfunkel, T. Gustafsson, and R. S. Urdahl, Applied Physics Letters **73,** 1517-1519 (1998).
10. S. K. Kang, D. H. Ko, E. H. Kim, M. H. Cho, and C. N. Whang, Thin Solid Films **353,** 8-11 (1999).
11. T. M. Klein, D. Niu, W. S. Epling, W. Li, D. M. Maher, C. C. Hobbs, R. I. Hegde, I. J. R. Baumvol, and G. N. Parsons, Applied Physics Letters **75,** 4001-4003 (1999).

12 I. Barin, *Thermochemical Data of Pure Substances* (VCH Verlagsgesellschaft, Weinheim, Germany, 1989).

13 J. J. Chambers and G. N. Parsons, submitted.

14 E. P. Gusev, H. C. Lu, T. Gustafsson, and E. Garfunkel, Physical Review B-Condensed Matter **52,** 1759-1775 (1995).

15 E. M. Levin, C. R. Robbins, and H. F. McMurdie, *Phase Diagrams for Ceramists: 1969 Supplement*, Vol. Figure 2388 (The American Ceramic Society, Columbus, Ohio, 1969).

16 J. F. Moulder, W. F. Stickle, P. E. Sobol, and K. D. Bomben, *Handbook of X-ray Photoelectron Spectroscopy* (Perkin-Elmer Corporation, Eden Prairie, MN, 1992).

17 J. J. Chambers and G. N. Parsons, in progress.

18 K. H. Lee and S. A. Campbell, J. Appl. Phys. **73,** 4434 (1993).

19 J. J. Chambers and G. N. Parsons, submitted.

20 J. E. E. Baglin, F. M. Dheurle, and C. S. Petersson, Journal of Applied Physics **52,** 2841-2846 (1981).

21 A. Pellissier, R. Baptist, and G. Chauvet, Surface Science **210,** 99-113 (1989).

22 M. Navi and S. T. Durham, Appl. Phys. Lett. **72,** 2111 (1998).

23 Y. Wu, H. Niimi, H. Yang, G. Lucovsky, and R. B. Fair, J. Vac. Sci. Technol. B **17,** 1813 (1999).

24 S. Q. Wang and J. W. Mayer, J. Appl. Phys. **64,** 4711 (1988).

25 J.-J. Liang, A. Navrotsky, T. Ludwig, H. J. Seifert, and F. Aldinger, J. Mater. Res. **14,** 1181 (1999).

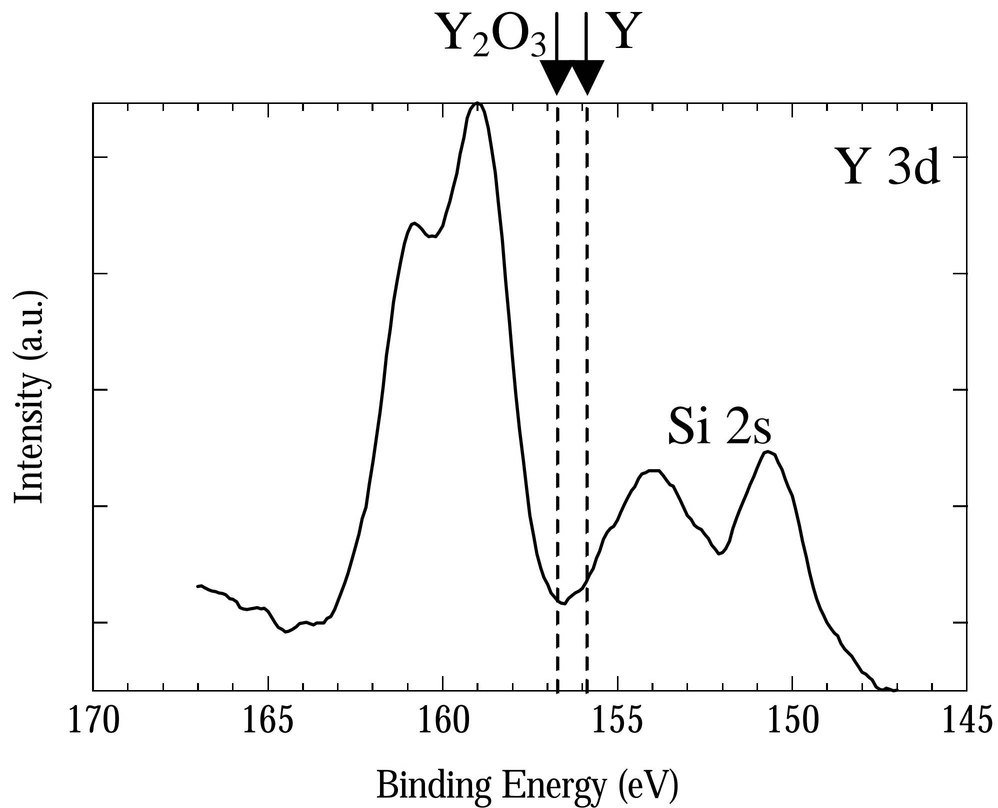

Figure 5.1a Y 3d region of the XP spectrum for a Y-O-Si film formed by oxidation of an ~8 Å yttrium film on silicon at 900 °C for 15 seconds. The chemical shift of the Y 3d peak to higher binding energy is consistent with a significant fraction of Y-O-Si bonding in the film.

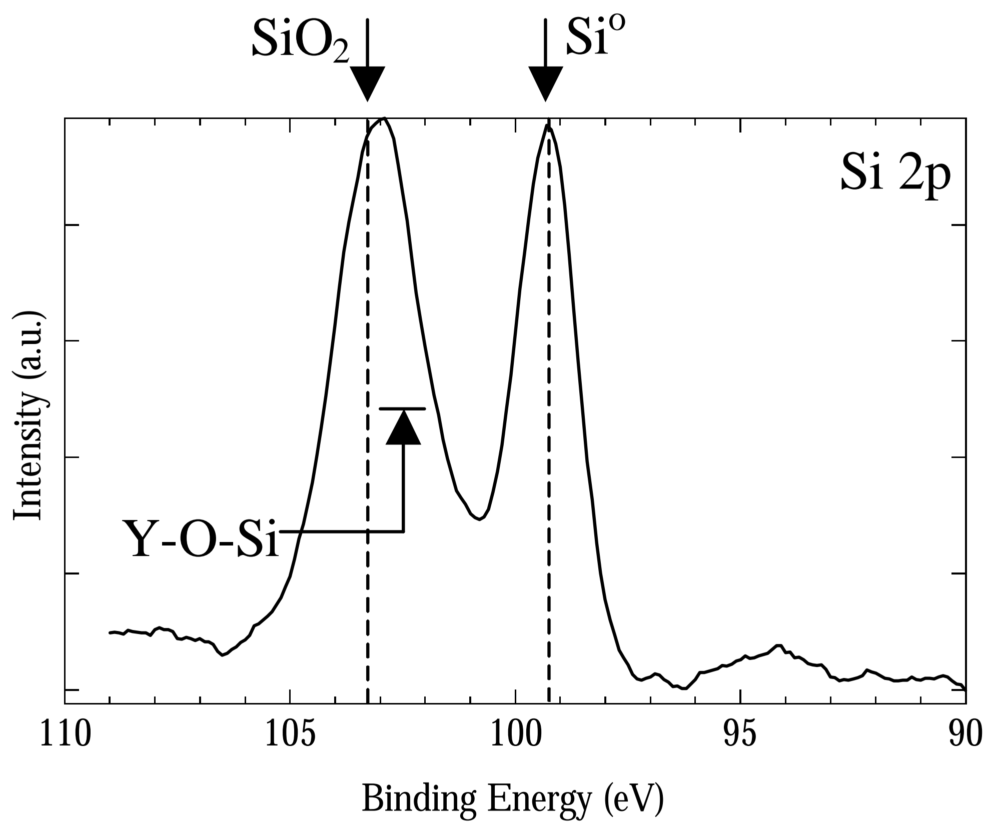

Figure 5.1b Si 2p region of the XP spectrum for a Y-O-Si film formed by oxidation of an ~8 Å yttrium film on silicon at 900 °C for 15 seconds. Si 2p Si-O peak is measured at lower binding energy than SiO_2.

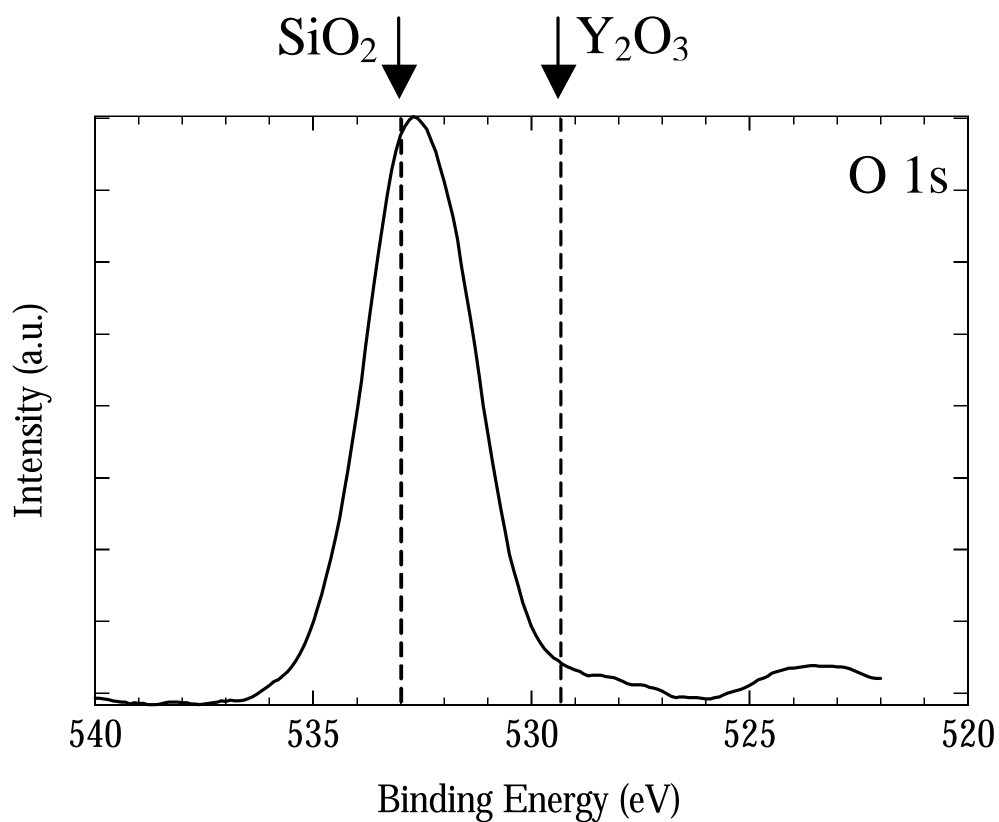

Figure 5.1c O 1s region of the XP spectrum for a Y-O-Si film formed by oxidation of an ~8 Å yttrium film on silicon at 900 °C for 15 seconds. The O 1s peak results from a combination of oxygen bound to yttrium and to silicon.

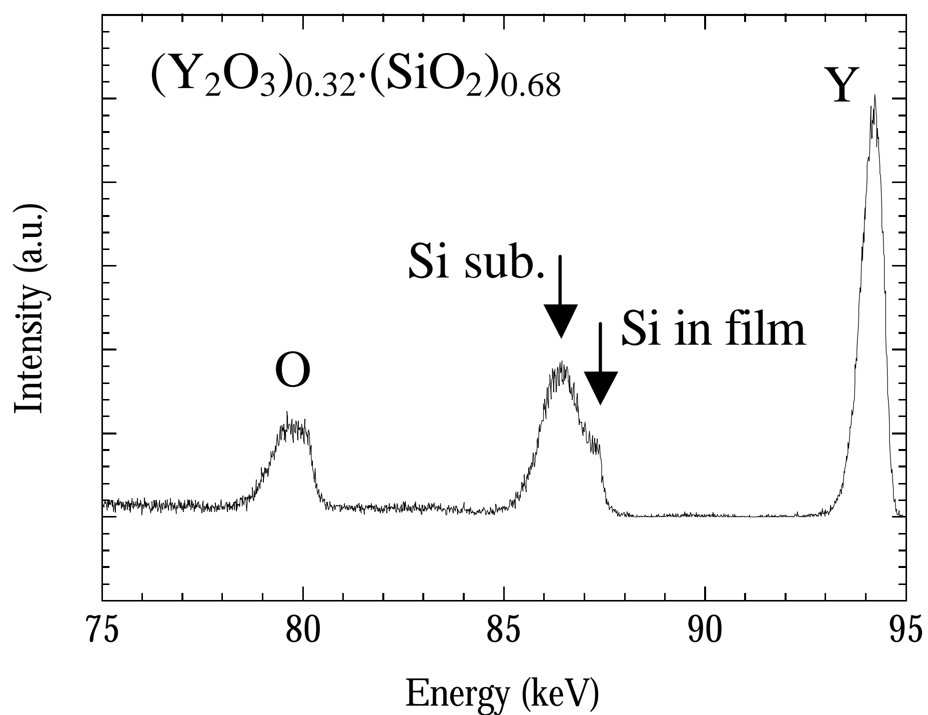

Figure 5.2 MEIS spectrum for a Y-O-Si film formed by oxidation of an ~8 Å yttrium film on silicon at 900 °C for 15 seconds. Near surface silicon is detected as the shoulder (~87 keV) on the silicon substrate peak. The composition of this film determined from the spectrum is $(Y_2O_3)_{0.32}\cdot(SiO_2)_{0.68}$.

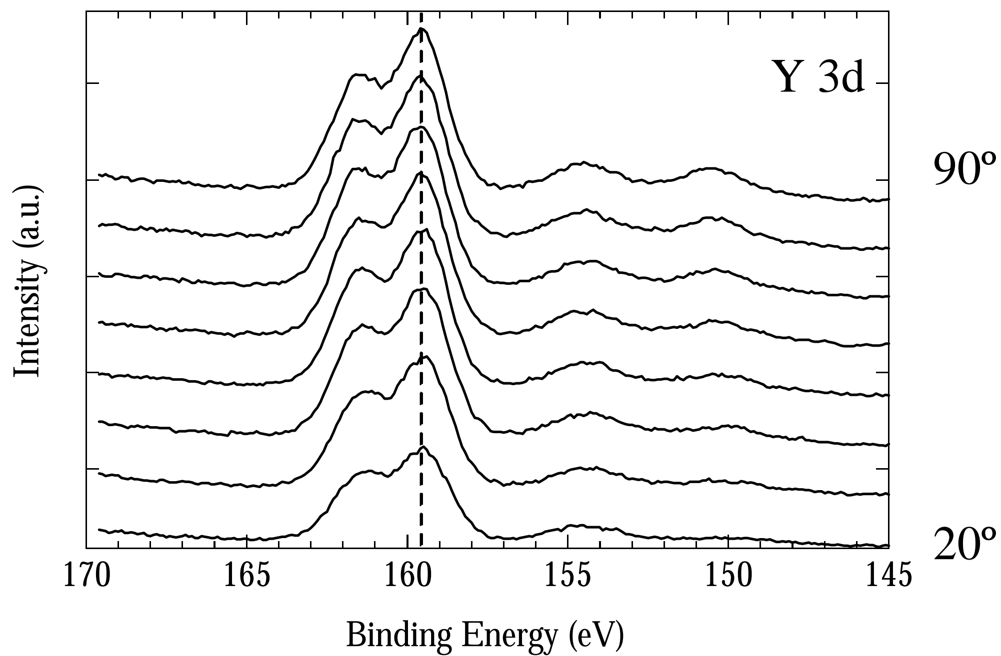

Figure 5.3a Angle resolved XPS of the Y 3d region for a Y-O-Si film formed by oxidation of a ~25 Å yttrium film on silicon at 900 °C for 2 minutes. No interface layer can be discerned, and the chemical states are consistent throughout the film.

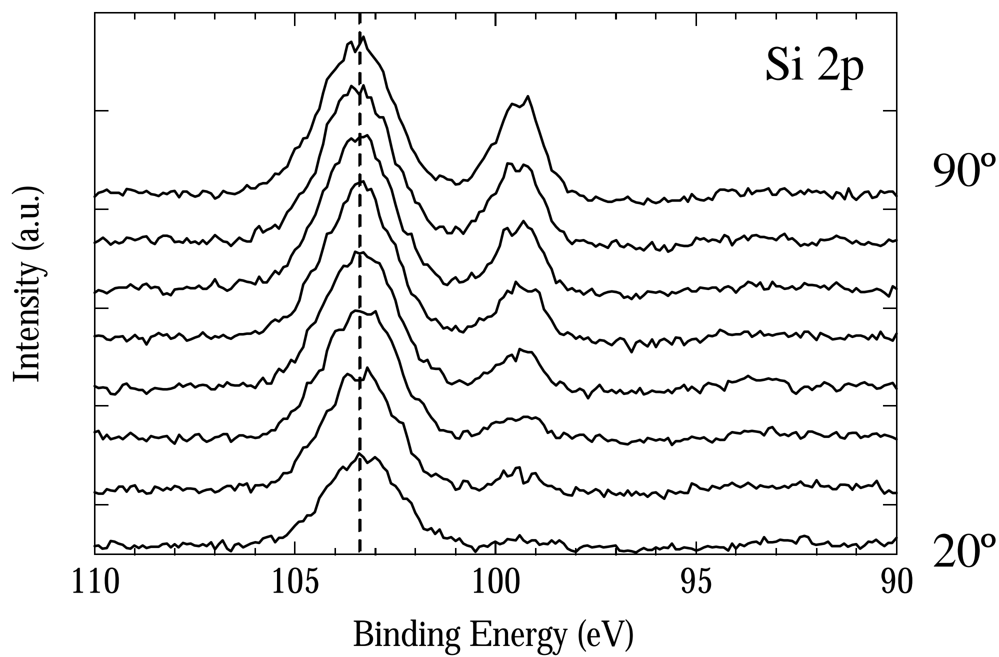

Figure 5.3b Angle resolved XPS of the Si 2p region for a Y-O-Si film formed by oxidation of a ~25 Å yttrium film on silicon at 900 °C for 2 minutes.

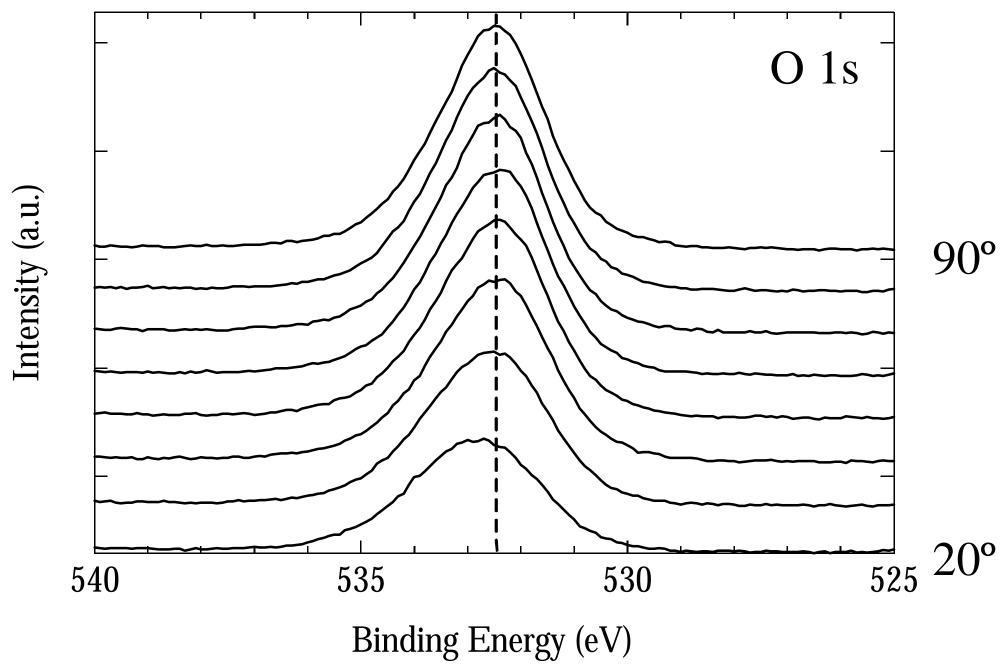

Figure 5.3c Angle resolved XPS of the O 1s region for a Y-O-Si film formed by oxidation of a ~25 Å yttrium film on silicon at 900 °C for 2 minutes.

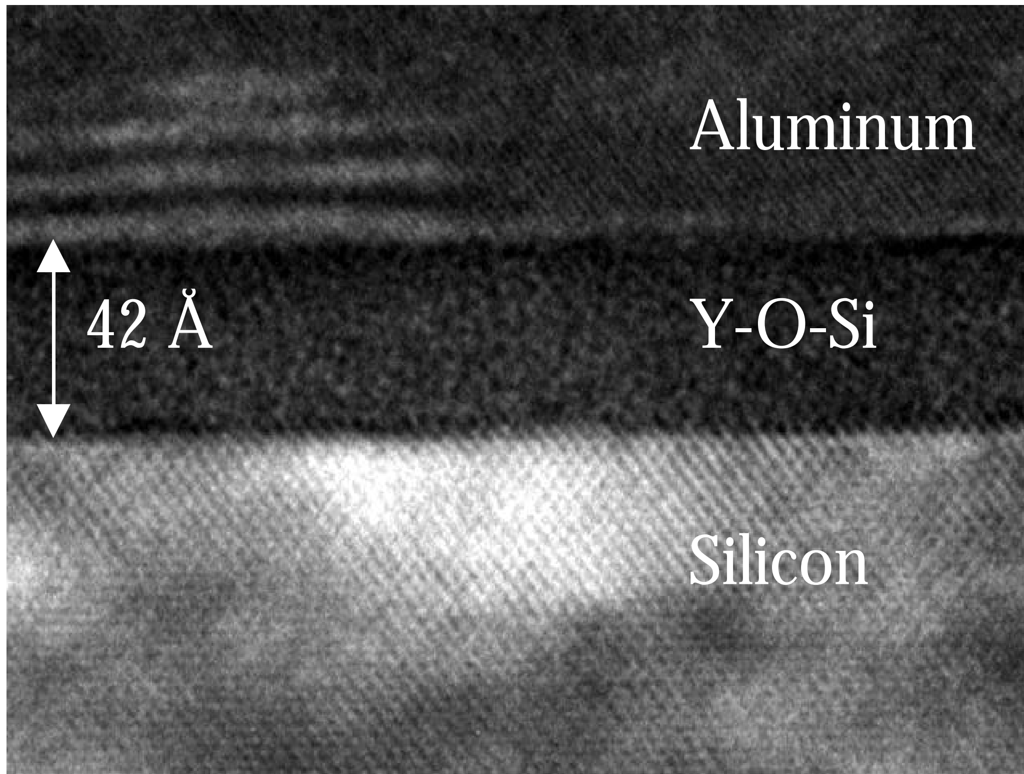

Figure 5.4 Cross-sectional TEM image of a Y-O-Si film formed by oxidation of an ~8 Å yttrium film on silicon at 900 °C for 15 seconds. The film appears amorphous with no interface layer.

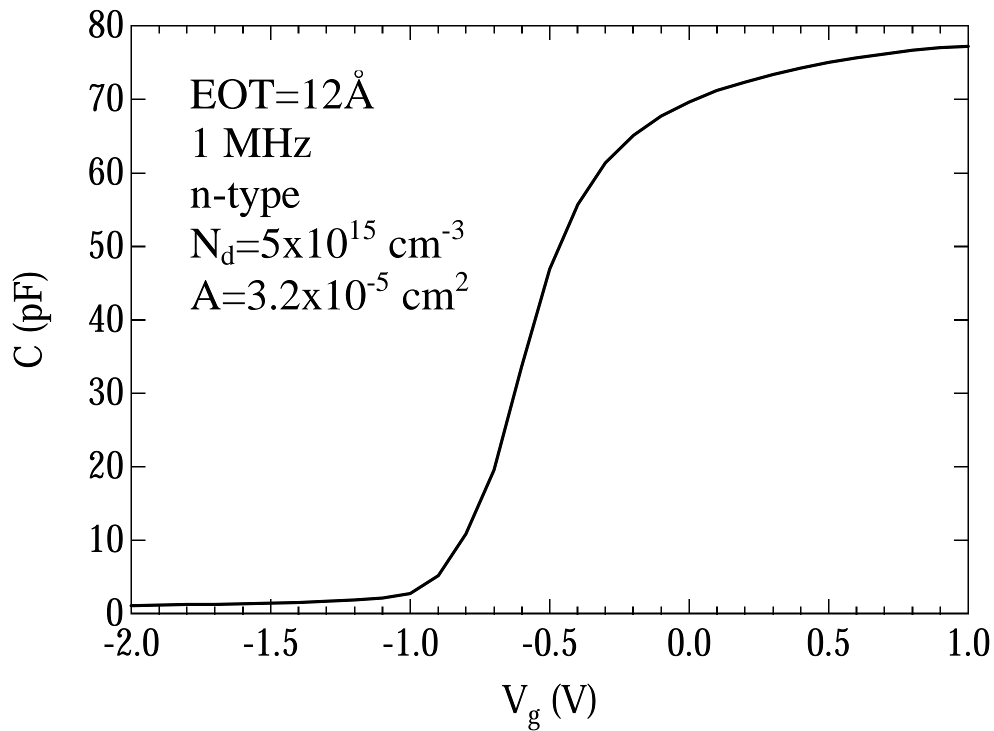

Figure 5.5 Typical 1 MHz C-V curve for an Al/Y-O-Si/n-type capacitor. The Y-O-Si was formed by oxidation of an ~8 Å film on silicon at 900 °C for 15 seconds. The Y-O-Si film has an equivalent oxide thickness of 12 Å.

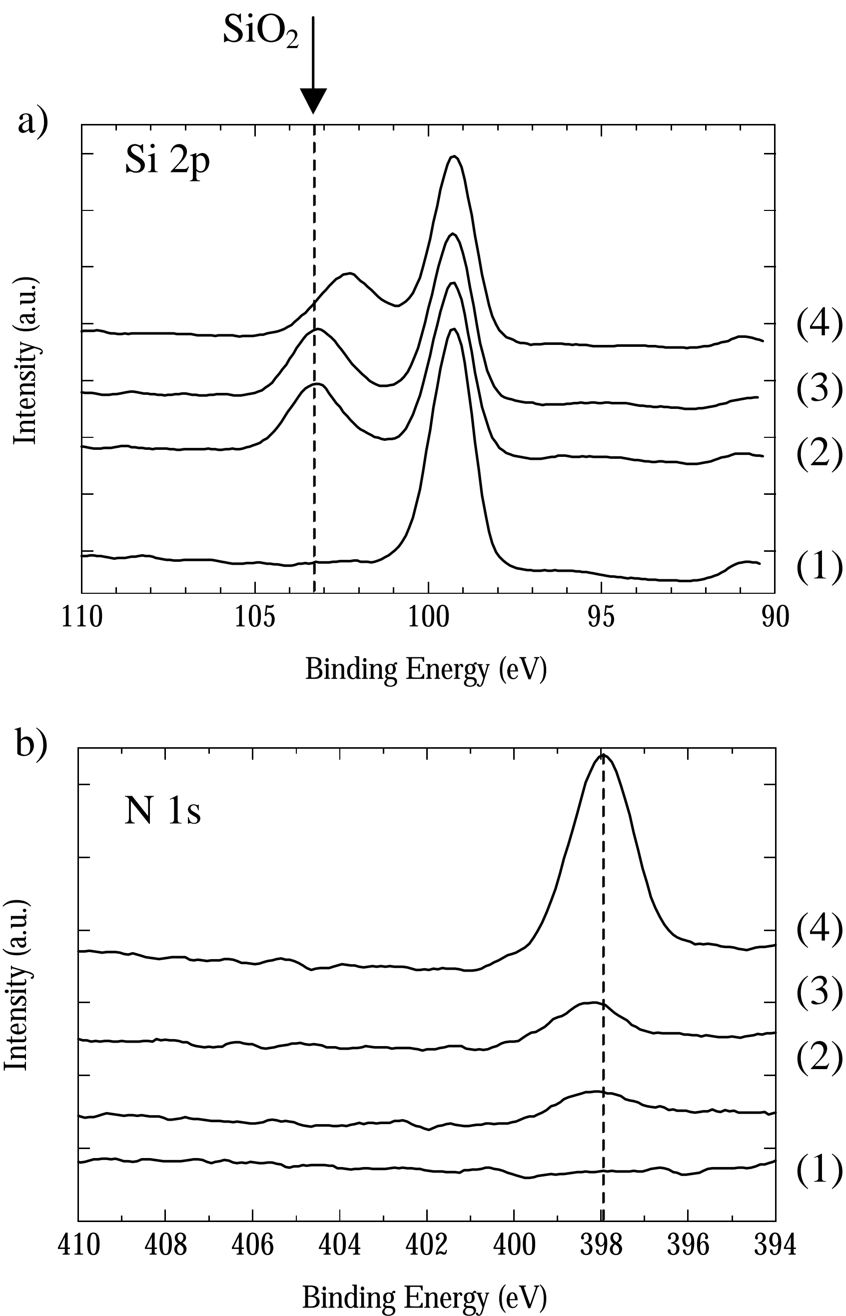

Figure 5.6 Si 2p (a) and N 1s (b) spectra for the silicon surface pretreatments used in this study: (1) clean silicon, (2) plasma oxidized silicon, (3) plasma nitrided-oxidized silicon, and, (4) plasma nitrided silicon. The thickness of the plasma surface treatments is estimated using the attenuation of the silicon substrate peak as 5-10 Å.

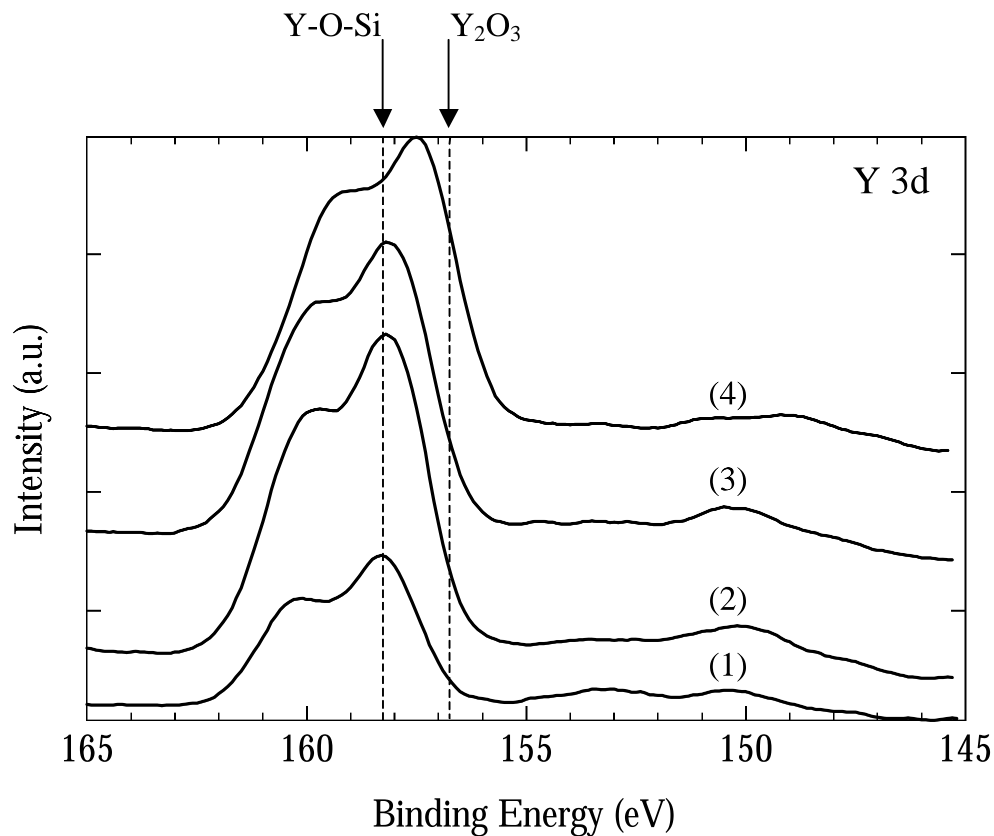

Figure 5.7a Y 3d regions of the XP spectra for the Y-O-Si films formed on: (1) clean silicon, (2) plasma oxidized silicon, (3) plasma nitrided-oxidized silicon, and, (4) plasma nitrided silicon. The spectra of the films formed on (1)-(3) are consistent with Y-O-Si bonding. The film formed on (4) has significantly more Y-O-Y bonding than the films formed on (1)-(3), as denoted by the chemical shift of the Y 3d peak.

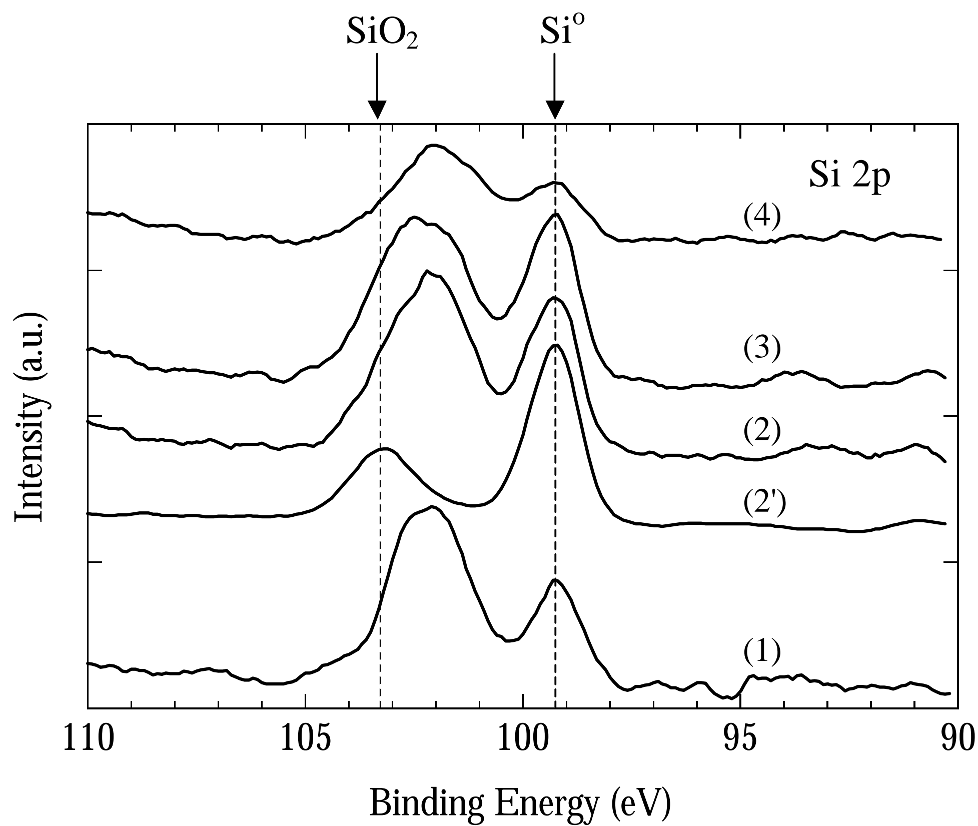

Figure 5.7b Si 2p region of the XP spectra for the Y-O-Si films formed on: (1) clean silicon, (2) plasma oxidized silicon, (3) plasma nitrided-oxidized silicon, and, (4) plasma nitrided silicon. The spectra of the films formed on (1)-(3) are consistent with Y-O-Si bonding.

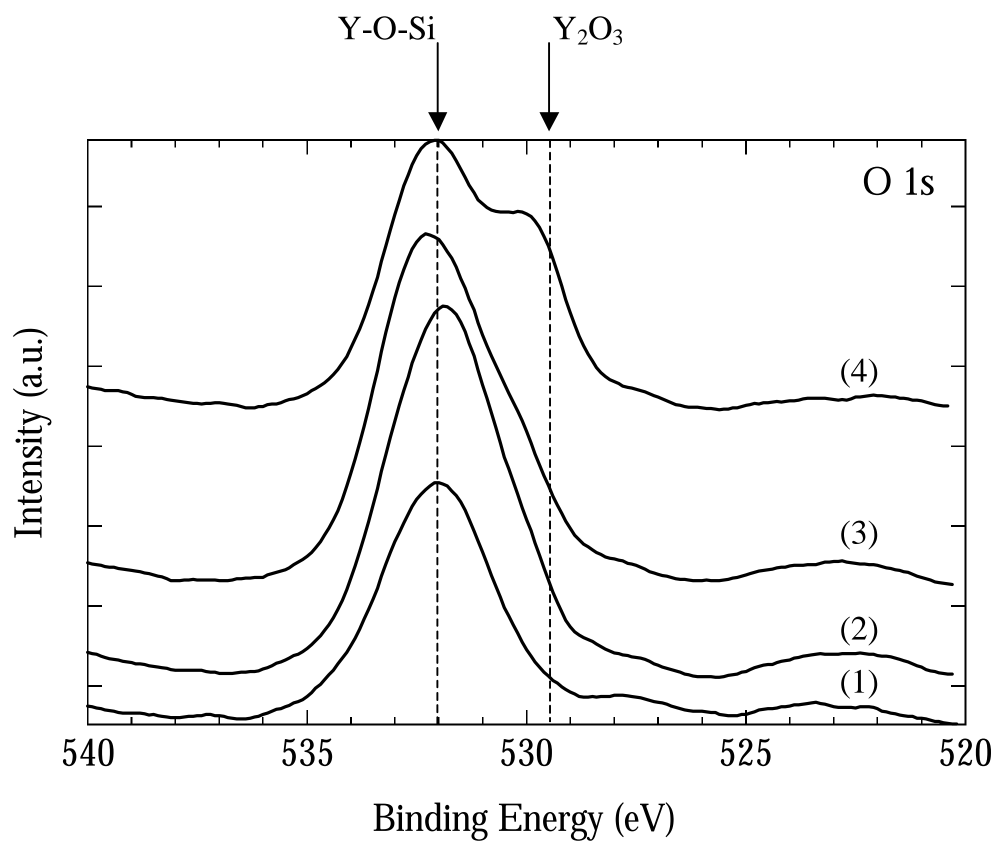

Figure 5.7c O 1s region of the XP spectra for the Y-O-Si films formed on: (1) clean silicon, (2) plasma oxidized silicon, (3) plasma nitrided-oxidized silicon, and, (4) plasma nitrided silicon. The film formed on (4) has significantly more Y-O-Y bonding than the films formed on (1)-(3), as denoted by the shoulder on the O 1s peak.

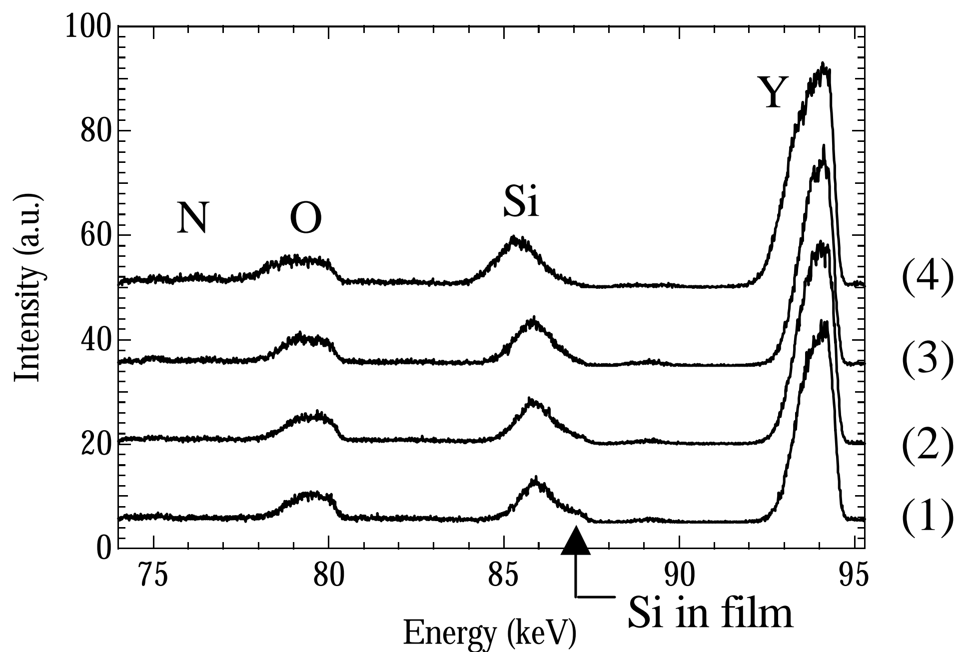

Figure 5.8 MEIS spectra for the Y-O-Si films formed on: (1) clean silicon, (2) plasma oxidized silicon, (3) plasma nitrided-oxidized silicon, and, (4) plasma nitrided silicon. The shoulder (~87 keV) on the silicon substrate peak represents silicon in the film. The Y-O-Si film formed on (1) has the highest silicon fraction and the Y-O-Si film formed on (4) has the lowest silicon fraction of the films tested.

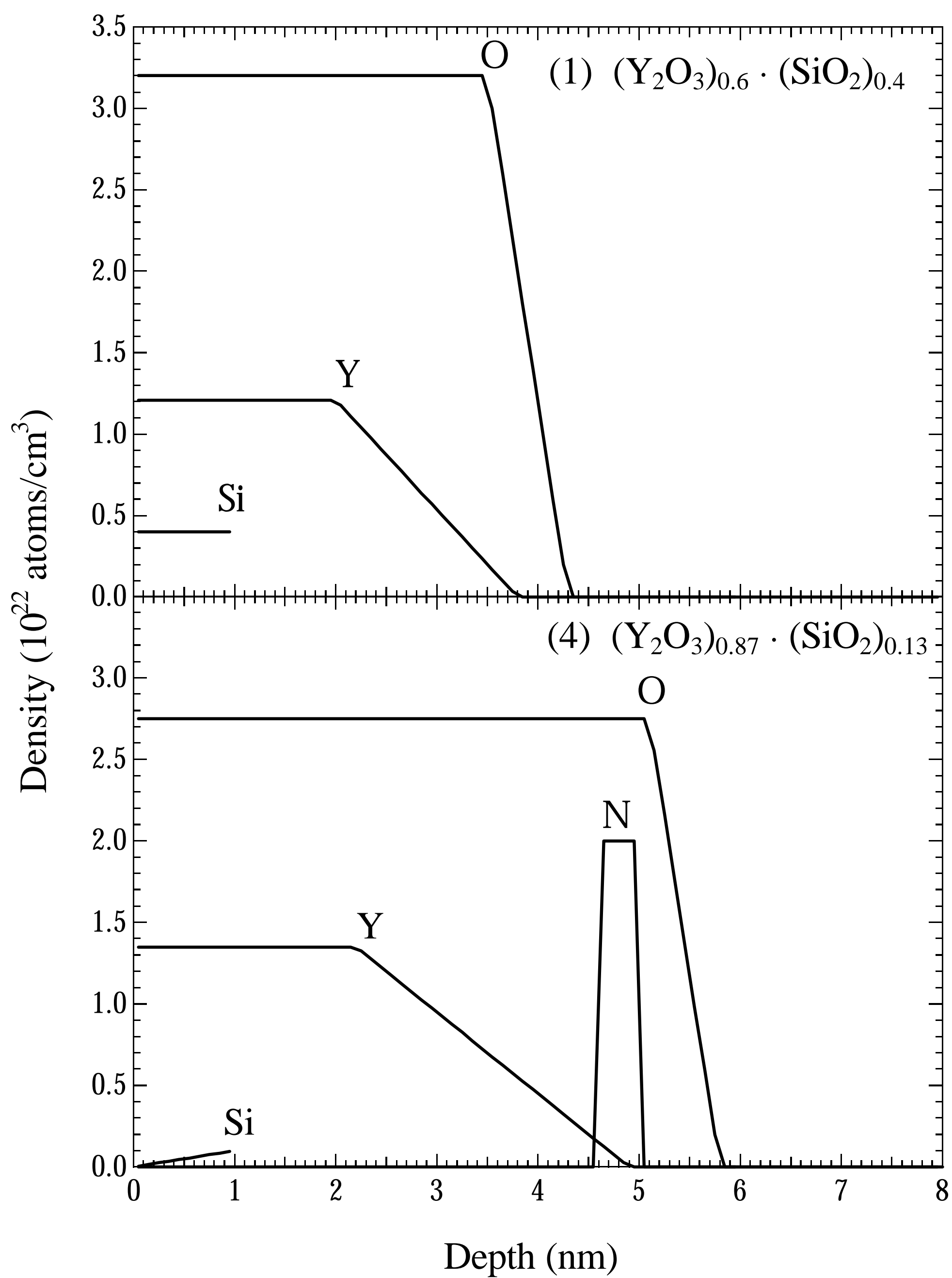

Figure 5.9 Calculated MEIS depth profiles for the Y-O-Si films formed on (1) clean silicon and (4) nitrided silicon. The profile for the Y-O-Si film formed on (4) clearly exhibits the interfacial nitrogen.

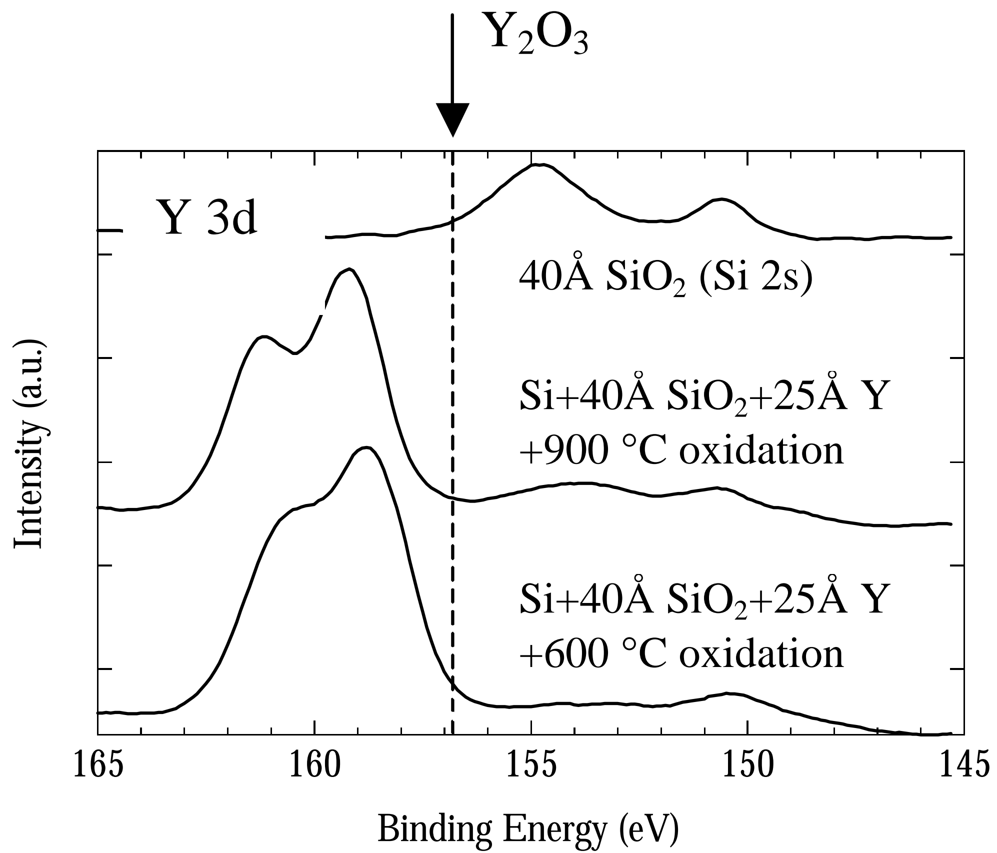

Figure 5.10a Y 3d spectra for a 40 Å reference SiO_2 and ~25 Å yttrium films on 40 Å SiO_2 oxidized at 600 and 900 °C for 2 minutes. The chemical shift of the Y 3d peak is consistent with Y-O-Si.

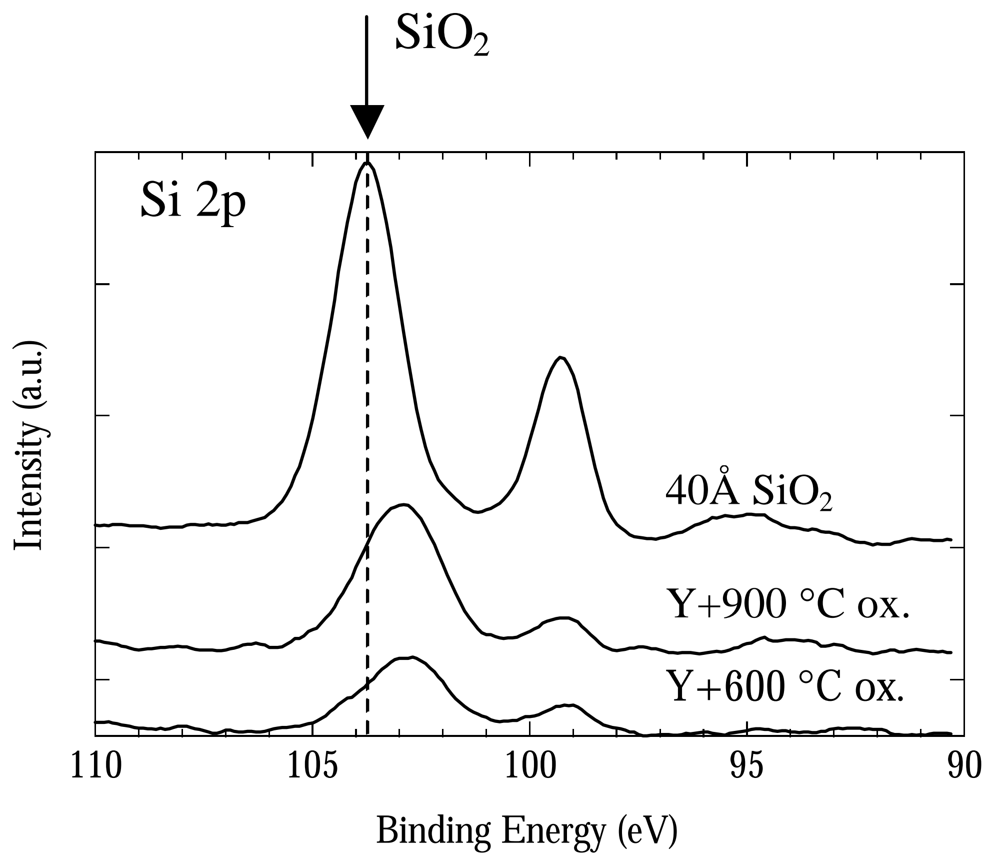

Figure 5.10b Si 2p spectra for a 40 Å reference SiO_2 and ~25 Å yttrium films on 40 Å SiO_2 oxidized at 600 and 900 °C for 2 minutes. The Si-O peaks shift to lower binding energy after metal deposition and oxidation.

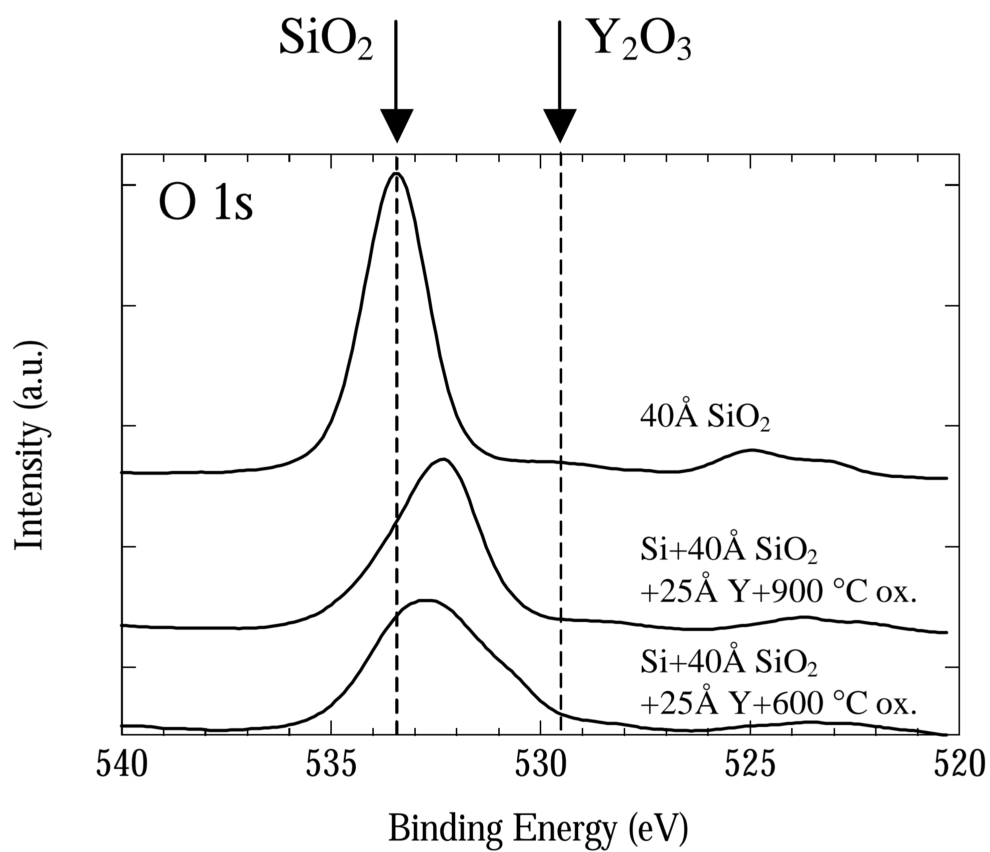

Figure 5.10c O 1s spectra for a 40 Å reference SiO_2 and ~25 Å yttrium films on 40 Å SiO_2 oxidized at 600 and 900 °C for 2 minutes. The O 1s peaks are broad consistent with oxygen bound to yttrium and to silicon.

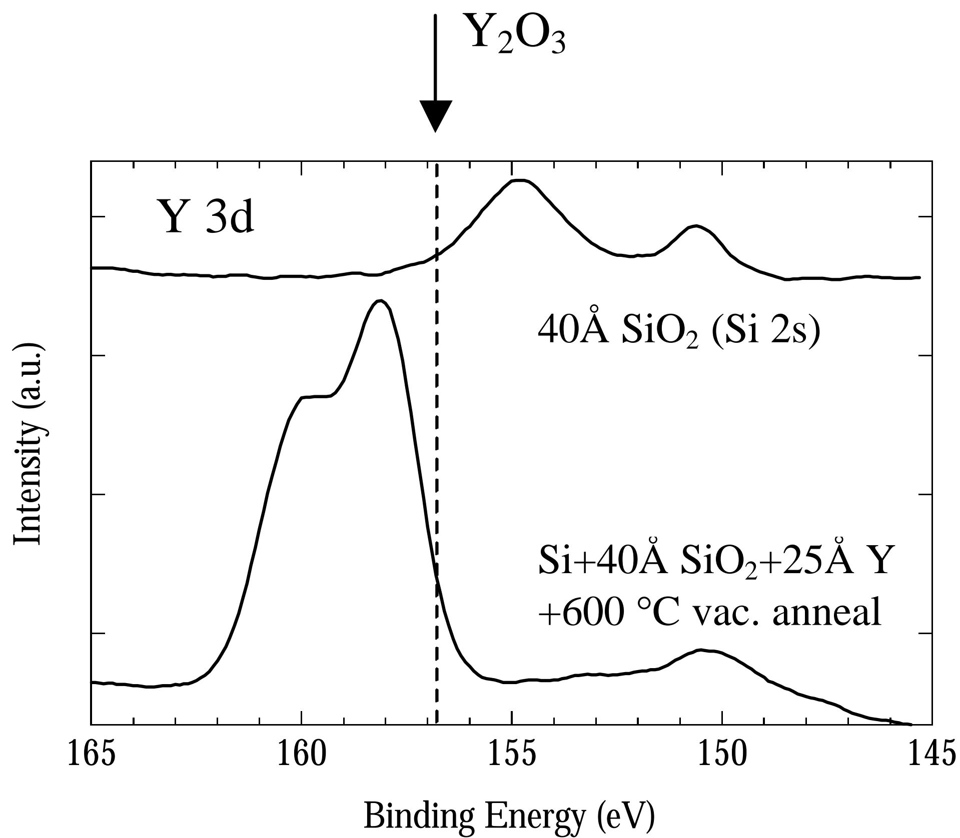

Figure 5.11a Y 3d spectra for a 40 Å reference SiO_2 and a ~25 Å yttrium film on 40 Å SiO_2 annealed in vacuum at 600 °C for 2 minutes. The Y 3d peak position is consistent with Y-O-Si.

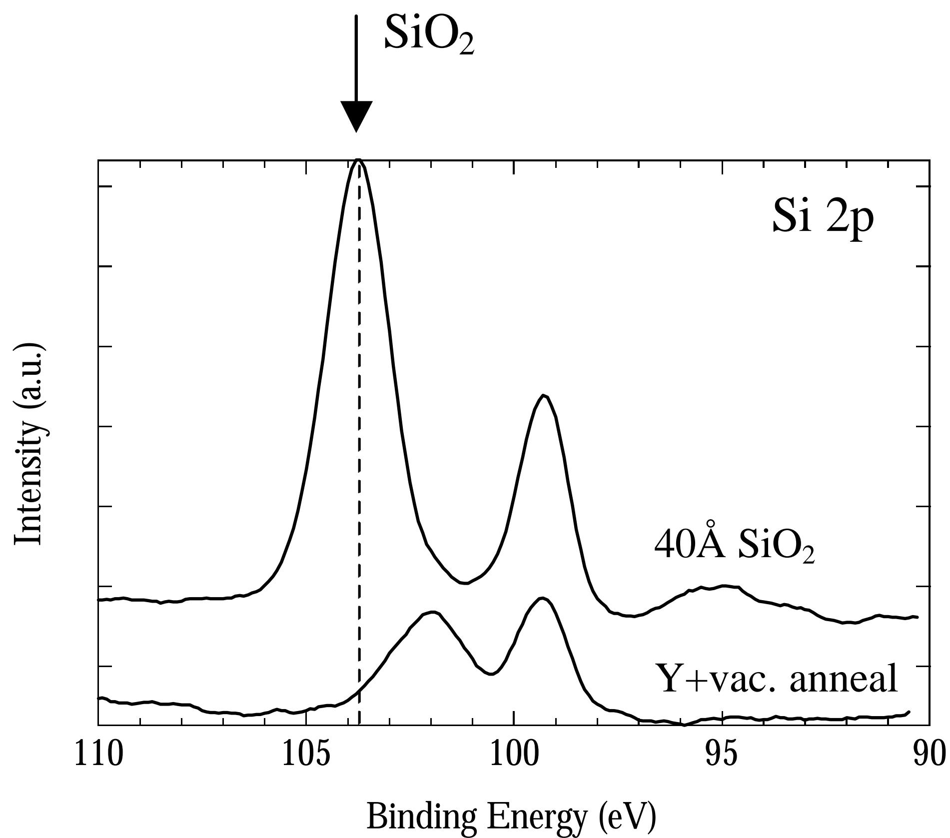

Figure 5.11b Si 2p spectra for a 40 Å reference SiO_2 and a ~25 Å yttrium film on 40 Å SiO_2 annealed in vacuum at 600 °C for 2 minutes. The Si-O peak shifts to lower binding energy and broadens after metal deposition and annealing.

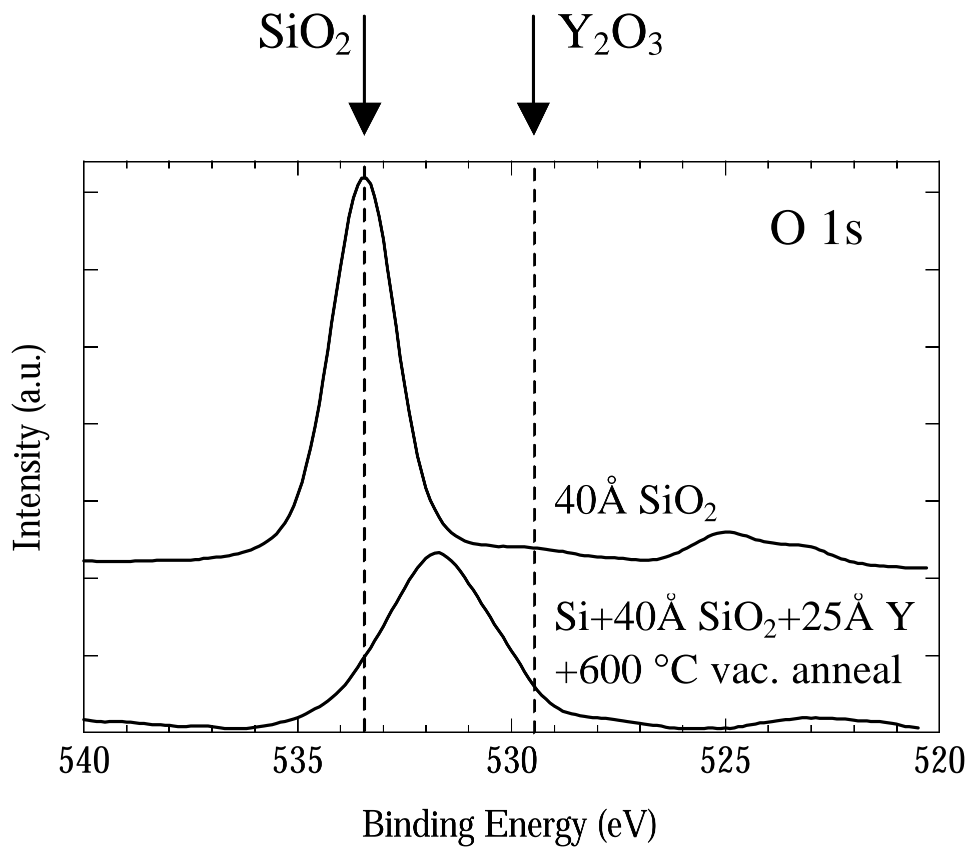

Figure 5.11c O 1s (c) spectra for a 40 Å SiO_2 and a ~25 Å yttrium film on 40 Å SiO_2 annealed in vacuum at 600 °C for 2 minutes. The O 1s peak position is consistent with Y-O-Si.

Chapter 6 is a reprint of an article to be submitted to the

Journal of Vacuum Science and Technology

EFFECT OF OXIDATION TEMPERATURE ON YTTRIUM/SILICON INTERFACE REACTIONS DURING YTTRIUM SILICATE FORMATION ON Si(100)

J. J. Chambers, B. W. Busch, E. Garfunkel, T. M. Klein and G. N. Parsons

ABSTRACT

The chemical bonding and composition of yttrium silicate films oxidized at temperatures from 25-900 °C are investigated using X-ray photoelectron spectroscopy and medium energy ion scattering. The silicate films are formed by oxidation of yttrium on silicon. The film formation occurs through interface reaction between yttrium and silicon with oxidation to form yttrium silicate, and the consumption of silicon depends on the oxidation temperature. Yttrium silicate films formed at 600 °C have a composition of $(Y_2O_3)_{0.60}\cdot(SiO_2)_{0.40}$ consistent with Y_2SiO_5 with excess Y_2O_3. Yttrium films formed at 900 °C have a composition of $(Y_2O_3)_{0.45}\cdot(SiO_2)_{0.55}$ consistent with Y_2SiO_5. Oxidation of yttrium on silicon at 25 °C results in consumption of silicon at a lesser degree than oxidation at elevated temperature. The increase (~1.3 eV) in the Y 3d and Si 2p binding energies, as well as the increase in film thickness (~40 to 80 Å), for oxidation at 25 to 900 °C is attributed to the increased silicon

fraction at higher oxidation temperature. The activation energy for silicon consumption from 500-900 °C is measured to be 0.3-0.5 eV. The increase in silicon consumption at higher oxidation temperature results from the increased diffusivity and reactivity of silicon. The reactions described here can also occur during chemical vapor deposition and physical vapor deposition of other high-k materials.

CHAPTER 6

EFFECT OF OXIDATION TEMPERATURE ON YTTRIUM/SILICON INTERFACE REACTIONS DURING YTTRIUM SILICATE FORMATION ON Si(100)

6.1 INTRODUCTION

Excessive direct tunneling of electrons through the thin silicon dioxide gate dielectric is an intrinsic limitation to continued scaling of metal-oxide-semiconductor-field-effect-transistors (MOSFETs).[1] Since the magnitude of the tunneling current is exponentially dependent on the insulator thickness, a modest increase in the thickness nets a large reduction in the tunneling current. However, high drive current requires the channel capacitance to remain high, and an increase in the dielectric constant of the gate insulator must accompany any increase in the dielectric thickness. Recent interest in high dielectric constant (high-k) materials currently focuses on the eventual replacement of silicon dioxide.

The most common materials proposed to replace silicon dioxide are the metal oxides, including Ta_2O_5, TiO_2, HfO_2, ZrO_2, Y_2O_3, and Al_2O_3, and the metal silicates, including Hf, Zr and Y silicates.[2-7] Integration of any high-k material into the existing MOS process flow requires chemical stability at the high-k/Si interface. The high-k/Si interface must maintain its stability during the strenuous dopant drive-in anneal (~1000 °C, ~30s). However, reactions forming low-k interface layers often occur at the high-k/Si interface during chemical vapor deposition (CVD), physical vapor deposition (PVD) and post-deposition anneals of metal oxides.[8-11] Low-k interfaces reduce the effective dielectric constant of the stack and counteract the benefits of the high-k dielectric. Formation of

silicon-containing oxide interface layers has been attributed to oxidation of the underlying silicon substrate during deposition or during post-deposition heat treatment from excess oxygen in the film or annealing chamber.[8,12] However, recent investigations indicate that the interface layers also contain metal and exhibit silicate properties.[9-11] These findings indicate that additional factors other than the oxidation of silicon to form SiO_2, such a metal oxide/silicon interaction[11] and CVD precursor/silicon interaction,[10] are active during interface layer formation. For instance, if interface formation solely results from oxidant diffusing through the metal oxide, then the thickness of the interface layer should depend on the thickness of the metal oxide. However, the interface layer thickness shows no dependence on the thickness of Ta_2O_5,[11] but strongly depends on the deposition[11] or annealing temperature.[8] Engineered interfaces, such as silicon nitride, have been used effectively to reduce interaction between high-k materials and the silicon substrate.[3,5,13,14] We propose that one mechanism of interface formation is the reaction between silicon and metal with subsequent oxidation to form a silicate interface layer.

We have used X-ray photoelectron spectroscopy (XPS) and medium energy ion scattering (MEIS) to study interfacial reactions between metal films and silicon for a range of oxidation temperatures. Specifically, we investigate the formation of yttrium silicate by the oxidation of yttrium on silicon at temperatures from 25-900 °C. We find that the extent of silicon incorporation into the silicate film depends on the oxidation temperature and that the silicon incorporation has an activation energy (0.3-0.5 eV) similar to other metal-silicon reactions. Specific trends in the binding energies of the Y 3d and Si 2p core levels, film thickness and Si/Y fraction are described with respect to the oxidation temperature. These results suggest metal-silicon interaction as a possible mechanism for interface layer formation in high-k/silicon systems.

6.2 EXPERIMENTAL

Samples were cut into 25 X 25 mm substrates from commercial 100 mm Si(100) wafers with resistivity of 0.1-0.3 Ω-cm. The silicon surface was prepared by dipping for 5 minutes in JTB 100 (a tetramethylammonium hydroxide based alkaline solution with a carboxylate buffer), rinsing in deionized water, drying with N_2, etching the native oxide in buffered hydrogen fluoride for 0.5 minutes with no final rinse and loading immediately into vacuum. The system described in detail elsewhere was used to sputter the yttrium films (25 Å) onto cleaned silicon at room temperature.[15] *Ex situ* oxidation of the yttrium films on silicon was performed in a standard 100 mm tube furnace. Yttrium films on silicon were oxidized for 2 minutes in 1 atm. N_2O with a flow rate of 5 slpm at a range of temperatures between 500-900 °C. Also included is a 25 Å yttrium film on silicon oxidized at ambient conditions (25 °C, 1 atm. air) for ~ 1 day.

The films after yttrium deposition and oxidation were investigated *ex situ* using X-ray photoelectron spectroscopy (XPS) and medium energy ion scattering (MEIS). Standard XPS was performed using a Riber LAS3000 with a MAC2 electron energy analyzer (single-pass cylindrical mirror analyzer with an input lens). The photoelectrons were excited using non-monochromated Mg Kα ($h\nu$ = 1253.6 eV). Y 3d, Si 2p, O 1s and C 1s detailed spectra were recorded at 0.1 eV step sizes and with a resolution of ~1.5 eV at a take-off angle of 90°. The binding energies of the core levels were corrected by setting the silicon substrate Si 2p peak at 99.3 eV, which set the C 1s peak at ~285 eV. The raw data were smoothed using an 11-point Savitsky-Golay algorithm. When peak fitting was necessary to locate peak position or integrate area, Gaussian functions were generated by minimizing the misfit error. Film thickness was determined by analyzing the attenuation of the Si 2p substrate peak using:

$$\text{Thickness} = -\lambda \cdot \text{Ln}\left(\frac{I_o}{I_\infty}\right) \quad (6.1)$$

where λ = 25 Å is the mean free path of Si 2p photoelectrons, I_∞ is the Si 2p intensity for a clean silicon surface and I_o is the Si 2p intensity of the silicon substrate peak when an overlayer is present. Angle resolved XPS was performed using a Kratos Axis 165 and Al Kα ($h\nu$ = 1486.6 eV) radiation with a spot size of 120 μm. Y 3d, Si 2p, O 1s and C 1s spectra were taken with a resolution of ~0.8 eV at take-off angles from 20° to 90° at 10° increments. Again, the binding energies of the core electrons were corrected by setting the Si 2p substrate peak to 99.3 eV. The angle resolved XPS data were not smoothed. MEIS, a low-energy (50-300 keV) high resolution (~5 Å) version of Rutherford backscattering spectroscopy, was used to obtain proton energy spectra.[16] Energy spectra of the scattered protons (~100 keV) are collected using a toriodal electrostatic energy analyzer with ~ 110 eV resolution configured in a double-aligned geometry. The average film compositions determined by MEIS are denoted with the notation $(Y_2O_3)_x{\cdot}(SiO_2)_{1-x}$, where x ranged from 0.45 to 0.6 for this work. The known yttrium silicates correspond to x = 0.33 (keiviite) and x = 0.5 (yttrium orthosilicate). We generally refer to all the films described in this article as yttrium silicate or simply as Y-O-Si.

6.3 RESULTS

Figure 6.1 presents the Y 3d (a), Si 2p (b) and O 1s (c) regions of the photoelectron spectrum for Y-O-Si films formed by the oxidation of thin (25 Å) yttrium films on silicon in 1 atm. N_2O at temperatures between 500 and 900 °C. Figure 6.1 also presents the spectra for a 25 Å yttrium film on silicon exposed in ambient conditions (25 °C, 1 atm. air) for ~1 day. Consistent with silicate bonding, the Y 3d peaks (Fig. 6.1a) for films oxidized at 25-900

°C are all shifted to higher binding energy than expected for Y $3d_{3/2}$ and Y $3d_{5/2}$ (158.8 and 156.8 eV, respectively)[17] in Y_2O_3. The Y $3d_{5/2}$ peaks shift from 158.0 eV for oxidation at 25 °C to 159.3 eV for oxidation at 900 °C. The Y 3d spectrum for the film oxidized at 25 °C exhibits a shoulder near ~156.0 eV consistent with yttrium metal (156.0 eV) or Y_2O_3 (156.8 eV), but the spectrum does not indicate the presence of any yttrium silicide (155.8 eV).[18] The Y 3d spectra for the Y-O-Si films oxidized at 500-700 °C do not exhibit evidence for Y_2O_3, yttrium metal or yttrium silicide. The Y 3d satellite and Si 2s photoelectrons cause the small peaks at ~153 and ~151 eV. The low binding energy peak in the Si 2p spectra (Fig. 6.1b) is assigned to the silicon substrate (99.3 eV) and the higher binding energy peaks are assigned to silicon bound to oxygen. The Si-O peak positions are consistent with silicon bound to oxygen in a metal silicate (102-103 eV).[17] The Si-O mode shifts from 101.8 eV for oxidation at 25 °C to 103.1 eV for oxidation at 900 °C. The Si-O mode also increases in intensity when the oxidation temperature is increased, and the Si-O mode for oxidation at 900 °C is ~3 times the integrated area of the Si-O mode for the film oxidized at 25 °C. The intensity of the silicon substrate peak is largest for oxidation at 25 °C. Increasing the oxidation temperature results in an increasingly attenuated silicon substrate peak consistent with an increase in overlayer thickness. The O 1s peak (Fig. 6.1c) positions for oxidation from 25-900 °C are measured at ~532 eV. The O 1s peaks are broad peaks resulting from a combination of oxygen bonding to yttrium and to silicon. As a result, the full-width-half-maximum (FWHM) for all the O 1s peaks is ~3.0 eV, which is considerably wider than for a binary oxide (i.e. measured FWHM for SiO_2 is 1.8 eV). The FWHM generally decreases when the oxidation is performed at higher temperature, and the measured FWHM is 3.0 and 2.6 eV for oxidation at 25 and 900 °C, respectively. The spectrum for the Y-O-Si film

oxidized at 25 °C exhibits a shoulder at ~530.5 eV, which is consistent with an increase in O-Y-O bonding.

The Y 3d spectra of Fig. 6.2, the Si 2p spectra of Fig. 6.3 and the O 1s spectra of Fig. 6.4 present angle resolved XPS results for take-off angles from 20° to 90° for a Y-O-Si sample oxidized at 600 °C and a sample oxidized at 900 °C. The take-off angle is changed from 20° to 90° from grazing to normal incidence in order to probe the near surface and far surface, respectively. In Figs. 6.2, 6.3, and 6.4 the Y $3d_{5/2}$, Si-O Si 2p and O 1s peaks remain fixed at 158.7, 102.6 and 531.9 eV, respectively, for the Y-O-Si film oxidized at 600 °C. Similarly in Figs. 6.2, 6.3 and 6.4 the Y $3d_{5/2}$, Si-O Si 2p and O 1s peaks remain fixed at 159.6, 103.4 and 532.5 eV, respectively, for the Y-O-Si film oxidized at 900 °C. (Note: The angle resolved XPS system measures SiO_2 at ~104.0 eV.) Consistent with the increased depth probed for take-off angles from 20° to 90°, the silicon substrate peak in Fig. 6.3 increases in magnitude for both oxidation temperatures. In Fig. 6.4, the O 1s peaks for take-off angles 20° exhibit slight shifting attributed to adsorbed water and/or adventitious carbon on the sample surface. The angle resolved XPS results for oxidation at 600 and 900 °C indicate similar temperature dependencies as observed in Fig. 6.1: (a) the Y 3d peaks (Fig. 6.2) for oxidation at 600 °C are at lower binding energy than for oxidation at 900 °C, (b) the Si 2p Si-O peaks (Fig. 6.3) for oxidation at 600 °C are at lower binding energy compared to oxidation at 900 °C, and, (c) the intensity of the Si-O features for oxidation at 600 °C is less than that observed for oxidation at 900 °C. Similar results are observed in the angle resolved XPS spectra for oxidation at 500, 700 and 800 °C (not shown) where the Y 3d, Si 2p and O 1s peak positions remained fixed throughout the depth probed, but with

shifting of the Y 3d and Si 2p Si-O peaks with the oxidation temperature consistent with the results presented in Fig. 6.1.

The MEIS proton energy spectra for Y-O-Si films oxidized at 600 and 900 °C are presented in Fig. 6.5. Consistent with the XPS results of Figs. 6.1-4, the MEIS spectra exhibit peaks for yttrium (~94 keV), silicon (~86.5 keV) and oxygen (~79.5 keV). The MEIS detects near surface silicon as a high energy (~87 keV) shoulder on the larger silicon substrate background. The outstanding difference between the two spectra is the shoulder for silicon in the film. Consistent with a decreased silicon fraction, the shoulder is much smaller for oxidation at 600 °C than for 900 °C. The composition calculated from the MEIS spectrum of the film oxidized at 600 °C is $(Y_2O_3)_{0.60}\cdot(SiO_2)_{0.40}$, which represents a greater metal fraction than the most metal-rich yttrium silicate, Y_2SiO_5. The absence of phase separated Y_2O_3 in the Y 3d XPS spectrum (Fig. 6.1a) may be due to instrument sensitivity, or due dispersal of the Y_2O_3 clusters within the silicate bulk. The composition calculated from the MEIS spectrum of the film oxidized at 900 °C is $(Y_2O_3)_{0.45}\cdot(SiO_2)_{0.55}$, which is consistent with Y_2SiO_5 (x = 0.50) considering the experimental error of x ± 0.04.

A summary of the results from Figs. 6.1 and 6.4 is presented in Fig. 6.6, which displays the temperature dependencies from 25 to 900 °C of the Y 3d (squares) and Si 2p (down triangles) binding energies, Si-O/Y area ratio (circles) and overlayer thickness (diamonds) all derived from the XPS results presented in Fig. 6.1 and the Si/Y ratio (up triangles) determined from the MEIS compositions calculated from the results presented in Fig. 6.5. The Si/Y area ratio was calculated by integrating the area under the Si-O Si 2p and Y 3d peaks and taking the ratio. The overlayer thickness was calculated using equation (6.1).

The dashed lines connecting the data points only illustrate the trends in the data and are not meant to indicate any fit or modeling of the data.

6.4 DISCUSSION

Oxidation of yttrium on silicon results in reaction between silicon and yttrium with oxidation to form a film predominately consisting of Y-O-Si bonding structure. The Y 3d, Si 2p and O 1s peak positions (Figs. 6.1-4) are different from either Y_2O_3 or SiO_2, and the formation of Y-O-Si bonding explains these chemical shifts. The chemical shifts result from transfer of electron density from the less electronegative yttrium (1.2 on the Pauling scale) to the more electronegative oxygen (3.5) and silicon (1.8). The transfer of electron density away from yttrium results in an increase in the binding energy of the Y 3d (Fig. 6.1a) core electrons compared to Y 3d in Y_2O_3 (156.8 eV), a decrease in the binding energy of Si-O Si 2p (Fig. 6.1b) core electrons compared to Si-O Si 2p in SiO_2 (103.3 eV) and the O 1s (Fig. 6.1c) core electrons become bound at an intermediate binding energy between O 1s in Y_2O_3 (529.5 eV) and SiO_2 (533 eV). When ~25 Å yttrium films on silicon are oxidized at different temperatures, changes in the Y 3d (Fig. 6.1a) and Si 2p (Fig. 6.1b) spectra suggest chemical distinctions between the Y-O-Si films. The shifting (~1.3 eV) of the Si 2p Si-O peak to higher binding energy with increasing oxidation temperature could be attributed to the formation of a buried SiO_2 layer. However, the Y 3d peak shift (~1.3 eV) to higher binding energy with increasing oxidation temperature indicates chemical changes occurring in the Y-O-Si film. The positions of the Y 3d and the Si-O Si 2p peaks (Fig. 6.6) are observed to increase in binding energy when the oxidation temperature is increased. The increase in binding energy is considerable for oxidation temperatures >600 °C. The increase in the binding energies of the Y 3d and Si 2p peaks is attributed to increased silicon incorporation into the Y-O-Si film causing yttrium to have an increased number of silicon second nearest

neighbors. The increase in the intensity of the Si-O feature (Fig. 6.1b) as the oxidation temperature is increased indicates increased silicon consumption and incorporation into the Y-O-Si film consistent with the MEIS results of Fig. 6.5 where the shoulder (~87 keV) representing silicon in the Y-O-Si film increases for oxidation at 900 °C. The dependence of the silicon fraction on the oxidation temperature is illustrated in Fig. 6.6, which displays the Si-O/Y area ratio from XPS and the Si/Y ratio from MEIS. Similar to the Y 3d and Si 2p binding energies, the Si-O-Y area ratio increases slowly for oxidation temperatures <600 °C and increases rapidly for oxidation temperatures >600 °C. The Si/Y ratio calculated from the MEIS results of Fig. 6.5 increases from 0.33 for the Y-O-Si film oxidized at 600 °C to 0.61 at 900 °C. The attenuation of the Si 2p (Fig. 6.1b) substrate peak (99.3 eV) indicates that the overlayer thickness increases when the oxidation is performed at higher temperature, as illustrated in Fig. 6.6. As a result of increased silicon incorporation into the Y-O-Si film, the film thickness increase from ~40 Å to ~80 Å for oxidation at 25 to 900 °C, respectively. The thickness increase is moderate between 25 and 500 °C, but increases steadily for oxidation from 500 to 900 °C.

The chemical bonding within the Y-O-Si films does not vary with depth in the film and the silicon interface is free of SiO_2, as indicated by the angle resolved XPS spectra of Figs. 6.2-4. The Y 3d, Si 2p and O 1s peak positions in the angle resolved spectra do not vary with the depth probed signifying a constant chemical state within the Y-O-Si films. The Y 3d and Si 2p peaks observed in Fig. 6.1 exhibit considerable chemical shifts (~1.3 eV) when the composition changes (as illustrated in Fig. 6.6). The angle resolved XPS does not detect chemical shifts of the Y 3d and Si 2p peaks (for oxidation at 600 or 900 °C) indicating constant composition throughout the depth of the Y-O-Si films. The Si-O features in the Si

2p spectra of Fig. 6.3 do not exhibit any high binding energy asymmetry resulting from the presence of a buried SiO_2 layer consistent with the Y 3d and Si 2p Si-O chemical shifts observed in Fig. 6.1. The symmetry of the O 1s peaks in Fig. 6.4 indicates that the ratio of oxygen bound to silicon to oxygen bound to yttrium does not vary with depth.

The Y 3d and Si 2p binding energies, Si/Y ratios and film thickness exhibit similar behaviors with increasing oxidation temperature. For oxidation below 500-600 °C, the temperature dependence is moderate, and Fig. 6.6 indicates only a gradual increase in the parameters. However, above oxidation at 600 °C, the parameters all increase at a noticeable rate. The parametric increase is attributed to increased silicon incorporation into the Y-O-Si films. Minimal silicon incorporation occurs for oxidation below 600 °C. The silicon incorporation rapidly increases for oxidation >600 °C. The properties of the Y-O-Si films strongly depend on the amount of silicon incorporated in the films. The ratio of the Si 2p Si-O and Si 2p substrate integrated peak areas approximates the relative amounts of silicon in the Y-O-Si. The integrated area of the Si 2p Si-O is a measure of the total amount of silicon in the Y-O-Si film, and the integrated area of the Si 2p substrate peak is a measure of total film thickness, which also takes into account the attenuation of the Si 2p Si-O mode due to the increase in film thickness. The intensity of the Si-O mode for thick Y-O-Si films with the same composition as the thin films would be needed to accomplish a more detailed analysis of the silicon consumption using the XPS data. However, the similar results are obtained using the two points from the MEIS analysis by multiplying the silicon fraction times the film thickness. An Arrhenius plot of the Si-O/Si ratio and (MEIS silicon fraction)*(thickness) versus 1/T for oxidation from 500-900 °C is presented in Fig. 6.7. The activation energies (E_a) for the consumption of silicon during the oxidation of yttrium

obtained from the Arrhenius plot are E_a = 0.3 eV and E_a = 0.5 eV for the Si-O/Si area data and (MEIS silicon fraction)*(thickness), respectively. These activation energies are strictly a measure of the barrier to silicon incorporation and do not reflect the energetics of the overall reaction. The E_a = 0.3-0.5 eV for the Y/Si system is consistent with the activation energy for Gd/Si, Tb/Si and Er/Si reaction (0.37, 0.35 and 0.5 eV eV, respectively).

The following overall unbalanced reactions can occur in the yttrium, silicon and oxygen system (for the process reported here, as well as, for CVD and PVD):

$$(Y)_s + (O_2)_g \rightarrow (Y_2O_3)_s \quad (6.2)$$

$$(Y)_s + (Si)_s \rightarrow (Y\text{-}Si)_s \quad (6.3)$$

$$(Y\text{-}Si)_s + (O_2)_s \rightarrow (Y\text{-}O\text{-}Si)_s \quad (6.4)$$

When formulating a rate law it is convenient to assume a mechanism, such as reactions (6.2)-(6.4) above, presuppose one of the reactions is the rate-limiting step and develop a rate expression that describes the behavior of the overall reaction. This rate expression must then be tested against the experimental results to determine the validity of the expression. If reaction (6.2) is rate limiting, then reaction (6.3) should run to completion. However, Fig. 6.6 illustrates that the oxidation temperature strongly influences the amount of silicon incorporated in the film. Increasing the oxidation temperature causes an increase in the Si/Y ratio consistent with an increase in silicon diffusivity and reactivity at higher temperature. If reaction (6.3) is rate limiting, then reaction (6.2) should completely consume the yttrium to form Y_2O_3. The results presented here for the oxidation of thin (~25 Å) yttrium films on silicon do not indicate the formation of any Y_2O_3 (156.8 eV), as observed in Figs. 6.1a and 6.2, for oxidation at 500 °C or higher. Although, the Y 3d spectrum (Fig. 6.1a) for the Y-O-Si film oxidized at 25 °C exhibits a shoulder at ~156 and the O 1s

spectrum (Fig. 6.1c) exhibits a shoulder at ~530.5 eV, which can be attributed to Y_2O_3-like bonding. The consumption of silicon has been observed to depend on the initial thickness of the yttrium film, as described elsewhere. When the initial yttrium film below some critical thickness (~<40 Å), yttrium and silicon react and oxidize to form a Y-O-Si film, and, when the initial yttrium film is greater than some critical thickness (~>80 Å), then the reaction between yttrium and silicon is not fast enough to consume the entire yttrium film leaving metal available for oxidation to Y_2O_3 and forming a Y_2O_3/Y-O-Si bi-layer on silicon.[15] However, the results presented here indicate the consumption of silicon (Figs. 6.1b and 6.3) for the entire range of oxidation temperature tested. Also, the MEIS and angle resolve XPS results indicate the presence of silicon near the surface of the Y-O-Si films oxidized at 600 and 900 °C, which provides further evidence that reaction (6.3) is not rate limiting. If reaction (6.4) is rate limiting, then the XPS should indicate the presence of un-oxidized yttrium metal or yttrium silicide. However, the oxidation rate seems quite fast, since oxidation for two minutes at 500-900 °C completely oxidized the Y-O-Si films presented here, and exposure to ambient condition for ~1 day appears to completely oxidize the 25 Å yttrium film as well.

Complete analysis of this reaction system becomes difficult without being able to determine a rate-limiting step. However, the results presented here and elsewhere[15] indicate that competition exists between silicon/yttrium reaction and oxidation, and the rates of the individual reactions must be comparable. When the oxidation is performed at reduced temperature, yttrium can oxidize to form more Y_2O_3-like bonding resulting in a reduced silicon fraction compared to Y-O-Si films oxidized at higher temperature. Previous research has investigated the effects of silicon surface pretreatment on silicon consumption, and a

nitrided silicon surface was found to impede reaction between yttrium and silicon resulting in a composition close to Y_2O_3.[14] When oxidation is performed at 900 °C, the reaction between yttrium and silicon is significant resulting in a composition close to Y_2SiO_5. Further study is required to isolate reactions (6.2)-(6.4) to determine the individual reaction rates, which would aid in developing a reaction model for the oxidation of yttrium on silicon. Reactions similar to the Y/Si reactions described here are expected to occur during CVD and PVD of HfO_2, ZrO_2 and La_2O_3, etc. During CVD, a possible mechanism would involve decomposition of the metal-organic precursor on the silicon substrate likely forming a metal-silicon bond and subsequent oxidation of the metal ligand. The potential exists for the chemisorbed metal ligand to react with silicon to form a silicate layer through reactions similar to the ones described here. During PVD, metal atoms that impinge the silicon substrate (normally at elevated temperature) have significant opportunity to react with silicon to form a silicate layer.

6.5 CONCLUSIONS

When a reactive metal is brought into contact with silicon in an oxidizing ambient, the potential exists for both reaction with silicon and reaction with oxygen. We find the oxidation of yttrium on silicon results in reaction between yttrium and silicon with oxidation to form a Y-O-Si film. The silicon content in the Y-O-Si films is dependent on the oxidation temperature, and high temperature oxidation generally results in greater silicon incorporation. The binding energies of core levels and the film thickness depend on the silicon content as a result of the oxidation temperature. The reaction between yttrium and silicon exhibits an activation energy of 0.3-0.5 eV consistent with the reaction of other rare-earth metals and silicon. The reactions described here for yttrium and silicon are also

possible during the CVD and PVD of other high-k materials of interest, such as HfO_2, ZrO_2 and La_2O_3.

6.6 ACKNOWLEDGMENTS

The authors gratefully acknowledge support from the SRC/SEMATECH Center for Front End Processes and NSF CTS – 0072784.

6.7 REFERENCES

1 D. A. Buchanan and S.-H. Lo, Microelect. Engr. **36,** 13 (1997).

2 M. Gurvitch, L. Manchanda, and J. M. Gibson, Appl. Phys. Lett. **51,** 919-921 (1987).

3 B. He, T. Ma, S. A. Campbell, and W. L. Gladfelter, Tech. Dig. Int. Electron Devices Meet.**,** 1038 (1998).

4 L. Manchanda, W. H. Lee, J. E. Bower, F. H. Baumann, W. L. Brown, C. J. Case, R. C. Keller, Y. O. Kim, E. J. Laskowski, M. D. Morris, R. L. Opila, P. J. Silverman, T. W. Sorsch, and G. R. Weber, Tech. Dig. Int. Electron Devices Meet.**,** 605 (1998).

5 K.-A. Son, A. Y. Mao, B. Y. Kim, F. Liu, E. D. Pylant, D. A. Hess, J. M. White, D. L. Kwong, D. A. Roberts, and R. N. Vrtis, J. Vac. Sci. Technol. A **16,** 1670 (1998).

6 M. Balog, M. Schieber, S. Patai, and M. Michman, J. Cryst. Growth **17,** 298 (1972).

7 M. Copel, M. Gribelyuk, and E. Gusev, Appl. Phys. Lett. **76,** 436 (2000).

8 S. K. Kang, D. H. Ko, E. H. Kim, M. H. Cho, and C. N. Whang, Thin Solid Films **353,** 8-11 (1999).

9 G. B. Alers, D. J. Werder, Y. Chabal, H. C. Lu, E. P. Gusev, E. Garfunkel, T. Gustafsson, and R. S. Urdahl, Appl. Phys. Lett. **73,** 1517-1519 (1998).

10 T. M. Klein, D. Niu, W. S. Epling, W. Li, D. M. Maher, C. C. Hobbs, R. I. Hegde, I. J. R. Baumvol, and G. N. Parsons, Appl. Phys. Lett. **75,** 4001-4003 (1999).

11 H. Ono and K.-I. Koyanagi, Appl. Phys. Lett. **75,** 3521 (1999).

12 R. A. B. Devine, Appl. Phys. Lett. **68,** 1924 (1996).

13 H. C. Lu, N. Yasuda, E. Garfunkel, T. Gustafsson, J. P. Chang, R. L. Opila, and G. Alers, Microelect. Engr. **48,** 287 (1999).

14 J. J. Chambers and G. N. Parsons, submitted.

15 J. J. Chambers and G. N. Parsons, submitted.

16 E. P. Gusev, H. C. Lu, T. Gustafsson, and E. Garfunkel, Phys. Rev. B **52,** 1759-1775 (1995).

17 J. F. Moulder, W. F. Stickle, P. E. Sobol, and K. D. Bomben, *Handbook of X-ray Photoelectron Spectroscopy* (Perkin-Elmer Corporation, Eden Prairie, MN, 1992).

18 R. Baptist, A. Pellissier, and G. Chauvet, Solid State Commun. **68,** 555 (1988).

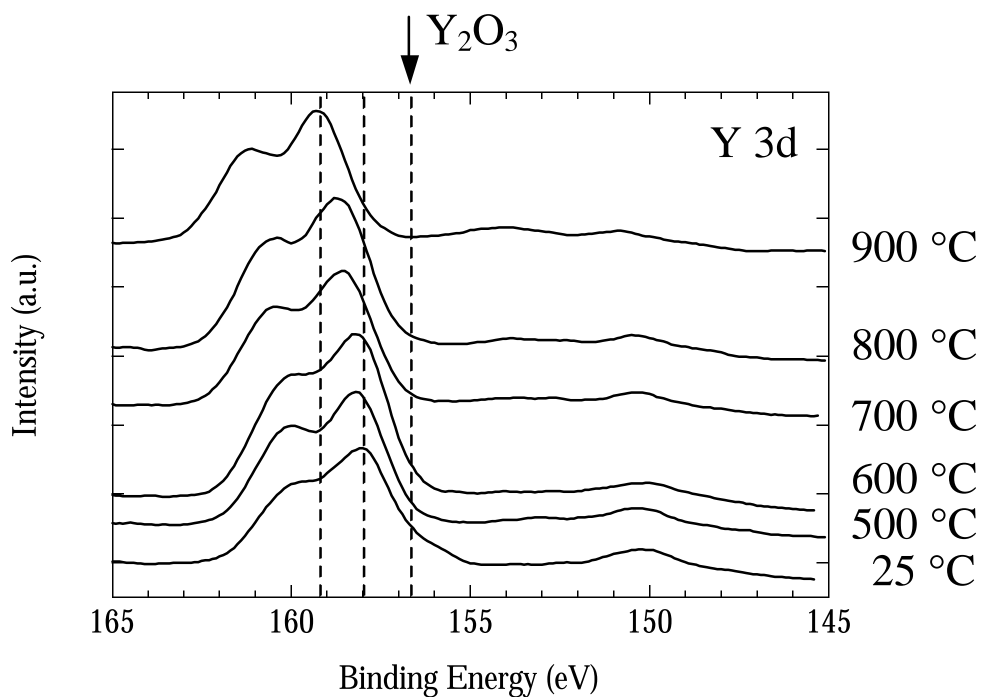

Figure 6.1a Y 3d region of the photoelectron spectra for oxidation at 25 to 900 °C of 25 Å yttrium films on silicon. The Y 3d peak shifts ~1.3 eV for oxidation at 25 to 900 °C.

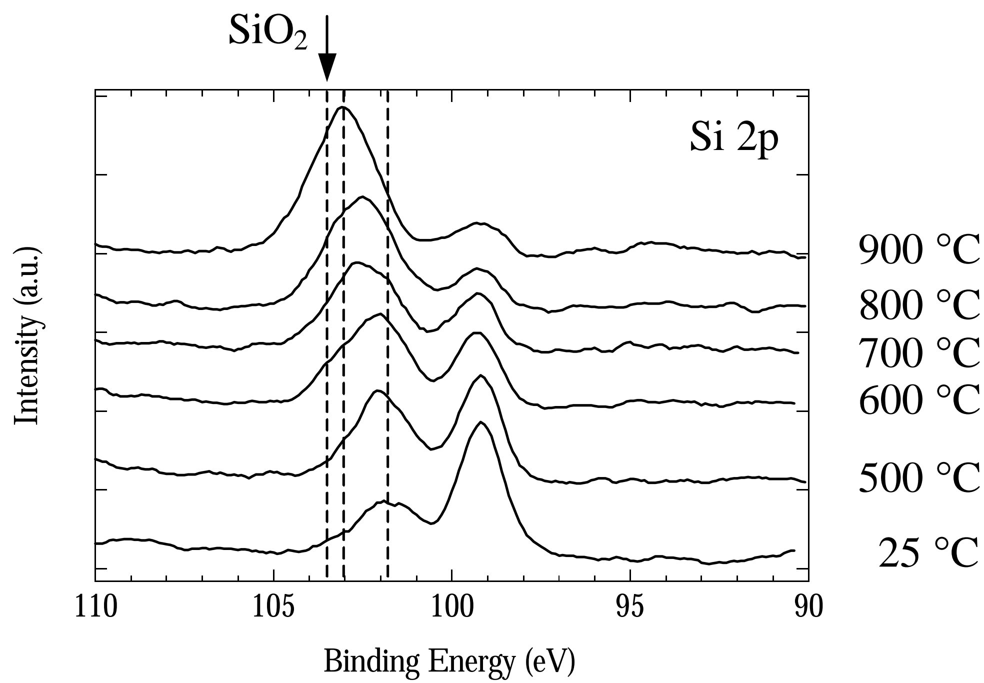

Figure 6.1b Si 2p region of the photoelectron spectra for oxidation at 25 to 900 °C of 25 Å yttrium films on silicon. The Si 2p peak shifts ~1.3 eV for oxidation at 25 to 900 °C.

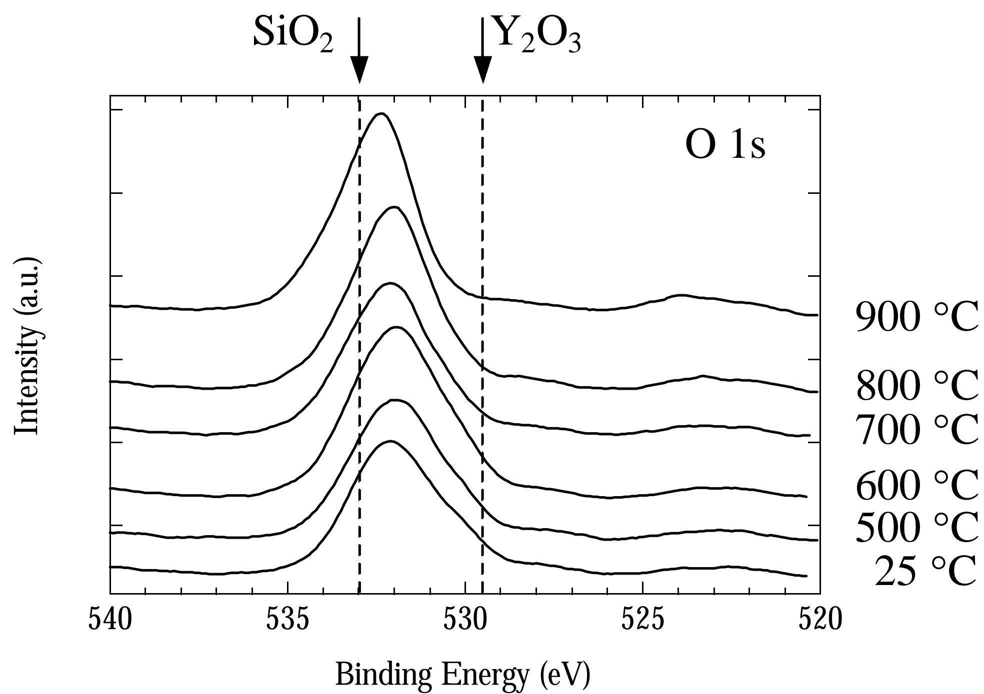

Figure 6.1c O 1s region of the photoelectron spectra for oxidation at 25 to 900 °C of 25 Å yttrium films on silicon. The O 1s peaks are consistent with Y-O-Si.

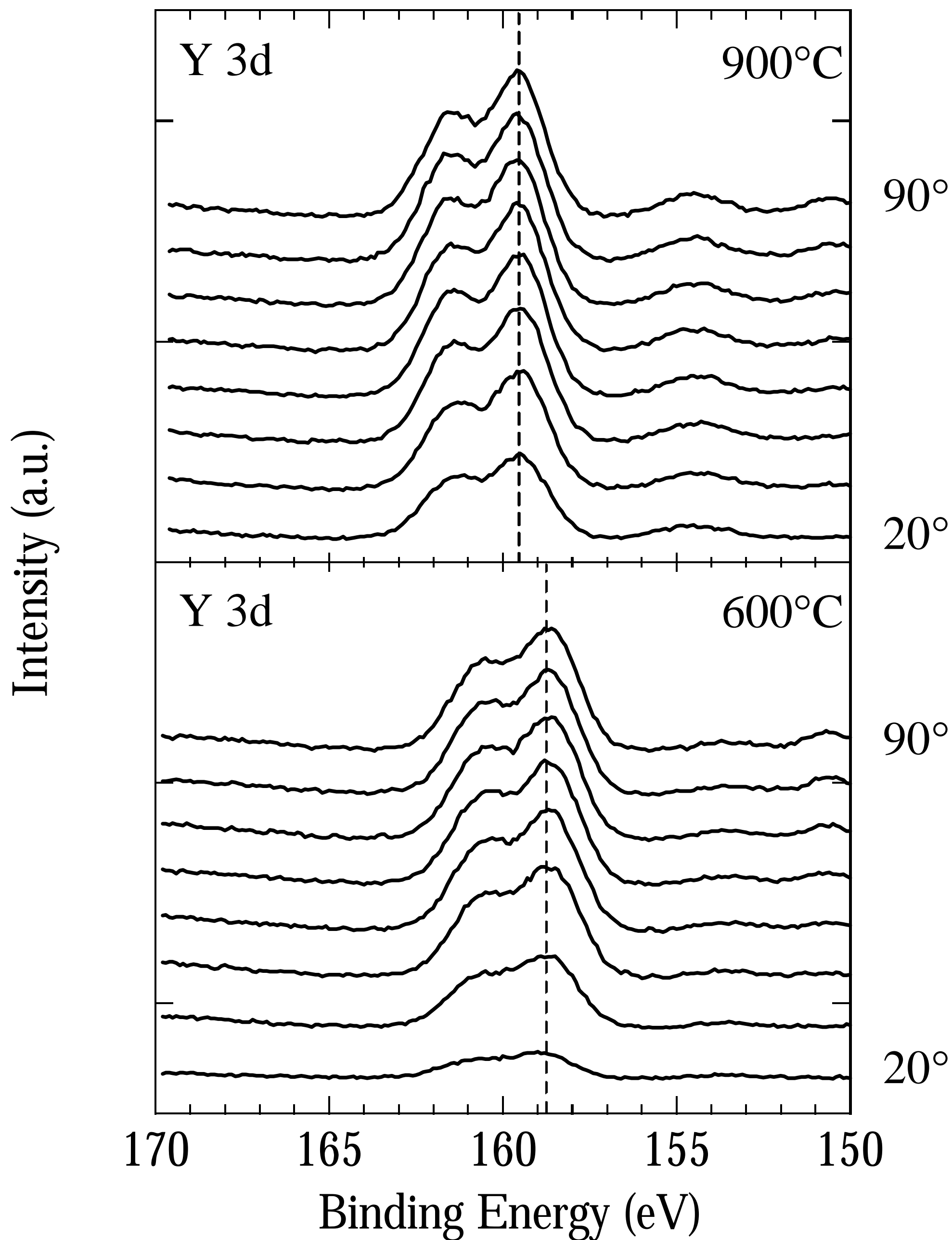

Figure 6.2 Y 3d angle resolved XPS spectra for take-off angles from 20° to 90° for 25 Å yttrium films on silicon oxidized at 600 and 900 °C. The Y 3d peak positions remain fixed as the depth probed increases.

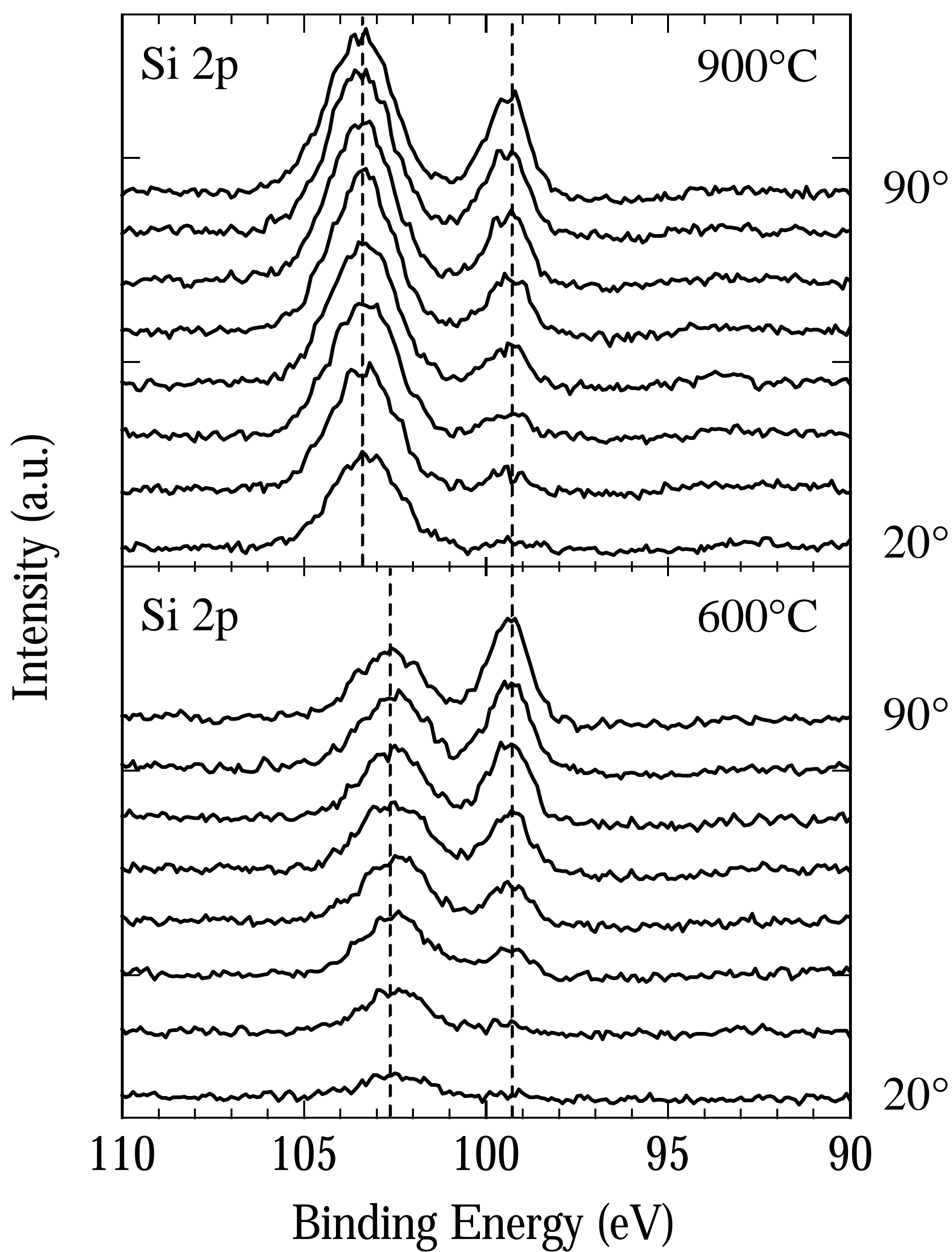

Figure 6.3 Si 2p angle resolved XPS spectra for take-off angles from 20° to 90° for 25 Å yttrium films on silicon oxidized at 600 and 900 °C. The spectra show no indication of buried SiO_2 layer at the Y-O-Si/Si interface.

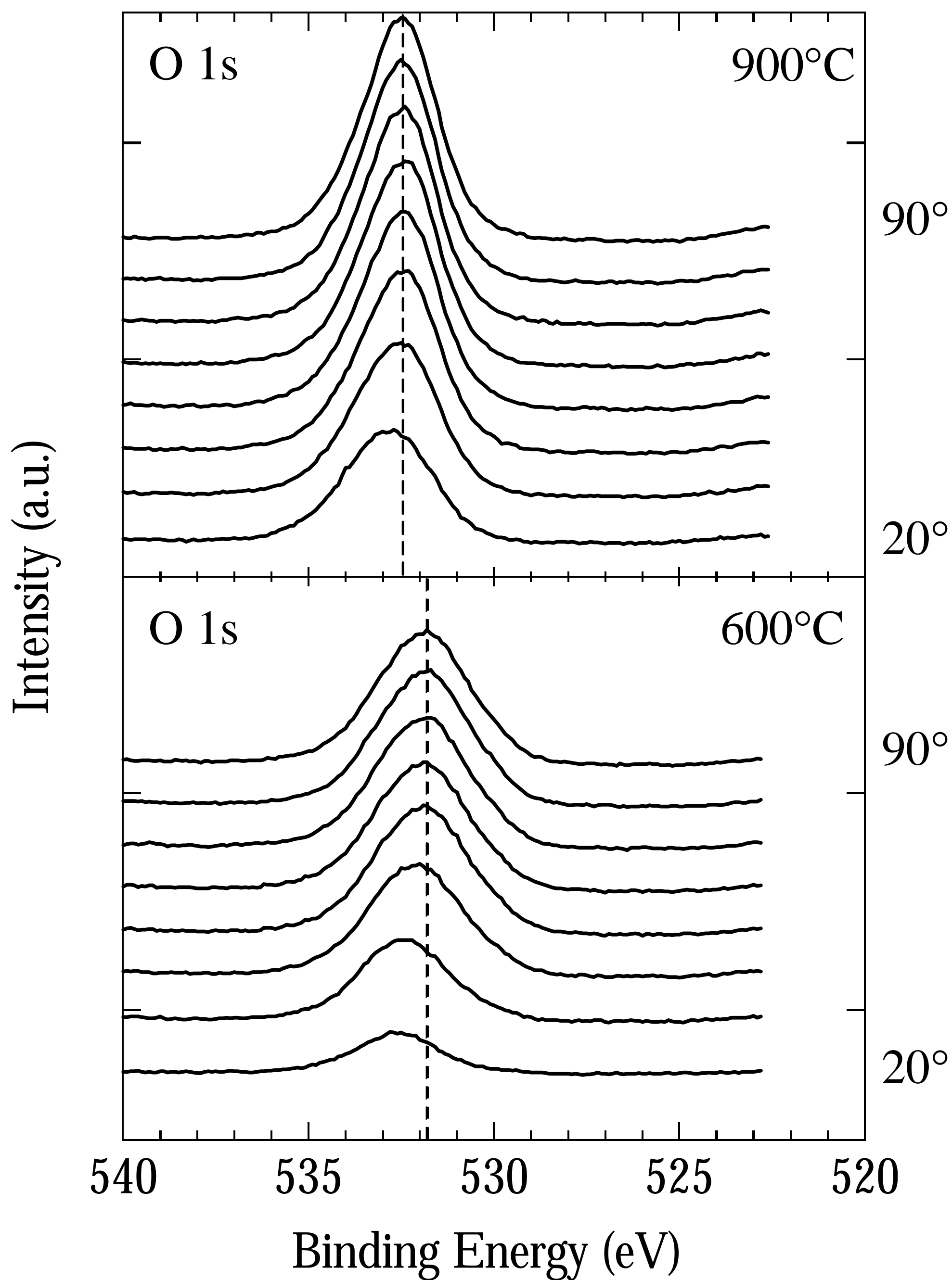

Figure 6.4 O 1s angle resolved XPS spectra for take-off angles from 20° to 90° for 25 Å yttrium films on silicon oxidized at 600 and 900 °C. The shifting of the O 1s peaks for take-off angles <40° is attributed to adsorbed water and adventitious carbon and the surface.

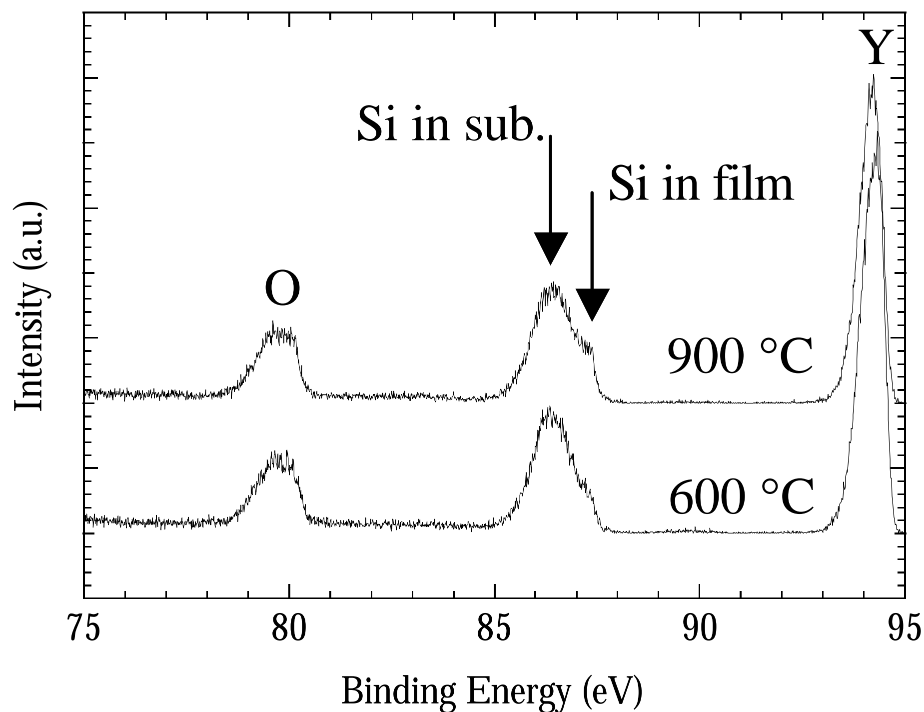

Figure 6.5 MEIS proton energy spectra for 25 Å yttrium films on silicon oxidized at 600 and 900 °C. The shoulder at 89 keV representing silicon in the Y-O-Si film is clearly larger for the sample oxidized at 900 °C.

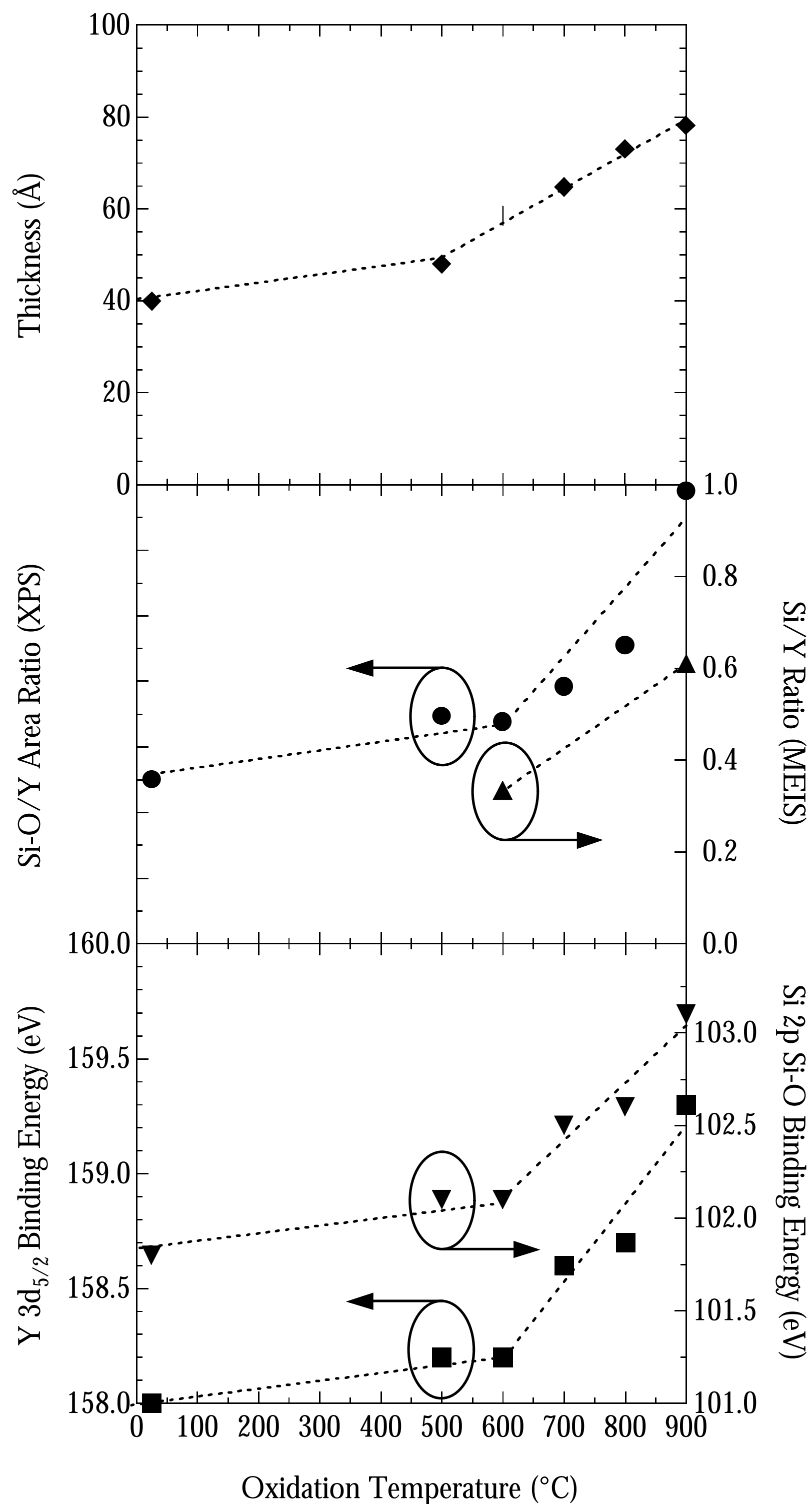

Figure 6.6 Compilation of the results presented in Figs. 6.1 and 6.5. The Y $3d_{5/2}$ ( ) and Si 2p ( ) binding energies, Si-O/Y area ratio ( ), Si/Y ratio ( ) and thickness (♦) are plotted versus the oxidation temperature. Similar temperature dependence is observed for each of the parameters.

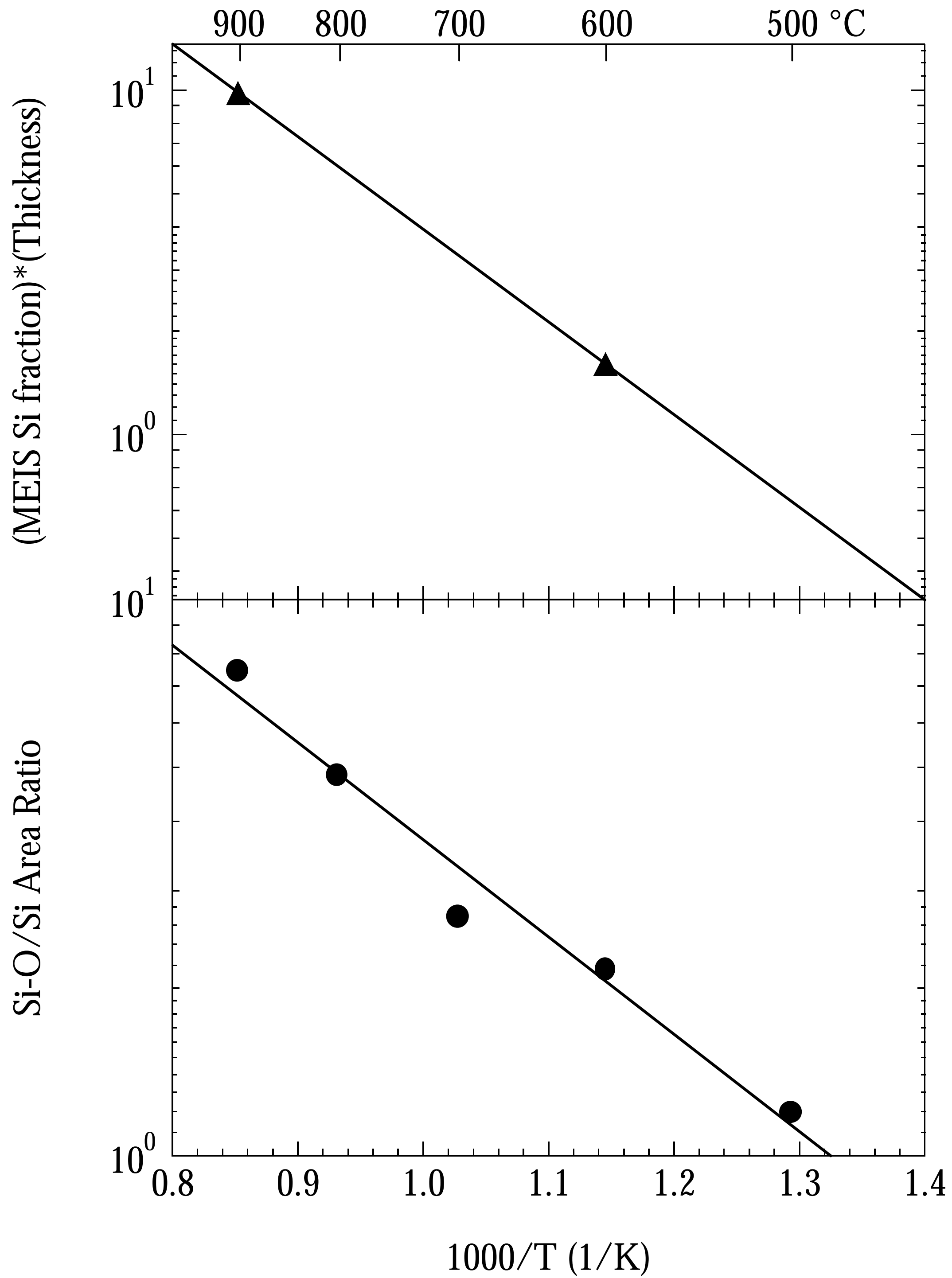

Figure 6.7 Arrhenius plot of the Si-O/Si area ratio ( ) and MEIS silicon fraction times thickness ( ) versus inverse temperature for oxidation from 500 to 900 °C. The activation energy for the consumption of silicon is 0.3-0.5 eV.

Chapter 7 is a draft of a manuscript to be submitted to the

Journal of Vacuum Science and Technology

CHEMICAL BONDING AND STRUCTURAL CHARACTERIZATION OF YTTRIUM SILICATE FILMS FORMED BY REMOTE PLASMA OXIDATION OF YTTRIUM ON SILICON

J. J. Chambers and G. N. Parsons

ABSTRACT

Silicate films have attracted attention as possible replacements for silicon dioxide in deep sub-micron field-effect-transistors. In this article, we described yttrium silicate dielectric films formed by remote N_2O plasma oxidation of sputtered yttrium. The incorporation of silicon into the Y-O-Si film is described by the formation of a silicide during the temperature ramp prior to oxidation. X-ray photoelectron spectroscopy, transmission electron microscopy, reflection high-energy electron diffraction, atomic force microscopy and current-voltage testing are used to characterize the Y-O-Si films. The chemical shifts of the Y 3d, Si 2p and O 1s peaks are consistent with donation of electron density from yttrium to the Si-O bonds and confirm the presence of Y-O-Si bonding structure. Remote plasma oxidation at 300 °C results in well-defined yttrium oxidation state, whereas, remote plasma oxidation at 100 °C results in mixed yttrium oxidation states. Annealing at 900 °C causes an increase in the consumption of silicon compared to oxidation at 100 or 300 °C. The Y-O-Si

films reported here are amorphous and smooth, as determined by RHEED and AFM, respectively. TEM analysis of films remote plasma oxidized at 100 °C and then annealed at 900 °C indicate the formation of a bi-layer structure and oxidation of the silicon substrate, respectively. J-V electrical analysis indicates leakage current of $8x10^{-7}$ A/cm^2 for a 40 Å Y-O-Si formed by remote N_2O plasma oxidation at 300 °C of 30 Å of yttrium on silicon. These results indicate the ability to form silicate films by low-temperature remote plasma oxidation of sputtered metal.

CHAPTER 7

CHEMICAL BONDING AND STRUCTURAL CHARACTERIZATION OF YTTRIUM SILICATE FILMS FORMED BY REMOTE PLASMA OXIDATION OF YTTRIUM ON SILICON

7.1 INTRODUCTION

Improvements in the speed and integration of metal-oxide-semiconductor-field-effect-transistors (MOSFETs) have traditionally been realized by reducing the gate length. A reduction in the gate length also requires an accompanying increase in the channel capacitance to achieve sufficient transconductance. The increase in channel capacitance has usually been accomplished by decreasing the thickness of the silicon dioxide gate dielectric. Recently, the thinning of the gate dielectric has caused degraded device performance. Specifically, boron penetration from the polysilicon gate electrode through the silicon dioxide gate dielectric into the channel region causes both an increase in the equivalent oxide thickness (EOT) and threshold voltage shifting. However, nitridation of the silicon dioxide has been demonstrated to reduce boron penetration, reduce electrically active traps and defects at the SiO_2/Si interface and improve device reliability.[1,2] Many techniques have been explored to achieve the desired nitrogen profiles in the thin silicon dioxide, including furnace annealing, rapid thermal annealing and remote plasma nitridation.[2-4] However, these are only near term solutions, since the thickness of the gate dielectric is rapidly approaches the proposed physical limit of 20-15 Å.[5] The physical limit is derived from analysis of the quantum mechanical tunneling of electrons, which for a change of dielectric thickness of ~35

to ~15 Å increases ~13 orders of magnitude from 10^{-12} A/cm^2 to 10 A/cm^2.[5] This drastic increase in leakage current raises severe reliability and power consumption concerns for device operation in this regime.

Recent interest has developed in the area of high dielectric constant (high-k) materials as a possible solution to the direct tunneling problem. Materials with a higher dielectric constant than silicon can be made physically thicker than silicon dioxide and still obtain the desired electrical thickness, since capacitance scales as the dielectric constant over the thickness. Transition metal oxides and metal silicate are currently being investigated as potential high-k replacements to silicon dioxide in MOSFET technology.[6-8] Physical vapor deposition (PVD) and chemical vapor deposition (CVD) are the main methods being investigated to form high-k dielectrics. In this article, we present metal is sputtering onto silicon followed by remote plasma oxidation as a unique low-temperature route to form dielectric films.

In this work, we describe Y-O-Si films formed by sputtering yttrium metal onto silicon followed by remote N_2O plasma oxidation. The physical properties of Y-O-Si films are characterized using X-ray photoelectron spectroscopy, transmission electron microscopy, reflection high-energy diffraction and atomic force microscopy, and the electrical properties are analyzed using current-voltage testing. Low-temperature (100-300 °C) remote plasma oxidation results in reaction between the yttrium and silicon with oxidation to form Y-O-Si films. The photoelectron spectra of the films described here are compared to reference spectra for Y_2O_3 and SiO_2 to ascertain the Y-O-Si bonding structure. The ability to form silicate films with an amorphous microstructure using the process described here provides an interesting means for the formation of high-k dielectrics.

7.2 EXPERIMENTAL

Samples were n-type Si(100) with a resistivity of 1-2 ·cm cut from commercial 100 mm wafers into 25x25 mm substrates. The substrates were cleaned by dipping for 5 minutes in JTB 100 (a tetramethylammonium hydroxide based alkaline solution with a carboxylate buffer), rinsing in deionized water (DI), etching in buffered hydrogen fluoride (HF) for 1 minute with no final rinse and immediately loading into vacuum. Yttrium sputtering and remote plasma oxidation were performed in the plasma reactor described elsewhere.[9] The plasma can be configured to run in a direct plasma mode to sputter yttrium and in a remote plasma mode to perform oxidation. Yttrium (99.1%, Ta is the major impurity) films (~30 Å) were sputtered in 4.3 mTorr argon, at room temperature and a radio frequency (rf) power of 380 W. The plasma ignited in the tube and the chamber under these conditions, which resulted in a sputter rate of ~15 Å/minute. The substrates were heated in vacuum better than 5×10^{-6} Torr to either 100 or 300 °C prior to remote plasma oxidation. The remote plasma oxidation was performed with 5 mTorr N_2O and a rf power of 200 W. The plasma was confined to the tube under these conditions and the sample was positioned ~15 cm downstream of the plasma glow. The sputter target was isolated from the chamber during the plasma oxidation step. Post-oxidation annealing was performed in a standard 100 mm tube furnace for 4 hours at 900 °C in 2.5 slpm N_2 at 1 atm. The films described in this article all contain substantial amount of silicon, and we generally refer to all the films as yttrium silicate or simply as Y-O-Si.

The films were characterized using X-ray photoelectron spectroscopy (XPS), cross-sectional transmission electron microscopy (TEM), reflection high-energy electron diffraction (RHEED), atomic force microscopy (AFM) and current-voltage (J-V) electrical

testing. The XPS instrument (Physical Electronics, PHI 3057) is equipped with a dual anode (Al/Mg) x-ray source (Mg Kα $h\nu$ = 1253.6 eV used for this study), 15 kV x-ray generator, spherical capacitor analyzer, Omni Focus III small area lens, 16-element multichannel detector, and amplifier/discriminator. The base pressure of the analysis chamber is $7x10^{-11}$ Torr. The binding energy of the core levels was corrected by setting the silicon substrate Si 2p peak to 99.3 eV. The cross-sectional TEM samples were prepared using a conventional "sandwich" technique. The images were obtained using a Topcon 002B High Resolution TEM with point-to-point resolution of 0.18 nm. Surface morphology was imaged using a Digital Instruments Dimension 3000 in an intermittent-contact mode. The cantilever probes were c-Si with nominal tip radius of 5-10 nm. Metal-insulator-semiconductor capacitors were formed by evaporating 2000 Å of Al onto blanket Y-O-Si films through a contact mask with holes ranging from $7x10^{-2}$ to $8x10^{-3}$ cm^2 in area. Contact was made to the backside of each sample with 2000 Å of evaporated Al. Current-voltage (J-V) measurements were taken using a Kiethly 236 source measure unit and scanned at least 2 V past flat band to ensure carrier generation would not limit the current.

7.3 RESULTS

Figure 7.1 presents the XPS characterization of three films: (1) yttrium (~30 Å) on silicon exposed to a remote N_2O plasma for 60 minutes at a substrate temperatures of 100 °C, (2) yttrium (~30 Å) on silicon exposed to a remote N_2O plasma for 60 minutes at a substrate temperature of 300 °C, and, (3) yttrium (~30 Å) on silicon exposed to a remote N_2O plasma for 60 minutes at a substrate temperature of 100 °C, then subjected to a post-oxidation anneal for 4 hours in 1 atm. N_2. A typical Y 3d spectrum consists of a doublet resulting from the spin-orbit splitting of the Y $3d_{3/2}$ and Y $3d_{5/2}$ peaks (more intense

component), which for a reference yttrium metal are at 158.0 and 156.0 eV, respectively.[10] Yttrium metal and yttrium silicide (Y $3d_{5/2}$ at 155.8 eV)[11] are not observed in the Y 3d spectra (Fig. 7.1a) of films (1)-(3). The Y 3d peak maxima for films (1)-(3) are measured at 158.8, 158.3 and 159.6 eV, respectively, and reside at higher binding energy than expected for Y_2O_3 (Y $3d_{5/2}$ at 156.8 eV)[10]. The Y 3d binding energies of the films oxidized at 100 and 300 °C are measured at 158.8 and 158.3 eV, respectively, however the Y 3d spectrum for the film oxidized at 100 °C exhibits blurring of the spin-orbit splitting indicating multiple yttrium oxidation states within film (1). The Y 3d spectrum for the annealed film is measured at higher binding energy (0.8 eV) than the 100 °C plasma oxidized film (1) indicating increased silicon incorporation after annealing at 900 °C. The small peaks from 150-154 eV result from the combination of the Y 3d satellite and Si 2s peaks. The Si 2p spectra (Fig. 7.1b) exhibit a peak at 99.3 eV assigned to the substrate and a higher binding energy peak assigned to silicon bound to oxygen. The Si 2p Si-O peak (102.5 eV) for the film plasma oxidized at 300 °C is ~2.5 times the area of the Si-O peak (102.7 eV) for the film plasma oxidized at 100 °C. The Si-O peaks for both of the plasma-oxidized films are consistent with silicon in metal silicates (102-103 eV).[10] The Si 2p Si-O peak for the post-oxidation annealed film is measured at 103.6 eV and has a larger intensity than the plasma-oxidized films consistent with the formation of a buried SiO_2 film. The anneal was performed in N_2, but the sample has continued to oxidize due to oxygen contamination in the furnace. The Si 2p spectra do not indicate the presence of yttrium silicide at 98.7 eV. The film thickness calculated from the attenuation of the silicon substrate peak for films (1), (2) and (3) is 52, 40 and 110 Å. The O 1s peak (Fig. 7.1c) maxima for films (1)-(3) are consistent with oxygen in metal silicates and measured at ~532 eV, which is intermediate to

O 1s in SiO_2 (533 eV) and Y_2O_3 (529.5 eV). The O 1s peaks are broad with the full-width-half-maximum (FWHM) for film (1), (2) and (3) equal to 3.4, 3.1 and 2.9 eV, respectively, which is broader than expected for an elemental oxide (measured O 1s FWHM for SiO_2 is 0.7 eV). The O 1s peaks for films (1)-(3) are broad due to a combination of oxygen bound to silicon and oxygen bound to yttrium. The O 1s features for the plasma oxidized films exhibit asymmetry on the low binding energy side of the peak near ~530 eV consistent with O-Y-O bonding in Y_2O_3 (O 1s at 529.5 eV). The O 1s feature for the annealed film exhibits asymmetry on the high binding energy near ~533 eV consistent with O-Si-O bonding (533 eV) and the presence of a buried SiO_2 film.

Figure 7.2 present cross-sectional TEM images for a 30 Å yttrium film on silicon remote N_2O plasma oxidized for 60 minutes at a substrate temperature of 100 °C (film "1") and a film prepared under the same conditions as film (1) with a post-oxidation anneal for 4 hours in 1 atm. N_2 (film "3"). The 100 °C plasma oxidized film exhibits a bi-layer structure with a thickness of 45 Å for each layer. The annealed film exhibits a faint demarcation between two layers with a thickness 57 and 76 Å for the upper layer and the layer in contact with the substrate, respectively. The images were taken a resolution insufficient to observe lattice fringes in the silicon substrate and to determine the microstructure of films (1) and (3). RHEED images of films (1)-(3) were obtained to determine their microstructure. The results of the RHEED characterization are presented in Fig. 7.3. The images exhibit the typical cloud pattern of an amorphous material containing no long-range order.

The surface morphology of films (1)-(3) was analyzed using AFM (Fig. 7.4). The AFM images are presented in a three-dimensional view with all three axes on the same scale. The image of the 100 °C plasma-oxidized film (film "1") exhibits an island-like structure

with a root-mean-square (RMS) roughness of 8.9 Å. The image of the 300 °C displays a smaller grain structure and a smoother surface (RMS roughness of 1.4 Å) than film (1). The image of the annealed film (film "3") faintly exhibits similar structure as film (1), but with a smoother surface (RMS roughness of 1.7 Å). As a reference, the measured RMS roughness of c-Si(100) ranges from 0.5 to 1 Å.

Figure 7.5 displays AFM images for 30 Å yttrium films on silicon remote N_2O plasma oxidized at 100 °C for zero (a), 5 (b), 10 (c) and 20 minutes (d). The film without oxidation exhibits the smoothest surface (RMS roughness of 1.15 Å). As the yttrium film is exposed to a remote N_2O plasma for increasing oxidation times, the surface roughness increases, and the RMS roughness is 2.28, 2.44, 5.73 and 8.9 Å for 5, 10, 20 and 60 (from Fig. 7.4) minute oxidation, respectively. Figure 7.6 presents the observed trend for 100 °C plasma oxidation for zero, 5, 10, 20 and 60 minutes (circles), 300 °C oxidation for 60 minutes (open square), and 100 °C plasma oxidation with 4 hour 900 °C anneal (up triangle). Figure 7.6 illustrates the trend of increasing surface roughness with increasing oxidation time, as well as, the smoother films obtained by oxidizing at 300 °C or annealing at 900 °C.

The J-V analysis of a 30 Å yttrium film on silicon exposed to a remote N_2O plasma for 60 minutes at a substrate temperature of 300 °C is presented in Fig. 7.7. The measured leakage at a bias of 1 V ranged from 8×10^{-7} to 1×10^{-4} A/cm^2. A "soft" breakdown is exhibited at a bias of ~1.7 V for one of the capacitors.

7.4 DISCUSSION

Yttrium and silicon react and oxidized to form a Y-O-Si film, when yttrium on silicon is exposed to a remote N_2O plasma at 100 or 300 °C. When a remote plasma oxidized film is subjected to high temperature (900 °C) annealing conditions, the Y-O-Si film incorporates additional silicon and the silicon substrate oxidizes to form SiO_2. After the yttrium films on silicon are either exposed to plasma oxidizing or annealing conditions, the Y 3d (Fig. 7.1a) spectra for films (1)-(3) do not indicate the presence of yttrium metal or Y_2O_3, and the Y 3d and Si 2p (Fig. 7.1b) spectra for do not exhibit peaks for yttrium silicide. Since yttrium metal and yttrium silicide are not observed, the yttrium and silicon in the films are completely oxidized. The chemical shifts of the Y 3d, Si 2p and O 1s (Figs. 7.1a, 7.1b and 7.1c, respectively) peaks for films (1)-(3) are consistent with donation of electron density from yttrium to the Si-O bond in the Y-O-Si in accordance with the relative electronegativities of yttrium, silicon and oxygen (1.2, 1.8, 3.5 on the Pauling scale). Remote plasma oxidation of yttrium on silicon at 100 °C results in a film with multiple oxidation states, as observed by the blurring of the Y 3d spin-orbit splitting, consistent with a silicon-poor Y-O-Si on a silicon-rich Y-O-Si film. Remote plasma oxidation at 300 °C results in a Y-O-Si film with a well-defined oxidation state consistent with a Y-O-Si film containing a constant Y/Si fraction throughout the film. The Y 3d chemical shift of the annealed film to higher binding energy compared to either of the plasma-oxidized films is consistent with the incorporation of additional silicon, as illustrated by the large Si-O peak in the Si 2p spectrum (Fig. 7.1b). The Si-O peak for plasma oxidation at 300 °C is ~1.5 times larger than observed for plasma oxidation at 100 °C consistent with an increased silicon fraction at higher temperature. The shoulder (~530 eV) on the O 1s (Fig. 7.1c) peak for plasma oxidation at

100 °C is consistent with a silicon-poor Y-O-Si film. The O 1s peak for oxidation at 300 °C exhibits a smaller shoulder compared to oxidation at 100 °C consistent with the increased silicon incorporation at higher temperature leading to an increase in Y-O-Si bonding. The O 1s peak for the annealed film is consistent with a Y-O-Si film on SiO_2, in accordance with the Si-O peak position (103.6 eV) observed in the Si 2p spectrum.

When a reactive metal, such as yttrium, that forms stable silicides and a stable oxide is deposited onto silicon and then oxidized, the potential exists for both reaction with the silicon substrate and reaction with oxygen. The chance for reaction with the silicon substrate is increased here, since the yttrium film on silicon is heated in vacuum before exposure to oxygen. For plasma oxidation at 300 °C, the 30 Å yttrium film on silicon is heated from room temperature to 300 °C in vacuum and held at 300 °C for 10 minutes prior to N_2O plasma exposure. Previous researchers have demonstrated yttrium silicide formation by a similar process.[12] Therefore, the yttrium film on silicon likely forms yttrium silicide before being exposed to the remote N_2O plasma at 300 °C. We have previously demonstrated the formation of Y-O-Si by the thermal oxidation of yttrium silicide films. The Y 3d chemical shift of the 300 °C oxidized film to 158.3 eV is consistent with the peak position observed for Y-O-Si films formed by thermal oxidation of yttrium silicide at 600 °C.[9] Remote plasma oxidation of yttrium on silicon at 100 °C also indicate the incorporation of silicon, but not to the extent observed for oxidation at 300 °C. We have previously demonstrated that the formation of Y-O-Si films by the oxidation of yttrium silicide results in films with more silicon than films formed by oxidation of yttrium on silicon.[9] It is possible that at 100 °C the silicide formation is not complete when the plasma oxidation is started resulting in a film with a decreased silicon fraction and mixed yttrium

oxidation states. When a Y-O-Si film formed at 100 °C is annealed at 900 °C, additional silicon is incorporated into the film and the substrate oxidizes to form a buried SiO_2 layer.

The TEM images presented in Fig. 7.2 are consistent with the XPS results of Fig. 7.1. The image for the yttrium on silicon plasma oxidized at 100 °C exhibits a bi-layer structure, which can be attributed to either Y_2O_3/Y-O-Si or a silicon-poor Y-O-Si on a silicon-rich Y-O-Si. The absence of Y_2O_3 in the Y 3d spectrum (Fig. 7.1a) for film (1) increases the likelihood of a silicon-poor Y-O-Si on a silicon-rich Y-O-Si structure. Additionally, the blurring of the spin-orbit splitting of the Y 3d spectrum of film (1) is in the expected range for two silicates with different compositions.[13] The TEM image for the annealed film (film "3") indicates an increase in overlayer thickness from 90 to 133 Å and the absence of a clear bi-layer structure as observed in the TEM image for film (1). The shift to higher binding energy (~0.7 eV) of the annealed film compared to films (1) and (2) indicates a silicon-rich Y-O-Si film, but the Si 2p spectrum (Fig. 7.1b) for film (3) also indicates the presence of a buried SiO_2 layer. From these results, it is difficult to ascertain the structure of film (3). It is possible that the Y-O-Si film has incorporated silicon to form a silicon-rich Y-O-Si film and then the substrate has oxidized. Since there is no clear contrast between the top and bottom of the film, it is also possible that the yttrium has re-distributed throughout the entire layer.

Although the microstructure of films (1) and (2) was not evident from the TEM images, the RHEED images indicate the amorphous nature of films (1)-(3). Pure metal oxide films tend to crystallize at relatively moderate temperatures (crystallites begin forming in TiO_2 at ~200 °C).[7] Therefore, it is not unexpected to observe crystallization in Y_2O_3 in the ~200 °C temperature range. Crystallization in high-k materials is generally considered a

disadvantage due to proposed problems associated with possible high conductivity pathways through grain boundaries.[7] The films reported here do not exhibit crystallization up to anneal temperatures of 900 °C. The high temperature stability of the microstructure is attributed to the formation of Y-O-Si bonds, which enables the formation of glassy phases.

The plasma oxidation of yttrium on silicon results in films with relatively smooth surface structure. The deposition of ~30 Å of yttrium on silicon results in complete coverage of the silicon surface with a smooth (RMS roughness of 1.15 Å). Exposure of the yttrium film to a remote N_2O plasma increases the roughness of the surface as the oxidation time is increased, as illustrated in Fig. 7.6. The highest RMS roughness of 8.9 Å reported here for oxidation at 100 °C for 60 minutes still only represents roughness on the order of 3-4 monolayers. Prolonged exposure to the remote plasma increases the surface roughness possibly by causing damage with the low-energy bombardment of ions. Performing the oxidation at higher temperature (300 °C) or high temperature (~900 °C) annealing of plasma oxidized films results in extremely smooth films with RMS roughness on the order observed for c-Si (0.5-1.0 Å).

The lowest leakage measured for a film formed by remote N_2O plasma oxidation of a 30 Å yttrium film on silicon (film "2") is 8×10^{-7} A/cm^2. The physical thickness of this film measured using the attenuation of the Si 2p substrate peak was 40 Å. The measured leakage is higher than the $\sim 1 \times 10^{-9}$ A/cm^2 expected for a silicon dioxide film of similar thickness, but lower than reported for hafnium silicate film of similar physical thickness.[8]

7.5 CONCLUSIONS

We have described the formation of Y-O-Si based dielectric films by yttrium sputter onto silicon followed by remote N_2O plasma oxidation. When yttrium on silicon at 300 °C is exposed to a remote N_2O plasma, the yttrium reacts with silicon and is then oxidized. The films formed in this manner are consistent with Y-O-Si films formed by the thermal oxidation of yttrium silicide at 600 °C. When yttrium on silicon at 100 °C is exposed to a remote N_2O plasma, the resulting Y-O-Si film contains less silicon than the film formed at 300 °C. The films formed at 100 °C are consistent with the oxidation of yttrium on silicon, which results in less silicon incorporation than the oxidation of yttrium silicide. The Y-O-Si films reported here are amorphous and smooth, as determined by RHEED and AFM, respectively. The results presented here for Y-O-Si films formed at 300 °C demonstrate the feasibility of forming silicate films by remote plasma oxidation of sputtered metal.

7.6 ACKNOWLEDGEMENTS

The authors gratefully acknowledge support from the SRC/SEMATECH Center for Front End Processes and NSF CTS – 0072784. The authors thank A. Michel and Dr. H. H. Lamb for their assistance in obtaining the XPS results, R. Johnson and Dr. G. Lucovsky for the RHEED results, Dr. D. M. Maher for the TEM analysis and K. Bray for the AFM analysis.

7.7 REFERENCES

1. H. Hwang, W. Ting, D.-L. Kwong, and J. Lee, IEEE Electron Device Lett. **12** (1991).

2. Y. Wu, H. Niimi, H. Yang, G. Lucovsky, and R. B. Flair, J. Vac. Sci. Tecnol. B **17,** 1813 (1999).

3. H. Hwang, W. Ting, B. Maiti, D. -L. Kwong, and J. Lee, Appl. Phys. Lett. **57,** 1010 (1990).

4. D. Bouvet, P. A. Clivaz, M. Dutoit, C. Coluzza, J. Almeida, G. Margaritondo, and F. Pio, J. Appl. Phys. **79,** 7114 (1996).

5. D. A. Buchanan, IBM J. Res. Dev. **43,** 245 (1999).

6. K.-A. Son, A. Y. Mao, B. Y. Kim, F. Liu, E. D. Pylant, D. A. Hess, J. M. White, D. L. Kwong, D. A. Roberts, and R. N. Vrtis, J. Vac. Sci. Technol. A **16,** 1670 (1998).

7. A. Campbell, H.-S. Kim, D. C. Gilmer, B. He, T. Ma, and W. L. Gladfelter, IBM J. Res. Dev. **43,** 383 (1999).

8. G. D. Wilk, R. M. Wallace, and J. M. Anthony, J. Appl. Phys. **87,** 484 (2000).

9. J. J. Chambers and G. N. Parsons, to be submitted.

10. J. F. Moulder, W. F. Stickle, P. E. Sobol, and K. D. Bomben, *Handbook of X-ray Photoelectron Spectroscopy* (Perkin-Elmer Corporation, Eden Prairie, MN, 1992).

11. R. Baptist, A. Pellissier, and G. Chauvet, Solid State Commun. **68,** 555 (1988).

12. T. L. Lee and L. J. Chen, J. Appl. Phys. **73,** 8258-8266 (1993).

13. J. J. Chambers and G. N. Parsons, to be submitted.

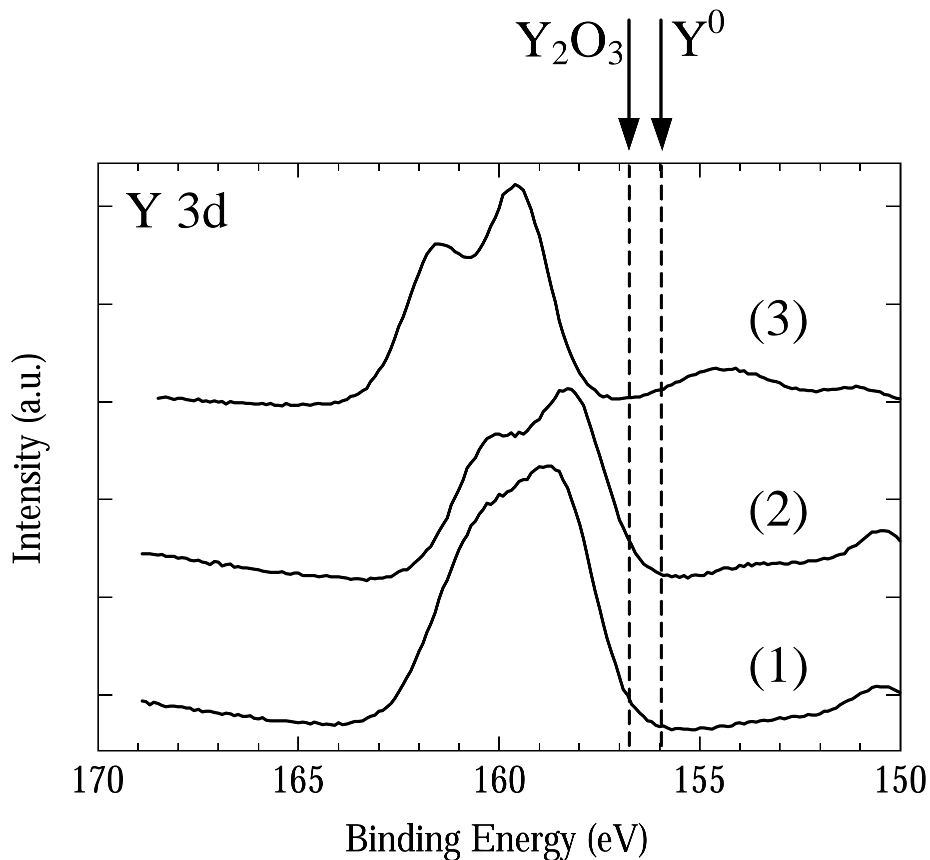

Figure 7.1a Y 3d region of the photoelectron spectra for (1) 30 Å yttrium on silicon remote N_2O plasma oxidized for 60 minutes at 100 °C, (2) 30 Å yttrium on silicon remote N_2O plasma oxidized for 60 minutes at 300 °C, and, (3) 30 Å yttrium on silicon remote N_2O plasma oxidized for 60 minutes at 100 °C followed by post-oxidation anneal for 4 hours at 900 °C in 1 atm. N_2. The Y 3d shifts are consistent with Y-O-Si.

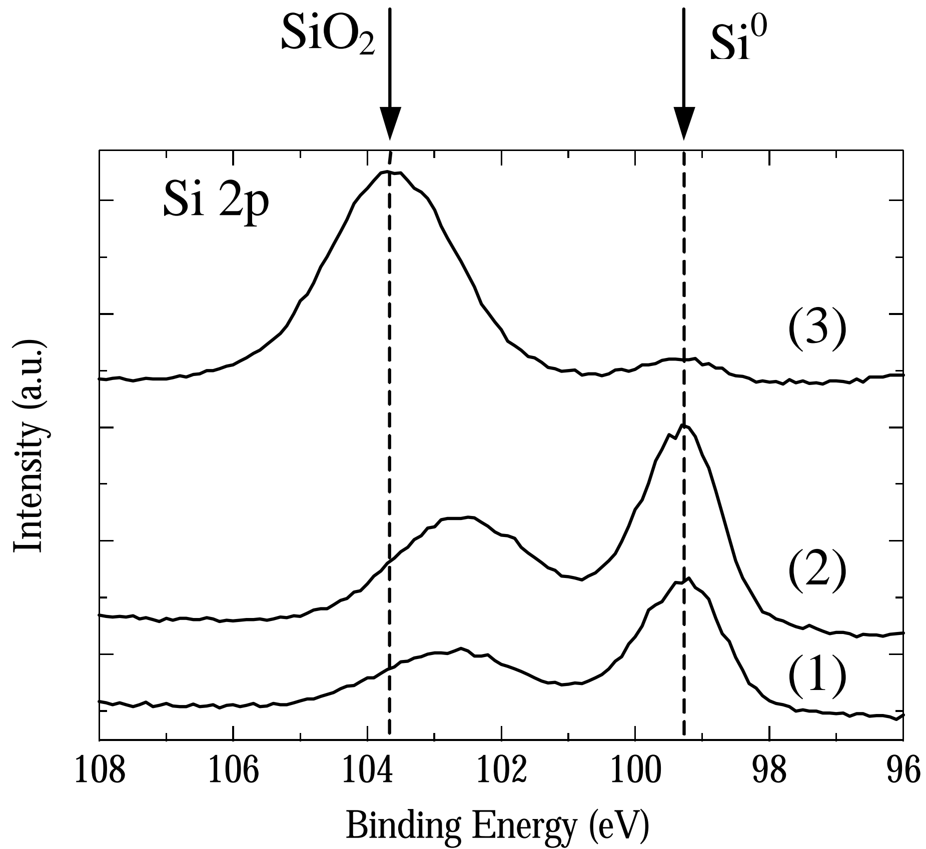

Figure 7.1b Si 2p region of the photoelectron spectra for (1) 30 Å yttrium on silicon remote N_2O plasma oxidized for 60 minutes at 100 °C, (2) 30 Å yttrium on silicon remote N_2O plasma oxidized for 60 minutes at 300 °C, and, (3) 30 Å yttrium on silicon remote N_2O plasma oxidized for 60 minutes at 100 °C followed by post-oxidation anneal for 4 hours at 900 °C in 1 atm. N_2. A buried SiO_2 layer has formed during the 900 °C anneal (3) due to oxygen contamination.

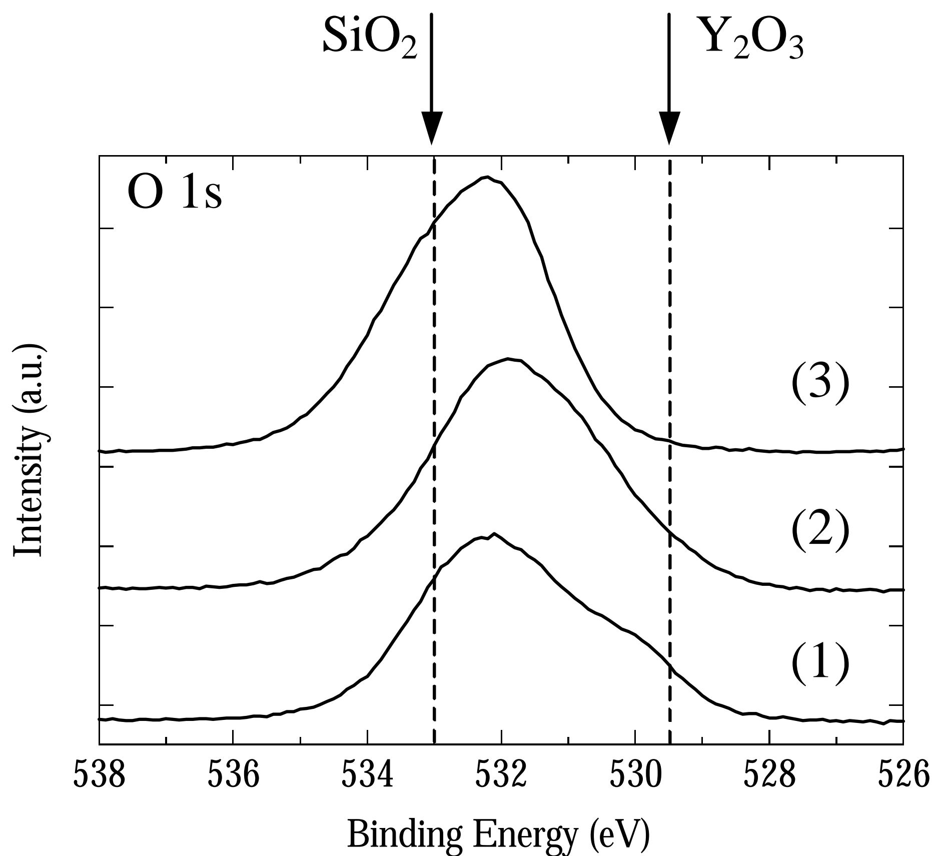

Figure 7.1c O 1s region of the photoelectron spectra for (1) 30 Å yttrium on silicon remote N_2O plasma oxidized for 60 minutes at 100 °C, (2) 30 Å yttrium on silicon remote N_2O plasma oxidized for 60 minutes at 300 °C, and, (3) 30 Å yttrium on silicon remote N_2O plasma oxidized for 60 minutes at 100 °C followed by post-oxidation anneal for 4 hours at 900 °C in 1 atm. N_2. The O 1s peaks are broad due to oxygen bound to silicon and to yttrium.

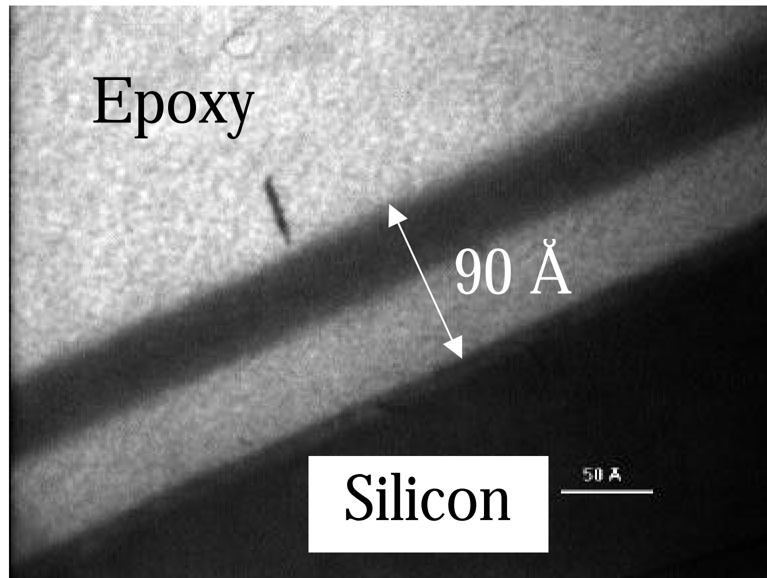

Figure 7.2.1 Cross-sectional TEM image of a 30 Å yttrium film on silicon remote N_2O plasma oxidized for 60 minutes at 100 °C.

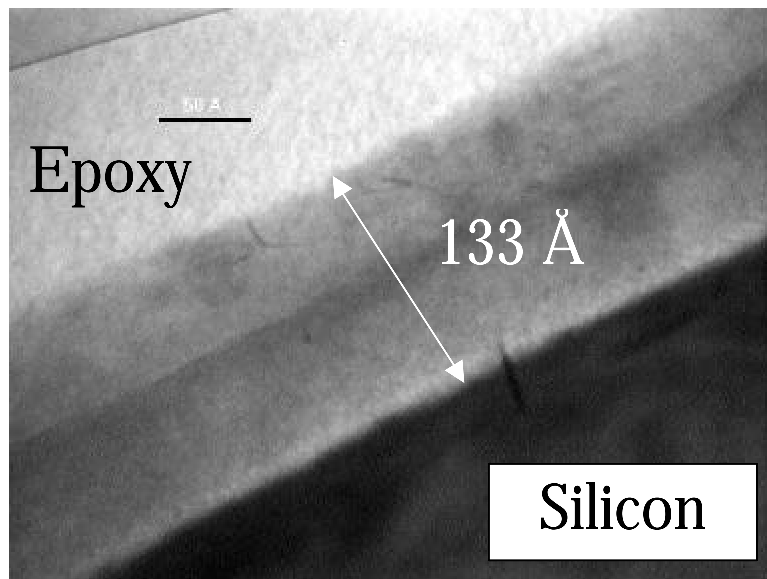

Figure 7.2.3 Cross-sectional TEM image of a 30 Å yttrium film on silicon remote N_2O plasma oxidized for 60 minutes at 100 °C followed by a post-oxidation anneal for 4 hours at 900 °C in N_2.

Figure 7.3.1 RHEED image of a 30 Å yttrium film on silicon remote N_2O plasma oxidized for 60 minutes at 100 °C.

Figure 7.3.2 RHEED image of a 30 Å yttrium film on silicon remote N_2O plasma oxidized for 60 minutes at 300 °C.

Figure 7.3.3 RHEED image of a 30 Å yttrium film on silicon remote N_2O plasma oxidized for 60 minutes at 100 °C followed by a post-oxidation anneal for 4 hours at 900 °C in N_2.

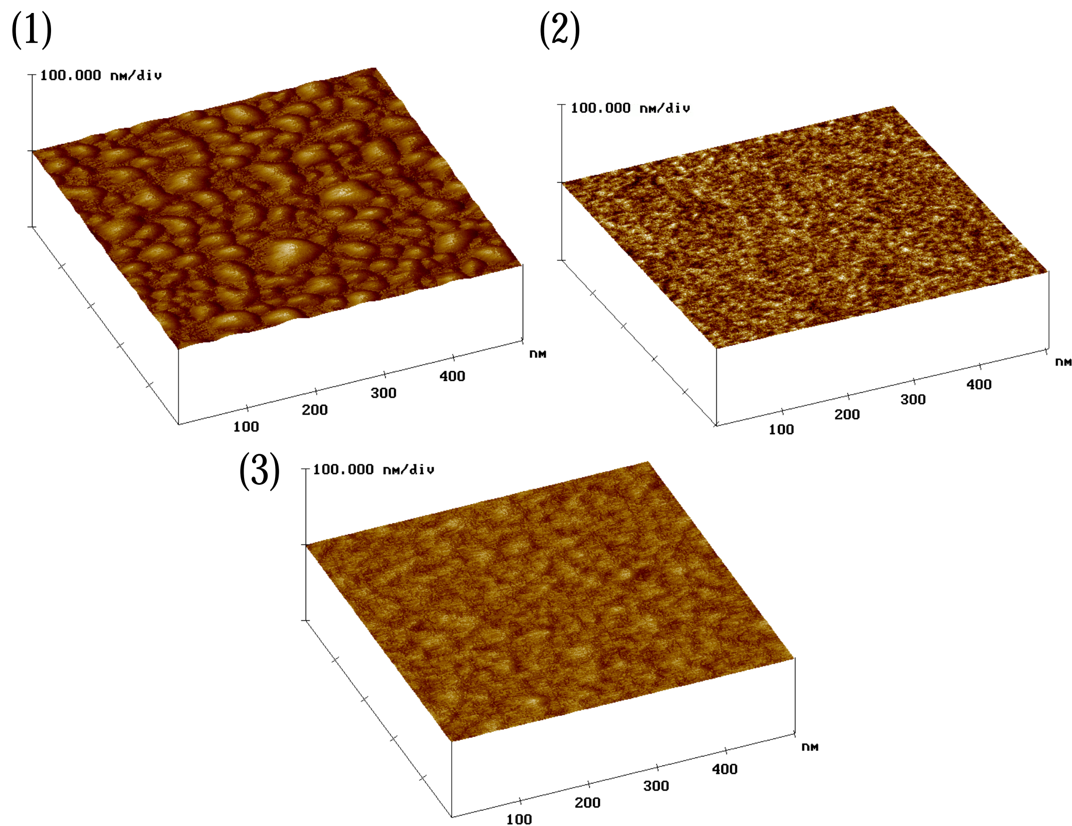

Figure 7.4 AFM images for (1) 30 Å yttrium on silicon remote N_2O plasma oxidized for 60 minutes at 100 °C (RMS = 8.9 Å), (2) 30 Å yttrium on silicon remote N_2O plasma oxidized for 60 minutes at 300 °C (RMS = 1.4 Å), and, (3) 30 Å yttrium on silicon remote N_2O plasma oxidized for 60 minutes at 100 °C followed by post-oxidation anneal for 4 hours at 900 °C in 1 atm. N_2 (RMS = 1.7 Å).

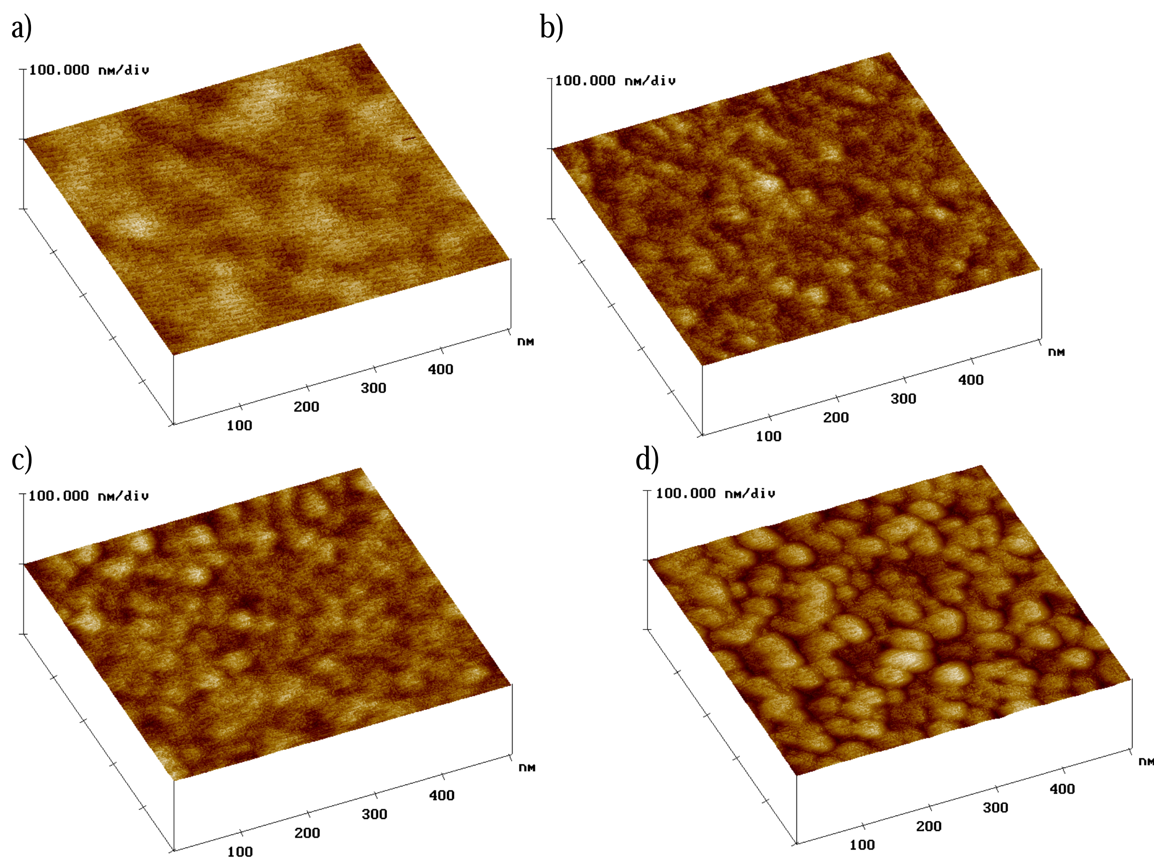

Figure 7.5 AFM images for 30 Å yttrium on silicon remote N_2O plasma oxidized for zero (a), 5 (b), 10 (c) and 20 minutes (d) at 100 °C. The RMS roughness for the films are 1.15, 2.28, 2.44 and 5.73 Å for (a)-(d), respectively.

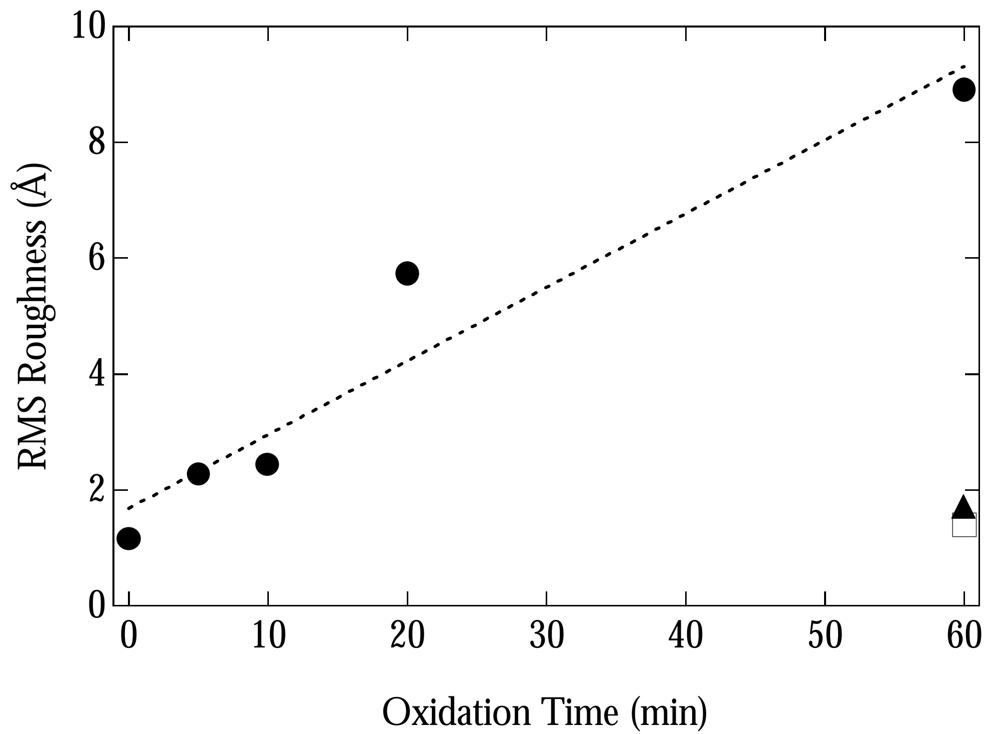

Figure 7.6 Results of AFM RMS roughness measurements for 30 Å yttrium on silicon remote N_2O plasma oxidation for zero, 5, 10, 20 and 60 minutes at 100 °C ( ), remote N_2O plasma oxidized for 60 minutes at 300 °C (□) and film post-oxidation annealed for 4 hours at 900 °C in 1 atm. N_2 ( ).

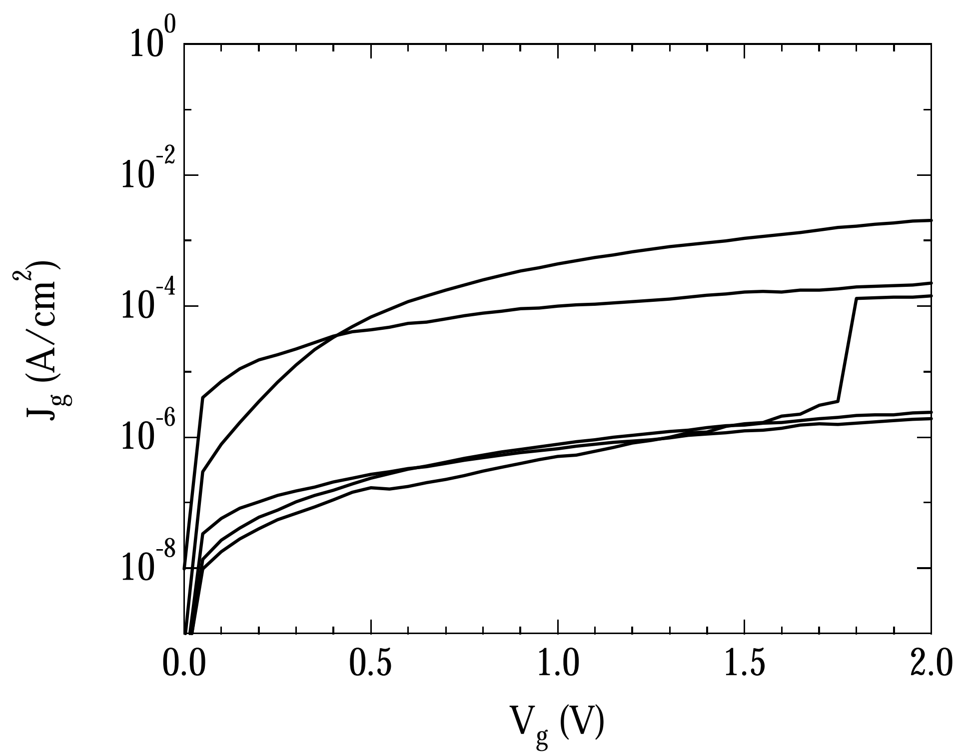

Figure 7.7 Results of J-V testing of a 30 Å yttrium on silicon remote N_2O plasma oxidation for 60 minutes at 300 °C. Lowest leakage measured at bias of 1 V was ~8x10^{-7} A/cm^2.

Chapter 8 is a reprint of a manuscript that appeared in the

Journal of Vacuum Science and Technology B **16**, 2996 (1998)

END-POINT UNIFORMITY SENSING AND ANALYSIS IN SILICON DIOXIDE PLASMA ETCHING USING *IN-SITU* MASS SPECTROMETRY

J. J. Chambers, K. Min, and G. N. Parsons

ABSTRACT

Mass spectroscopy is used to characterize the end-point uniformity of silicon dioxide etching in an electron cyclotron resonance (ECR) plasma etch process. Etch products are observed using a two stage differentially pumped mass spectrometry system attached to the ECR process chamber. Specifically, using CF_4 and D_2 etch gases, the partial pressure of CO-containing etch products decays near the endpoint, and the rate of signal decay is directly correlated with the uniformity determined from optical interferometry thickness measurements. To correlate the mass spectrometer signal with the etch rate variation across the wafer, etch uniformity is altered by changing the ECR electromagnet geometry, and by modifying the initial oxide uniformity. A COF_2 etch product material balance is developed to model the observed concentration versus time data, resulting in a quantitative correlation between change in end-point slope and uniformity. The ability to utilize a process-state

sensor, such as a mass spectrometer, for wafer-state information will result in new approaches for sensing, optimizing, and controlling integrated circuit fabrication processes.

CHAPTER 8

END-POINT UNIFORMITY SENSING AND ANALYSIS IN SILICON DIOXIDE PLASMA ETCHING USING *IN-SITU* MASS SPECTROMETRY

8.1 INTRODUCTION

Integrated circuit etch and deposition steps typically utilize monitor wafers for process characterization and control. Not every run is monitored, so yield can be reduced before an out-of-spec run is detected. Increasing wafer costs, along with demands on yield and cost-of-ownership, make monitor wafers less attractive, and promote the need for real-time process monitoring and control.

The sensors currently available for real-time process monitoring and control are either "wafer-state" or "process-state" sensors. Process-state sensors generally detect gas phase reactant and product species, whereas wafer-state sensors directly observe changes on the wafer surface. Wafer-state and process-state sensors, including reflectometers,[1] ellipsometers,[2-4] interferometers,[2, 5] optical emission spectrometers,[2, 6-11] rf sensors[12] and mass spectrometers,[7, 9, 10, 13] have been used to monitor end-point, uniformity and process faults.[14, 15] Although process-state sensors are usually easier to implement than wafer-state sensors, they are not generally expected to provide direct information of local or wafer scale effects.

Dry etch processes offer high resolution, but often suffer from etch rate non-uniformity and poor selectivity. Poor selectivity and over-etching to compensate for non-uniformity can result in unwanted removal of the underlying layer. These losses could be minimized through *in-situ* determination of etch uniformity.

Etch uniformity has been previously correlated to the shape of optical emission end-point data, where a statistical model was used to link the thickness distribution function across the wafer to the derivative of the optical emission signal.[16] A good correlation (R^2=0.71) was observed. However, this correlation may not be sufficient for a real-time sensor to be an effective metric for uniformity determination. A new approach presented in this article, involving a material balance etch end-point model, may better explain the correlation between the process-state and uniformity.

This article demonstrates how *in-situ* wafer-state information, specifically plasma etch end-point uniformity, can be obtained using a process-state sensor, such as a mass spectrometer. A two stage differentially pumped mass spectrometry system samples gaseous species directly from an electron cyclotron resonance silicon dioxide etch chamber. Real-time mass spectrometry data is used to estimate etch uniformity by observing the decay of the partial pressure of CO-containing products (i.e. CO, CO_2, COF_2, etc.) near the end-point. We establish that the rate of signal decay correlates to etch uniformity for two situations: 1) uniform etching of non-uniform oxide films; and 2) non-uniform etching of uniform oxide films. Using a COF_2 etch product material balance, an etch end-point uniformity model is developed to illustrate the correlation between the slope and the uniformity.

8.2 EXPERIMENTAL SYSTEM AND PROCEDURE

8.2.1 ECR ETCHING SYSTEM

Silicon dioxide etching investigations were performed in the divergent field electron cyclotron resonance (ECR) plasma etch system[7] shown in Fig. 8.1. The ECR is attached to a multiple process cluster tool with 100 mm wafer processing capability. The wafers are introduced into the ECR via a load lock and a central wafer handling system. The reactor

consists of an alumina-lined 12 cm I.D. source cavity mounted on a 25.4 cm I.D. processing chamber. The base pressure of the reactor is $7x10^{-7}$ Torr. The ECR source includes a 1000 W, 2.45 GHz microwave source and two external solenoid electromagnets (390 mm O.D. and 150 mm thick). The spacing between the electromagnets is adjustable from 5 to 55 mm. An upper gas dispersal ring introduces the helium carrier gas into the source chamber. A lower gas dispersal ring introduces the carbon tetrafluoride and deuterium etch gases into the source cavity. Deuterium is used instead of hydrogen to enable secondary ion mass spectroscopy tracking of deuterium contamination within the cluster tool. An 1100 l/s turbomolecular pump backed by a dry mechanical pump is used for process gas pumping. The process pressure is controlled via a closed loop system containing a motorized gate valve and a pressure transducer located in the processing chamber. Wafer cooling is accomplished through an aluminum thermal contact and positive He back pressure. A 13.56 MHz rf power supply and matching network provide wafer bias for independent control of the ion bombardment energy.

8.2.2 MASS SPECTROMETRIC PROCESS SENSING SYSTEM

A two stage differentially pumped mass spectrometer (Fig. 8.2) was used to sense the stable gaseous species within the reactor. The base pressure of the mass spectrometer system is $2x10^{-8}$ Torr. A 50 mm O.D. flexible tube connects the first stage of the mass spectrometer system to the ECR process chamber. The first stage contains a 70 l/s turbomolecular pump and a mechanical backing pump. The operating pressure in the first stage is typically $5x10^{-4}$ Torr. A 19 mm O.D. flexible tube connects the first stage to the second stage, where the mass spectrometer is located. The second stage also contains another 70 l/s turbomolecular pump and mechanical pump. The operating pressure in the second stage is typically $5x10^{-6}$ Torr. The mass spectrometer contained in the second stage

is a Leybold-Inficon closed ion source TS300 mass spectrometer capable of sampling masses up to 300 a.m.u. and operated with the electron multiplier enabled. The sampling rate is approximately 1.5 seconds per eight mass data points.

The differential pumping systems allows process sensing in the mTorr range, while the mass spectrometer operates at 5×10^{-6} Torr. In the ECR chamber and near the mass spectrometer system inlet, the Knudsen number is approximately 0.5, indicating the flow is transitional between molecular and continuum. The Peclet number is approximately 0.5, indicating the system is mixed and diffusive. Therefore, gases that enter the first stage are representative of the gas population in the ECR process chamber. In both stages of the mass spectrometer, the flow is molecular ($Kn > 1$). The absolute intensities of the species detected in the mass spectrometer depend on the individual diffusivities, pumping efficiencies and wall sticking coefficients for the molecules entering the first stage. However, intensity changes sensed by the mass spectrometer are representative of partial pressure changes in the process chamber.

8.2.3 SILICON DIOXIDE ETCHING PROCEDURES

The substrates were 100 mm Si (100) p-type (resistivity 25-50 Ω-cm). Each wafer initially had either 1000 or 3000 Å of thermal wet oxide with a thickness uniformity of 97.7% blanketing the front. For all experiments, the flow rates of the He, CF_4 and D_2 were held constant at 50, 10 and 20 sccm, respectively. The reactor pressure was held constant at 3.2 mTorr. In addition, the microwave and rf power were held constant at 250 W and 30 W, respectively. The position of the ECR's electromagnets was changed between runs to manipulate the etch uniformity.

We calculated etch rate and uniformity using optical interferometry with better than ±2% accuracy to obtain oxide thickness data for nine points evenly distributed in a plus sign

pattern across the wafer. Etch rates are reported as the arithmetic mean of the change in oxide thickness at the nine points on the wafer divided by the etch time. Etch uniformity is calculated using:

$$\text{Uniformity}(\%) = \left(1 - \frac{\max_{\text{rate}} - \min_{\text{rate}}}{2 \cdot \text{average}_{\text{rate}}}\right) \cdot 100 \tag{8.1}$$

and thickness uniformity is calculated using an analogous equation.

The mass spectrometer was used to determine the species present during oxide etching with $He/CF_4/D_2$. Up to 100 a.m.u., a large number of species attributed to reactant and product gases are observed. Signals at 21, 28, 47, 50, 52, 66, 69 and 85 a.m.u. (Table 8.1) from a typical run are shown in Fig. 8.3 as a function of time. These signals generally exhibit consistent run-to-run behavior.

We evaluated the mass spectrometer's ability to sense etch uniformity through two sets of experiments: 1) etching of controlled non-uniform oxide films with the most uniform etch process; and 2) etching of uniform oxide films with various degrees of process uniformity. For both sets of experiments, the intensity of the signals listed above was measured as a function of time with the mass spectrometer. When etching non-uniform oxide films with the most uniform etch process, the end-point behavior will deviate from that observed when etching uniform films. When etching uniform oxide films with various degrees of process uniformity, distinguishable changes in the mass spectrometer signal are observed and analyzed.

In the first set of experiments, the etching of non-uniform films simulates etch rate non-uniformity. Non-uniform films were fabricated from wafers covered by 1000 Å of thermal wet oxide. Photolithography was used to mask 25% or 50% of the wafer, and one

half of the film thickness was etched in buffered oxide etch. Thickness was confirmed using optical interferometry. One set of wafers had a 1000 Å film covering 75% and a 500 Å film covering 25% of the wafer (75%/25%). Another set of wafers had a 1000 Å film covering half of the wafer and a 500 Å film covering the other half (50%/50%). The non-uniform films were etched at the optimal process conditions (94.7% uniformity). Using equation 8.1, the thickness uniformity of the 75%/25% and the 50%/50% wafers was 60% and 67%, respectively. Since the thickness uniformity of these films was substantially worse than the etch uniformity (94.7%), the uniformity for analysis purposes was taken as the thickness uniformity of the non-uniform films.

In the second set of experiments, the process uniformity was altered by changing the spacing between the ECR's electromagnets. The spacing can range from 5 to 55 mm along four points on the electromagnets' perimeter. Two points were held constant at 55 mm and two points were adjusted at three positions from 47 to 55 mm to achieve the three uniformity conditions. The uniformity for each electromagnet position was determined by performing a calibration run. The calibration involved a partial etch of 1.5 min on a 3000 Å blanket oxide wafer. Using equation 8.1, the uniformity was calculated by measuring the thickness at nine points on this wafer. For the three electromagnet positions, the uniformity was found to be 86.2%, 92.1% and 94.7%. The etch rate distribution for the 94.7% uniformity case follows the typical bull's eye pattern with the fastest etching occurring at the wafer center. Changing the electromagnet's position shifts the center of this pattern towards the wafer edge. Using the calibration condition, a 1000 Å oxide was completely etched while monitoring the end-point with the mass spectrometer. These steps were repeated for two other electromagnet positions.

8.3 RESULTS

8.3.1 MASS SPECTROMETRIC SENSING OF ETCH PROCESS

The typical trends during oxide etch in He/CF_4/D_2 are shown in Fig 8.3. The assignments and sources for the mass signals in Fig. 8.3 are presented in Table 8.1. The CO- and Si-containing species can result from the following reactions:[17-21]

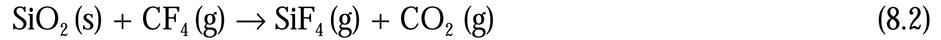

$$SiO_2\,(s) + CF_4\,(g) \rightarrow SiF_4\,(g) + CO_2\,(g) \quad (8.2)$$

$$SiO_2\,(s) + 2CF_2\,(g) \rightarrow SiF_4\,(g) + 2CO\,(g) \quad (8.3)$$

$$CF_x\,(g) + C_yF_z\,(s) \rightarrow C_{y+1}F_{z+x}\,(s) \quad (8.4)$$

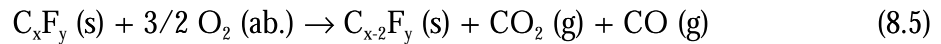

$$C_xF_y\,(s) + 3/2\ O_2\,(ab.) \rightarrow C_{x-2}F_y\,(s) + CO_2\,(g) + CO\,(g) \quad (8.5)$$

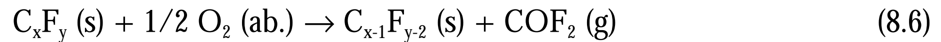

$$C_xF_y\,(s) + 1/2\ O_2\,(ab.) \rightarrow C_{x-1}F_{y-2}\,(s) + COF_2\,(g) \quad (8.6)$$

The gaseous reactants and products from these reactions enter the mass spectrometer where they are cracked and ionized. We find the CO^+ (28 a.m.u.) signal the most desirable to monitor for uniformity sensing because it exhibits a high signal-to-noise ratio and consistent end-point behavior.

8.3.2 MASS SPECTROMETRIC END-POINT UNIFORMITY SENSING

Figure 8.4 displays the results from etching non-uniform oxides. These results exhibit the mass spectrometer's ability to sense gross non-uniformity and provide a wide uniformity range for the analysis presented in Section 8.4. The CO^+ signal for the wafer with a 1000 Å uniform oxide rapidly increases when the discharge is ignited (point A in Fig. 8.4) and quickly attains a steady state value. At the process end-point (point B for the uniform oxide), the signal begins to decrease and continues until the rapid drop when the plasma is extinguished (point C). This signal exhibits the expected behavior for a process with high uniformity. The signals for the wafers with non-uniform oxides effectively display two end-points, one for the 500 Å film (point B') and one for the 1000 Å film (point B).

When etching begins, 100% of the wafer is covered with oxide and the signal intensity represents etching from the entire surface. After the first end-point, the CO^+ intensity is reduced due to the reduction in oxide surface coverage. It is clear from Fig. 8.4 that the CO^+ intensity when etching oxide from 75% of the wafer is greater than the intensity when 50% of the wafer is being etched.

Figure 8.5 exhibits the results from etching the uniform oxides and confirms the mass spectrometer's ability to sense small changes in uniformity. Fig. 8.6 presents a detailed view of the end-point region from Fig. 8.5 and contains analysis explained in the next Section 8.4.1. The CO^+ traces for 94.7%, 92.1% and 86.2% uniformity exhibit that the end-point decays most rapidly for the most uniform etch process. The 94.7%, 92.1% and 86.2% uniformity runs had etch rates of 674, 680 and 688 Å/min, respectively, and were executed in that order. Since the etch rates are similar, one may expect similar steady state signal intensities for these runs. The change in signal intensity for the different runs is attributed to changes in the mass spectrometer sensitivity. This change is not expected to significantly affect the end-point transition.

8.4 UNIFORMITY ANALYSIS AND DISCUSSION

8.4.1 ETCH END-POINT UNIFORMITY SENSING

Figure 8.4 illustrates the mass spectrometer's capability to distinguish uniformity by sensing the CO^+ intensity. The drop in the signal intensity at point B' for the non-uniform oxides is largest for the most uniform film. For etching uniform oxides, the data in Fig. 8.5 is consistent with the CO^+ signal decaying as the silicon substrate is exposed and the surface coverage of oxide decreases. For a non-uniform etch process, uneven oxide clearing will result in a slowly changing end-point signal.

To establish a quantitative correlation between the mass spectrometer signal and etch uniformity, the initial end-point slope is averaged over several points. Averaging is used to help distinguish the true end-point from random noise. The average slope is equal to the signal intensity change across four points divided by the time interval. As each data point is collected, a new average slope value can be determined. An example for the four point averaged slope is shown in Fig. 8.6, where the averaged slope at the fourth point for each set is represented as the slope across the two solid points. From the data in Fig. 8.6, the four point slope is calculated as a function of time and is shown in Fig. 8.7 for 94.7%, 92.1% and 86.2% uniformity. As the end-point begins, the slope changes from zero to a negative value and then slowly increases back to zero.

As discussed in the etching procedures (Section 8.2.3), the non-uniform etching was concentric for the 94.7% uniformity wafer, but deviated from concentric for the more non-uniform cases. This deviation is most noticeable for the 86% uniformity etch process, and is evident in the collected average slope data. As observed in Fig. 8.7 for the 94.7% uniformity data and will be shown in Section 8.4.2, the slope is expected to decrease, then slowly increase to zero for a concentric non-uniform etching pattern. After four slope values are collected (down arrow in Fig. 8.7) for the 86% uniformity data, the slope continues to decrease, indicating deviation from the concentric pattern. This trend in the measured slope could be used to sense the presence of azimuthally asymmetric etching.

It is clear from Fig. 8.7 that the initial change in slope at the etch end-point is sensitive to etch uniformity. This initial change in slope for the four point averaging is shown in Fig. 8.7 as the difference between the last zero slope point (up arrows in Fig. 8.7) and the slope four points later (down arrows). This analysis is also performed for the non-uniform films by averaging the slope of the end-point signal across the B'-B transition

shown in Fig. 8.4. The measured correlation between change in slope and uniformity for the cases of uniform etching of non-uniform films and non-uniform etching of uniform films is shown as the points in Fig. 8.8, where etch uniformity is plotted versus the inverse of the initial slope. The solid line in Fig. 8.8 represents the correlation predicted by the [COF_2] model, which is presented in Section 8.4.2. It is clear from Fig. 8.8 that the initial end-point slope of the mass spectrometer data from the uniform and non-uniform films correlates well with the etch end-point uniformity. The uniformity trend in the experimental data suggests that, in a perfect etch and sense system, a 100% uniform etch process would produce a signal with an inverse slope of zero. The correlation between the uniform and non-uniform film experimental data presented in Fig. 8.8 illustrates the robustness of the analysis.

8.4.2 ETCH END-POINT UNIFORMITY MODEL

An etch product material balance is developed to model the mass spectrometer's response to etch end-point uniformity. Specifically, the concentration of the COF_2 etch product as a function of time is obtained, and the first derivative is related to the etch end-point uniformity. Starting from an overall etch reaction:

$$SiO_2 + 2CF_4 \rightarrow SiF_4 + 2COF_2 \qquad (8.7)$$

a general mole balance on COF_2 can be written:

$$\frac{d[COF_2]}{dt} = \frac{F_{in}^{COF_2}}{V} + \frac{2\rho}{V} \cdot \int_0^{\theta(t)} \int_{r(t)}^{R} [ER(r,\theta) \cdot r] dr d\theta - \frac{F_{out}^{COF_2}}{V} - \frac{k_{cons.}[COF_2]}{V} \qquad (8.8)$$

where [COF_2] is the COF_2 concentration in the reactor , F is the molar flow rate, V is the reactor volume, ρ is the SiO_2 molar density, $ER(r,\theta)$ is the non-uniform etch rate distribution across the wafer, R is the wafer radius, r(t) describes how the radius of the

clearing oxide film changes with time and $k_{cons.}$ is the rate constant for reactions where COF_2 is consumed. The integral represents COF_2 generation from SiO_2 etching (etch rate x area), where the integration limits are time dependent due to non-uniform SiO_2 clearing. The flow rate of COF_2 into the reactor is zero, and $k_{cons.}$ is assumed to be zero. The flow rate of COF_2 out of the reactor written in terms of concentration is:

$$F_{out}^{COF_2} = [COF_2] \cdot v_o \tag{8.9}$$

where v_o is the total volumetric flow rate. Applying the above assignments reduces equation 8.8 to:

$$\frac{d[COF_2]}{dt} + \frac{[COF_2]}{\tau} = \frac{2\rho}{V} \int_0^{\theta(t)} \int_{r(t)}^{R} [ER(r,\theta) \cdot r] dr d\theta \tag{8.10}$$

where $\tau = V/v_o$ is the reactor residence time. An infinite series solution can be obtained for equation 8.10. An analytical solution is obtained by assuming that the residence time is short enough that the accumulation term becomes negligible. This assumption is supported by the data in Fig. 8.6. Using τ=0.1s, $d[COF_2]/dt << [COF_2]/\tau$ and equation 8.10 simplifies to:

$$[COF_2] = \frac{2\rho\tau}{V} \cdot \int_0^{\theta(t)} \int_{r(t)}^{R} [ER(r,\theta) \cdot r] dr d\theta \tag{8.11}$$

A reasonable approach is to assume an azimuthally symmetric (concentric) etching pattern and compare the predicted trend in $[COF_2]$ to the measured data. Deviations from this case

will result from asymmetric etch profiles. The non-uniformity for the 94.7% uniformity case was symmetric in θ, with the maximum rate occurring at the wafer center. The etch rate is described as a function of radius:

$$ER(r) = a - b \cdot r^2 \tag{8.12}$$

where a and b are constants determined from the etch rate at the wafer center and the uniformity. The function r(t), which describes the time when SiO_2 is completely cleared at a given radius, is obtained from an SiO_2 balance. The thickness of SiO_2, z, at any radius versus time is given by:

$$z(r,t) = z_o - ER(r) \cdot t \tag{8.13}$$

where z_o is the initial SiO_2 film thickness. Solving equation 8.13 for r(t) at zero thickness yields:

$$r(t) = \left[\frac{a}{b} - \frac{z_o}{bt}\right]^{\frac{1}{2}} \tag{8.14}$$

Combining equations 8.11, 8.12, and 8.14 and integrating gives the COF_2 concentration versus time:

$$[COF_2] = \frac{4\pi\rho\tau}{V} \cdot \left\{\left(\frac{aR^2}{2} - \frac{bR^4}{4}\right) - \left(\frac{a^2}{4b} - \frac{z_o^2}{4b} \cdot \frac{1}{t^2}\right)\right\} \tag{8.15}$$

where the first term in parentheses corresponds to the steady-state concentration of COF_2 before the etch begins to clear, and the second term is the time dependent concentration drop as the oxide coverage decreases. This equation is valid over times from z_o/a to $z_o/(a-bR^2)$. Assuming the parabolic etch rate distribution given in equation 8.12 and given an initial oxide thickness, the COF_2 concentration at steady state and during the end-point can be predicted for any uniformity. This model is also valid for any sensor that detects a change in $[COF_2]$ at the end-point.

To relate the change in COF_2 concentration to the uniformity, equation 8.15 is differentiated:

$$\frac{d[COF_2]}{dt} = \frac{-2\pi\rho\tau z_o^2}{Vb} \cdot \frac{1}{t^3} \tag{8.16}$$

The calculated first derivative of the COF_2 concentration is shown versus time in Fig. 8.9 for 95%, 90% and 85% uniformity. The trends in Fig. 8.9 are qualitatively similar to the average slope data presented in Fig. 8.7. It is clear from Fig. 8.9 that the magnitude of the first derivative at the beginning of the end-point signal ($t=z_o/a$) is sensitive to the etch uniformity. This value is difficult to obtain experimentally, although averaging the initial end-point slope supplies a measure of this value. Combining the uniformity equation (equation 8.1) and the etch rate equation (equation 8.12) yields the uniformity as a function of the constants a and b:

$$\text{Uniformity}(\%) = \left(1 - \frac{bR^2}{2a - bR^2}\right) \cdot 100 \tag{8.17}$$

Equations 8.16 and 8.17 combine to provide the uniformity as a function of two parameters: the constant a; and the magnitude of the change in the first derivative at the end-point. The constant "a" is directly obtained from the known initial film thickness and the time at which the mass spectrometer signal first deviates form steady state ($t=z_o/a$). The change in the first derivative is estimated from the mass spectrometer data, as shown in Fig. 8.7. Using a similar approach, uniformity was determined from the modeled and measured [COF_2] versus time data, and the results are shown in Fig. 8.8. The solid line in Fig. 8.8 represents the model, which has been normalized to experimental data at 94.7% uniformity. Normalization is necessary because the mass spectrometer system was not calibrated for COF_2. Fig. 8.8 verifies the COF_2 material balance model predicts a large initial end-point slope indicates high etch uniformity, as suggested from the experimental data. The model fits the data quite well for the four point averaged slope of the uniform films. The mass spectrometer data for the non-uniform films deviates slightly from the model, probably because the non-uniform films were not azimuthally symmetric and the end-point slope was averaged over a long time frame.

The uniformity information obtained by this method is acquired early during the end-point, so that real-time control operations could be enacted. For example, once the uniformity is obtained, the controller could switch to a more selective etch and then estimate an etch-stop time. A concern with transferring this algorithm to real-time arises from a time lag created by the analysis procedure. The analysis described in Section 8.4.1 uses subsets of four data points to estimate the initial end-point slope. Similar analyses were performed using two and six point subsets, and the results are shown in Fig. 8.10 for the 94.7% uniformity case. When the number of points taken in the subsets decreases from six to two, the minimum in the first derivative shifts by seven seconds and noise becomes

evident in the second derivative. The data is broken into four point subsets to smooth the noise in the data and obtain a clear end-point signal. In principle, this analysis will work for patterned wafers as well, although the steady state intensity sensed by the mass spectrometer will scale with the percentage of open area. This method is well suited for processes such as spacer etch, where the film covers the entire wafer and a large percentage is cleared.

8.5 CONCLUSIONS

Wafer-state etch end-point uniformity is determined from process-state data by analyzing the rate of decay of the end-point signal sensed with mass spectrometry. For silicon dioxide etching with CF_4 and D_2, the initial end-point slope of the CO^+ intensity versus time correlates with the uniformity. This correlation was demonstrated by: 1) performing a uniform etch of non-uniform oxides; and 2) controlling the etch uniformity on uniform blanket oxide wafers. The correlation is justified with a material balance etch end-point model, which is valid for any sensor that detects a change in the COF_2 concentration at the end-point. Performing this analysis during data collection would allow mass spectrometry to be a valuable *in-situ* uniformity sensor for wafer-state analysis.

8.6 ACKNOWLEDGMENTS

This work has been supported by the NSF Engineering Research Centers Program through the Center for Advanced Electronic Materials Processing (Grant EEC 8721505).

8.7 REFERENCES

[1] T. E. Benson, L. I. Kamlet, P. Klimecky, and F. L. Terry, Jr., *Journal of Electronic Materials* **25**, 955 (1996)

[2] D. Economou, E. S. Aydil, and G. Barna, *Solid State Technology* **34**, 107 (1991)

[3] H. L. Maynard, N. Layadi, and J. T. Lee, *J. Vac. Sci. Technol.* B **15**, 109 (1997)

[4] S. Vallon, O. Joubert, L. Vallier, F. Ferrieu, B. Drevillon, and N. Blayo, *J. Vac. Sci. Technol.* A **15**, 865 (1997)

[5] I. Tepermeister, W. T. Conner, T. Alzaben, H. Barnard, K. Gehlert, and D. Scipione, *Solid State Technology* **39**, 63 (1996)

[6] J. L. Cecchi, J. E. Stevens, R. L. Jarecki, Jr., and Y.C. Huang, *J. Vac. Sci. Technol.* B **9**, 318 (1991)

[7] Z. Wan, J. Liu, and H. H. Lamb, *J. Vac. Sci. Technol.* A **13**, 2035 (1995)

[8] P. K. Mozumder and G. G. Barna, *IEEE Trans. Semicond. Manuf.* **7**, 1 (1994)

[9] S. Thomas III, H. H. Chen, C. K. Hanish, J. W. Grizzle, and S. W. Pang, *J. Vac. Sci. Technol.* B **14**, 2531 (1996)

[10] K. Sung and S. W. Pang, *Jpn. J. Appl. Phy.* **33**, 7112 (1994)

[11] M. J. Buie, J. T. Pender, J. Soniker, M. L. Brake, and M. Elta, *J. Vac. Sci. Technol.* A **13**, 1930 (1995)

[12] H. L. Maynard, E. A. Reitman, J. T. C. Lee, and D. E. Ibbotson, *J. Electrochem. Soc.* **143**, 2029 (1996)

[13] P. J. Wolf, Masters Thesis, North Carolina State University (1996)

[14] L. L. Tedder, G. W. Rubloff, I. Shareef, M. Anderle, D. H. Kim, and G. N. Parsons, *J. Vac. Sci. Technol.* B **13**, 1924 (1995)

[15] A. I. Chowdhury, W. W. Read, G. W. Rubloff, L. L. Tedder, and G. N. Parsons, *J. Vac. Sci. Technol.* B **15**, 127 (1997)

[16] P. K. Mozumder and G. G. Barna, Technical Activity Report, Semiconductor Process and Design Center, Texas Instruments, Dallas, Texas, August (1991)

[17] J. W. Coburn and H. F. Winters, *J. Vac. Sci. Technol.* **16**, 391 (1979)

[18] M. Oshima, *Surf. Sci.* **86**, 858 (1979)

[19] J. W. Butterbaugh, D. C. Gray, and H. H. Sawin, *J. Vac. Sci. Technol.* B **9**, 1461 (1991)

[20] G. S. Oehrlein, Y. Zhang, D. Vender, and M. Haverlag, *J. Vac. Sci. Technol.* A **12**, 323 (1994)

[21] N. R. Rueger, J. J. Beulens, M. Schaepkens, M. F. Doemling, J. M. Mirza, T. E. F. M. Standaert, and G. S. Oehrlein, *J. Vac. Sci. Technol.* A **15**, 1881 (1997)

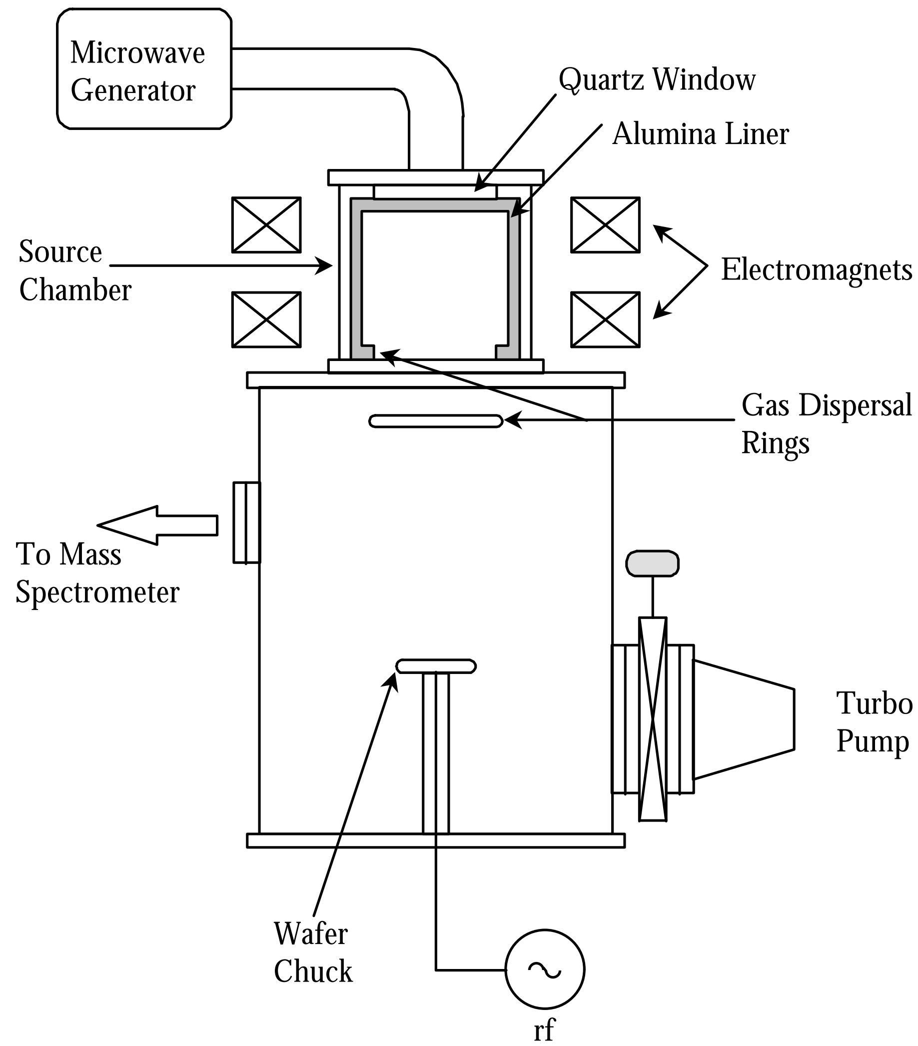

Figure 8.1 Electron cyclotron resonance plasma reactor used for silicon dioxide etching. The mass spectrometer system senses gases directly from the process chamber as shown.

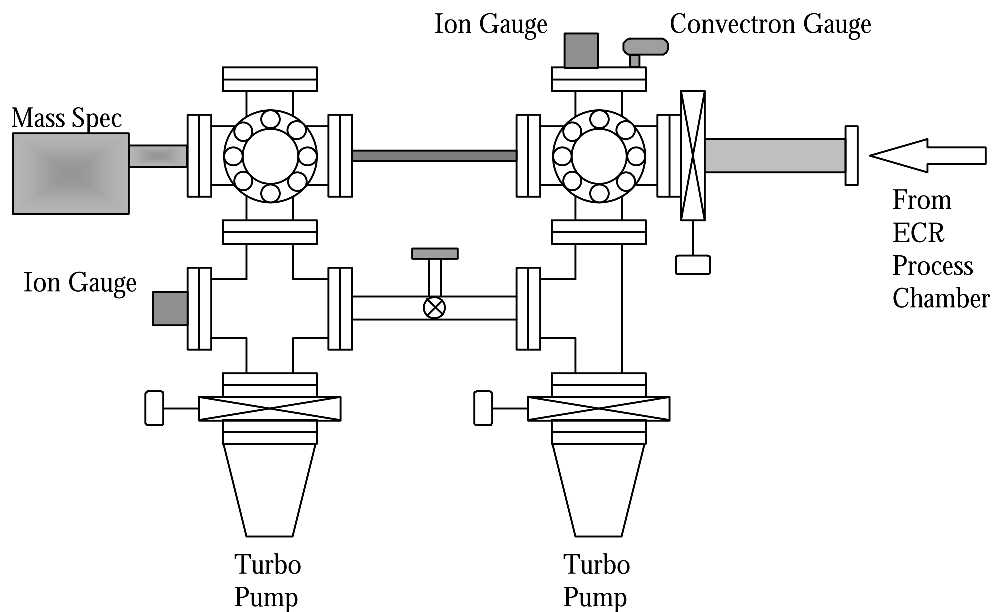

Figure 8.2 Schematic of the two stage differentially pump mass spectrometer system utilized in these investigations. Two stages of pumping reduce the pressure from the mTorr range of the ECR to 5 X 10^{-6} Torr for operation of the mass spectrometer.

Table 8.1 Assignments and sources for masses shown in Fig. 8.3. See text for reactions (8.2) to (8.6).

a.m.u.	Species	Possible Source
21	DF^+	F scavenging by D
28	CO^+	Reactions (8.2), (8.3), (8.5) and (8.6)
47	COF^+ and SiF^+	Reactions (8.2), (8.3) and (8.6)
50	CF_2^+	CF_4 reactant
52	CF_2D^+	Polymer reaction product
66	COF_2^+ and SiF_2^+	Reactions (8.2), (8.3) and (8.6)
69	CF_3^+	CF_4 reactant
85	SiF_3^+	Reactions (8.2) and (8.3)

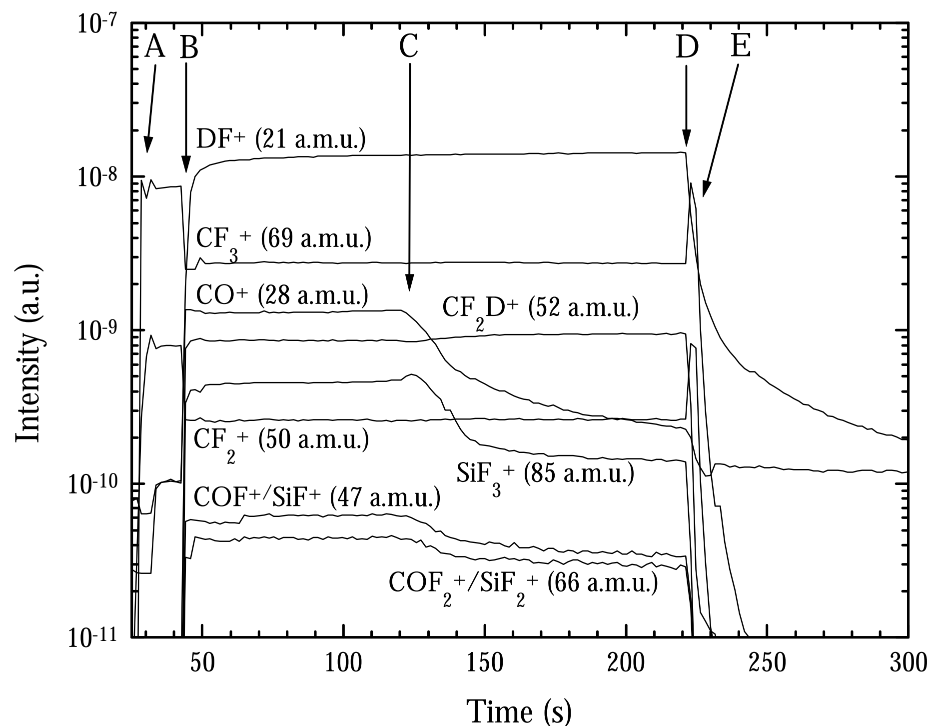

Figure 8.3 Real-time intensity signals for the masses monitored in these investigations. See Table 8.1 and text for a.m.u. assignments. A: Gases on; B: Plasma on; C: End-point signal; D: Plasma off; E: Gases off

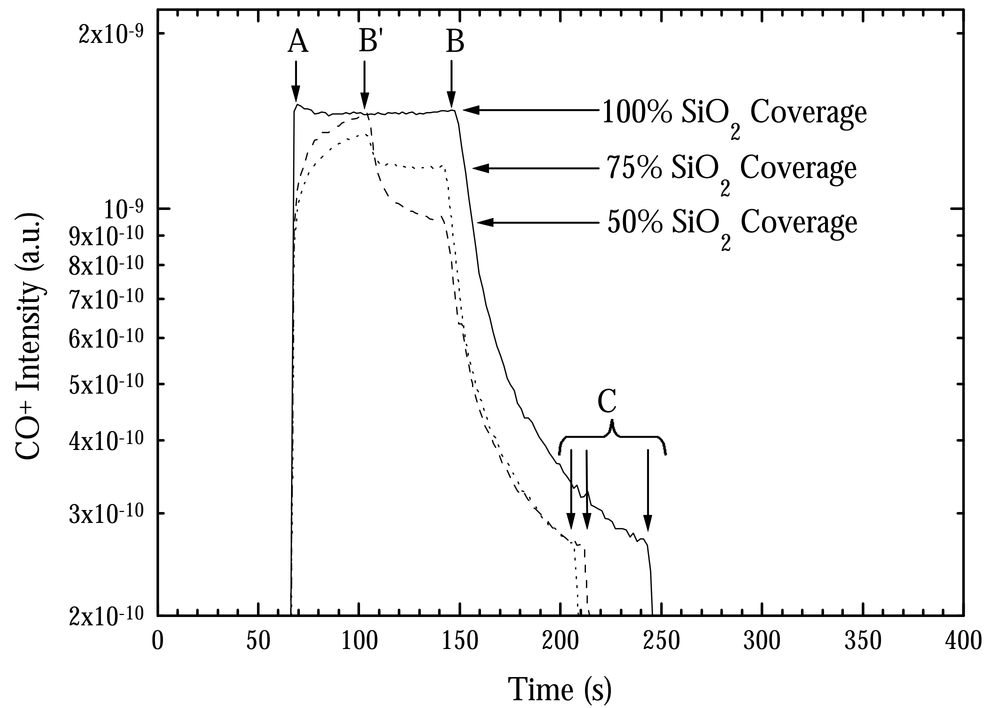

Figure 8.4 Real-time CO^+ intensity for wafer uniformly (97.7%) covered by 1000 Å oxide (solid line), 67% thickness uniformity (50% 1000 Å SiO_2 coverage) wafer (dashed line) and 60% thickness uniformity (75% 1000 Å SiO_2 coverage) wafer (dotted line). The arrows indicate the CO^+ intensity for 100%, 75% and 50% SiO_2 coverage on the wafer. The CO^+ intensity drops as the surface coverage of oxide drops. A: Plasma on; B': 500 Å film end-point; B: 1000 Å film end-point; C: Plasma off

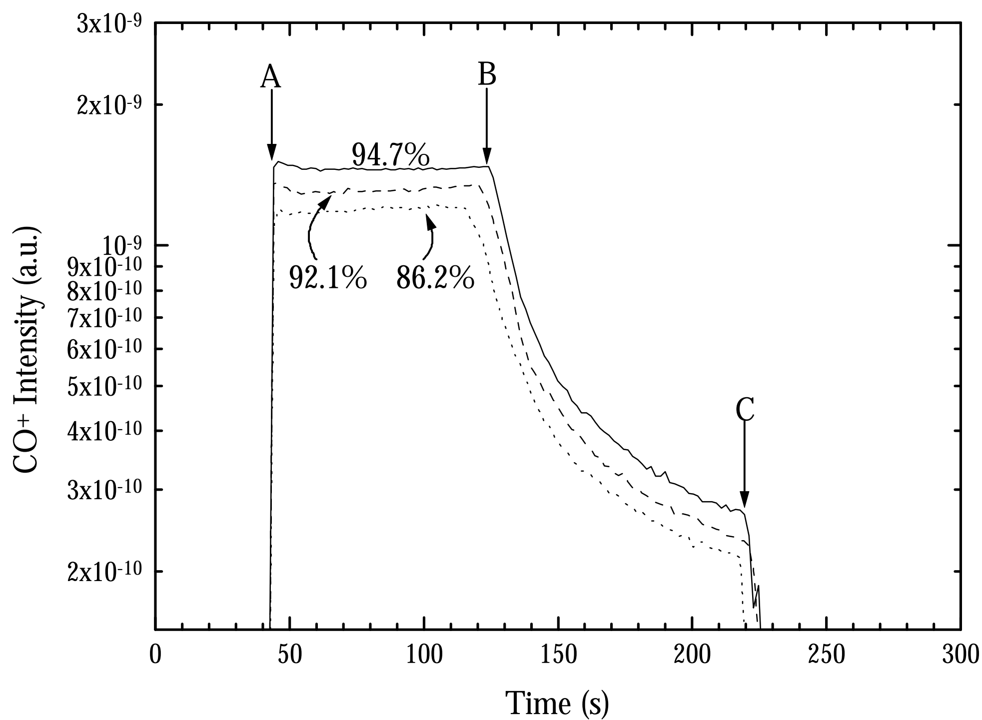

Figure 8.5 Real-time CO^+ intensity for uniformity series performed on uniform oxide films. The rate of decay at the end-point is indicative of a particular etch uniformity. 94.7% uniformity (solid line); 92.1% uniformity (dashed line); 86.2% uniformity (dotted line); A: Plasma on; B: End-point signal; C: Plasma off

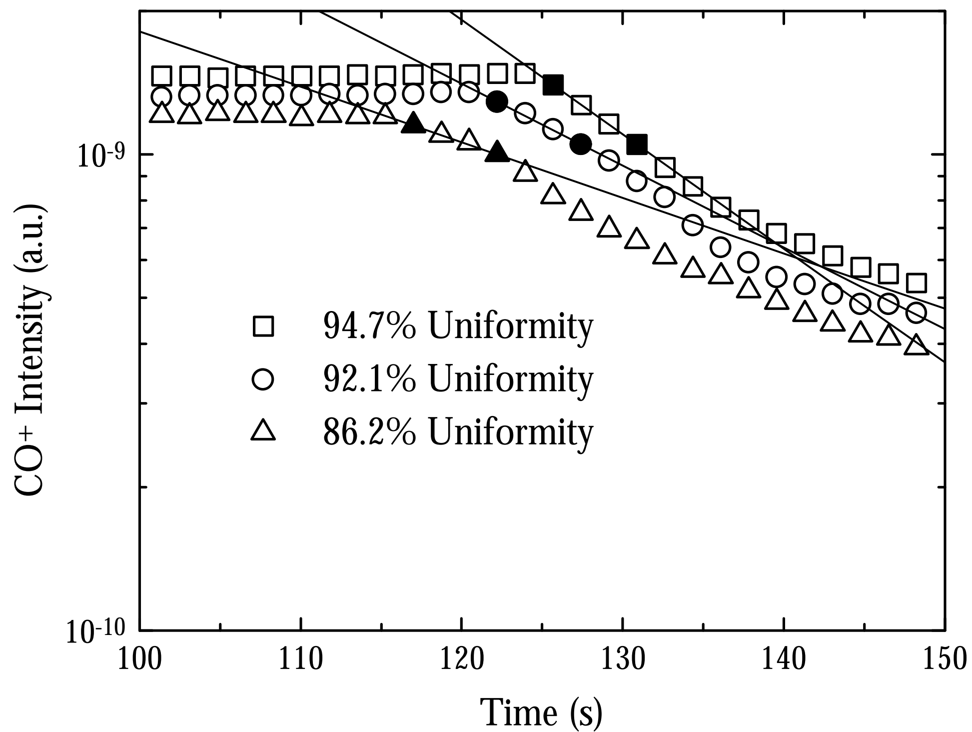

Figure 8.6 Real-time CO^+ intensity for uniformity series performed on uniform oxide films. Detailed version of end-point region from Fig. 8.5. The average slope is calculated as the slope across the end points (solid markers) of each subset.

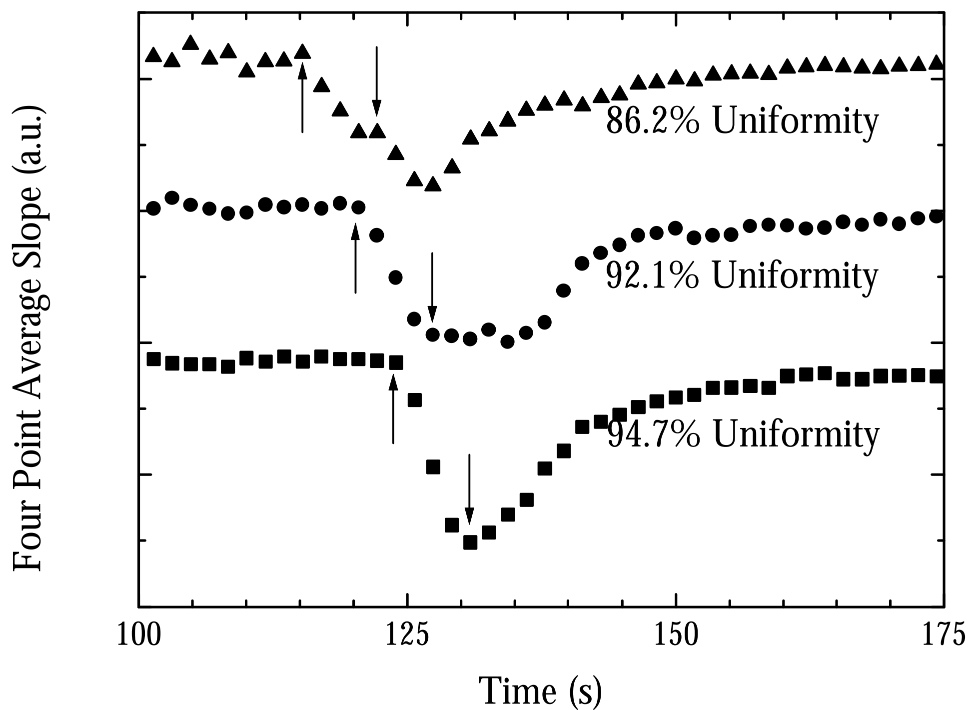

Figure 8.7 Averaged slope of real-time CO^+ intensity for 94.7%, 92.1% and 86.2% uniformity versus time. The slope quickly changes from zero to a negative value at the end-point signal. The up arrows represent the last zero slope point and the down arrows represent the slope four points later, both of which are used in the uniformity correlation.

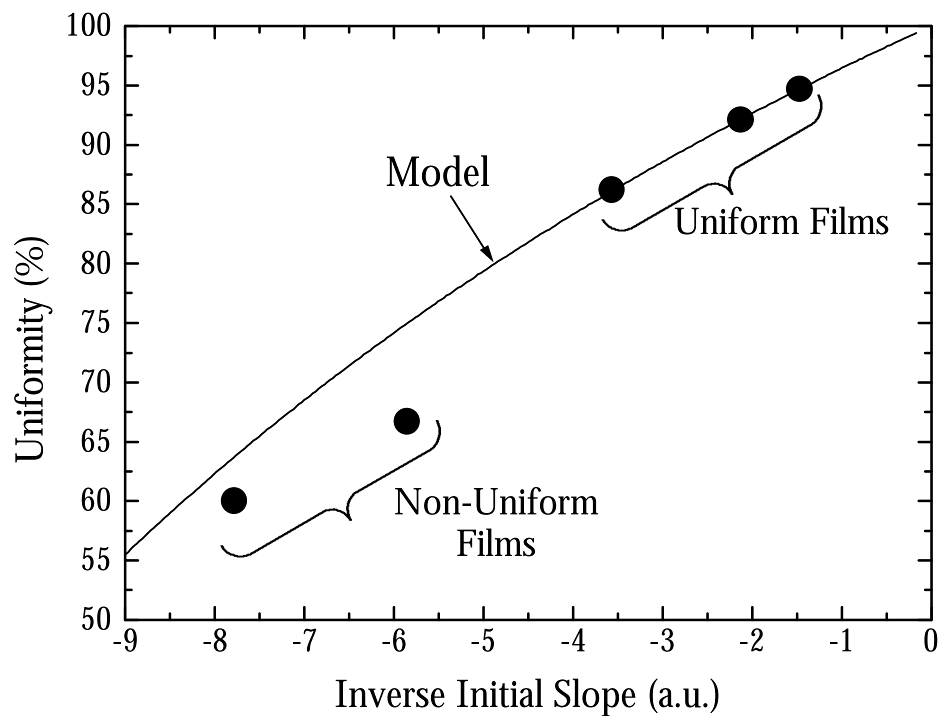

Figure 8.8 Uniformity versus the inverse of the initial slope [s/a.u./10^{10}] for the uniform and non-uniform films (solid points) and first derivative [s-cm^3/moles/2.6x10^{12}] of the model (solid line). A high rate of decay in the CO^+ signal corresponds to high etch uniformity.

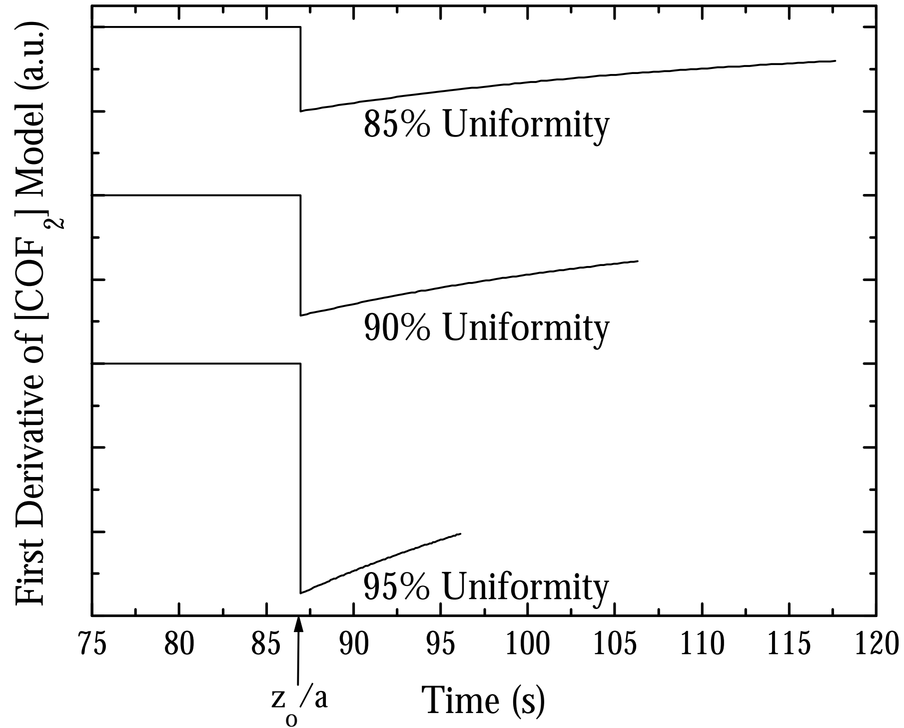

Figure 8.9 First derivative versus time of COF_2 concentration from material balance model. The first derivative at the end-point beginning ($t=z_o/a$) is correlated with the uniformity in Fig. 8.8.

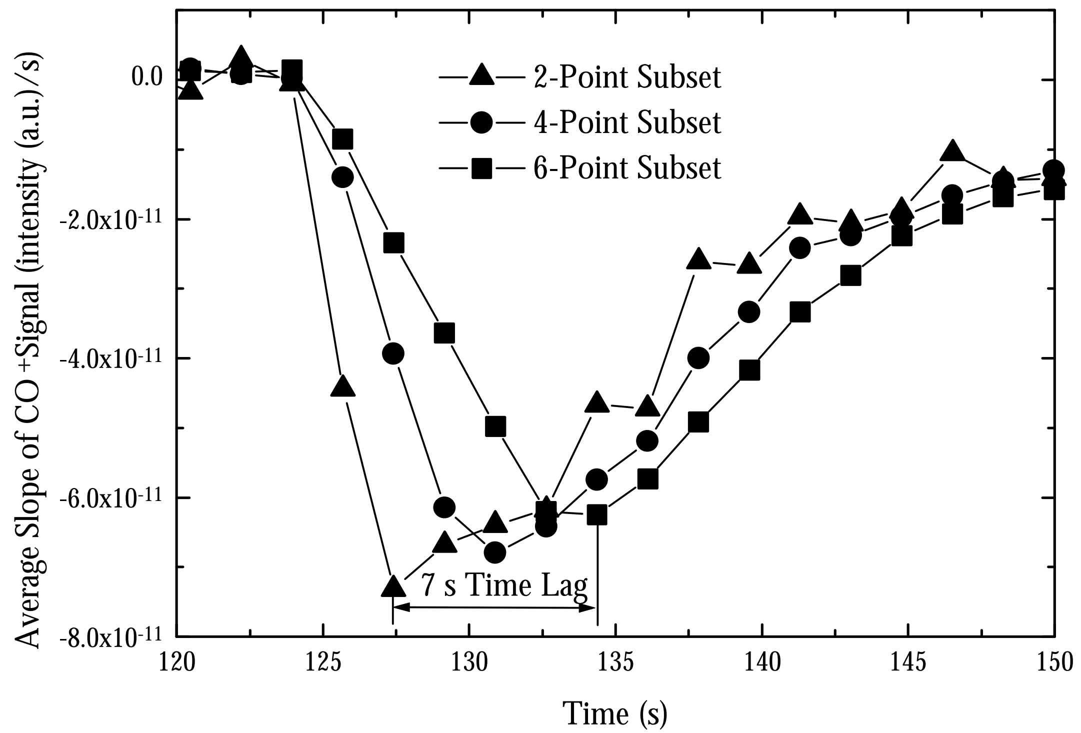

Figure 8.10 Average slope of real-time CO^+ intensity for the 94.7% uniformity case. As the subset size is decreased from six points (squares) to four points (circles) to two points (triangles), the time required to detect a change in the CO^+ intensity decreases by seven seconds.

CHAPTER 9

SUMMARY

9.1 SUMMARY

We have described the physical and electrical properties of yttrium silicate thin films for application as high-k dielectrics. The following is a summary of the key results presented in this research.

9.1.1 OXIDATION OF YTTRIUM SILICIDE

Although the oxidation of many silicides results in the growth of a SiO_2 film over a metal silicide, the oxidation of yttrium silicide results in yttrium silicate. XPS and FTIR analyses of thick (4500 Å) yttrium silicate films reveal the formation of Y-O-Si bonding structure with properties in accordance with the donation of electron density away from the less electronegative yttrium toward the more electronegative silicon and oxygen. The Y-O-Si bonding structure leads to spectroscopic properties that are different than either SiO_2 or Y_2O_3. Oxidation of thin (<50 Å) yttrium silicide films results in similar yttrium silicate structure to silicates formed by the oxidation of yttrium on silicon, but with increased silicon incorporation.

9.1.2 OXIDATION OF YTTRIUM ON SILICON

When a metal, such as yttrium, that has a high affinity for oxygen and forms stable silicides is deposited on silicon and oxidized, a competition between metal-silicon reaction and metal oxidation develops. When the thickness of the metal is less than some critical thickness (~40-80 Å), the metal-silicon reaction consumes the metal layer before significant metal oxidation can occur resulting in a metal-O-Si film. When the metal is thicker than some critical thickness, significant metal oxidation can occur before the metal-silicon

reaction can consumes the entire metal film resulting in a metal oxide/silicate bi-layer. In the process described here where a thin metal is deposited onto silicon then oxidized, the high reactivity of yttrium with silicon and oxygen is an advantage that enables the formation of a Y-O-Si interface free of SiO_2. The formation of thin Y-O-Si films is thought to result from concurrent yttrium-silicon reaction and oxidation to form Y-O-Si bonding units. Amorphous yttrium silicate films (~40 Å) with EOT = 11 Å have been formed by the oxidation of thin yttrium films on silicon. These results demonstrate that an yttrium-based silicate can be scaled down to the EOT ~ 10 Å regime.

9.1.3 YTTRIUM/SILICON INTERFACE REACTIONS

When yttrium (which forms a silicide and a stable oxide) is deposited onto silicon and oxidized, concurrent metal-silicon reaction and metal oxidation results in a layer with significant silicate composition. This intermixing also occurs when the surface is oxidized before metal deposition. Because yttrium has a very high affinity for oxygen, annealing results in reduction of the available silicon oxide, leading to a silicate layer. When ~1 monolayer of nitrogen is present at the interface, the silicon diffusion from the substrate is impeded. Any silicon oxide on top of the N layer will still react with the metal to form a silicate. However, when only nitrided silicon is present, oxidation of deposited metal results in a structure closer to pure metal oxide, consistent with impeded silicon diffusion through the nitrided layer.

Since the interface reaction between yttrium and silicon competes with oxidation, the oxidation temperature mediates the silicon consumption. High temperature oxidation generally results in greater silicon incorporation. The reaction between yttrium and silicon exhibits an activation energy of 0.3-0.5 eV consistent with other rare-earth silicon reactions.

The properties of yttrium silicate films strongly depend on the silicon content, and as a result the interfacial reaction between yttrium and silicon.

Annealing or oxidation of yttrium on thermal SiO_2 results in a solid-state interface reaction that converts the SiO_2 to silicate. XPS analysis of the conversion of SiO_2 to silicate reveals similar microstructure to silicate films formed by oxidation of either yttrium on silicon or yttrium silicide. The conversion of SiO_2 to silicate demonstrates an interesting method to convert the existing SiO_2 gate dielectric to a high-k dielectric in a straightforward manner using thermal oxidation of silicon followed by metal deposition, annealing and re-oxidation.

The interface reactions reported here for the case of yttrium are expected for other metals that form silicides and stable oxides on silicon including Hf, Zr, La, etc. CVD of metal oxides may also include formation of metal-silicon bonds, so similar reactions reported here for PVD films are expected to be active during CVD, and these reactions probably play an important role in interface layer formation.

9.1.4 PLASMA OXIDATION OF YTTRIUM ON SILICON

Yttrium silicate formation by the remote N_2O plasma oxidation of yttrium on silicon can result in films with similar properties to thermally oxidized silicates. The yttrium silicate films formed by plasma oxidation are amorphous, but display greater surface roughness that thermally oxidized films. The silicate films formed at 300 °C demonstrate the feasibility of forming silicate films using a low thermal budget plasma oxidation process.

9.1.5 END-POINT UNIFORMITY SENSING

Wafer-state etch end-point uniformity can be determined from process-state data by analyzing the rate of decay of the end-point signal sensed with mass spectrometry. For silicon dioxide etching with CF_4 and D_2, the initial end-point slope of the CO^+ intensity versus time correlates with the uniformity. The correlation is justified with a material balance etch end-point model, which is valid for any sensor that detects a change in the COF_2 concentration at the end-point. Performing this analysis during data collection would allow mass spectrometry to be a valuable *in-situ* uniformity sensor for wafer-state analysis.

9.2 SUGGESTIONS FOR FUTURE WORK

The following suggestions for further study have been raised by this work:

1) The two-step oxidation involving vacuum annealing of yttrium on silicon (to first form silicide) followed by thermal oxidation has produced films with improved electrical properties over direct oxidation of yttrium on silicon. Specifically, silicate films formed by the two-step process exhibit reduced flat band shifting. Further investigation is required to fully demonstrate the effectiveness of this process.

2) The conversion of SiO_2 to yttrium silicate is a potentially advantageous process. The electrical properties of silicates formed by this process must be addressed.

3) The electrical properties of Y-O-Si films formed on oxidized silicon and nitrided silicon engineered interface should be investigated to determine their feasibility as gate dielectrics.

APPENDICES

APPENDIX A

THERMAL OXIDATION OF SPUTTERED YTTRIUM

A.1 TWO-STEP OXIDATION

Chapter 3 presented electrical results for yttrium silicates formed by the thermal oxidation of sputtered yttrium. Oxidation of ~8 Å of yttrium on silicon for 15 seconds at 900 °C in 1 atm. N_2O resulted in an EOT = 11-12 Å with a considerable flat band (V_{fb}) shift of 0.7-0.8 V. A two-step oxidation process is presented here, for which the initial results indicate an improvement in the V_{fb} shift. The two-step process involves annealing the yttrium film on silicon in vacuum to form yttrium silicide prior to oxidation. Figure A.1 compares the C-V characteristics films formed by the one-step oxidation (original process) to films formed by the two-step oxidation. The film formed by the one-step oxidation was deposited by sputtering ~25 Å of yttrium onto silicon at room temperature and oxidizing for 5 minutes in 1 atm. air. The film formed by the two-step oxidation process was deposited by sputtering ~25 Å of yttrium onto silicon at room temperature, annealing in vacuum for 5 minutes at 600 °C and oxidizing for 15 seconds in 1 atm. air. The C-V measurements were performed using a Four Dimensions CV map 92-A mercury probe. The expected V_{fb} for a MOS capacitor with a Hg contact is ~0.55 V for moderately doped p-type c-Si. The measured V_{fb}'s for the one-step and two-step oxidation processes are –1.6 and –0.51 V, respectively. The fixed charge densities (Q_f) of the one-step and two-step oxidation are ~$2x10^{12}$ and $9x10^{10}$ cm^{-2}. Clearly, the one-step oxidation process results in a large defect density, and the two-step oxidation process results in a small defect density. Since silicide

and oxidation reactions are occurring simultaneously in the one-step oxidation process, the large charge density is attributed to unsatisfied bonds. In Chapter 3, it was shown that the one-step oxidation results in a lower silicon fraction that the two-step oxidation. Dangling bonds may result from the reduced silicon fraction since the Y-O-Si bonds cannot arrange themselves in a configuration similar to the crystal structures presented in Figs. 3.1a and 3.1b. The two-step oxidation separates the silicide and oxidation reactions allowing the yttrium and silicon to react completely before oxidation, thus allowing all bonds to be satisfied and resulting in a reduced Q_f.

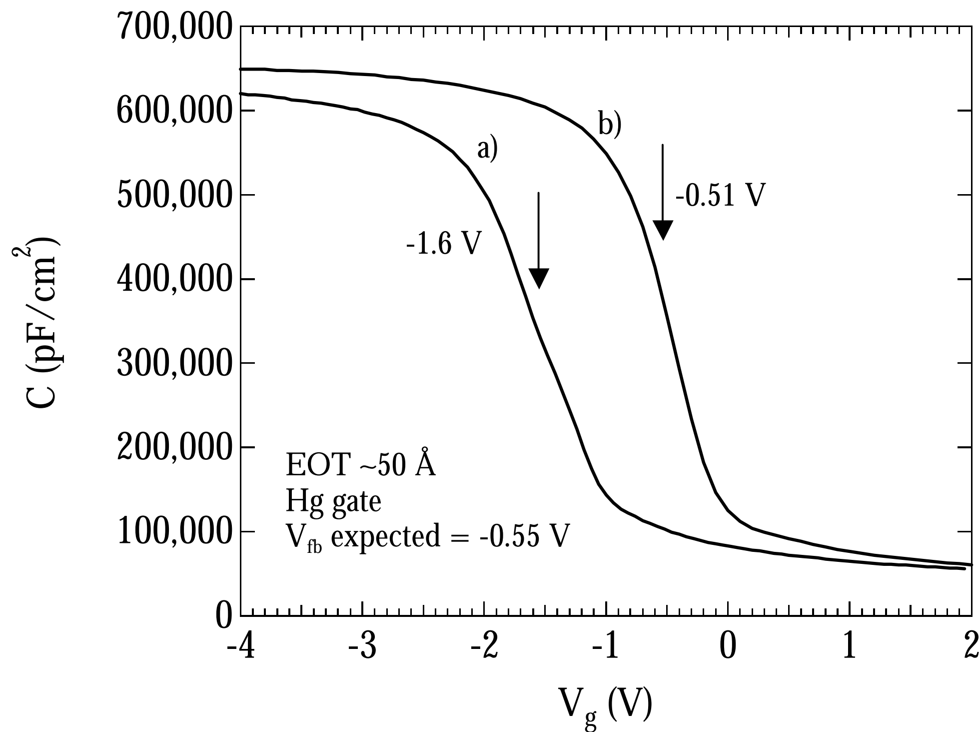

Figure A.1 C-V curves for one- (a) and two-step (b) oxidation processes.

A.2 SPUTTER AUGER ELECTRON SPECTRSCOPY

Figure A.2 presents sputter Auger electron spectroscopy (AES) results for a yttrium silicate film formed by oxidizing ~8 Å of yttrium on silicon for 15 seconds at 900 °C in air. The surface spectrum of the film indicates the presence of yttrium, silicon, oxygen and carbon near the surface. The depth profile indicates mixing of yttrium and silicon throughout the film with a gradient in the silicon concentration. This gradient is in contrast to MEIS results on similar films (see Section 5.3.2), which show a constant silicon concentration near the surface. Since silicon is a lighter element than yttrium, preferential sputtering of silicon would result in a similar profile.

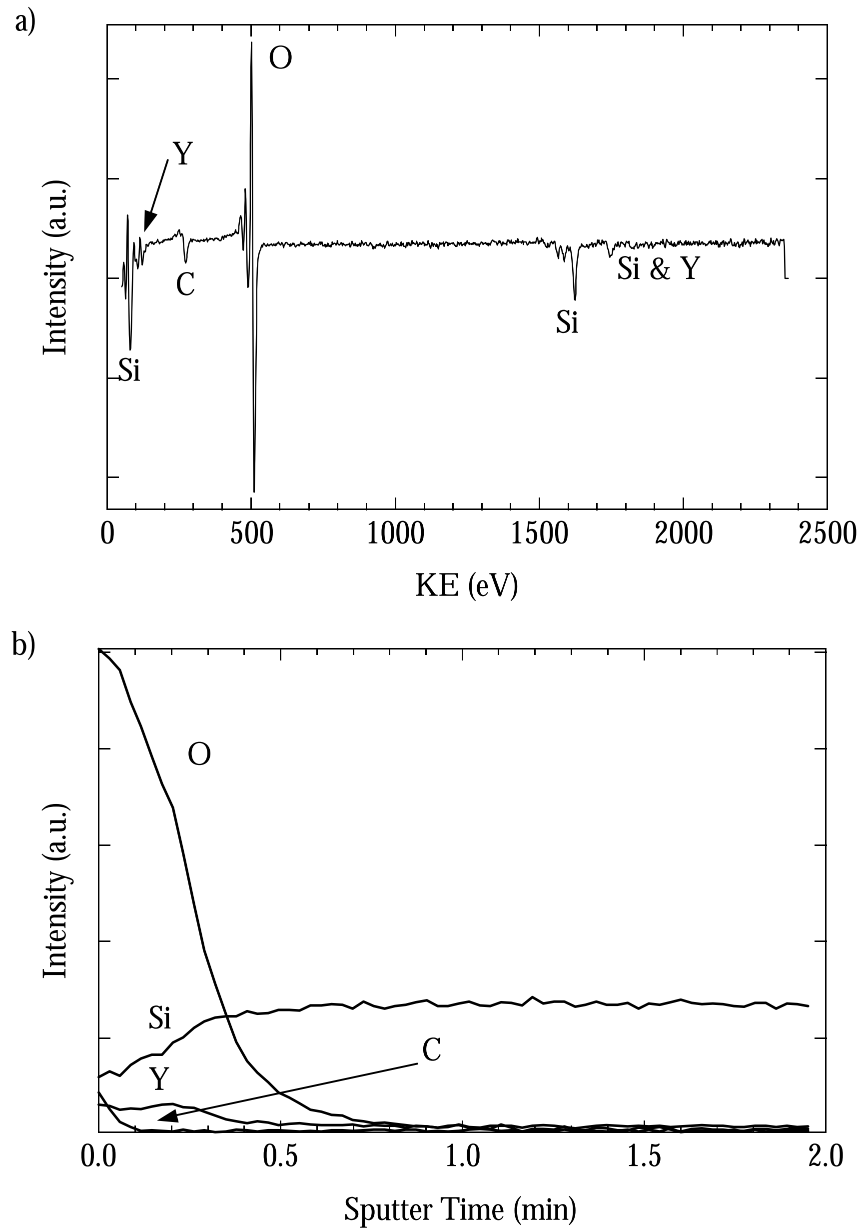

Figure A.2 AES surface spectrum (a) and AES depth profile (b) for ~8 Å yttrium film on silicon oxidized for 15 seconds in 1 atm. air.

A.3 ADDITIONAL TEM STUDIES

Figures A.3, A.4 and A.5 present the compilation of all the TEM studies performed on yttrium silicate formed by thermal oxidation of sputtered yttrium. All of the films in Figs. A.3, A.4 and A.5 were formed with ~8 Å of yttrium and oxidation at 900 °C in air for times from 1 second to 20 minutes. Figure A.3 presents the TEM images of films oxidized for 6, 15 and 60 seconds that were capped with 2000 Å of Al with no post-metallization anneal. The thickness of the films is 30, 42 and 42 Å for oxidation for 6, 15, and 60 seconds. In all instances, lattice fringes are observed in the silicon substrate, but not in the Y-O-Si film indicating amorphous Y-O-Si structure. The interface for the 6 seconds oxidation appears slightly roughened, perhaps due to the presence of silicide, but the interface is smooth for oxidation at 15 and 60 seconds. The images in Fig. A.3 all indicate the presence of one layer without any SiO_2 at the Y-O-Si/Si interface. Figure A.4 presents the TEM images of films oxidized for times ranging from 1s to 20 minutes. These films were not capped with Al, and the top layer in each image is epoxy. The thickness for oxidation of 1.0 s, 0.25, 1, 2 and 20 minutes is 31, 43, 45, 44 and 75 Å. In between the 2 minute and the 20 minute oxidation, SiO_2 grows beneath the Y-O-Si layer. For the images in Fig. A.4, where there was not an Al capping layer, contrast is observed between the top and bottom of the film. This contrast is not thought to result from the presence of a two-layer structure, as exhibited in Fig. A.5. Figure A.5 presents two TEM images taken from the same film (0.25 minute oxidation), but at different transmission thickness (i.e. different spots on the dimple). The degree of contrast and the thickness of the contrast region changes when the transmission thickness is changed indicating that the contrast results from instrument effects.

a)

b)

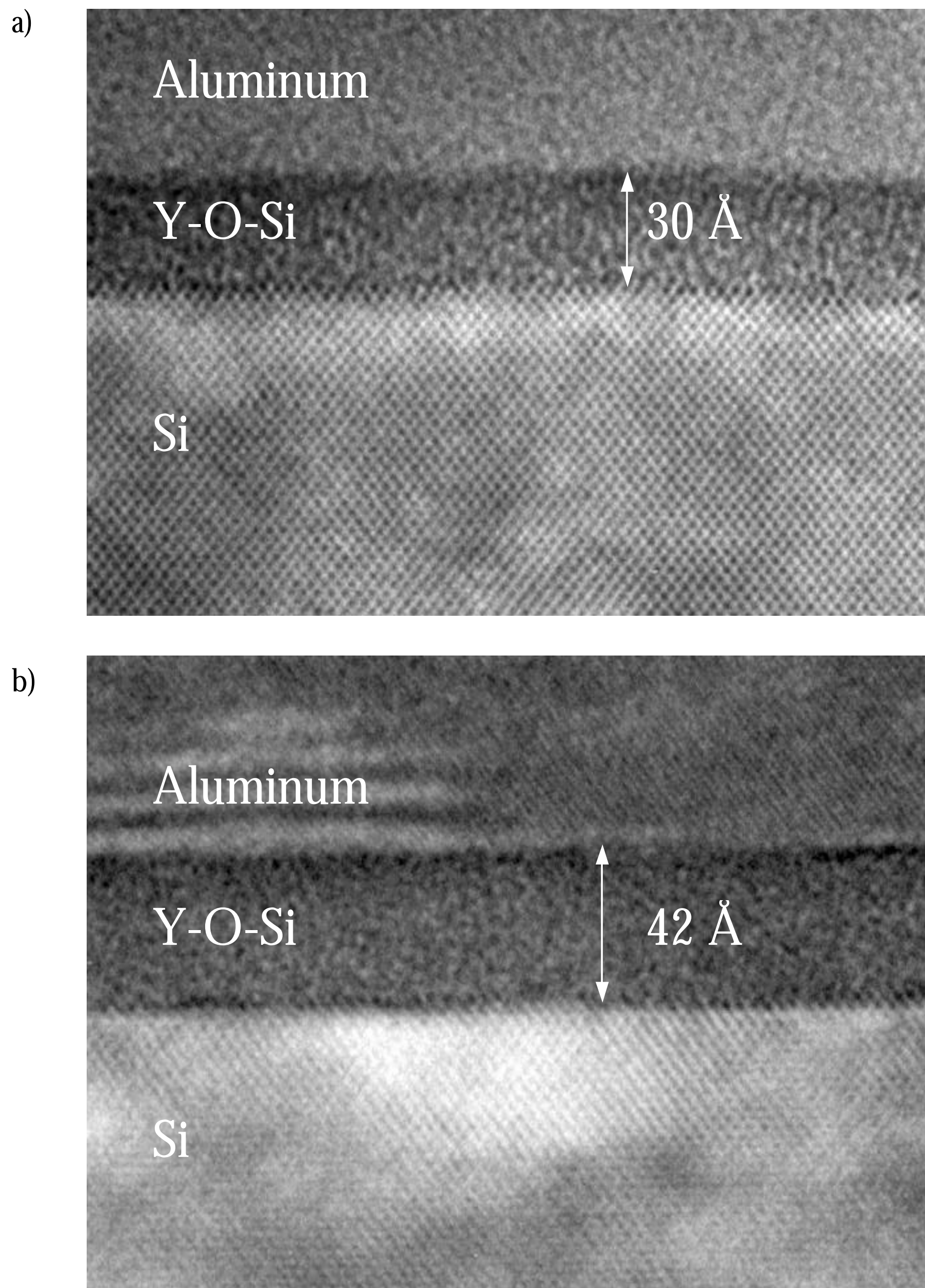

Figure A.3.1 TEM images for 6 second (a) and 15 second (b) oxidation.

c)

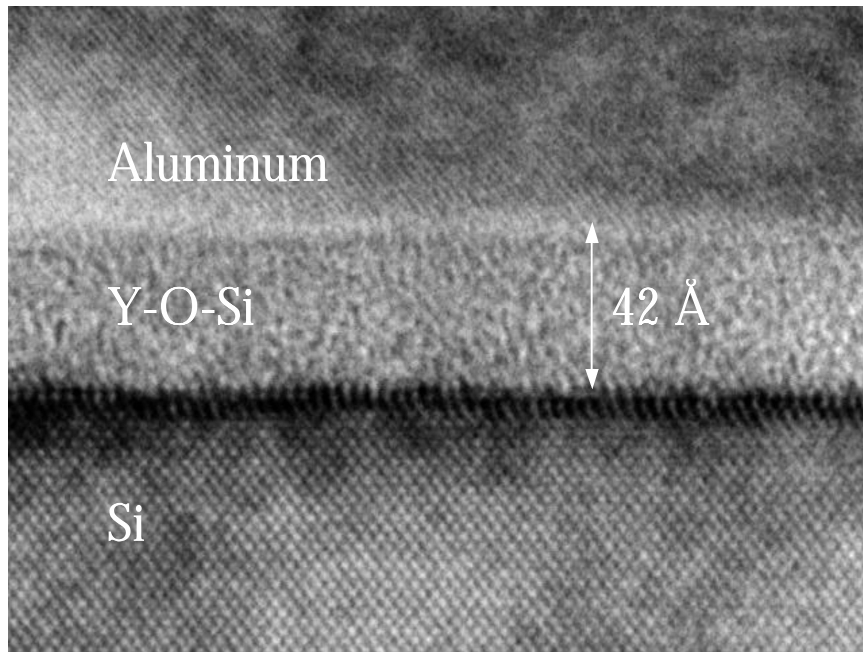

Figure A.3.2 TEM image for 60 second (c) oxidation.

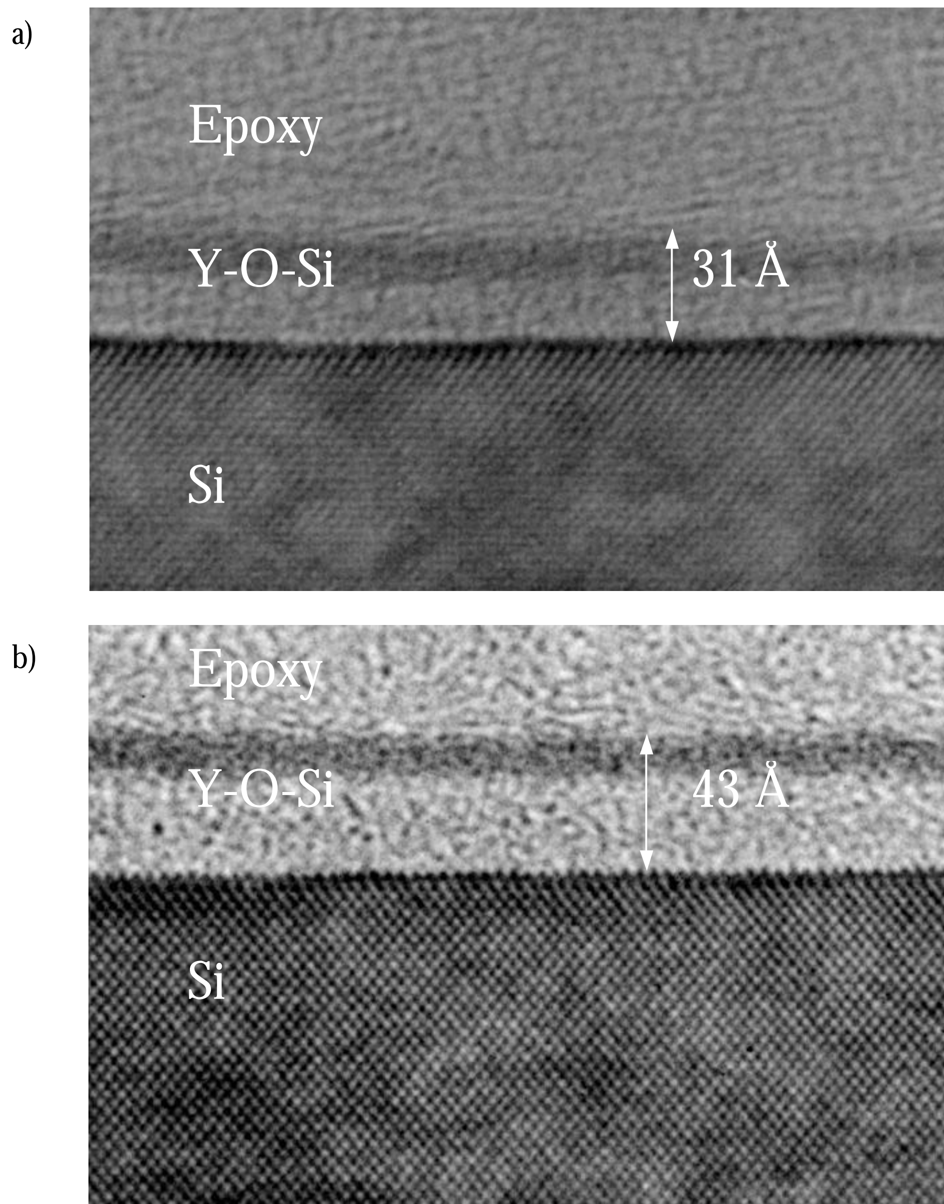

Figure A.4.1 TEM images for 1 second (a) and 15 second (b) oxidation.

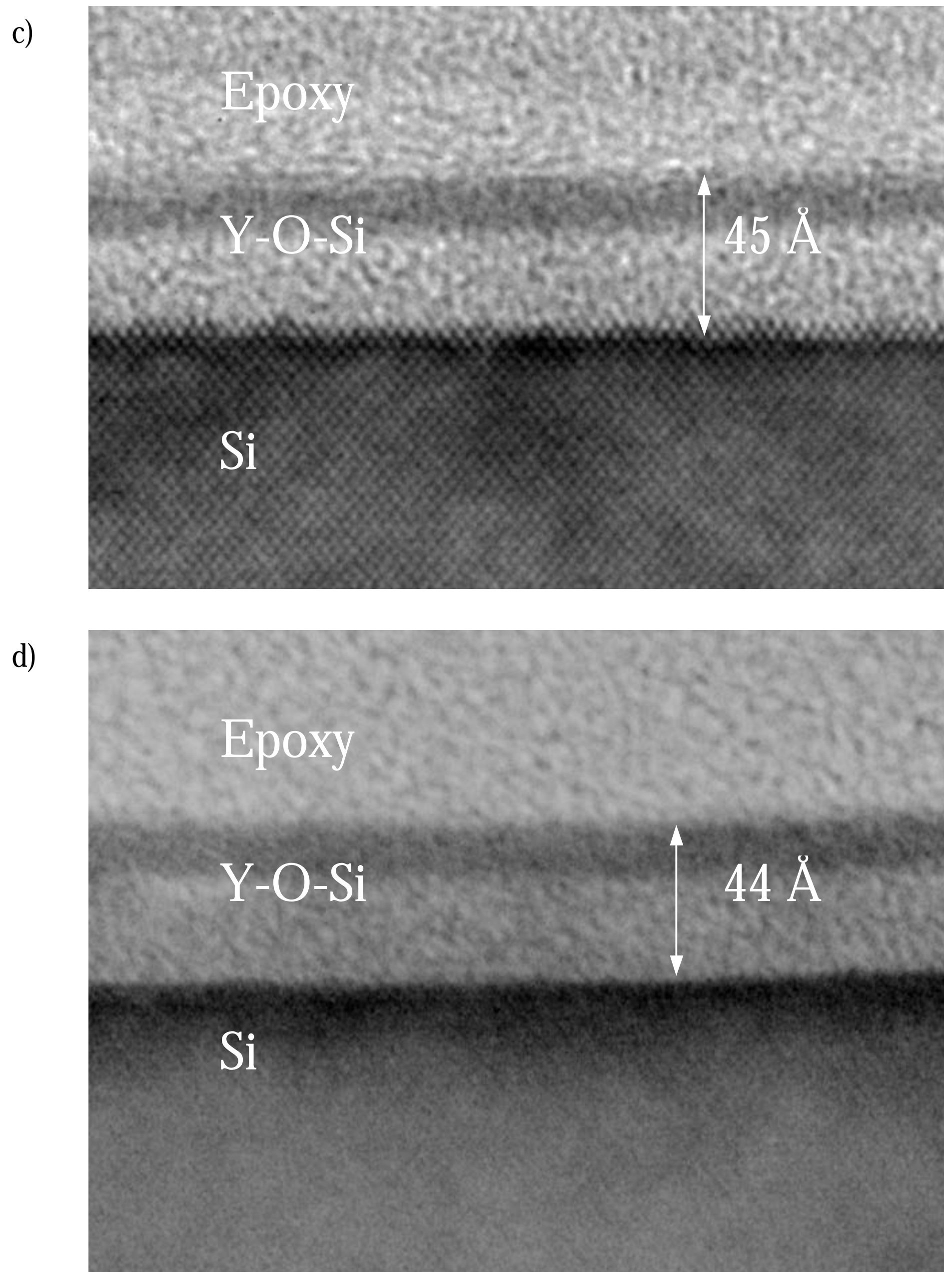

Figure A.4.2 TEM images for 1 minute (c) and 2 minute (d) oxidation.

e)

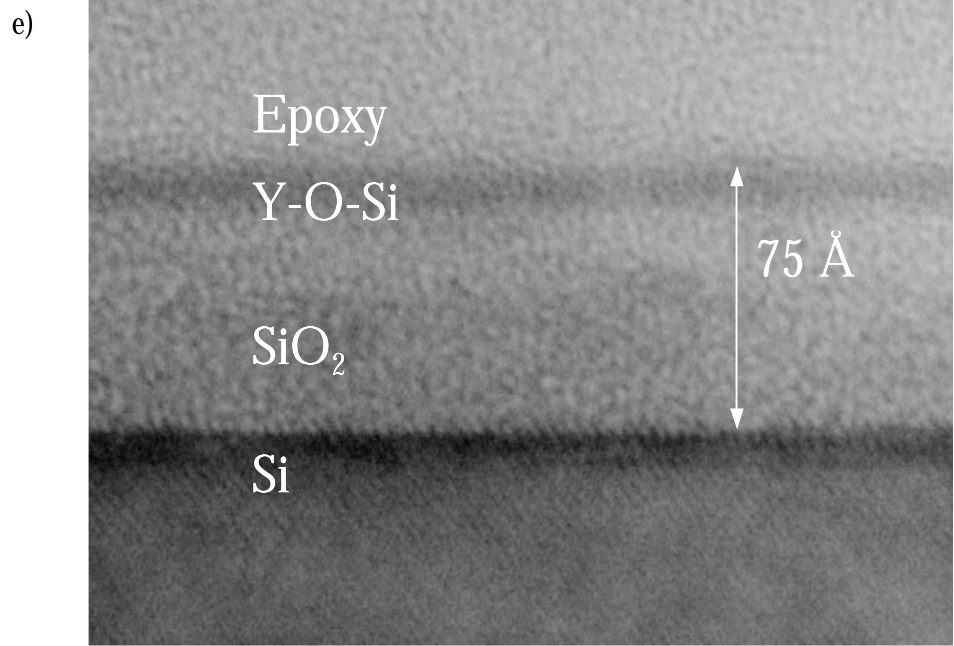

Figure A.4.3 TEM image for 20 minute (e) oxidation.

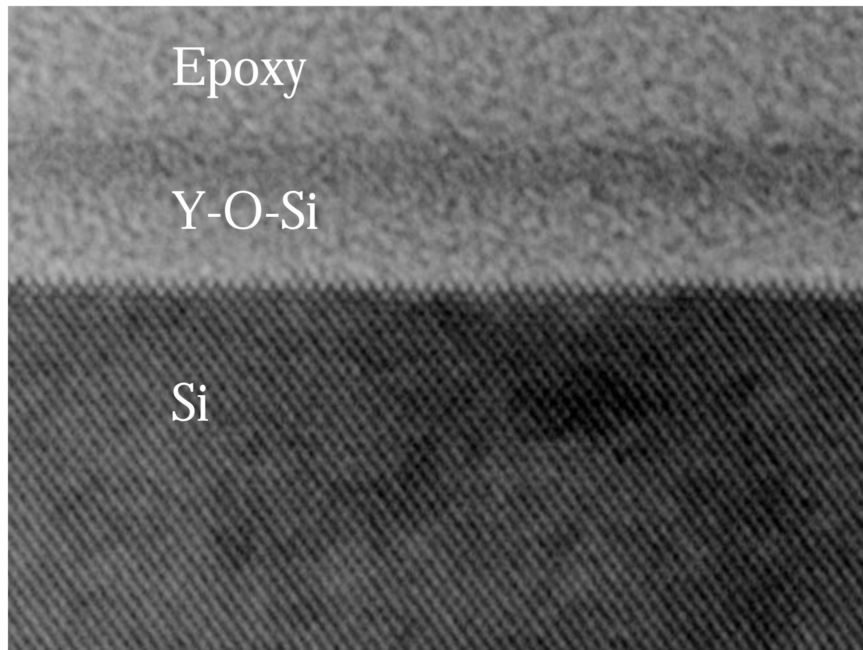

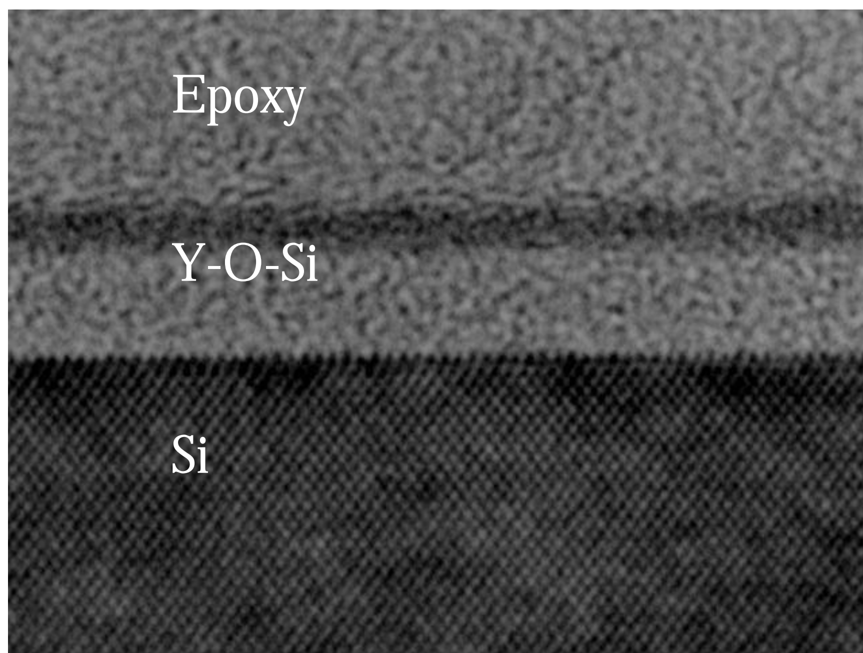

Figure A.5 TEM images for 15 second oxidation taken at different transmission thickness.

APPENDIX B

PLASMA OXIDATION

B.1 C-V TESTING OF PLASMA OXIDIZED Y-O-Si FILMS

Figure B.1 displays the results of C-V testing of a Y-O-Si film formed by sputtering ~25 Å of yttrium onto clean Si, annealing in vacuum at 300 °C for 10 minutes and remote N_2O plasma oxidizing at 300 °C for 20 minutes. The measurement was performed using a Four Dimensions CV map 92-A mercury probe at a frequency of 1 MHz. The measured EOT is 41 Å. The expected flat band voltage is –0.55 V and the measured flat band voltage is –0.48 V. The shift indicate the presence of negative fixed charge with $Q_f = 2x10^{11}$ cm^{-2}. This result is the best to date using this process.

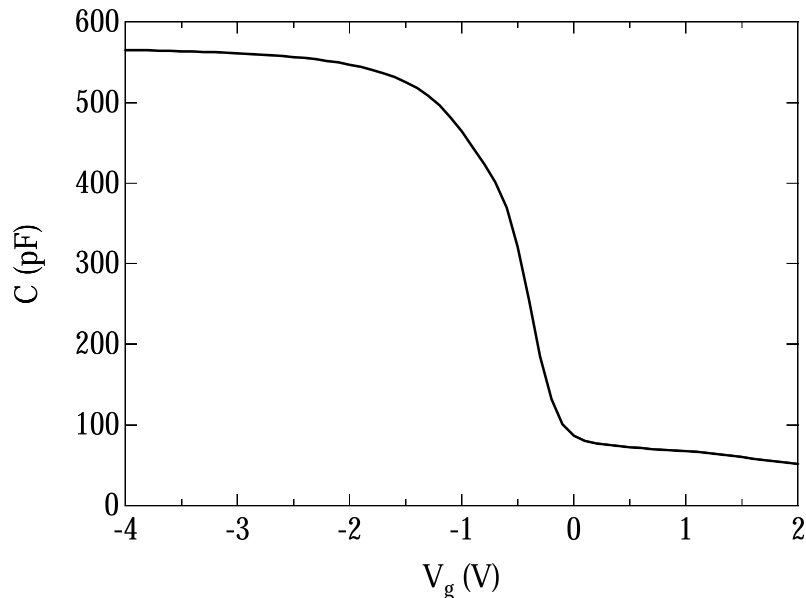

Figure B.1 C-V of Y-O-Si film formed by remote N_2O plasma oxidation.

B.2 REMOTE PLASMA OXIDATION OF TANTALUM ON SILICON

Initial results were obtained for the remote N_2O plasma oxidation of tantalum on silicon. Figure B.2 presents the Ta 4f, Si 2p and O 1s regions of the XP spectrum for Ta films sputtered for 1, 5 and 10 minutes then remote plasma oxidized in 5 mTorr N_2O at 100 °C for 10 minutes. The Ta 4f spectrum indicates that very little Ta is sputtered until ~10 minutes of sputter time. The Ta 4f peak position is consistent with Ta_2O_5, contrasting the results (Chapter 7) for the remote plasma oxidation of yttrium on silicon, which results in the Y 3d peak shifting to higher binding energy than expected for Y_2O_3 (i.e. Y-O-Si formation). The Si-O Si 2p peak positions for Ta sputter times of 1 and 5 minutes are consistent with SiO_2. For a Ta sputter time of 10 minutes, the Si-O Si 2p peak is broadened and shifted to lower binding energy consistent with a silicate. The O 1s peaks for 1 and 5 minutes Ta sputter are consistent with SiO_2. The O 1s peak for 10 minute Ta sputter is broadened towards lower binding energy consistent with a combination of oxygen-silicon and oxygen-tantalum bonding. For the 10 minute Ta sputter, since the Ta 4f peak is consistent with Ta_2O_5 and the Si-O Si 2p peak is consistent with Ta-O-Si, it is not possible to determine from these results if the remote plasma oxidation of Ta on silicon results in a Ta_2O_5 film or a Ta-O-Si film. Similar to Al-O-Si (Klein, *et al.*, APL **75**, 4001 (1999)), it is possible that the Ta 4f peak does not experience the same shifting observed for the Y 3d peak in a Y-O-Si film.

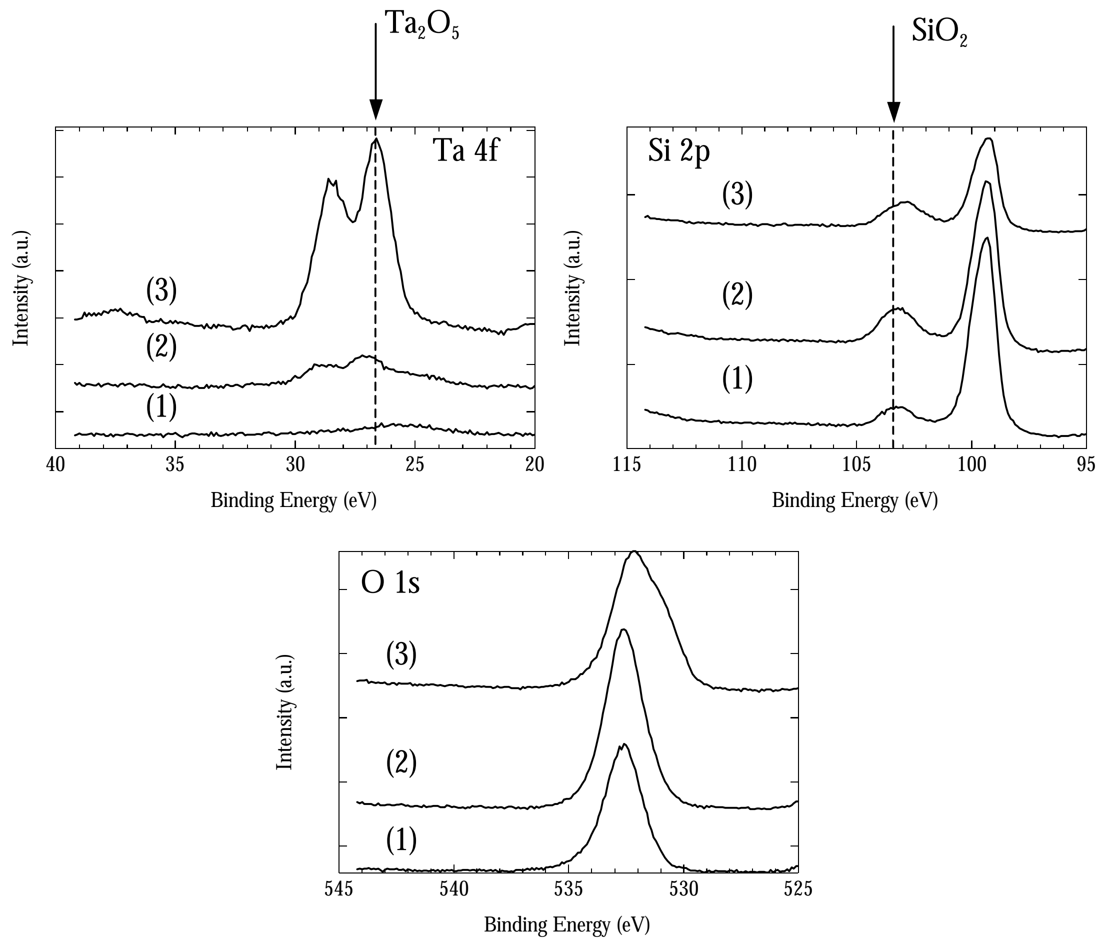

Figure B.2 Ta 4f, Si 2p and O 1s regions of the XP spectrum for Ta films on silicon remote plasma oxidized at 100 °C. (1) 1 minute Ta sputter; (2) 5 minute Ta sputter; (3) 10 minute Ta sputter

APPENDIX C

REACTIVE SPUTTERING OF YTTRIUM

C.1 ELLIPSOMETRY

Yttrium silicate films were formed using reactive sputtering. The sputtering was generally performed at an Ar:N_2O ratio of 1:2, however, some films were sputtered in 100% N_2O. The substrate temperature was held at a range of temperatures between 25-500 °C. Figure C.1 presents thickness and refractive index (n) (600 nm) results obtained using the Woolam VASE ellipsometer. The thickness versus sputter time follows a linear relationship with the y-intercept at zero and a sputter rate from the slope of ~6 Å/minute. These results do not indicate any temperature dependence of the thickness. The refractive index ranged from 1.4–1.8, exhibited a thickness dependence and a temperature dependence. The refractive index was generally lower for thinner films and lower substrate temperature.

C.2 FTIR

Figure C.2 presents FTIR results for reactively sputtered films deposited at room temperature, aged for 12 hours and annealed for 10 minutes at 900 °C in N_2. Below 700 cm^{-1}, the FTIR spectra exhibit broad modes associated with Y-O stretching. The Y-O stretching peak sharpens considerable after the film is annealed. Near 1050 cm^{-1}, the spectra exhibit a peak assigned to Si-O stretching. The Si-O stretch increases in intensity after annealing indicating silicon incorporation during the annealing step. The films deposited at 25 °C and aged for 12 hours exhibit peaks at ~1400 and ~3500 cm^{-1} assigned to absorbed carbon and water contamination, respectively. Both of these peaks have increased in

intensity after the film has aged 12 hours in ambient indicating that the contamination increases and the film degrades over time. The peaks for carbon and for water contamination do not appear in the annealed film indicating the removal of the contamination during the annealing step.

C.3 XPS

Figure C.3 presents the Y 3d, Si 2p and O 1s regions of the XP spectra for Y-O-Si films formed by reactive sputtering. The reactive sputtering was performed at Ar:N_2O ratios of 1:1, 1:2, 1:5 and 100 % N_2O at a substrate temperature of 500 °C and a sputter time of 8 minutes. The Y 3d peaks are measured at higher binding energy (~158.5 eV) than expected for Y_2O_3 (156.8 eV) indicating the presence of Y-O-Si bonding structure. For Ar:N_2O ratios from 1:1, 1:2 and 1:5, the Y 3d intensity decreases indicating that less yttrium is deposited. The decreases in sputter rate with increasing N_2O fraction is attributed changes occurring in the plasma. When the reactive sputtering is performed in 100 % N_2O, the Y 3d intensity is greatest indicating a higher yttrium deposition rate. Si-O modes (~102-103 eV) are observed in the Si 2p spectra consistent with Y-O-Si bonding. The O 1s peaks are measured at ~532.5 eV consistent with silicate bonding. During reactive sputtering of yttrium on silicon, the metal can react with the silicon during oxidation resulting in Y-O-Si bonding structure similar to the results of the preceding chapters.

C.4 ELECTRICAL TESTING

Figures C.4 presents electrical testing of Y-O-Si films deposited by reactive sputtering. The film in Fig. C.4 was deposited at a substrate temperature of 500 °C in 100 % N_2O with a sputter time of 8 minutes. The C-V testing was performed using a HP 4284a LCR meter at a test frequency of 1 MHz. The gate electrode was Al and the expected V_{fg} is

~1 V. The measured V_{fb} is –2.4, which is a shift of >1 V and clearly unacceptable. The EOT including the quantum mechanical correction is 17 Å. Using the sputter rate calculated from the ellipsometry measurements, the film thickness is ~48 Å, which corresponds to a k of ~11 consistent with a silicate film. The EOT is relatively small, but the C_{max} does not saturate and the flat band shift is excessive. The large fixed charge may result from the plasma processing and could possibly be annealed out.

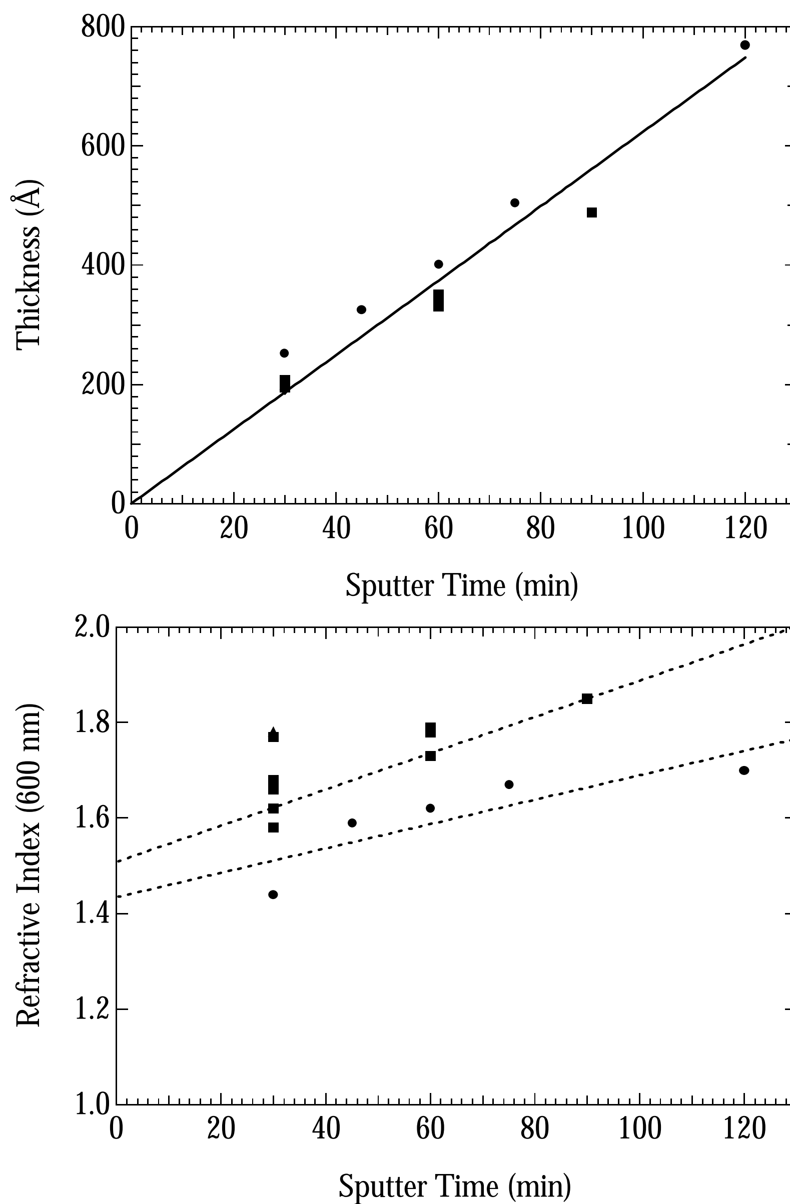

Figure C.1 Thickness (a) and refractive index (600 nm) (b) from ellipsometry for reactively sputtered Y-O-Si films. ( ) 25 °C; ( ) 300 °C; (♦) 500 °C

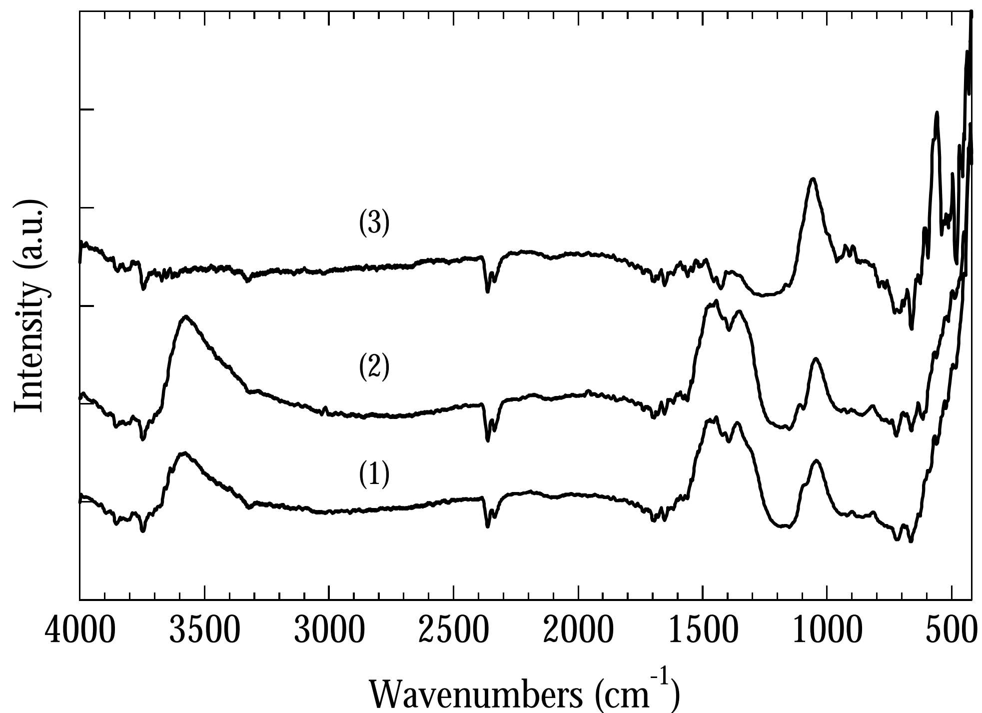

Figure C.2 FTIR spectra for reactively sputtered Y-O-Si films. The films were deposited with a Ar:N_2O ratio of 1:2 at a substrate temperature of 25 °C. The films were ~800 Å thick. (1) as deposited; (2) aged 12 hours in ambient; (3) anneal at 900 °C in N_2

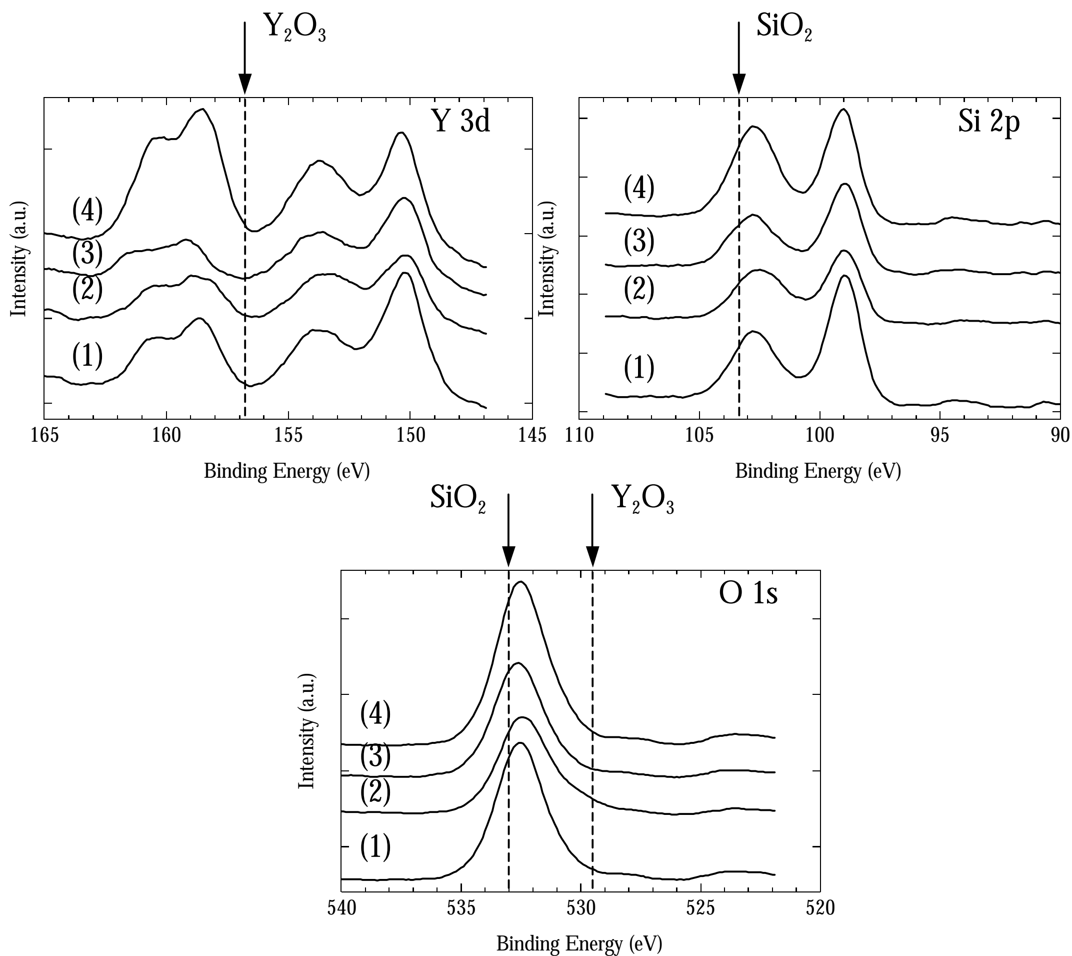

Figure C.3 Y 3d, Si 2p and O 1s regions of the XP spectra for Y-O-Si films deposited by reactive sputtering. The films were ~50 Å thick and were deposited at a substrate temperature of 500 °C using Ar:N_2O ratios of : (1) 1:1; (2) 1:2; (3) 1:5; (4) 100 % N_2O.

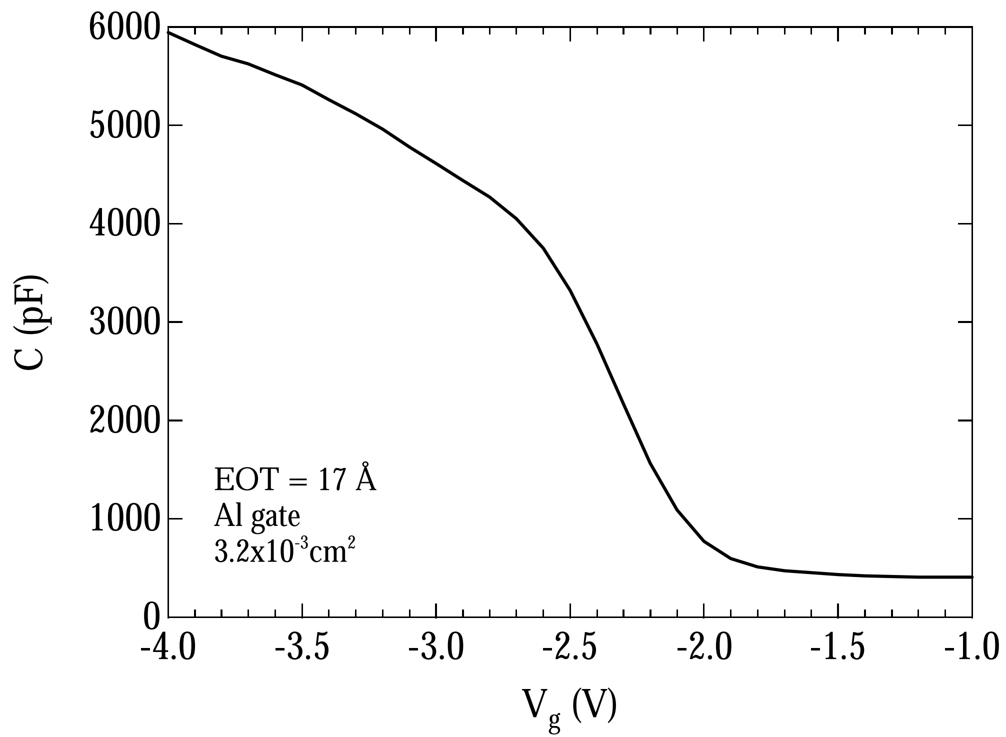

Figure C.4 C-V characteristic of Y-O-Si film deposited by reactive sputtering.

“If we only wanted to be happy, it would be easy;

but we want to be happier than other people, which is difficult,

since we think them happier than they are.”

Montesquieu (1689-1755)